



저작자표시-비영리-동일조건변경허락 2.0 대한민국

이용자는 아래의 조건을 따르는 경우에 한하여 자유롭게

- 이 저작물을 복제, 배포, 전송, 전시, 공연 및 방송할 수 있습니다.
- 이차적 저작물을 작성할 수 있습니다.

다음과 같은 조건을 따라야 합니다:



저작자표시. 귀하는 원저작자를 표시하여야 합니다.



비영리. 귀하는 이 저작물을 영리 목적으로 이용할 수 없습니다.



동일조건변경허락. 귀하가 이 저작물을 개작, 변형 또는 가공했을 경우에는, 이 저작물과 동일한 이용허락조건하에서만 배포할 수 있습니다.

- 귀하는, 이 저작물의 재이용이나 배포의 경우, 이 저작물에 적용된 이용허락조건을 명확하게 나타내어야 합니다.
- 저작권자로부터 별도의 허가를 받으면 이러한 조건들은 적용되지 않습니다.

저작권법에 따른 이용자의 권리는 위의 내용에 의하여 영향을 받지 않습니다.

이것은 [이용허락규약\(Legal Code\)](#)을 이해하기 쉽게 요약한 것입니다.

[Disclaimer](#)

공학박사 학위논문

**Characteristics of Cu(In,Ga)Se₂
Thin Film Solar Cells Fabricated by
RF Sputtering of Single CIGS Targets**

CIGS 단일 타겟의 RF 스퍼터링에 의해 제조된
Cu(In,Ga)Se₂ 박막형 태양전지의 특성

2014년 2월

서울대학교 대학원

재료공학부

정 성 목

Characteristics of Cu(In,Ga)Se₂ Thin Film Solar Cells Fabricated by RF Sputtering of Single CIGS Targets

CIGS 단일 타겟의 RF 스퍼터링에 의해 제조된
Cu(In,Ga)Se₂ 박막형 태양전지의 특성

지도 교수 유 상 임

이 논문을 공학박사 학위논문으로 제출함
2014 년 2 월

서울대학교 대학원
재료공학부
정 성 목

정성목의 박사 학위논문을 인준함
2014 년 2 월

위 원 장 박 병 우 (인)

부위원장 유 상 임 (인)

위 원 박 찬 (인)

위 원 김 영 환 (인)

위 원 조 소 혜 (인)

Abstract

Characteristics of Cu(In,Ga)Se₂ Thin Film Solar Cells Fabricated by RF Sputtering of Single CIGS Targets

Sung-Mok Jung

Department of Materials Science and Engineering

The Graduate School

Seoul National University

Solar cells have attracted great attention with the increase of problems such as an energy crisis and an environmental pollution. Particularly, thin film solar cells have been extensively investigated due to their small consumption of raw materials and possibility of lightweight. Among them, Cu(In,Ga)Se₂ (CIGS) solar cell has attracted worldwide attention due to its merits of high conversion efficiency and stability. However, a very complicated fabrication process, so-called three-stage co-evaporation process, is required for the achievement of the highest conversion efficiency of ~20%. In addition, this method has a difficulty to produce large-area film with uniform composition.

In this thesis, the properties of CIGS films and CIGS solar cells prepared by RF sputtering of single CIGS targets were investigated. In addition, antireflection (AR) coating and transparent conducting Al-doped ZnO (AZO) films was studied, which are necessary to enhance efficiency. The major

results are as in the following.

First, multi-layer antireflection (AR) coatings such as double- and triple-layer with ZnS and MgF₂ were investigated. For this study, ZnS and ZnS-MgF₂ composite films were prepared on soda-lime glass substrates and their optical constants were determined by envelope method. And MgF₂ film was deposited on GaAs substrate by rf magnetron sputtering and their optical constants were determined by spectroscopic ellipsometry. In particular, ZnS-MgF₂ composite films were fabricated by co-sputtering of ZnS and MgF₂ target to obtain intermediate refractive index material for a middle layer in the triple-layer AR coating and these films exhibited the desired intermediate refractive index. All films were highly transparent in the range from visible and near-infrared (IR). In the case of ZnS-MgF₂ composite film, optical absorption edge was continuously shifted to short wavelength and refractive index decreased with increasing concentration of Mg and F. Based on the extracted optical constants, single-, double- and triple-layer AR coatings on GaAs substrates were designed by using a quarter-wave thickness at a normal incidence and fabricated by rf magnetron sputtering. The experimental results of AR coating were compared to simulated results. Low reflectance could be obtained from single-layer AR coating only at a specific wavelength and could be obtained from multi-layer AR coating at wide wavelength regime. Additionally, incident angle dependence of the reflectance of the multi-layer AR coatings was also investigated and showed different behavior according to a number of layers.

Second, the characteristics of the transparent conducting Al-doped ZnO (AZO) films were investigated. Al-doped ZnO films were deposited on soda-

lime glass substrates by using dc magnetron sputtering as a function of argon gas pressure, O₂/Ar gas ratio and substrate temperature, and their electrical and optical properties were investigated. As a result, the resistivity of the AZO films decreased with decreasing argon gas pressure or O₂/Ar gas ratio. As the substrate temperature was increased, resistivity decreased continuously and the lowest value of resistivity was obtained at the temperature of 250 °C in pure Ar and 250-300 °C in O₂/Ar ratio of 1.23%, respectively. The higher substrate temperature increased the resistivity a little. The transmittance was found to be very sensitive to O₂/Ar gas ratio and substrate temperature. Addition of a very small amount of oxygen to argon (1.23% of O₂/Ar ratio) or slight increase of the substrate temperature from room temperature to 150 °C enhanced the transmittance in visible region remarkably. Conclusively, the AZO films with low resistivity of order of 10⁻⁴ Ωcm and high transparency in visible region could be prepared at the substrate temperatures of above 150 °C (the lowest resistivity of 3.19 × 10⁻⁴ Ωcm at 250 °C) by dc magnetron sputtering and these films are applicable to various fields which require transparent conducting oxide films as well as solar cell field.

Third, the properties of CIGS absorber layers prepared by RF sputtering without selenization were investigated. For this study, various single CIGS sputtering targets with the nominal compositions of Cu_x(In_{0.7}Ga_{0.3})Se_y (x=0.95~1, y=2~2.5) were fabricated. Employing these targets, CIGS films were deposited on Mo coated soda lime glass (SLG) substrates by using RF magnetron sputtering. When the CIGS precursor film deposited at room temperature using a stoichiometric CIGS target was annealed in an Ar atmosphere, grain growth of the CIGS film did not occur regardless of the

post-annealing temperature. Grain size of the CIGS films was increased with increasing a deposition temperature. However, rough and porous surface morphology with the faceted grains was obtained and therefore very low efficiencies were achieved. For enhancing the efficiency and obtaining the smooth surface morphology, various CIGS targets with the nominal compositions of $\text{Cu}_{0.95}(\text{In}_{0.7}\text{Ga}_{0.3})\text{Se}_{2.5}$ and $\text{Cu}_{0.95}(\text{In}_{0.7}\text{Ga}_{0.3})\text{Se}_{2.1}$ were used to fabricate CIGS absorber layer. Grain size of these films was smaller than that of the CIGS film fabricated using a stoichiometric CIGS target. This result is thought to be caused by Cu-poor composition of these CIGS targets. Although the CIGS films with a smoother surface morphology can be obtained by using Cu-poor CIGS targets, surface morphology becomes rough with increasing deposition temperature. Conversion efficiency of about 2% was obtained from the CIGS solar cell fabricated using the $\text{Cu}_{0.95}(\text{In}_{0.7}\text{Ga}_{0.3})\text{Se}_{2.5}$ target. However, the CIGS solar cells fabricated using the $\text{Cu}_{0.95}(\text{In}_{0.7}\text{Ga}_{0.3})\text{Se}_{2.1}$ target, containing the smaller quantity of Se, showed the lower conversion efficiency. Meanwhile, for supplement of selenium, CIGS films fabricated by using the single target of $\text{Cu}(\text{In}_{0.7}\text{Ga}_{0.3})\text{Se}_{2.5}$ powder were annealed in Ar atmosphere with selenium. These films showed the densely packed surface morphology. Conversion efficiency of the solar cells fabricated using these CIGS films was enhanced. Consequentially, selenization process is beneficial to improvement of structural and electrical properties. Hence, in the next study, the effect of selenization of CIGS precursor film was systematically investigated.

Finally, the characteristics of CIGS absorber layers after selenization of CIGS precursor film deposited at room temperature were systematically investigated. In this study, the CIGS targets with various compositions of

$\text{Cu}_x(\text{In}_{0.7}\text{Ga}_{0.3})\text{Se}_y$ (where $x=0.9, 1; y=2, 2.2, 2.5$) were fabricated. Utilizing these targets, the CIGS precursor films were produced by RF magnetron sputtering at room temperature. The CIGS precursor films were then selenized in a tube furnace under Se atmosphere using Se powder. From the stoichiometric CIGS target, Cu-rich CIGS films were obtained and very low conversion efficiencies were achieved due to inappropriate composition and porous and rough surface morphology with large grains. In contrast, the CIGS films fabricated by using the Cu-poor CIGS target showed the device-quality stoichiometry ratio and densely packed surface morphology with small grains, as well as the chalcopyrite structure without the second phases. Increase of the Se content in the single CIGS target led to decrease of the Cu content and increase of the (In+Ga) content in the CIGS film, which created the ordered vacancy compound (OVC) phases and increased the band gap (E_g) of the CIGS film resulting in increase of the open-circuit voltage (V_{oc}). The difference between $E_g/q - 0.5\text{V}$ and V_{oc} was remarkably decreased with the formation of the OVC phases. The highest efficiency of 6.88% could be achieved from the CIGS solar cell fabricated by using the Cu-poor and Se-excess target with the nominal composition of $\text{Cu}_{0.9}(\text{In}_{0.7}\text{Ga}_{0.3})\text{Se}_{2.2}$. Consequently, the composition of the single CIGS target was found to play a key role in the structural and electrical properties of the CIGS film and CIGS thin film solar cell efficiency.

Characteristics of CIGS films selenized using mixing powders with various weight ratios of alumina to selenium were investigated. For this experiment, the CIGS precursor films were deposited using the single CIGS targets with the nominal compositions of $\text{Cu}_{0.9}(\text{In,Ga})\text{Se}_2$ and $\text{Cu}_{0.9}(\text{In,Ga})\text{Se}_{2.5}$. As the

results, regardless of target composition, grain size was increased with increasing the Se ratio of mixing powder. The MoSe₂ layer was formed between the CIGS and the Mo layer and its thickness was also increased with increasing the Se ratio of mixing powder. The MoSe₂-layer thickness of the CIGS film fabricated using the Cu_{0.9}(In_{0.7}Ga_{0.3})Se_{2.5} target is thicker than that of the CIGS film fabricated using the Cu_{0.9}(In_{0.7}Ga_{0.3})Se₂ target because of larger amount of Se in the CIGS film fabricated using the Cu_{0.9}(In_{0.7}Ga_{0.3})Se_{2.5} target. From the auger electron spectroscopy (AES) depth profiles after selenization of the CIGS films, it was found that each element of the CIGS film was evenly distributed in the CIGS films without grading of elements. This means that the CIGS phases including the OVC phase in the CIGS film fabricated using Cu_{0.9}(In_{0.7}Ga_{0.3})Se_{2.5} target are evenly distributed. The open-circuit voltages of the CIGS solar cells fabricated using the Cu_{0.9}(In_{0.7}Ga_{0.3})Se_{2.5} target were generally higher than those of solar cells fabricated using the Cu_{0.9}(In_{0.7}Ga_{0.3})Se₂ target. However, the open-circuit voltage of the CIGS solar cells fabricated using the Cu_{0.9}(In_{0.7}Ga_{0.3})Se_{2.5} target was decreased with decreasing Se ratio of mixing powder used for selenization.

Also, characteristics of CIGS films selenized using nanocrystalline precursor film were investigated. CIGS films were deposited at various temperatures using a single quaternary Cu_{0.9}(In_{0.7}Ga_{0.3})Se_{2.5} target. Based on the results of XRD patterns and TEM images, as-deposited CIGS films fabricated at the temperatures of 120 °C and 130 °C were considered as the nano-crystalline CIGS precursor films and selenized at 475 °C for 30min. The CIGS films showed a (112) preferred orientation. All of the selenized CIGS films had the

similar composition regardless of deposition temperature although Cu content in the film was slightly different. From the Raman spectra of the CIGS films, the existence of OVC phase which can lead to decrease of open-circuit voltage loss was identified. The CIGS film with smooth and dense surface morphology as well as the large grain size was obtained by increase of Se ratio in a tube furnace and using the nano-crystalline CIGS precursor film. And the thickness of the MoSe₂ layer was decreased after selenization of the nano-crystalline CIGS precursor film compared to that of the amorphous CIGS precursor film. The highest efficiency was achieved from the CIGS solar cell fabricated using the nanocrystalline CIGS precursor film deposited at 130 °C and its value is 8.09 % with the open-circuit voltage of 0.571V, short-circuit current density of 26.58 mA/cm² and the fill factor of 53.28%. This result is thought to be achieved by the beneficial factors such as the existence of an OVC phase, the thickness reduction of a MoSe₂ layer, smooth surface morphology and the decrease of defect density achieved by dense CIGS film with large grain.

Keywords: CIGS thin film solar cell, single quaternary CIGS target, selenization, nanocrystalline CIGS precursor film, Orderd vacancy compound, Zinc sulfide, Magnesium fluoride, Antireflection coating, Optical constants, RF magnetron sputtering, Al-doped ZnO, Substrate temperature, Oxygen partial pressure, DC magnetron sputtering

Student Number: 2007-30808

Contents

List of Tables and Figures	xi
Chapter 1 General Background.....	1
1.1 Historical reviews on solar cells.....	1
1.2 CIGS thin film solar cell.....	2
1.2.1 Growth process of CIGS film	2
1.2.1.1 Three-stage co-evaporation process	2
1.2.1.2 Two step process	4
1.2.1.3 Other deposition processes.....	4
1.3 Architecture of CIGS solar cells.....	5
1.3.1 Architecture	5
1.3.1.1 CIGS absorber layer	5
1.3.1.2 Buffer layer.....	6
1.3.1.3 Window layer.....	7
1.3.1.4 Electrode (bottom, top).....	8
Chapter 2 Design and fabrication of multi-layer antireflection coating for III-V solar cell	20
2.1 Introduction	20
2.2 Experimental.....	21
2.3 Results and discussion.....	23
2.4 Summary.....	26
Chapter 3 Characteristics of transparent conducting Al-doped ZnO films prepared by dc magnetron sputtering....	36

2.1	Introduction	36
2.2	Experimental	37
2.3	Results and discussion.....	38
2.4	Summary.....	43
Chapter 4	CIGS absorber layers prepared by RF sputtering without selenization for CIGS solar cells.....	59
4.1	Introduction	59
4.2	Experimental.....	59
4.3	Results and discussion.....	62
4.3.1	CIGS layers prepared using the single CIGS targets of various compositions.....	62
4.3.2	CIGS layers prepared using the single target of Cu(In _{0.7} Ga _{0.3})Se _{2.5} powder.....	64
4.4	Summary.....	66
Chapter 5	CIGS absorber layers prepared by RF sputtering with selenization for CIGS solar cells	83
5.1	Introduction	83
5.2	Experimental.....	85
5.3	Results and discussion.....	87
5.3.1	CIGS layers prepared using the single CIGS targets of various compositions	87
5.3.1.1	A CIGS target with the nominal composition of Cu(In _{0.7} Ga _{0.3})Se ₂	87
5.3.1.2	A Cu-poor CIGS target with the nominal composition of Cu _{0.9} (In _{0.7} Ga _{0.3})Se ₂	89

5.3.1.3 A Cu-poor and a Se-excess CIGS targets with the nominal compositions of $\text{Cu}_{0.9}(\text{In}_{0.7}\text{Ga}_{0.3})\text{Se}_{2.2}$ and $\text{Cu}_{0.9}(\text{In}_{0.7}\text{Ga}_{0.3})\text{Se}_{2.5}$	92
5.3.2 Effect of selenization condition on the CIGS layers	95
5.3.3 CIGS layers prepared using nanocrystalline precursor film	100
5.4 Summary.....	106
Chapter 6 Summary.....	148
Publications.....	154
Abstract in Korean.....	156

List of Tables

Table. 1.1. Experimental details for coating of CdS layer.....	15
Table. 3.1. Optical band gap values of the AZO films deposited at various process parameters.	47
Table. 4.1. Summary of conversion efficiencies shown in Fig. 4.13.....	69
Table 5.1. Composition of the CIGS films fabricated using a stoichiometric CIGStarget.	112
Table 5.2. Composition of the CIGS films fabricated using a Cu-poor CIGS target ($\text{Cu}_{0.9}(\text{In}_{0.7}\text{Ga}_{0.3})\text{Se}_2$).	113
Table 5.3. Composition of the CIGS films fabricated using Se-excess CIGS targets with a Cu-poor composition.	114
Table 5.4. Summary of efficiency of the CIGS solar cells fabricated in this study. (As a function of target composition and selenization temperature). .	115
Table 5.5. Composition before and after selenization of CIGS precursor films deposited using the single CIGS targets with the nominal compositions of (a) $\text{Cu}_{0.9}(\text{In,Ga})\text{Se}_2$ and (b) $\text{Cu}_{0.9}(\text{In,Ga})\text{Se}_{2.5}$. The CIGS films were selenized using mixing powders with various weight ratios of alumina to selenium... .	116
Table 5.6. Summary of the conversion efficiencies shown in Fig. 5.17.....	117

Table 5.7. Intensity ratio of the CIGS films shown in Fig. 5.19.	118
Table 5.8. Composition before and after selenization of the CIGS precursor films deposited at (a) room temperature, (b) 120 and (c) 130 °C.....	119
Table 5.9. RMS roughness of the CIGS films shown in Fig. 5.25.....	120
Table 5.10. Summary of the conversion efficiencies shown in Fig. 5.26.....	121

List of Figures

Fig. 1.1. Best research-cell efficiencies chart for various photovoltaic technologies, which is compiled by National Renewable Energy Laboratory (NREL).....	16
Fig. 1.2. Schematic of three-stage co-evaporation process.....	17
Fig. 1.3. Cross-sectional schematic of a CIGS solar cell.....	18
Fig. 1.4. Experimental procedure for coating of the CdS layer.....	19
Fig. 2.1. Transmittance spectra of ZnS and ZnS-MgF ₂ films on SLG substrates depending on wavelength.....	30
Fig. 2.2. (a) Refractive index and (b) extinction coefficient of ZnS-MgF ₂ composite films depending on rf power applied to MgF ₂ . Optical constants of pure ZnS and MgF ₂ were also exhibited.	31
Fig. 2.3. EPMA results and refractive index variation at the wavelength of 632 nm for ZnS-MgF ₂ composite films depending on rf power applied to MgF ₂	32
Fig. 2.4. Simulated reflectance spectra of GaAs substrate with single-, double- and triple-layer antireflection coating depending on wavelength. All structures are designed by quarter-wave coating at a reference wavelength of 600 nm. Reflectance spectra were theoretically calculated by Essential Macleod program.	33
Fig. 2.5. Measured (solid line) and simulated (dash line) reflectance spectra of	

GaAs substrate with (a) single-layer (b) double-layer and (c) triple-layer antireflection coating. ZnS50W-MgF₂140W composite film was used as intermediate refractive index material in triple-layer AR coating..... 34

Fig. 2.6. Simulated reflectance spectra of (a) double-layer and (b) triple-layer AR coating as a function of incident angle. 35

Fig. 3.1. (a) Resistivity, (b) carrier concentration and Hall mobility of the AZO films deposited at various argon gas pressures. 48

Fig. 3.2. FE-SEM images of the AZO films deposited at argon gas pressures of (a) 3 mTorr, (b) 5 mTorr, (c) 10 mTorr and (d) 15 mTorr..... 49

Fig. 3.3. Optical transmittance spectra of the AZO films depending on argon gas pressure in the visible and near-infrared wavelength region. 50

Fig. 3.4. (a) Resistivity and (b) transmittance of the AZO films deposited at room temperature with various O₂/Ar gas ratios..... 51

Fig. 3.5. XRD patterns of the AZO films deposited at room temperature with various O₂/Ar gas ratios. 52

Fig. 3.6. (a) Resistivity, (b) carrier concentration and Hall mobility of the AZO films depending on the substrate temperature..... 53

Fig. 3.7. FE-SEM images of the AZO films deposited at substrate temperature of (a) room temperature, (b) 150 °C, (c) 200 °C, (d) 250 °C, (e) 300 °C and (f) 350 °C under pure argon gas pressure..... 54

Fig. 3.8. Transmittance spectra of the AZO films deposited at various temperatures in (a) pure Ar and (b) O ₂ /Ar gas ratio of 1.23%	55
Fig. 3.9. (a) Resistivity, (b) carrier concentration and Hall mobility of the AZO films deposited at 250 °C with various O ₂ /Ar gas ratios.	56
Fig. 3.10. Transmittance spectra of the AZO films deposited at 250 °C with various O ₂ /Ar gas ratios.	57
Fig. 3.11. Optical band gap of the AZO films deposited at various substrate temperatures in (a) pure Ar and (b) O ₂ /Ar gas ratio of 1.23%	58
Fig. 4.1. Surface morphology of the CIGS film deposited at (a) room temperature and the CIGS films annealed at (b) 400 °C (c) 500 °C and (d) 600 °C in an Ar atmosphere. The CIGS film was fabricated using a stoichiometric CIGS (Cu(In _{0.7} Ga _{0.3})Se ₂) target.	70
Fig. 4.2. Surface morphology of the CIGS films deposited at (a) room temperature, (b) 300 °C, (c) 350 °C, (d) 400 °C and (e) 450 °C. The CIGS film was fabricated using a stoichiometric CIGS (Cu(In _{0.7} Ga _{0.3})Se ₂) target.	71
Fig. 4.3. Current-voltage characteristics of the CIGS solar cells fabricated using a stoichiometric CIGS (Cu(In _{0.7} Ga _{0.3})Se ₂) target. The CIGS absorber layers were deposited at the temperatures of 300, 350, 400 and 450 °C, respectively.	72
Fig. 4.4. Surface morphology and cross-sectional image of the CIGS films fabricated using a Cu _{0.95} (In _{0.7} Ga _{0.3})Se _{2.5} target. The CIGS film was deposited at 300 °C.	73

Fig. 4.5. Surface morphology of the CIGS films deposited at (a) 300 °C, (b) 350 °C, (c) 400 °C and (d) 450 °C. The CIGS film was fabricated using a $\text{Cu}_{0.95}(\text{In}_{0.7}\text{Ga}_{0.3})\text{Se}_{2.1}$ target.....	74
Fig. 4.6. XRD patterns of the CIGS films fabricated using $\text{Cu}_{0.95}(\text{In}_{0.7}\text{Ga}_{0.3})\text{Se}_{2.5}$ and $\text{Cu}_{0.95}(\text{In}_{0.7}\text{Ga}_{0.3})\text{Se}_{2.1}$ target.	75
Fig. 4.7. Current-voltage characteristics of the CIGS solar cells fabricated using the $\text{Cu}_{0.95}(\text{In}_{0.7}\text{Ga}_{0.3})\text{Se}_{2.5}$ and $\text{Cu}_{0.95}(\text{In}_{0.7}\text{Ga}_{0.3})\text{Se}_{2.1}$ target. The CIGS absorber layers were deposited at the temperatures of 300 °C and 350 °C, respectively.	76
Fig. 4.8. Ternary phase diagram of the CIGS targets and the CIGS films fabricated using these CIGS targets	77
Fig. 4.9. Surface morphology of the CIGS films deposited at (a) room temperature (b) 350 °C, (c) 400 °C, (d) 450 °C and (e) 500 °C. The CIGS film was fabricated using the single target of $\text{Cu}(\text{In}_{0.7}\text{Ga}_{0.3})\text{Se}_{2.5}$ powder.....	78
Fig. 4.10. Surface morphology after selenization of the CIGS films deposited at (a) room temperature (b) 350 °C, (c) 400 °C, (d) 450 °C and (e) 500 °C. The CIGS film was fabricated using the single target of $\text{Cu}(\text{In}_{0.7}\text{Ga}_{0.3})\text{Se}_{2.5}$ powder.	79
Fig. 4.11. XRD patterns (a) before and (b) after selenization of the CIGS films deposited at room temperature, 350, 400, 450 and 500 °C. The CIGS film was fabricated using the single target of $\text{Cu}(\text{In}_{0.7}\text{Ga}_{0.3})\text{Se}_{2.5}$ powder.	80

Fig. 4.12. (a) Resistivity before and after selenization of the CIGS film as a function of deposition temperature. And Hall resistance after selenization of the CIGS films deposited at (b) 400 °C and (c) 450 °C. 81

Fig. 4.13. Current-voltage characteristics of the CIGS solar cells fabricated using the single target of $\text{Cu}(\text{In}_{0.7}\text{Ga}_{0.3})\text{Se}_{2.5}$ powder. The solar cell A, B, C, D and E are fabricated after selenization CIGS precursor films deposited at the temperatures of 400, 450, 475 and 500 °C, respectively. 82

Fig. 5.1. FE-SEM images of the CIGS films (a) as-deposited and selenized at (b) 350 °C, (c) 375 °C, (d) 400 °C, (e) 425 °C and (f) 450 °C. CIGS precursor films were fabricated using a stoichiometric CIGS target and then selenized at various temperatures. 122

Fig. 5.2. XRD patterns of as-deposited and selenized CIGS films. CIGS precursor films were fabricated using a stoichiometric CIGS target and then selenized at the temperatures from 300 to 450 °C..... 123

Fig. 5.3. Current-voltage characteristics of the CIGS solar cells fabricated using a stoichiometric CIGS target. The solar cell A and B are fabricated using the CIGS absorber layers selenized at the temperatures of 400 and 450 °C, respectively..... 124

Fig. 5.4. FE-SEM images of the CIGS films (a) as-deposited and selenized at (b) 400 °C, (c) 450 °C, (d) 475 °C and (e) 500 °C. CIGS precursor films were fabricated using a Cu-poor CIGS target and then selenized at various temperatures. 125

Fig. 5.5. XRD patterns of as-deposited and selenized CIGS films. CIGS

precursor films were fabricated using a Cu-poor CIGS target and then selenized at the temperatures from 400 to 500 °C..... 126

Fig. 5.6. Composition mapping images of the CIGS film selenized at the temperature of 400 °C. 127

Fig. 5.7. Current-voltage characteristics of the CIGS solar cells fabricated using a Cu-poor CIGS target. The solar cell C, D, E and F are fabricated using the CIGS absorber layers selenized at the temperatures of 400, 450, 475 and 500 °C, respectively. 128

Fig. 5.8. FE-SEM images after selenization of the CIGS precursor films fabricated using (a) $\text{Cu}_{0.9}(\text{In}_{0.7}\text{Ga}_{0.3})\text{Se}_2$, (b) $\text{Cu}_{0.9}(\text{In}_{0.7}\text{Ga}_{0.3})\text{Se}_{2.2}$ and (c) $\text{Cu}_{0.9}(\text{In}_{0.7}\text{Ga}_{0.3})\text{Se}_{2.5}$ targets. All of the films are selenized at the temperature of 475 °C for 30minutes. 129

Fig. 5.9. (a) Current-voltage characteristics and (b) normalized quantum efficiency of the CIGS solar cells fabricated using various CIGS targets. (c) Band gap determination from EQE data. (d) A plot of V_{oc} versus band gap (E_g). The solar cell E, G and H are fabricated by using $\text{Cu}_{0.9}(\text{In,Ga})\text{Se}_2$, $\text{Cu}_{0.9}(\text{In,Ga})\text{Se}_{2.2}$ and $\text{Cu}_{0.9}(\text{In,Ga})\text{Se}_{2.5}$ target, respectively. 130

Fig. 5.10. XRD patterns after selenization of the CIGS precursor films fabricated using $\text{Cu}_{0.9}(\text{In}_{0.7}\text{Ga}_{0.3})\text{Se}_2$, $\text{Cu}_{0.9}(\text{In}_{0.7}\text{Ga}_{0.3})\text{Se}_{2.2}$ and $\text{Cu}_{0.9}(\text{In}_{0.7}\text{Ga}_{0.3})\text{Se}_{2.5}$ targets. All of the films are selenized at the temperature of 475 °C for 30minutes. 131

Fig. 5.11. FE-SEM images of the (a) as-deposited CIGS film and the CIGS films selenized using mixing powders with weight ratios of alumina to

selenium of (b) 0:0, (c) 12:1, (d) 8:1, (e) 6:1 and (f) 4:1. The CIGS precursor film was fabricated using a single quaternary CIGS target with the nominal compositions of $\text{Cu}_{0.9}(\text{In}_{0.7}\text{Ga}_{0.3})\text{Se}_2$ 132

Fig. 5.12. FE-SEM images of the (a) as-deposited CIGS film and the CIGS films selenized using mixing powders with weight ratios of alumina to selenium of (b) 0:0, (c) 12:1, (d) 8:1, (e) 6:1 and (f) 4:1. The CIGS precursor film was fabricated using a single quaternary CIGS target with the nominal compositions of $\text{Cu}_{0.9}(\text{In}_{0.7}\text{Ga}_{0.3})\text{Se}_{2.5}$ 133

Fig. 5.13. XRD patterns before and after selenization of the CIGS precursor films fabricated using the single quaternary CIGS targets with the nominal compositions of (a) $\text{Cu}_{0.9}(\text{In}_{0.7}\text{Ga}_{0.3})\text{Se}_2$ and (b) $\text{Cu}_{0.9}(\text{In}_{0.7}\text{Ga}_{0.3})\text{Se}_{2.5}$. The CIGS films were selenized using mixing powders with the weight ratios of alumina to selenium of 0:0, 12:1, 8:1, 6:1 and 4:1, respectively. 134

Fig. 5.14. Raman spectra after selenization of the CIGS films fabricated using the single quaternary CIGS targets with the nominal compositions of $\text{Cu}_{0.9}(\text{In}_{0.7}\text{Ga}_{0.3})\text{Se}_2$ and $\text{Cu}_{0.9}(\text{In}_{0.7}\text{Ga}_{0.3})\text{Se}_{2.5}$. The CIGS films were selenized using mixing powders with the weight ratio of alumina to selenium of 8:1 ... 135

Fig. 5.15. Auger electron spectroscopy (AES) depth profiles after selenization of the CIGS films fabricated using the single quaternary CIGS targets with the nominal compositions of (a) $\text{Cu}_{0.9}(\text{In}_{0.7}\text{Ga}_{0.3})\text{Se}_2$ and (b) $\text{Cu}_{0.9}(\text{In}_{0.7}\text{Ga}_{0.3})\text{Se}_{2.5}$. The CIGS films were selenized using mixing powders with the weight ratio of alumina to selenium of 8:1. 136

Fig. 5.16. Photoluminescence (PL) spectra after selenization of the CIGS films fabricated using the single quaternary CIGS targets with the nominal

compositions of $\text{Cu}_{0.9}(\text{In}_{0.7}\text{Ga}_{0.3})\text{Se}_2$ and $\text{Cu}_{0.9}(\text{In}_{0.7}\text{Ga}_{0.3})\text{Se}_{2.5}$. The CIGS films were selenized using mixing powders with the weight ratio of alumina to selenium of 8:1. 137

Fig. 5.17. Current-voltage characteristics of the CIGS solar cells fabricated using the single CIGS targets with the nominal compositions of (a) $\text{Cu}_{0.9}(\text{In,Ga})\text{Se}_2$ and (b) $\text{Cu}_{0.9}(\text{In,Ga})\text{Se}_{2.5}$. Detail conditions and values of the sample A to H are in table 5.6. 138

Fig. 5.18. (a) Linear scale and (b) logarithmic scale XRD patterns of the as-deposited CIGS films deposited at various temperatures using a single quaternary $\text{Cu}_{0.9}(\text{In}_{0.7}\text{Ga}_{0.3})\text{Se}_{2.5}$ target. 139

Fig. 5.19. (a), (c) TEM bright-field images and (b), (d) high resolution TEM images of the CIGS precursor films deposited at 120 and 130 °C. And Fast Fourier Transformation (FFT) patterns of region (1) and (2) in figure (d). .. 140

Fig. 5.20. XRD patterns of the CIGS films selenized using mixing powders with the weight ratios of alumina to selenium of (a)(b) 8:1, (c)(d) 6:1 and (e)(f) 4:1. 141

Fig. 5.21. Raman spectra of the CIGS films selenized using mixing powders with the weight ratios of alumina to selenium of (a) 8:1 and (b) 4:1 142

Fig. 5.22. FE-SEM images of the (a) as-deposited CIGS film deposited at room temperature and the CIGS films selenized using mixing powders with weight ratios of alumina to selenium of (b) 8:1, (c) 6:1 and (d) 4:1. CIGS precursor films were fabricated using a single quaternary CIGS target with the nominal composition of $\text{Cu}_{0.9}(\text{In}_{0.7}\text{Ga}_{0.3})\text{Se}_{2.5}$ 143

Fig. 5.23. FE-SEM images of the (a) as-deposited CIGS film deposited at 120 °C and the CIGS films selenized using mixing powders with weight ratios of alumina to selenium of (b) 8:1, (c) 6:1 and (d) 4:1. CIGS precursor films were fabricated using a single quaternary CIGS target with the nominal composition of $\text{Cu}_{0.9}(\text{In}_{0.7}\text{Ga}_{0.3})\text{Se}_{2.5}$ 144

Fig. 5.24. FE-SEM images of the (a) as-deposited CIGS film deposited at 130 °C and the CIGS films selenized using mixing powders with weight ratios of alumina to selenium of (b) 8:1, (c) 6:1 and (d) 4:1. CIGS precursor films were fabricated using a single quaternary CIGS target with the nominal composition of $\text{Cu}_{0.9}(\text{In}_{0.7}\text{Ga}_{0.3})\text{Se}_{2.5}$ 145

Fig. 5.25. (a) RMS roughness and (b) AFM image of the CIGS films as a function of deposition temperature and selenization condition with various weight ratios of alumina to selenium. Details for the deposition temperature and weight ratio of alumina to selenium are given in the figure. 146

Fig. 5.26. Current-voltage characteristics of the CIGS solar cells fabricated using the CIGS precursor films deposited at (a) room temperature, (b) 120 °C and (c) 130 °C. The CIGS precursor films were selenized using mixing powders with weight ratios of alumina to selenium of 8:1, 6:1 and 4:1, respectively..... 147

Chapter 1. General background

1.1. Historical reviews on solar cells

Recently, solar cells have attracted great attention with the increase of problems such as an energy crisis and an environmental pollution caused by overuse of fossil fuels. The photovoltaic effect was first discovered in an electrolyte solution by Becquerel in 1839. In 1954, the first silicon solar cell with an efficiency of 6% was developed at Bell Labs by Chapin et al. [1]. In the same year, Reynolds et al. [2] reported the solar cell based on $\text{Cu}_2\text{S}/\text{CdS}$ with an efficiency of 6%. GaAs pn junction solar cell of 6% was reported in 1956 by Jenny et al. [3]. Meanwhile, CuInSe_2 (CIS) solar cell, basis of CIGS solar cell, was first fabricated using p-type single crystals of CuInSe_2 in 1974 by Wagner et al. [4]. And first CIS thin film solar cell was reported by Kazmerski et al. using films fabricated by evaporation of CuInSe_2 powder in 1976 [5]. With achieving a conversion efficiency of 9.4% by Boeing in 1981, CIS thin film solar cell began to receive great attention. The efficiencies of these many kinds of solar cells have been gradually enhanced up to the present time. Fig. 1.1 shows the different photovoltaic cell technologies and their respective growth in highest efficiencies from 1977 to 2013. As shown in Fig. 1.1, among all kinds of solar cell, the highest conversion efficiency of 44% has been achieved from the multijunction cells by using $\text{InGaP}/\text{GaAs}/\text{InGaAs}$. Also, from the crystalline Si solar cell, high conversion efficiency of about 25% has been achieved. However, these solar cells are fabricated by using a crystalline substrate and therefore consume

the large amount of raw materials. Solar cells are generally classified as a crystalline solar cell and a thin film solar cell. Especially, thin film solar cells have been extensively investigated by many researchers due to their merits such as small consumption of raw materials and possibility of lightweight. Among thin film solar cells, Cu(In,Ga)Se_2 (CIGS) solar cell has achieved the highest conversion efficiency of ~20% as shown in Fig. 1.1.

1.2. CIGS thin film solar cells

1.2.1 Growth process of CIGS film

The CIGS absorber layers have been grown by using various vacuum and nonvacuum processes. Vacuum processes such as three-stage co-evaporation process and two-step (stage) process have been widely used and the highest conversion efficiency of ~20% has been achieved from CIGS films deposited by a three-stage co-evaporation method. Meanwhile, nonvacuum processes such as electrodeposition and ink-based deposition have been studied due to its merit in terms of cost. Details for the fabrication method of CIGS film are as in the following.

1.2.1.1 Three-stage co-evaporation process

Three-stage co-evaporation method has been extensively studied [7-14] and the high conversion efficiencies above 20% have been achieved from the CIGS solar cell fabricated by using this method [13-15].

This method consists of three stages. First, In-Ga-Se layer is deposited on

Mo coated substrates at substrate temperature of 300~400 °C. Second, Cu-Se layer is deposited on In-Ga-Se layer at substrate temperature of 500~600 °C. In the third stage, In-Ga-Se layer is additionally deposited at the substrate temperature similar to second stage. Finally, the CIGS film with desired composition is formed [8, 12, 13]. In brief, the CIGS compound formation is represented by following equations.

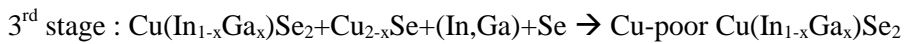
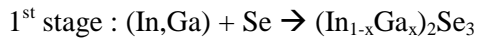


Fig. 1.1 shows the schematic of three-stage co-evaporation process developed by NREL group. The advantage of this method is its considerable flexibility to choose the process specifics and to control film composition and bandgap, allowing solar cells to achieve high efficiency [16]. Also, the CIGS films fabricated using this method show band gap grading caused by graded Ga incorporation as a function of depth [7, 8, 17-19], which lead to enhancement of conversion efficiency. However, good control of the elemental fluxs from each evaporation source is required for obtaining reproducibility. Although CIGS films are deposited by monitoring of flux, film thickness, composition, etc. during deposition, this method may give the difficulty in control. Also this method is difficult to obtain large-area film with uniform composition due to its complicated process and the lack of commercial equipment for large-area thermal evaporation [16].

1.2.1.2 Two-step process

Two-step process consists of deposition of metal precursor film and selenization of the precursor film. Although metal precursor films can be deposited by evaporation [20-23], the precursor films is commonly deposited by sputtering [24-29] such as co-sputtering [24, 25] and sequential sputtering [26-29] using separate elemental targets or metal alloy targets. Also, Cu-In-Ga ternary sputtering target can be used for fabrication of the precursor film [30]. After deposition of the metal precursor film, the film is selenized by using H_2Se gas or Se vapor in the furnace. As another method, after depositing Se onto the metal precursor film, the film is annealed by rapid thermal process (RTP). This two-step process is very attractive because this process enables to obtain the uniform film over large areas although this process has the limited ability to control composition and to increase band gap [31].

1.2.1.3 Other deposition processes (nonvacuum)

Nonvacuum processes have been studied due to its merit in terms of cost. These processes also consist of deposition of precursor film and selenization of the precursor film similar to two step in vacuum process. However, the precursor film is deposited by nonvacuum processes such as electrodeposition [32-34] and ink-based deposition [35-38]. Although these methods have the advantage in terms of reducing material waste, the maximum efficiency of the solar cell fabricated by nonvacuum processes is

lower than that of the solar cell fabricated by vacuum process.

1.3. Architecture of CIGS solar cell

1.3.1 Architecture

CIGS solar cell is composed of various thin film layers as shown in Fig. 1.3. Soda-lime glass (SLG) is commonly used as a substrate. Molybdenum (Mo) and ZnO is used as a bottom electrode and a transparent electrode at front of CIGS solar cell, respectively. CIGS is used as an absorber layer and CdS is used as a buffer layer between CIGS absorber layer and ZnO layer. For the measurement of the solar cell with a small area, metal electrode consisted of Ni and Al is generally used. Details for the each layer are as in the following.

1.3.1.1 CIGS absorber layer

As mentioned in chapter 1.2, the CIGS absorber layer has been generally deposited by a three-stage co-evaporation method. This method is very complicated and uniform film with large area is difficult to obtain; hence, it is not adequate for mass production of CIGS thin films.

In this study, the single quaternary CIGS targets with various compositions were used for fabricating the CIGS absorber layer or CIGS precursor layer by one-step process. This one-step process is very easy to obtain uniformly large-area CIGS films. The CIGS absorber layer was deposited at various temperatures by one-step process without selenization. And also, the CIGS

precursor films were deposited at room temperature and were selenized at various temperatures under Se atmosphere using Se powder.

1.3.1.2 Buffer layer

There is a large difference in a lattice constant and a band gap between the CIGS thin film and the ZnO thin film. Also, CIGS absorber layer can be damaged by the high-energy plasma during deposition of the ZnO layer. Hence, various buffer layers such as CdS, ZnS and InS have been applied between them. Among them, cadmium sulphide (CdS) is mainly used as a buffer layer. CdS has a band gap of 2.46eV and shows the n-type semiconducting property.

In this experiment, the cadmium sulphide was coated on a CIGS absorber layer. As shown in table 1.1, the solution was composed of 355 ml of deionized (D.I.) water (H_2O), 69.5 ml of ammonium hydroxide (NH_4OH), 50 ml of cadmium sulphate hydrate ($0.015\text{ M CdSO}_4 \cdot 8H_2O$) and 25ml of thiourea ($1.5\text{ M NH}_2\text{SCNH}_2$) [39]. These solution components were mixed in a bath at room temperature. And the CIGS film is immersed in the bath containing the solution. The bath containing the CIGS film was placed into a water-heated vessel of $78\text{ }^\circ\text{C}$ during 12 min. After deposition, the substrates were rinsed with D.I. water and dried at $60\text{ }^\circ\text{C}$ for 10min. Fig. 1.4 shows the experimental procedure for coating the CdS layer.

1.3.1.3 Window layer

In general, the ZnO bilayer (i-ZnO and n-ZnO) is used as a window layer. The i-ZnO layer with a high resistivity (HR) of 1~100 Ωcm is deposited on the CdS layer. This layer is necessary to improve the performance of the CIGS solar cell. For large area and polycrystalline devices like CIGS thin film solar cells, the same electronic quality over the entire area cannot be expected. Instead, the recombination can be occurred at grain boundaries or by local shunting paths, which deteriorates the cell performance. The influence of these regions on the cell performance can be reduced by using the i-ZnO layer. The high-resistivity ZnO film provides a local series resistance which prevents electrical inhomogeneities, e.g. sites of locally enhanced recombination, of the CIGS film. As a result, the improvement of the fill factor as well as the open circuit voltage can be achieved by using the i-ZnO layer [40]. Another role of the i-ZnO layer is for the protection from the high-energy plasma damage induced to the CIGS absorber surface and the CdS layer during deposition of the n-type ZnO layer [41]. The thickness of the i-ZnO layer has to be adjusted between about 50nm and 70nm. If i-ZnO layer thickness is greater than these thicknesses, the short circuit current density decreases because of an increase in series resistance of the solar cell. And the fill factor becomes worse due to an increase of leakage current for less than these thicknesses [42].

Meanwhile, in the CIGS solar cell, world record efficiencies have been achieved by using the CdS buffer layer among various buffer layers such as CdS, ZnS and InS. However, the thick CdS buffer layer absorbs short

wavelength light ($< 510\text{nm}$). So, any photocurrent can not be generated in the short wavelength region. Photocurrent in this region can be generated by increasing the band gap of the contact layer. And the contact layer must have high conductivity for lateral current collection. Hence, transparent conducting oxide (TCO) film onto the thin CdS layer has been applied because TCO film has the high conductivity as well as the wide band gap. Low deposition temperature of $<150\text{ }^\circ\text{C}$ should be concerned to apply TCO films to CIGS solar cells. Among the TCO films, ZnO based TCO film has been widely used due to its merits such as non-toxicity, abundance of element, use of inexpensive material and very low resistivity by doping. Low resistivity of the ZnO based TCO film can be also achieved at relatively low deposition temperature by sputtering.

In this study, the bilayered-ZnO film was applied to CIGS solar cells. A 50nm-thick i-ZnO film and a 400nm-thick Al-doped ZnO (2wt% Al_2O_3) film were sequentially deposited at room temperature on the CdS layer by using RF magnetron sputtering.

1.3.1.4 Metal electrode (bottom, top)

- Bottom electrode

In general, molybdenum (Mo) has been used as a bottom electrode of the CIGS solar cell among Ni, Al, and Au because which withstands corrossions against from Se and S, whereas Al or Au diffuses fast into CIGS layer and Ni reacts with CIGS. And the thermal expansion coefficient of Mo is similar to that of CIS [43]. Also, molybdenum allows Na diffusion from a soda lime

glass (SLG) substrate to a CIGS layer [44], which is beneficial to a conversion efficiency of CIGS solar cell. Characteristics of the Mo layer are strongly affected by process parameters such as sputtering power and working gas pressure. The Mo layer deposited at low Ar gas pressure shows densely packed microstructure and has low resistivity. However, the adhesion to SLG substrate is poor. On the contrary, the Mo film deposited at high Ar gas pressure has the good adhesion although the film has a high resistivity [45-49]. Therefore, the Mo bilayer film with the bottom layer sputtered at high pressure and the top layer sputtered at low pressure has been recommended [45, 48] and normally used as the bottom electrode of CIGS solar cell.

Meanwhile, the MoSe₂ layer is formed between the CIGS and the Mo layer when the CIGS precursor film is selenized. The MoSe₂ layer has a wider band gap (~1.4eV) than that of Cu(In_{1-x}Ga_x)Se ($x < \sim 0.6$) absorber layer, which would form the back surface field to avoid recombination of charge carriers at back [50]. And also, the MoSe₂ layer formed at the CIGS/Mo interface changes its contact type from a Schottky- to an ohmic-type contact [50, 51], which is beneficial to conversion efficiency. However, very thick MoSe₂ layer is detrimental to the conversion efficiency [52]. Therefore, it is important to obtain the MoSe₂ layer with an adequate thickness. The thickness of the MoSe₂ layer is affected by Mo layer properties such as microstructure, grain size and film density. For example, the Mo layer deposited at a low pressure has a thinner MoSe₂ layer [53]. And the growth rate of a MoSe₂ layer and the adhesion to the Mo layer is also dependent on growth orientation of the MoSe₂ grains. If the c-axis of the MoSe₂ grains is parallel to the Mo surface, thick MoSe₂ layer is easily formed and adhesion of MoSe₂ is much stronger

[53, 54]. In this experiment, the Mo electrode layer was deposited onto the soda lime glass substrate by the DC magnetron sputtering method. As mentioned above, properties of the Mo electrode layer are greatly influenced by deposition conditions. Therefore, to utilize the Mo layer as a bottom electrode of the CIGS solar cell, electrical and mechanical properties of the Mo electrode layer had been investigated through a preliminary experiment (not shown here). As a result, the Mo layer was deposited with RF power of 150watt under argon gas pressure of 5mTorr at 200 °C for 50min. The approximately 1um thick Mo film was deposited. The Mo film showed a low sheet resistance below 0.2 Ω /sq and good adhesion without peeling off.

- Top electrode (grid)

For the measurement of a solar cell with a small area, normally $\sim 1\text{cm}^2$, the bilayer-top metal electrode consisted of Ni and Al has been applied to a CIGS solar cell. First, several tens of nanometers of Ni are deposited on the TCO layer to prevent the formation of an oxide layer with high resistivity. And a few micrometers of Al are deposited on the Ni layer. The top electrode has to be designed as a grid with a small area to allow much light. This grid layer is generally deposited by evaporation through a metal shadow mask. In this experiment, Al grids for the enhancement of current collection were deposited by thermal evaporation.

References

- [1] D. M. Chapin, C.S. Fuller, G. L. Pearson, *J. Appl. Phys.* 25 (1954) 676.
- [2] D. C. Reynolds, G. Leies, L. L. Antes, R.E. Marberger, *Phys. Rev.* 96 (1954) 533.
- [3] D. Jenny, J. Loferski, P. Rappaport, *Phys. Rev.* 101 (1956) 1208.
- [4] S. Wagner, J. Shay, P. Migliorato, H. Kasper, *Appl. Phys. Lett.* 25 (1974) 434.
- [5] L. Kazmerski, F. White, G. Morgan, *Appl. Phys. Lett.* 29 (1976) 268.
- [6] http://www.nrel.gov/ncpv/images/efficiency_chart.jpg
- [7] A. M. Gabor, J. R. Tuttle, D. S. Albin, M. A. Contreras, R. Noufi, A. M. Hermann, *Appl. Phys. Lett.* 65 (1994) 198.
- [8] M. A. Contreras, J. R. Tuttle, A. M. Gabor, A. Tennant, K. Ramanathan, S. Asher, A. Franz, J. Keane, L. Wang, J. Scofield, R. Noufi, First WCPEC; Dec. 5-9, 1994; Hawaii, p68.
- [9] N. Kohara, T. Negami, M. Nishitani, T. Wada, *Jpn. J. Appl. Phys.* 34 (1995) L1141.
- [10] M. A. Contreras, B. Egaas, K. Ramanathan, J. Hiltner, A. Swartzlander, F. Hasoon, R. Noufi, *Pro. Photovolt: Res. Appl.* 7 (1999) 311.
- [11] T. Nakada, A. Kunioka, *Appl. Phys. Lett.* 74 (1999) 2444.
- [12] S. Chaisitsak, A. Yamada, M. Konagai, *Jpn. J. Appl. Phys.* 41 (2002) 507.
- [13] I. Repins, M. A. Contreras, B. Egaas, C. DeHart, J. Scharf, C. L. Perkins, B. To, R. Noufi, *Pro. Photovolt: Res. Appl.* 16 (2008) 235.
- [14] P. Jackson, D. Hariskos, E. Lotter, S. Paetel, R. Wuerz, R. Menner, W. Wischmann, M. Powalla, *Prog. Photovolt. Res. Appl.* 19 (2011) 894.
- [15] M. A. Green, K. Emery, Y. Hishikawa, W. Warta, E. D. Dunlop, *Prog. Photovolt. Res. Appl.* 22 (2014) 1.
- [16] A. Luque, S. Hegedus, *Handbook of Photovoltaic science and*

engineering, wiley, 2003, p583.

- [17] K. Ramanathan, M. A. Contreras, C. L. Perkins, S. Asher, F. S. Hasoon, J. Keane, D. Young, M. Romero, W. Metzger, R. Noufi, J. Ward, A. Duda, *Prog. Photovolt. Res. Appl.* 11 (2003) 225.
- [18] A. M. Gabor, J. R. Tuttle, M. H. Bode, A. Franz, A. L. Tennant, M. A. Contreras, R. Noufi, D. G. Jensen, A. M. Hermann, *Sol. Energy Mater. Sol. Cells* 41 (1996) 247.
- [19] P. Jackson, R. Wuerz, U. Rau, J. Mattheis, M. Kurth, T. Schlotzer, G. Bilger, J. H. Werner, *Prog. Photovolt. Res. Appl.* 15 (2007) 507.

Two-step process

- [20] B. M. Basol, V. K. Kapur, *Appl. Phys. Lett.* 54 (1989) 1918.
- [21] K. Kushiya, A. Shimizu, A. Yamada, M. Konagai, *Jpn. J. Appl. Phys.* 34 (1995) 54.
- [22] S. Nishiwaki, T. Satoh, S. Hayashi, Y. Hashimoto, S. Shimakawa, T. Negami, T. Wada, *Sol. Energy Mater. Sol. Cells* 67 (2001) 217.
- [23] R. Caballero, C. Guillen, *Sol. Energy Mater. Sol. Cells* 86 (2005) 1.
- [24] S.D. Kim, H.J. Kim, K.H. Yoon, J. Song, *Sol. Energy Mater. Sol. Cells* 62 (2000) 357.
- [25] D.G. Moon, S. Ahn, J.H. Yun, A. Cho, J. Gwak, S. Ahn, K. Shin, K. Yoon, H.D. Lee, H. Pak, S. Kwon, *Sol. Energy Mater. Sol. Cells* 95 (2011) 2786.
- [26] M. Marudachalam, H. Hichri, R. Klenk, R. W. Birkmire, W. N. Shafarman, J. M. Schultz, *Appl. Phys. Lett.* 67 (1995) 3978.
- [27] T. Nakada, A. Kunioka, *Jpn. J. Appl. Phys.* 37 (1998) L1065.
- [28] W. Li, Y. Sun, W. Liu, L. Zhou, *Solar Energy* 80 (2006) 191.
- [29] N. G. Dhere, K. W. Lynn, *Sol. Energy Mater. Sol. Cells* 41 (1996) 271.
- [30] G. S. Chen, J. C. Yang, Y. C. Chan, L. C. Yang, W. Huang, *Sol. Energy Mater. Sol. Cells* 93 (2009) 1351.
- [31] A. Luque, S. Hegedus, *Handbook of Photovoltaic science and engineering*, wiley, 2003, p584.

- [32] V. K. Kapur, B. M. Basol, E. S. Tseng, *Solar Cells* 21 (1987) 65.
- [33] M. Ganchev, J. Kois, M. Kaelin, S. Bereznev, E. Tzvetkova, O. Volobujeva, N. Stratieva, A. Tiwari, *Thin Solid Films* 511 (2006) 325.
- [34] D. Wang, L. Wan, Z. Bai, Y. Cao, *Appl. Phys. Lett.* 92 (2008) 211912.
- [35] C. R. Abernathy, C. W. Bates, A. A. Anani, B. Haba, G. Smestad, *Appl. Phys. Lett.* 45 (1984) 980.
- [36] S. J. Ahn, K. H. Kim, J. H. Yun, K. H. Yoon, *J. Appl. Phys.* 105 (2009) 113533.
- [37] W. Liu, D. B. Mitzi, M. Yuan, A. J. Kellock, S. J. Chey, O. Gunawan, *Chem. Mater.* 22 (2010) 1010.
- [38] E. J. Lee, S. J. Park, J. W. Cho, J. Gwak, M. K. Oh, B. K. Min, *Sol. Energy Mater. Sol. Cells* 95 (2011) 2928.
- [39] M. A. Contreras, M. J. Romero, B. To, F. Hasoon, R. Noufi, S. Ward, K. Ramanathan, *Thin Solid Films* 403 (2002) 204.
- [40] U. Rau, M. Schmidt, *Thin Solid Films* 387 (2001) 141.
- [41] N.F. Cooray, K. Kushiya, A. Fujimaki, D. Okumura, M. Sato, M. Ooshita, O. Yamase, *Jpn. J. Appl. Phys.* 38 (1999) 6213.
- [42] S. R. Kodigala, *Thin films and nanostructures*, vol. 35 “Cu(In_{1-x}Ga_x)Se₂ based thin film solar cells”, 2010, p606.
- [43] S. R. Kodigala, *Thin films and nanostructures*, vol. 35 “Cu(In_{1-x}Ga_x)Se₂ based thin film solar cells”, 2010, p630.
- [44] S. S. Wang, C. Y. Hsu, F. J. Shiou, P. C. Huang, D. C. Wen, *J. Electron. Mater.* 42 (2013) 71.
- [45] J. H. Scofield, A. Duda, D. Albin, B. L. Ballard, P. K. Predecki, *Thin Solid Films* 260 (1995) 26.
- [46] H. Khatri, S. Marsillac, *J. Phys.: Condens. Matter* 20 (2008) 055206.
- [47] S. A. Pethe, E. Takahashi, A. Kaul, N. G. Dhere, *Sol. Energy Mater. Sol. Cells* 100 (2012) 1.
- [48] H. M. Wu, S. C. Liang, Y. L. Lin, C. Y. Ni, H. Y. Bor, D. C. Tsai, F. S. Shieu, *Vacuum* 86 (2012) 1916.

- [49] C. H. Huang, H. L. Cheng, W. E. Chang, M. Y. Huang, Y. J. Chien, *Semicond. Sci. Technol.* 27 (2012) 115020.
- [50] T. Wada, N. Kohara, S. Nishiwaki, T. Negami, *Thin Solid Films* 387 (2001) 118.
- [51] L. Assmann, J. C. Bernede, A. Drici, C. Amory, E. Halgand, M. Morsli, *Appl. Surf. Sci.* 171 (2001) 15.
- [52] X. Zhu, Z. Zhou, Y. Wang, L. Zhang, A. Li, F. Huang, *Sol. Energy Mater. Sol. Cells* 101 (2012) 57.
- [53] T. Wada, N. Kohara, T. Negami, M. Nishitani, *Jpn. J. Appl. Phys.* 35 (1996) L1253.
- [54] D. Abou-Ras, G. Kostorz, D. Bremaud, M. Kalin, F.V. Kurdesau, A.N. Tiwari, M. Dobeli, *Thin Solid Films* 480 (2005) 433.

Table. 1.1. Experimental details for coating of CdS layer

Material		Molecular weight	Experimental detail		
			Concentration (M)	Material weight (g)	D.I. water (ml)
Deionized water	H ₂ O	18			355.5ml
Cadmium sulfate hydrate	CdSO ₄ ·8H ₂ O	769.55	0.015	0.194	50ml
Thiourea	NH ₂ SCNH ₂	76.12	1.5	2.883	25ml
Ammonium hydroxide	NH ₄ OH	35.03	1		69.5ml

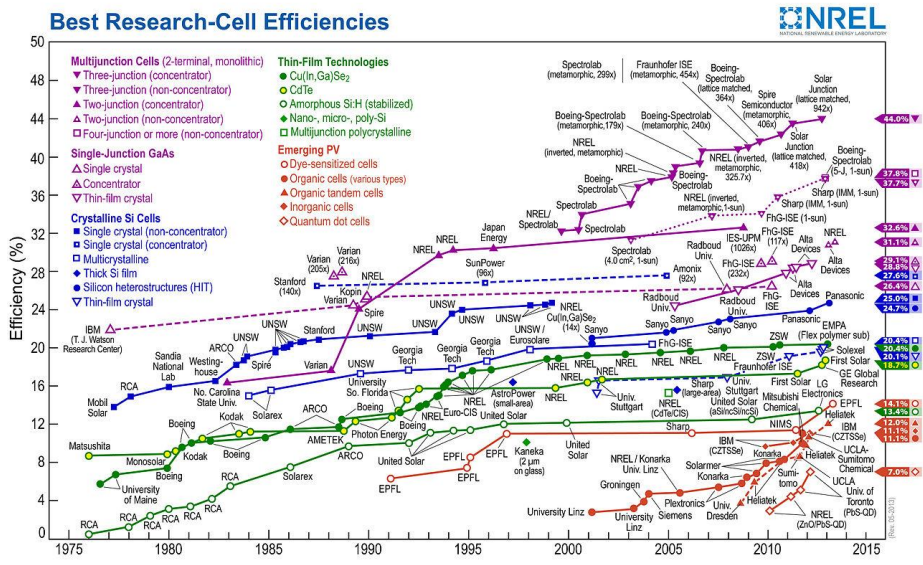


Fig 1.1 Best research-cell efficiencies chart for various photovoltaic technologies, which is compiled by National Renewable Energy Laboratory (NREL) [6]

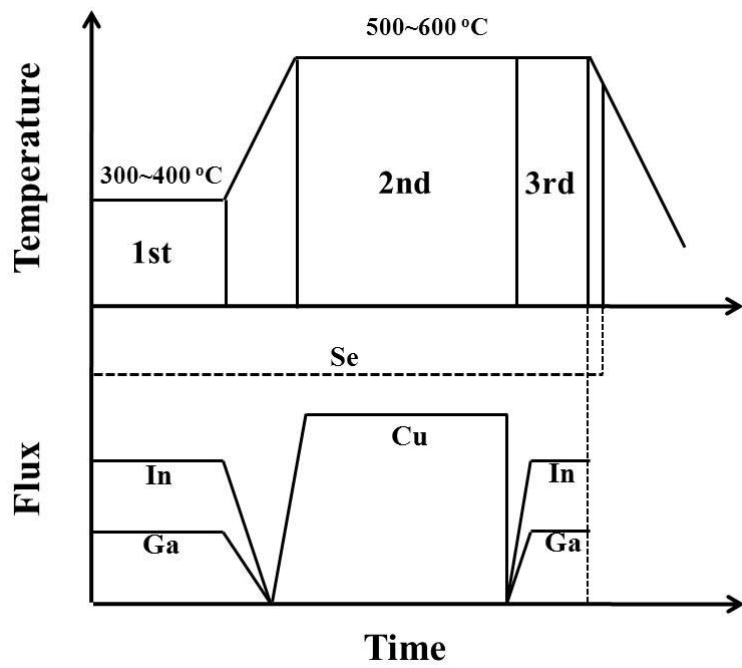


Fig. 1.2. Schematic of three-stage co-evaporation process. (Redrawn from ref. [8, 12, 13])

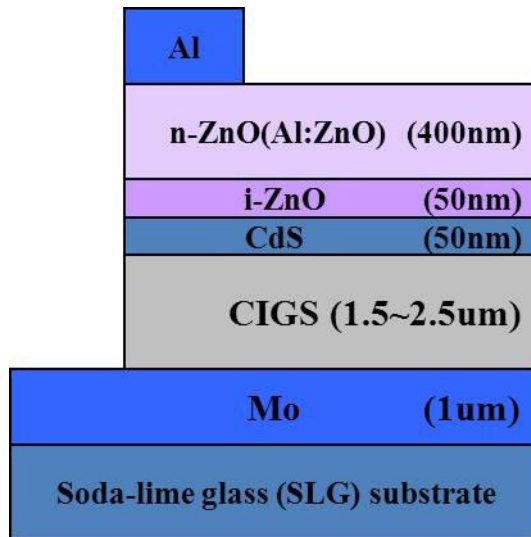


Fig. 1.3. Cross-sectional schematic of a CIGS solar cell.

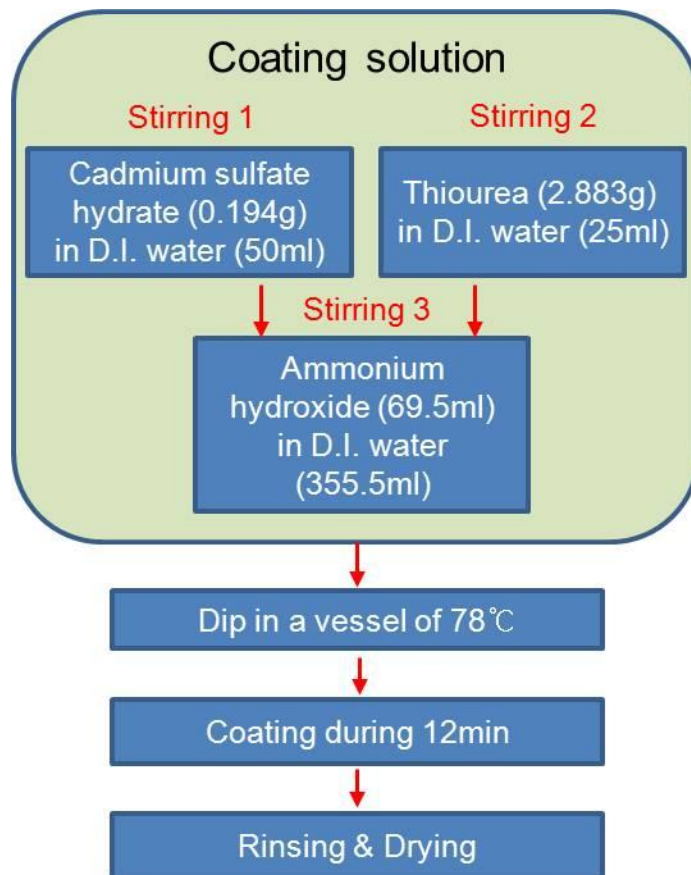


Fig. 1.4. Experimental procedure for coating of the CdS layer

Chapter 2. Design and fabrication of multi-layer antireflection coating for III-V solar cell

2.1. Introduction

Semiconductor materials such as GaAs and Si are known to have high reflectivity of about 30-40%. If these materials are applied to solar cells, high reflectivity has a harmful effect on solar cell efficiency. To reduce reflectivity and enhance solar cell efficiency, antireflection (AR) coating layer should be deposited on the solar cell surface. AR coatings have been studied in various optical fields for increasing transmittance and decreasing reflectance. Low reflectance can be obtained from a single-layer antireflection coating only at a specific wavelength. However, for a practical application to solar cells, low reflectance at wide wavelength regime from visible to near-infrared is required and can be achieved by a multi-layer antireflection coating such as double-layer and triple-layer antireflection coating. For the multi-layer antireflection coating, various materials with different refractive indices are necessary to achieve low reflectance.

Generally, ZnS, TiO₂ and CeO₂ are used as high refractive index material and MgF₂ and SiO₂ are used as low refractive index material in the AR coating. ZnS is very interesting material in the optical fields because it has a direct and wide band gap of 3.5-3.8 eV and transmits high energy photons [1-4]. And also MgF₂ has been universally used due to low refractive index and high transmittance in ultraviolet region [5]. Therefore, ZnS with a high

refractive index and MgF_2 with a low refractive index are commonly used for single- or double-layer AR coatings. Generally, refractive indices of ZnS and MgF_2 are known to be 2.354 and 1.377 at 630 nm, respectively [6,7]. However, refractive index is dependent on deposition method [8], deposition temperature [9,10], porosity [11-14] and stoichiometry [4], etc. Therefore, it is very important to look for the optimal deposition conditions irrespective of deposition method.

In this work, multi-layer AR coating such as double- and triple-layer was investigated with ZnS and MgF_2 . For a triple-layer AR coating, another material with an intermediate refractive index between those of ZnS and MgF_2 is needed and ZnS- MgF_2 composite film was suggested. ZnS, MgF_2 and ZnS- MgF_2 composite films were deposited by rf magnetron sputtering and their optical properties were examined. Based on the optical constants of each material, single-layer, double-layer and triple-layer AR coatings were designed and fabricated on the GaAs substrate. Especially, optical properties of co-sputtered ZnS- MgF_2 composite films were systematically investigated as a function of concentration of MgF_2 and ZnS in order to apply them to intermediate refractive index layer of triple-layer AR coating. And also experimental results of AR coating were compared to simulated results.

2.2. Experimental

ZnS and ZnS- MgF_2 composite films were prepared on soda-lime glass (SLG) substrates with optical grade by rf magnetron sputtering. Base pressure of vacuum chamber before deposition was approximately 3.0×10^{-6} Torr. ZnS

and MgF_2 target with a 99.99% high purity were used in this work. ZnS films were deposited with rf power of 50W under a working pressure of 5 mTorr. Substrate rotation was carried out at 3 rpm for film uniformity. ZnS- MgF_2 composite films were deposited by co-sputtering of ZnS and MgF_2 targets. To control the composition, rf power applied to MgF_2 target was varied with a fixed rf power to ZnS target. Thicknesses of ZnS film and ZnS- MgF_2 films were adjusted to be 600-800 nm, which is need to determine optical constants by using envelope method.

Transmittance of the ZnS and ZnS- MgF_2 composite films was measured in the wavelength range of 300-1500 nm by using UV-VIS-NIR spectrophotometer (Varian model, Cary 5000). Refractive indices (n), extinction coefficient (k) and thicknesses (d) of the ZnS film and ZnS- MgF_2 films were determined by envelope method. Additionally, optical constant of MgF_2 film was analyzed. Actually, it is difficult to determine optical constants of MgF_2 by envelope method due to small discrepancy of refractive index between glass substrate and MgF_2 . Therefore, in this experiment, MgF_2 film with a thickness needed for AR coating was deposited on GaAs substrates with rf power of 200W under Ar gas pressure of 10 mTorr and their optical constants were obtained by using spectroscopic ellipsometry (SE) at wide wavelength region. Quantitative analysis of ZnS- MgF_2 films was investigated by electron probe microanalyser (EPMA) for studying a relation between relative atomic concentration and refractive index of the film.

By using the extracted optical constant, single-, double-, and triple-layer AR coatings were designed and fabricated on GaAs substrate by rf magnetron sputtering and their reflectance were measured by using spectrophotometer.

Finally, reflectance spectra obtained by experiment were fitted and analyzed by computation of Essential Macleod program.

In the design of AR coatings, optical constants of the top layer of the III-V solar cell are important. In III-V solar cells, the top layer, on which AR coating is fabricated, is AlGaAs in the single-junction cell or InGaP(or AlGaP) in the multi-junction cells. In this work, we focused to investigate the characteristics of AR coatings depending on the number of AR coating layer, namely, single-, double- and triple-layer AR coating. For this purpose, GaAs single crystal substrates were used because they have uniform surface properties enough to compare the characteristics of AR coatings depending on the number of AR coating layer and also have similar optical constants to those of the top layers of III-V solar cells (refractive indices of GaAs and InGaP are ~ 3.85 and ~ 3.6 [15], respectively). Therefore, those results obtained in this work are very helpful to optimization of AR coatings for III-V solar cells.

2.3. Results and discussion

Fig. 2.1 shows the transmittance spectra of ZnS and ZnS-MgF₂ composite films on SLG substrates as a function of wavelength and also rf power dependence of transmittance of ZnS-MgF₂ films. It can be seen that all of the ZnS and ZnS-MgF₂ films were highly transparent in the wide wavelength region. The optical absorption edge shifted continuously toward short wavelength with increasing rf power to MgF₂. From these transmittance spectra, optical constants of ZnS and ZnS-MgF₂ films with wavelength could

be calculated by using envelope method. The refractive index (n) and extinction coefficient (k) were calculated using Swanepoel's method [16] which is based on the idea of Manifacier et al. [17].

Fig. 2.2 shows the refractive indices and extinction coefficients of ZnS-MgF₂ composite films depending on rf power to MgF₂ and those of ZnS and MgF₂ films. This figure indicates that all of the ZnS-MgF₂ composite films have intermediate refractive indices between those of ZnS and MgF₂, implying that these ZnS-MgF₂ composite films could be used as a middle layer of triple-layer AR coating. Refractive index of ZnS-MgF₂ composite film slightly decreased with increasing rf power to MgF₂. However, extinction coefficients of these films were similar and almost zero in visible region as well as infrared region. This result also indicates that all of these films are highly transparent between visible and infrared region.

In order to elucidate the origin of the variation of refractive index of the ZnS-MgF₂ composite film, film composition was investigated by EPMA. Fig. 2.3 shows the EPMA results of ZnS-MgF₂ films depending on rf power to MgF₂. As shown in Fig. 2.3, atomic concentrations of zinc and sulfur were slightly decreased with increasing the rf power up to 230W and then decreased abruptly at the rf power of 250W. This behavior is similar to that of refractive index as shown in this figure. This result indicates that refractive index of the ZnS-MgF₂ composite film is dependent on the film composition, namely, amount of ZnS with a high refractive index or MgF₂ with a low one is important to determine refractive index of ZnS-MgF₂ composite film. The more the amount of MgF₂ with a low refractive index, the lower the refractive index of ZnS-MgF₂ composite film and *vice versa*. As a result, ZnS-MgF₂

composite films having an intermediate refractive index for triple-layer AR coating could be successfully fabricated by co-sputtering of ZnS and MgF₂.

By using the optical constants of upper results, single (ZnS)-, double (ZnS/MgF₂)- and triple (ZnS/ZnS-MgF₂/MgF₂)-layer antireflection coatings were designed with a quarter-wave thickness at the reference wavelength of 600 nm for normal incidence. Therefore, the thickness of each layer could be calculated by using the equation of $nd = \lambda/4$ (n: refractive index, d: thickness, λ : wavelength). The thicknesses of MgF₂, ZnS-MgF₂ and ZnS layers, which used in three types of AR coatings, were 109.7, 81.2 and 64.6 nm, respectively. Fig. 2.4 presents the simulated reflectance spectra depending on the wavelength by using Essential Macleod program. As shown in Fig. 2.4, reflectance was dramatically changed according to a number of coating layers. However, in the triple-layer AR coating, although refractive index of ZnS-MgF₂ middle layer was changed from 1.842 to 1.654 at 632 nm, reflectance spectra were almost similar irrespective of refractive index. These results indicate that reflectance of AR coating is affected by a number of coating layers and a small change in the refractive index of the middle layer of triple-layer AR coating did not lead to a remarkable change in the reflectance of the triple-layer AR coating.

Based on designs of Fig. 2.4, single and multiple layers were coated on GaAs substrate. Fig. 2.5(a), (b) and (c) show reflectance spectra of GaAs substrate with single-, double- and triple-layer AR coating, respectively. ZnS 50W-MgF₂ 140W composite film was used as a middle layer with intermediate refractive index in triple layer AR coating. As shown in Fig. 2.5, as was expected, low reflectance could be obtained from a single-layer

antireflection coating only at a specific wavelength and could be obtained from double- and triple-layer antireflection coating at wide wavelength regime from visible to near-infrared. Especially, in the case of multi-layer AR coating, low reflectance was achieved by double-layer antireflection coating in the visible region and achieved by triple-layer antireflection coating in the near-UV and near-IR region. Reflectance spectra obtained by experiment were fitted by simulation by Essential Macleod. Solid line and dashed line indicate experimental results and simulated results, respectively. In the case of single-layer AR coating, experimental result was nicely consistent with the simulated result. However, reflectance of multi-layer AR coating had a small discrepancy between experimental result and simulated result, which can be caused by optical inhomogeneity [18] and difference between designed thickness and deposited one of each layer.

The effect of incident angle on the reflectance of multi-layer AR coating was investigated. Fig. 2.6 shows the simulated reflectance spectra of double- and triple-layer AR coating as a function of incident angle. As shown in Fig. 2.6, reflectance of double-layer increased gradually above 600 nm with increasing incident angle. On the other hand, reflectance of triple-layer decreased with increasing incident angle. It indicates that the triple-layer AR coating is efficient at the wavelength of above 600 nm in the case that incident angle is varied.

2.4. Summary

ZnS and MgF₂ film were fabricated on soda-lime glass substrate and GaAs

substrate and their optical constants were determined by envelope method and spectroscopic ellipsometry, respectively. Co-sputtered ZnS-MgF₂ composite films for applying to triple-layer AR coating were prepared on SLG substrate depending on rf power applied to MgF₂ and their optical constants were determined by envelope method. All films were highly transparent in the range from visible and near-IR. In the case of ZnS-MgF₂ composite film, optical absorption edge was continuously shifted to short wavelength and refractive index decreased with increasing concentration of Mg and F. Based on these optical constants, single-layer and multi-layer AR coatings were designed by using a quarter-wave thickness at a normal incidence and fabricated by using rf magnetron sputtering. Low reflectance could be obtained from a single-layer antireflection coating only at a specific wavelength and from multi-layer antireflection coating at wide wavelength region. However, range of low reflectance of double- and triple-layer AR coating was different although multilayer AR coating showed low reflectance at wide wavelength range. Double-layer AR coating showed low reflectance mainly in the visible region, which is important for solar cell application, and triple-layer AR coating showed low reflectance mainly in the near-UV and near-IR region. Incident angle dependence of reflectance of multi-layer AR coating showed different behavior according to a number of layers. So, before application of multi-layer AR coatings, their characteristics and application field should be considered to be used to the proper place.

References

- [1] R. Menner, B. Dimmler, R.H. Mauch, H.W. Schock, *J. Crystal Growth* 86 (1988) 906.
- [2] R. Nomura, T. Murai, T. Toyosaki, H. Matsuda, *Thin Solid Films* 271 (1995) 4.
- [3] Y.-Z. Yoo, T. Chikyow, P. Ahmet, Z.W. Jin, M. Kawasaki, H. Koinuma, *J. Crystal Growth* 237 (2002) 1594.
- [4] Y.P. Venkata Subbaiah, P. Prathap, K.T. Ramakrishna Reddy, *Appl. Surf. Sci.* 253 (2006) 2409.
- [5] T. Yoshida, K. Nishimoto, K. Sekine, K. Etoh, *Appl. Opt.* 45 (2006) 1375.
- [6] E.D. Palik, *Handbook of Optical Constants of Solids*. Academic, San Diego, 1998.
- [7] E.D. Palik, *Handbook of Optical Constants of Solids II*. Academic, San Diego, 1998.
- [8] T.D. Radjabov, I.E. Djamaletdinova, A.V. Sharudo, H. Hamidova, *Surf. Coat. Technol.* 72 (1995) 99.
- [9] F. Huang, Q. Song, M. Li, B. Xie, H. Wang, Y. Jiang, Y. Song, *Appl. Surf. Sci.* 255 (2008) 2006.
- [10] H. Yu, H. Qi, Y. Cui, Y. Shen, J.D. Shao, Z.X. Fan, *Appl. Surf. Sci.* 253 (2007) 6113.
- [11] S. Strehlke, S. Bastide, J. Guillet, C. Levy-Clement, *Mater. Sci. Eng. B* 69 (2000) 81.
- [12] V.M. Aroutiounian, K.R. Maroutyan, A.L. Zatikyan, K.J. Touryan, *Thin Solid Films* 403 (2002) 517.
- [13] S.H. Woo, Y.J. Park, D.H. Chang, K.M.A. Sobahan, C.K. Hwangbo, *J. Korean Phys. Soc.* 51 (2007) 1501.
- [14] J.-Q. Xi, J. Kim, E.F. Schubert, D. Ye, T.-M. Lu, S. Lin, *Opt. Lett.* 31 (2006) 601.

- [15] W. Yuan, Master thesis, Univ. of Notre Dame, Indiana, USA, Dec. 2009.
- [16] R. Swanepoel, *J. Phys. E: Sci. Instrum.* 16 (1983) 1214.
- [17] J.C. Manificier, J. Gasiot, J.P. Fillard, *J. Phys. E: Sci. Instrum.* 9 (1976) 1002.
- [18] X. Wu, F. Lai, L. Lin, J. Lv, B. Zhuang, Q. Yan, Z. Huang, *Appl. Surf. Sci.* 254 (2008) 6455.

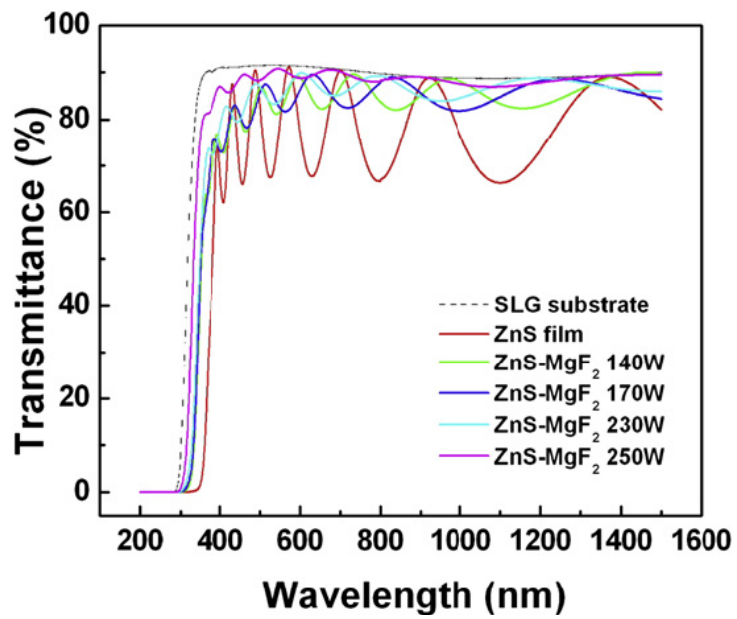


Fig. 2.1. Transmittance spectra of ZnS and ZnS-MgF₂ films on SLG substrates depending on wavelength.

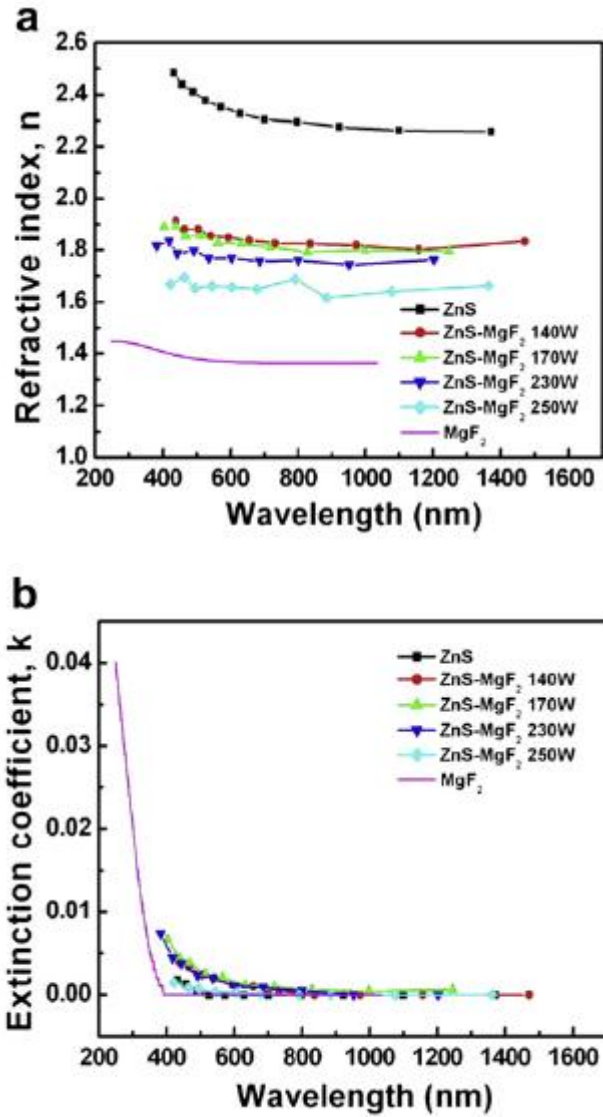


Fig. 2.2. (a) Refractive index and (b) extinction coefficient of ZnS-MgF₂ composite films depending on rf power applied to MgF₂. Optical constants of pure ZnS and MgF₂ were also exhibited.

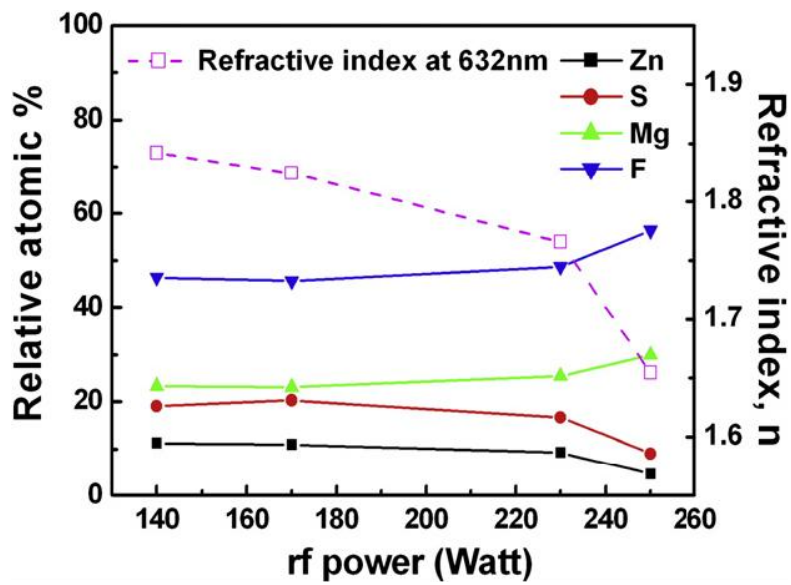


Fig. 2.3. EPMA results and refractive index variation at the wavelength of 632 nm for ZnS-MgF₂ composite films depending on rf power applied to MgF₂.

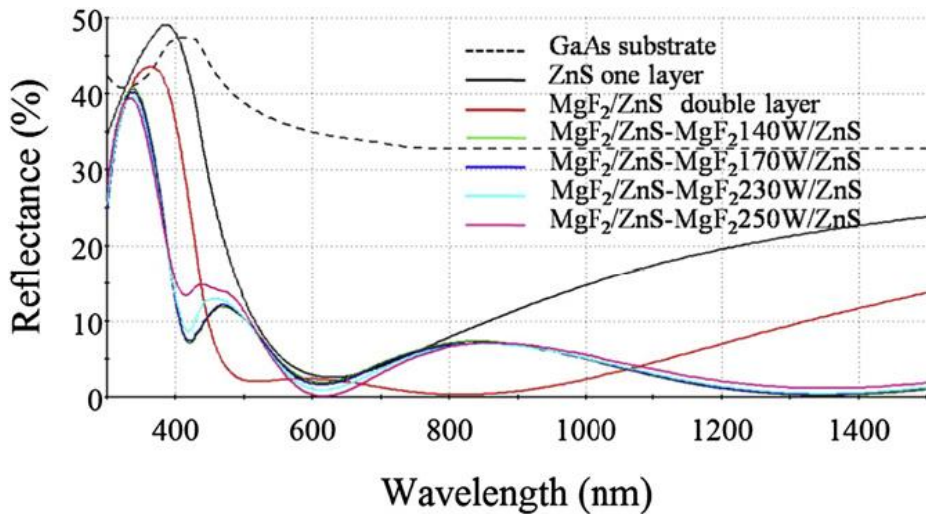


Fig. 2.4. Simulated reflectance spectra of GaAs substrate with single-, double- and triple-layer antireflection coating depending on wavelength. All structures are designed by quarter-wave coating at a reference wavelength of 600 nm. Reflectance spectra were theoretically calculated by Essential Macleod program.

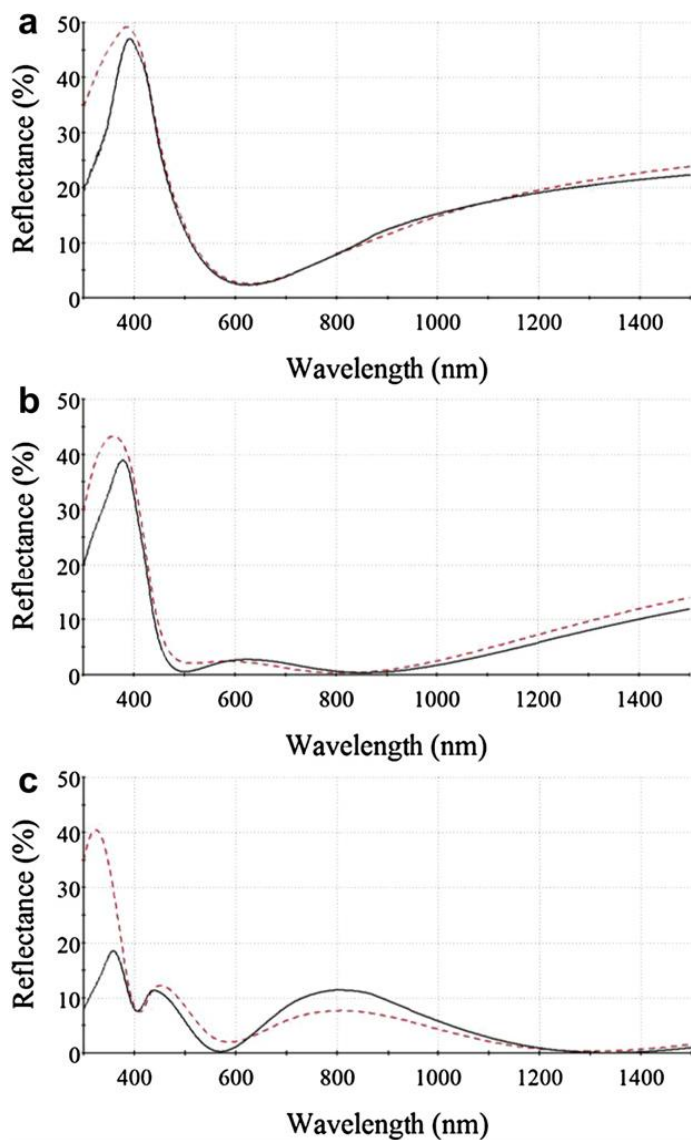


Fig. 2.5. Measured (solid line) and simulated (dash line) reflectance spectra of GaAs substrate with (a) single-layer (b) double-layer and (c) triple-layer antireflection coating. ZnS50W-MgF₂140W composite film was used as intermediate refractive index material in triple-layer AR coating.

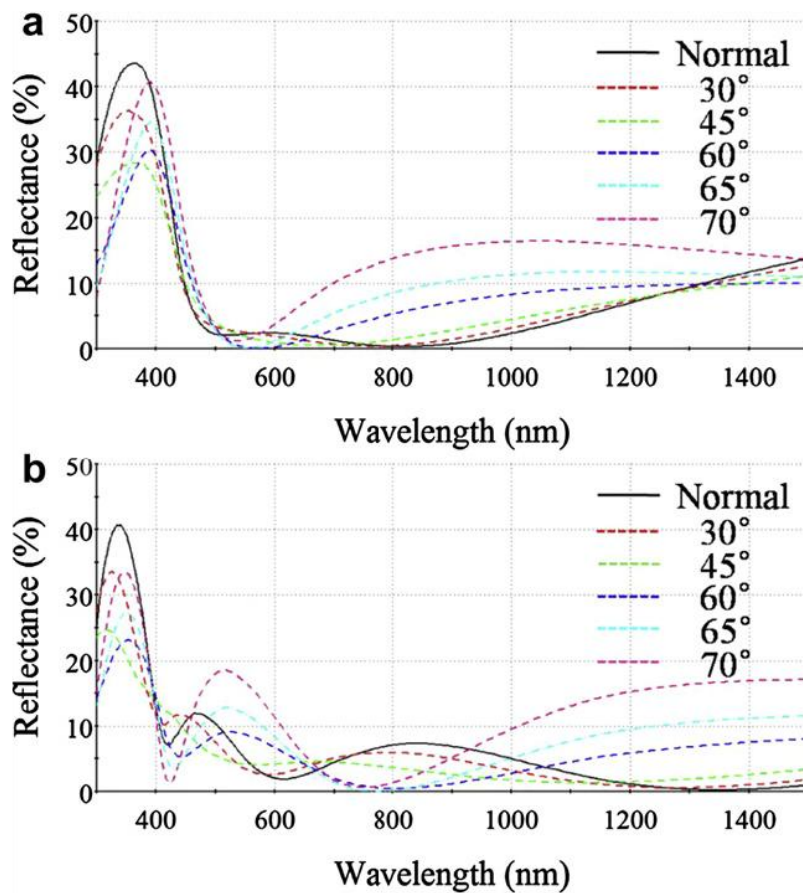


Fig. 2.6. Simulated reflectance spectra of (a) double-layer and (b) triple-layer AR coating as a function of incident angle.

Chapter 3. Characteristics of transparent conducting Al-doped ZnO films prepared by dc magnetron sputtering

3.1. Introduction

Transparent conducting oxide (TCO) films have been studied for various photo-electronic devices such as displays and solar cells. Indium tin oxide (ITO) is the most commonly-used TCO material because of its high conductivity and high transmittance. However, ITO has some demerits such as thermal instability and the high-cost of indium. On the other hand, zinc oxide (ZnO) based transparent conducting oxide has been investigated because of its various merits such as non-toxicity, abundance of element, use of inexpensive material, very low resistivity by doping and usefulness of various dopants. For obtaining ZnO-based TCO films, various processing methods such as sputtering [1-4], PLD [5,6], CVD [7], PECVD [8], MOCVD [9] sol-gel [10,11] and spray pyrolysis [12,13] have been extensively studied. Among them, sputtering method is generally used because it is simple process and is possible to fabricate the films with uniform surface over large area, dense structure and high crystallinity.

Meanwhile, the effects of various processing parameters such as substrate temperature [14], oxygen partial pressure [15] and doping material [16] have been investigated to improve electrical and optical properties of ZnO-based

TCO films. And it is revealed that these parameters have a significant effect on properties of ZnO-based TCO film. Recently, the flexible optoelectronic devices have attracted much attention and therefore it is important to decrease the substrate temperature to obtain TCO films with low resistivity and high transparency. In addition, in case of CIGS solar cells, low substrate temperature is very important to protect the underneath device structure of p-n junction. The substrate temperature below 200 °C is required to not deteriorate the p-n junction [17].

In this work, Al-doped ZnO (AZO) films were fabricated by using dc magnetron sputtering as a function of Ar gas pressure, O₂/Ar gas ratio and substrate temperature and their electrical, optical and structural properties were systematically investigated to obtain AZO films with both low resistivity of order of 10⁻⁴ Ωcm and high transparency in visible region. Especially, low substrate temperature of ≤ 200 °C was concerned to apply AZO films to CIGS solar cells.

3.2. Experimental

Al-doped ZnO films were deposited on soda-lime glass substrates with optical grade by using dc magnetron sputtering. Base pressure of vacuum chamber before deposition was approximately 3.0 × 10⁻⁶ Torr. 2 wt%-Al₂O₃ doped ZnO target with a high purity (99.99%) and low resistivity (below 1 Ωcm) was used in this work. AZO films were deposited with dc power of 100W under argon gas pressure of 3-15 mTorr at room temperature (R.T.). Substrate rotation was carried out at 3 rpm for film uniformity.

In order to obtain the AZO films with both high transparency and low resistivity for practical applications, the effects of substrate temperature and oxygen partial pressure on the properties of AZO films were systematically investigated. For this purpose, substrate temperature (T_s) was varied from R.T. to 350 °C and O_2/Ar gas ratio from 1.23 to 9.09 % at $T_s =$ R.T. and 250 °C. In these cases, working pressure and dc power were fixed at 5 mTorr and 100 W, respectively.

The AZO films were characterized with investigation of their electrical, optical and structural properties. Resistivity, carrier concentration and Hall mobility of the AZO films were measured by using Hall measurement system. Transmittance was measured in the wavelength range of 200-1500 nm by using UV-VIS-NIR spectrophotometer (Varian model, Cary 5000). Crystal structures and surface morphologies of the AZO films were investigated by using x-ray diffraction (XRD) with Cu-K α radiation and field emission scanning electron microscopy (FESEM), respectively.

3.3. Results and discussion

AZO films were deposited at room temperature with various argon gas pressures to investigate the effect of argon gas pressure on the properties of them. Fig. 3.1 shows the resistivity, carrier concentration and Hall mobility of the AZO films deposited at various argon gas pressures. As shown in Fig. 3.1, the resistivity increased with increasing argon gas pressure. On the contrary, carrier concentration and Hall mobility decreased with increasing argon gas pressure. Fig. 3.2 shows the surface morphologies of the AZO films

depending on argon gas pressure. With increasing argon gas pressure, the AZO films became less dense with larger grains due to the decreased deposition rate and growth attribute of ZnO. In general, ZnO film is known to grow preferentially with c-axis due to its lowest surface energy and it was confirmed by XRD measurement (not shown here) that all the AZO films were grown mainly with (001) preferred orientation irrespective of argon pressure. The deposition rate was almost linearly decreased with increasing argon gas pressure (21.8 nm/min for 3 mTorr to 13.3 nm/min for 15 mTorr) due to scattering effect. The increase of resistivity of the AZO films could be related to the change of surface morphology depending on the argon gas pressure. As shown in Fig. 3.2, with increasing argon gas pressure, the AZO film became less dense, that is, porous with larger grains, resulting in decrease of the mobility due to grain boundary scattering of charge carrier [18]. Therefore, the increase of resistivity with increasing argon gas pressure could be explained by the decrease of mobility due to grain boundary scattering of charge carrier as well as decrease of carrier concentration. Although the resistivity of the AZO films decreased with decreasing argon gas pressure and low resistivity of $\sim 10^{-3} \Omega\text{cm}$ could be obtained at room temperature, the transparency of them decreased, too. Fig. 3.3 shows the transmittance spectra of the AZO films depending on the argon gas pressure. As mentioned before, transmittance decreased with decreasing argon gas pressure. Especially, the AZO films deposited at 3 mTorr had light grey color, indicating that it was excessively lack of oxygen and had metallic properties in part, resulting in low resistivity and low transmittance. Therefore, to enhance the transmittance with sustaining low resistivity, a small amount of oxygen was mixed with

argon during sputtering.

Fig. 3.4 shows resistivity and transmittance of the AZO films deposited at R.T. depending on the O₂/Ar gas ratio of 1.23-9.09%. The transmittance of the AZO film was greatly enhanced with nearly sustaining low resistivity when a very small amount of oxygen (1.23%) was mixed. However, further increase of O₂/Ar gas ratio increased the resistivity as well as the transmittance, implying that oxygen content (or oxygen vacancy) plays a key role in resistivity of AZO film and careful control of oxygen content is needed for both low resistivity and high transmittance of the AZO films. Fig. 3.5 shows XRD patterns of the AZO films depending on O₂/Ar gas ratio. This figure indicates that growth behavior of the AZO film is dependent on O₂/Ar gas ratio. When O₂/Ar gas ratio was below 1.64%, the AZO films were grown with random orientation; however, texturing with preferential orientation of (001) appeared when O₂/Ar gas ratio was above 3.23%. Interestingly, resistivity of the AZO film showed dependency of growth orientation. The AZO films grown with random orientation had resistivity of order of 10⁻³ Ωcm, however, the resistivity increased abruptly to order of 10⁻¹ Ωcm or above when the AZO films were grown with preferential orientation. Further study is needed to know the precise transition point of O₂/Ar gas ratio from random to preferential growth of the AZO film and its effect on the resistivity.

In order to decrease the resistivity of the AZO film down to order of 10⁻⁴ Ωcm with high transmittance for a practical application, the AZO films were deposited at the substrate temperature of R.T.~350 °C with a step of 50 °C under pure argon gas and O₂/Ar gas ratio of 1.23%. Fig. 3.6 shows resistivity, carrier concentration and Hall mobility of the AZO films deposited at various

substrate temperatures. With increasing the substrate temperature up to 250 °C, resistivity was continuously decreased, however, further increase of the substrate temperature increased the resistivity slightly due to decrease of the mobility as shown in Fig. 3.6 (b). The decrease of the mobility at the substrate temperature above 300 °C may be explained by thickness effect. The mobility of Al(or Ga)-doped ZnO film was reported to decrease with decreasing film thickness [19,20]. At the substrate temperature above 300 °C, deposition rate decreased with increasing the substrate temperature and thus the film thickness decreased to 235 and 180 nm at 300 and 350 °C, respectively while it was 330 nm at 250 °C. Therefore, the decrease of the mobility of the AZO films deposited at 300 and 350 °C is attributable to the decreased film thickness.

Fig. 3.7 shows the surface morphologies of the AZO films deposited at various substrate temperatures under pure argon gas. It was observed that the AZO films became more compact and denser and grain boundary became vague with increasing substrate temperature. These results are in agreement with a modified Thornton model which was proposed by Kluth et al. [21] to describe structural changes of the RF sputtered AZO film. From the surface morphology change as shown in Fig. 3.2 and 3.7, the mobility of the AZO films is related to the film structure, namely, grain boundary scattering of charge carrier plays an important role in the mobility of the AZO film.

Resistivity of order of 10^{-4} Ωcm could be achieved by increasing the substrate temperature above 150 °C under pure argon gas and above 250 °C under O₂/Ar gas ratio of 1.23%, respectively. In this work, the AZO film deposited at T_s = 250 °C under pure argon gas exhibited the lowest resistivity

of $3.19 \times 10^{-4} \Omega\text{cm}$. Fig. 3.8 shows the transmittance spectra of the AZO films deposited at various substrate temperatures. As shown in Fig. 3.8, except the AZO film deposited at R.T. under pure argon gas, all the films exhibited transparent characteristics in visible region. Especially, transmittance in visible region was greatly enhanced with increasing the substrate temperature in the case of pure argon gas as shown in Fig. 3.8(a). As shown in Fig. 3.4, transmittance was also enhanced by adding a small amount of oxygen to argon gas, indicating that transmittance of the AZO film is very sensitive to the substrate temperature and oxygen content in the sputtering gas. In near-infrared wavelength region, the transmittance decreased with decrease of resistivity of the AZO film because transmittance in the near-infrared region is affected by free carrier absorption.

The effect of O_2/Ar gas ratio at the substrate temperature of 250°C was also investigated. Fig. 3.9 shows resistivity, carrier concentration and Hall mobility of the AZO film deposited at $T_s = 250^\circ\text{C}$ depending on O_2/Ar gas ratio. As shown in Fig. 3.9, with increasing O_2/Ar gas ratio, resistivity increased and carrier concentration, Hall mobility decreased. This tendency is consistent with that of the AZO films deposited at room temperature, implying that oxygen content in the sputtering gas is critical to the electrical properties of the AZO film, irrespective of substrate temperature. Fig. 3.10 shows the transmittance spectra of the AZO films according to O_2/Ar gas ratio. As can be expected from the results shown in Fig. 3.8, all the AZO films without exception showed high transparency in the visible region due to high substrate temperature of 250°C . The decrease of transmittance in near-infrared wavelength region was also observed with decrease of resistivity.

Optical band gap of AZO films was investigated. Fig. 3.11 shows the optical band gap (E_g) of the AZO films deposited at various substrate temperatures under pure argon gas and O_2/Ar gas ratio of 1.23 %. As shown in Fig. 3.11, optical band gap increased with increasing substrate temperature up to 250 °C and further increase of the substrate temperature decreased E_g . It has a maximum value of 3.7 eV at the substrate temperature of 250 °C under pure argon gas. It was found that the optical band gap increased with decreasing O_2/Ar gas ratio and it showed similar tendency depending on the O_2/Ar gas ratio regardless substrate temperature although its value was different. Table 3.1 shows the optical band gap values of the AZO films depending on the substrate temperatures and the O_2/Ar gas ratios. As a whole, the optical band gap of the AZO film was closely related to the carrier concentration, namely, it was increased with increasing carrier concentration. This is consistent with Burstein-Moss effect [22].

3.4. Summary

AZO films were deposited on soda-lime glass substrates by dc magnetron sputtering as a function of argon gas pressure, O_2/Ar gas ratio and substrate temperature, and their electrical, optical and structural properties were systematically investigated. When the AZO films were deposited at room temperature, both resistivity and transmittance decreased with decreasing argon gas pressure. Small addition of oxygen to argon (O_2/Ar ratio of 1.23 %) enhanced the transmittance greatly with sustaining low resistivity, however, further addition increased the resistivity. This dependency of resistivity on the

O₂/Ar ratio was exhibited irrespective of the substrate temperature. As the substrate temperature was increased, resistivity decreased continuously and the lowest value of resistivity was obtained at the temperature of 250 °C in pure Ar and 250-300 °C in O₂/Ar ratio of 1.23 %, respectively. Further increase of the substrate temperature increased the resistivity slightly due to decrease of the Hall mobility at higher temperature. All of the AZO films were transparent in visible region except for AZO films deposited at room temperature in pure Ar. These results indicate that increase of temperature also enhances transparency of the AZO film in visible wavelength region. On the other hand, transmittance in near-infrared wavelength region gradually decreased with increasing the substrate temperature up to 250-300 °C because of free carrier absorption loss caused by high carrier concentration. Conclusively, the AZO films with low resistivity of order of 10⁻⁴ Ωcm and high transparency in visible region could be prepared at the substrate temperatures of above 150 °C (the lowest resistivity of 3.19 × 10⁻⁴ Ωcm at 250 °C) by dc magnetron sputtering and these films are applicable to various fields which require transparent conducting oxide films.

References

- [1] T. Minami, K. Oohashi, S. Takata, T. Mouri, N. Ogawa, *Thin Solid Films* 193-194 (1990) 721.
- [2] B.H. Choi, H.B. Im, J.S. Song, K.H. Yoon, *Thin Solid Films* 193-194 (1990) 712.
- [3] X. Yu, J. Ma, F. Ji, Y. Wang, X. Zhang, C. Cheng, H. Ma, *Appl. Surf. Sci.* 239 (2005) 222.
- [4] X. Bie, J.G. Lu, L. Gong, L. Lin, B.H. Zhao, Z.Z. Ye, *Appl. Surf. Sci.* 256 (2009) 289.
- [5] H. Kim, A. Piqué, J.S. Horwitz, H. Murata, Z.H. Kafafi, C.M. Gilmore, D.B. Chrisey, *Thin Solid Films* 377-378 (2000) 798.
- [6] S.M. Park, T. Ikegami, K. Ebihara, *Thin Solid Films* 513 (2006) 90.
- [7] T. Minami, H. Sato, H. Sonohara, S. Takata, T. Miyata, I. Fukuda, *Thin Solid Films* 253 (1994) 14.
- [8] J.J. Robbins, J. Harvey, J. Leaf, C. Fry, C.A. Wolden, *Thin Solid Films* 473 (2005) 35.
- [9] A.R. Kaul, O.Yu. Gorbenko, A.N. Botev, L.I. Burova, *Superlattices Microstruct.* 38 (2005) 272.
- [10] K.Y. Cheong, N. Muti, S.R. Ramanan, *Thin Solid Films* 410 (2002) 142.
- [11] R.F. Silva, M.E.D. Zaniquelli, *Thin Solid Films* 449 (2004) 86.
- [12] K.T.R. Reddy, T.B.S. Reddy, I. Forbes, R.W. Miles, *Surf. Coat. Technol.* 151-152 (2002) 110.
- [13] A. Mosbah, A. Moustaghfir, S. Abed, N. Bouhssira, M.S. Aida, E. Tomasella, M. Jacquet, *Surf. Coat. Technol.* 200 (2005) 293.
- [14] J. Mass, P. Bhattacharya, R.S. Katiyar, *Mater. Sci. Eng. B.* 103 (2003) 9.
- [15] K. Ellmer, F. Kudella, R. Mientus, R. Schieck, S. Fiechter, *Thin Solid Films* 247 (1994) 15.
- [16] T. Minami, *Thin Solid Films* 516 (2008) 1314.
- [17] O. Kluth, G. Schöpe, B. Rech, R. Menner, M. Oertel, K. Orgassa, H.W.

- Schock, *Thin Solid Films* 502 (2006) 311.
- [18] Q.B. Ma, Z.Z. Ye, H.P. He, S.H. Hu, J.R. Wang, L.P. Zhu, Y.Z. Zhang, B.H. Zhao, *J. Cryst. Growth* 304 (2007) 64.
- [19] X. Yu, J. Ma, F. Ji, Y. Wang, C. Cheng, H. Ma, *Appl. Surf. Sci.* 245 (2005) 310.
- [20] W.J. Jeong, S.K. Kim, G.C. Park, *Thin Solid Films* 506 (2006) 180.
- [21] O. Kluth, G. Schöpe, J. Hüpkes, C. Agashe, J. Müller, B. Rech, *Thin Solid Films* 442 (2003) 80.
- [22] E. Burstein, *Physiol. Rev.* 93 (1954) 632.

Table. 3.1. Optical band gap values of the AZO films deposited at various process parameters.

Temperature (°C)	Optical band gap (eV)				
	Pure Ar	O ₂ /Ar=1.23%	O ₂ /Ar=1.64%	O ₂ /Ar=3.23%	O ₂ /Ar-9.09%
RT	3.36	3.40	3.36	3.28	3.28
150	3.60	3.49			
200	3.66	3.60			
250	3.70	3.68	3.57	3.49	3.30
300	3.67	3.67			
350	3.61	3.56			

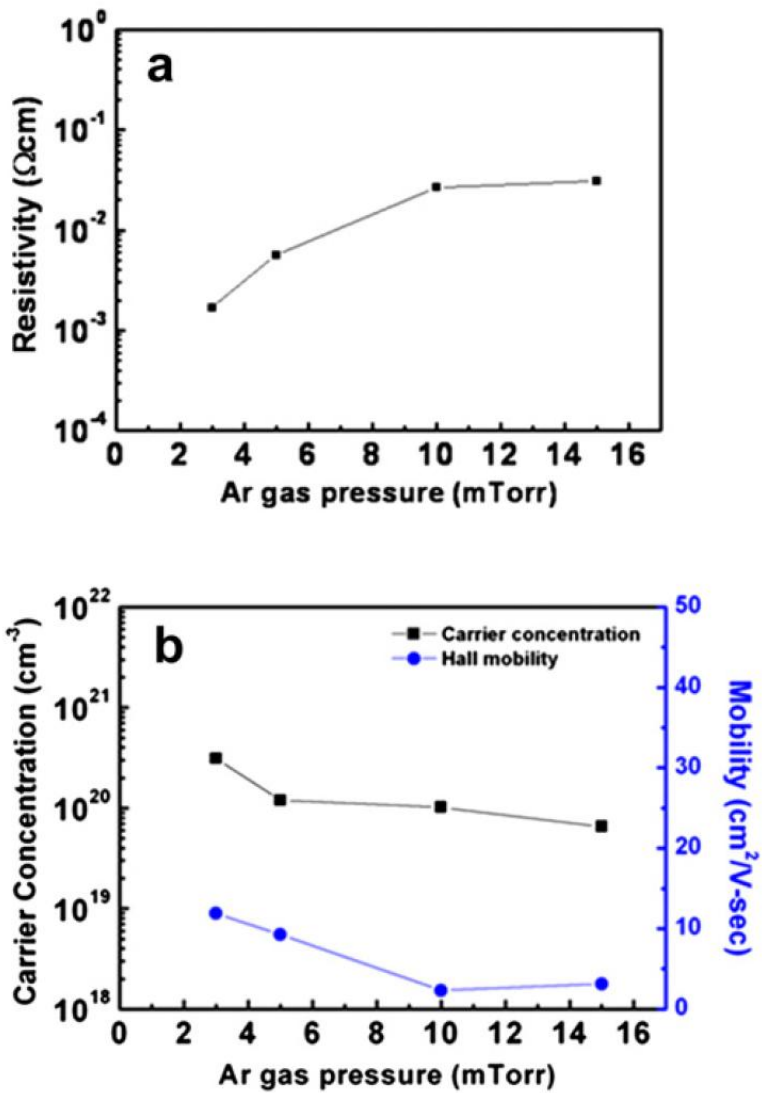


Fig. 3.1. (a) Resistivity, (b) carrier concentration and Hall mobility of the AZO films deposited at various argon gas pressures.

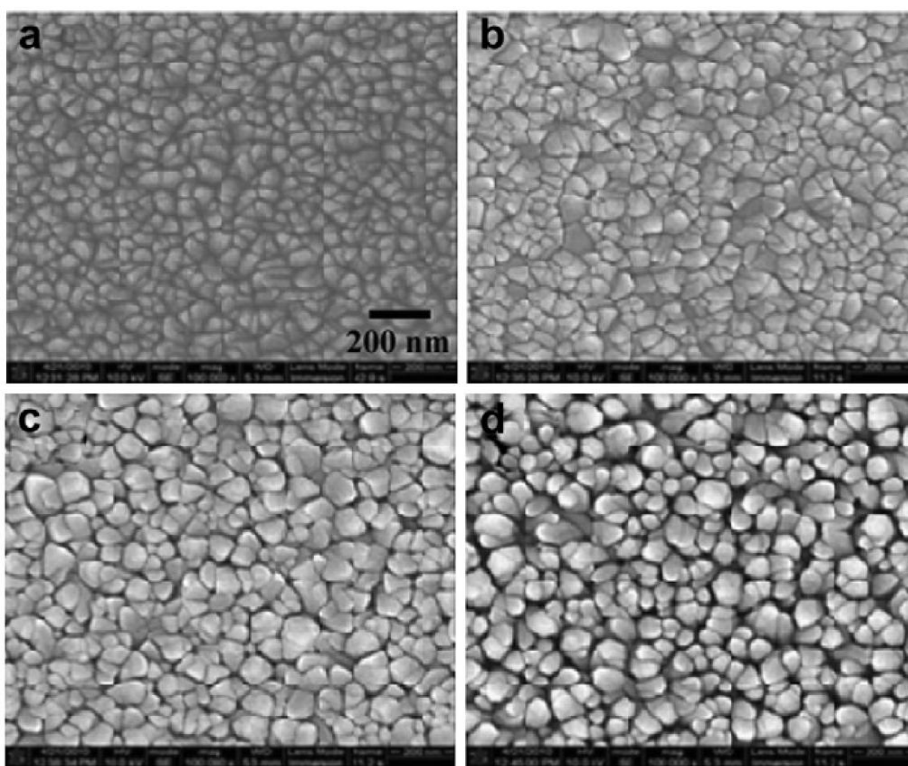


Fig. 3.2. FE-SEM images of the AZO films deposited at argon gas pressures of (a) 3 mTorr, (b) 5 mTorr, (c) 10 mTorr and (d) 15 mTorr.

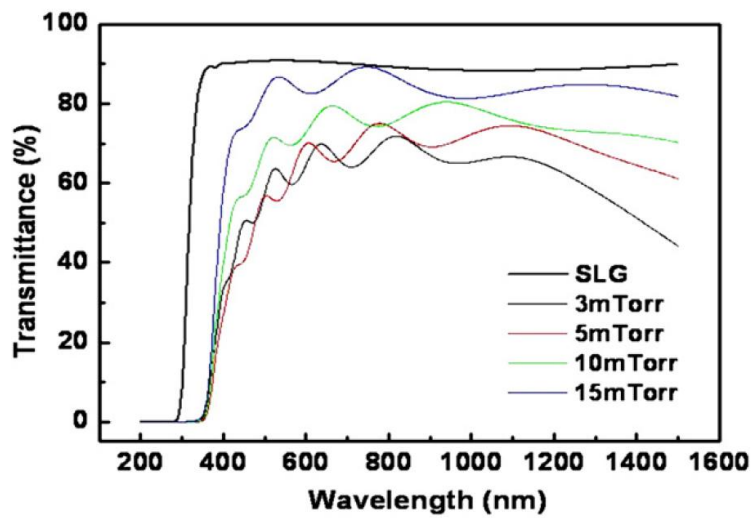


Fig. 3.3. Optical transmittance spectra of the AZO films depending on argon gas pressure in the visible and near-infrared wavelength region.

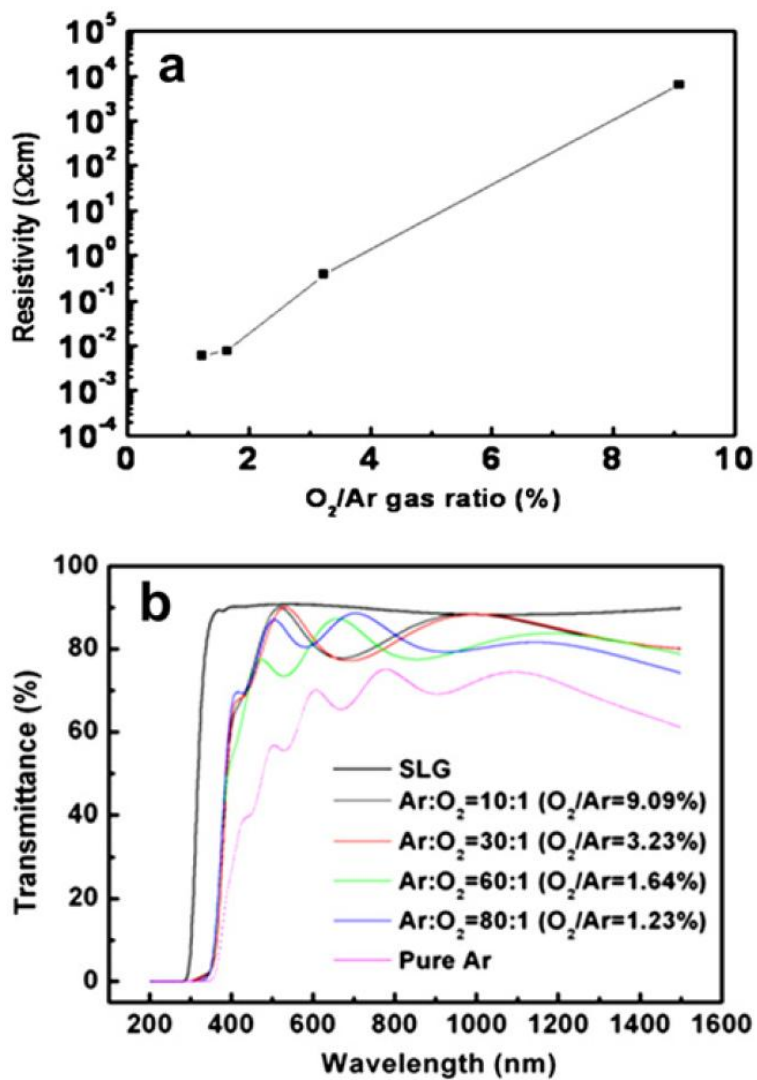


Fig. 3.4. (a) Resistivity and (b) transmittance of the AZO films deposited at room temperature with various O_2/Ar gas ratios.

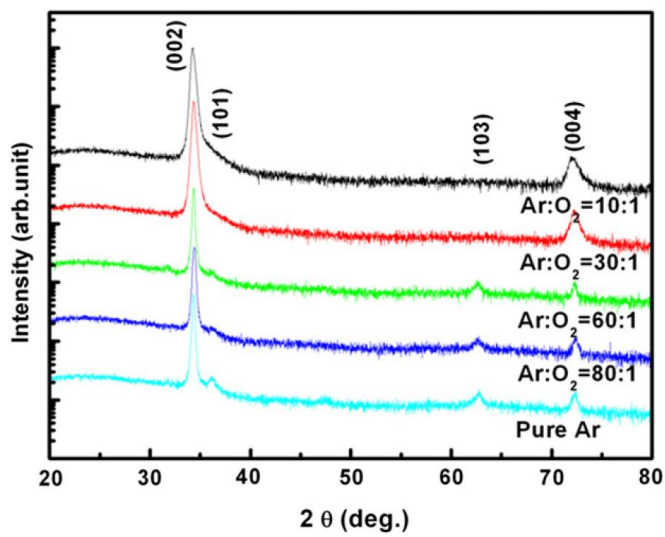


Fig. 3.5. XRD patterns of the AZO films deposited at room temperature with various O₂/Ar gas ratios.

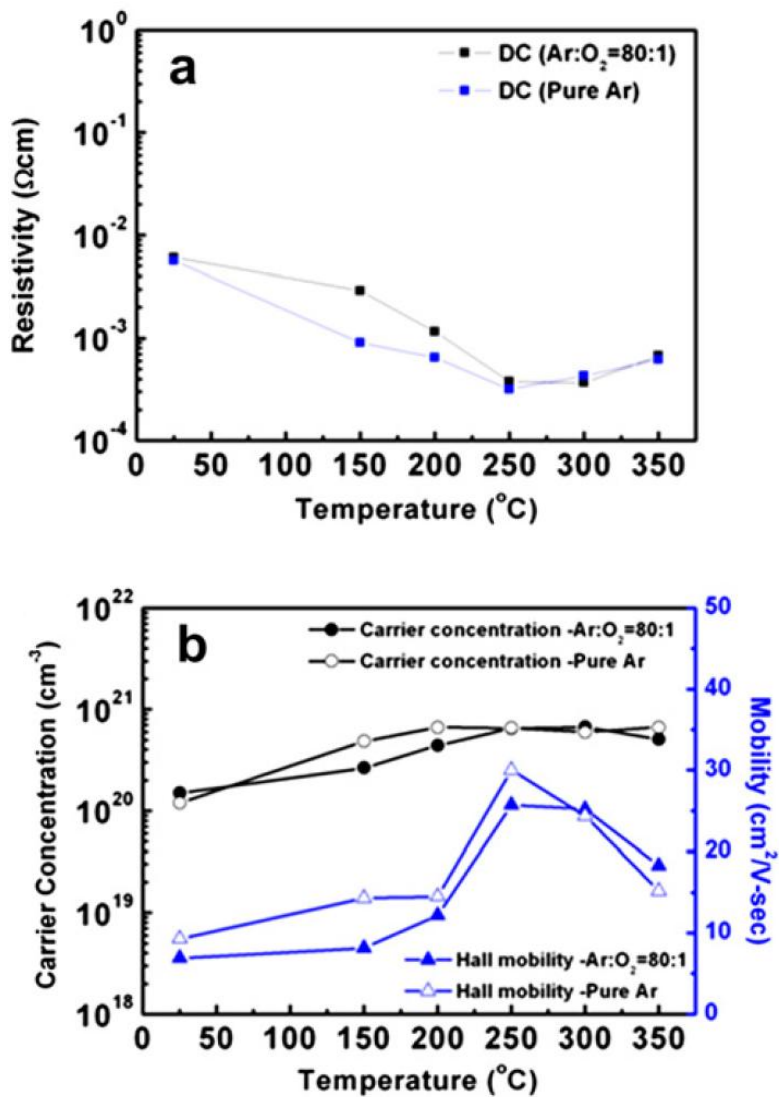


Fig. 3.6. (a) Resistivity, (b) carrier concentration and Hall mobility of the AZO films depending on the substrate temperature.

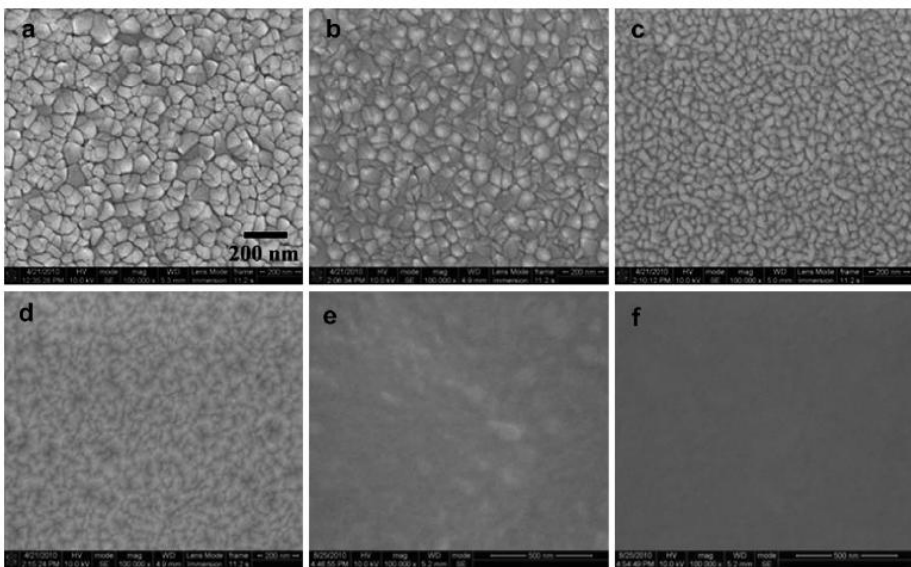


Fig. 3.7. FE-SEM images of the AZO films deposited at substrate temperature of (a) room temperature, (b) 150 °C, (c) 200 °C, (d) 250 °C, (e) 300 °C and (f) 350 °C under pure argon gas pressure.

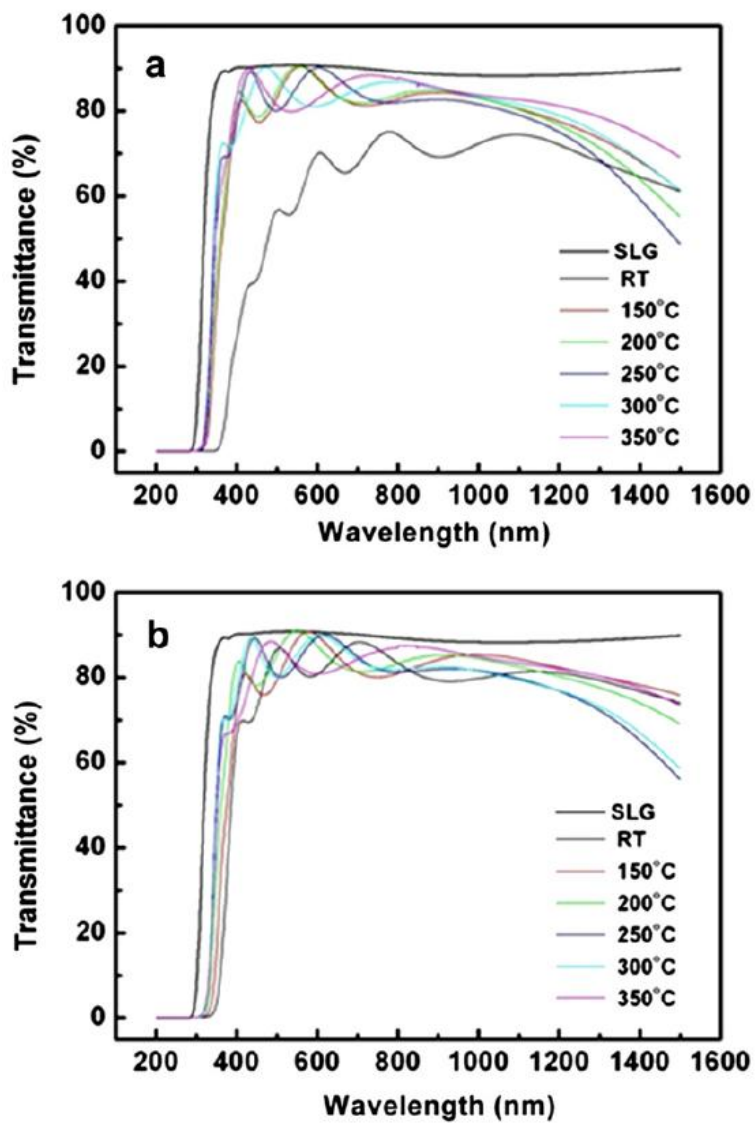


Fig. 3.8. Transmittance spectra of the AZO films deposited at various temperatures in (a) pure Ar and (b) O₂/Ar gas ratio of 1.23%.

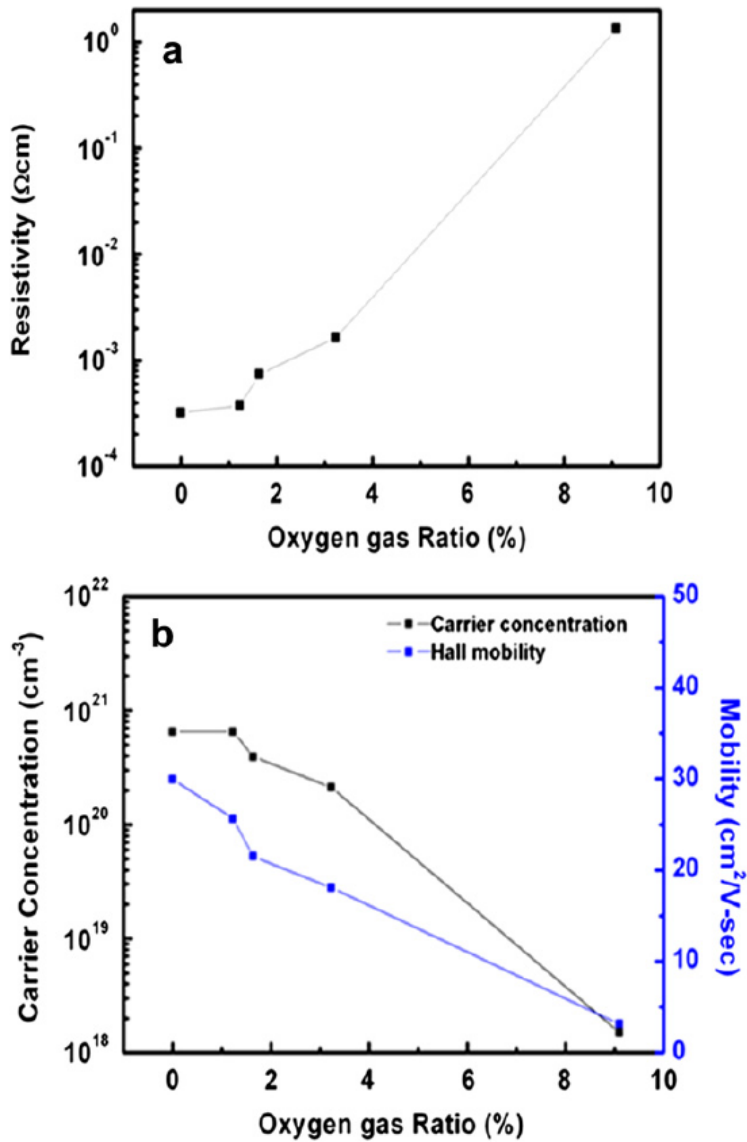


Fig. 3.9. (a) Resistivity, (b) carrier concentration and Hall mobility of the AZO films deposited at 250 °C with various O₂/Ar gas ratios.

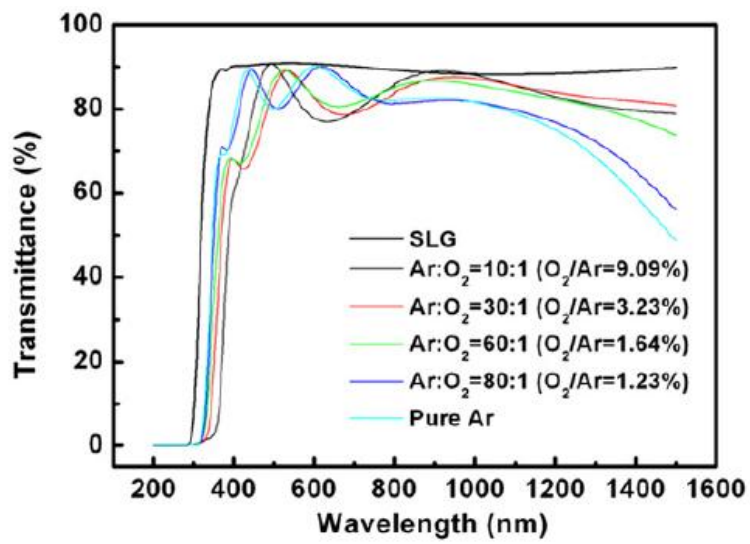


Fig. 3.10. Transmittance spectra of the AZO films deposited at 250 °C with various O₂/Ar gas ratios.

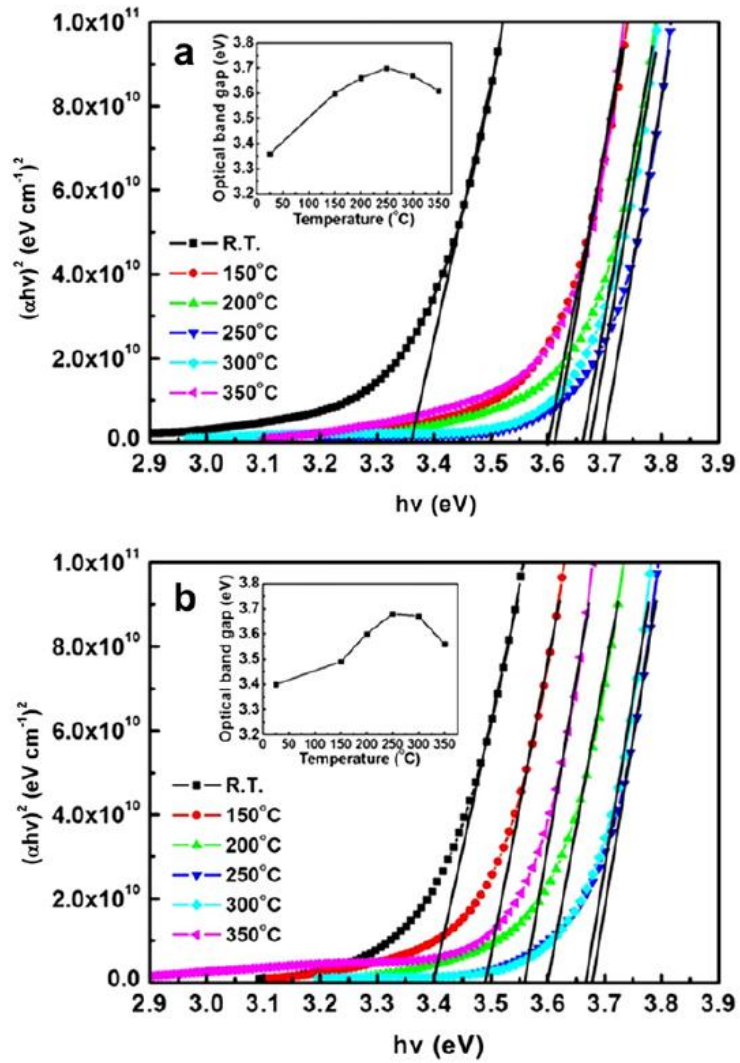


Fig. 3.11. Optical band gap of the AZO films deposited at various substrate temperatures in (a) pure Ar and (b) O₂/Ar gas ratio of 1.23%.

Chapter 4. CIGS absorber layers prepared by RF sputtering without selenization for CIGS solar cells

4.1. Introduction

Cu(In_{1-x}Ga_x)Se₂ (CIGS) thin film solar cell has attracted great attention as one of the most promising solar cells mainly due to its high conversion efficiency which can be achieved via direct band gap characteristics, high absorption coefficient, and ease in band gap engineering of CIGS film. It also has the advantages of excellent resistance to high energy radiation and long-term outdoor stability. However, a very complicated fabrication process, so-called three-stage co-evaporation process, is required for the achievement of the highest conversion efficiency of ~20% [1-3]. In addition, this method has a difficulty to produce large-area film with uniform composition. Meanwhile, a two-step process, which includes deposition of the metal precursor film by sputtering and selenization process, has been studied by many research groups since uniform films with large area can be fabricated through this process. To date, various sputtering methods such as co-sputtering [4, 5] and sequential sputtering [6-8] using separate elemental targets or metal alloy targets have been used for preparing the metal precursor films. And also, single quaternary CIGS target has been recently used for fabricating the CIGS precursor film [9] via one-step process. This one-step process is very easy to obtain large-area

CIGS films with uniform composition because this process simplifies the fabrication process by reducing the number of targets. However, this method still needs the post-selenization process. In general, H₂Se gas is used as a Se source for selenization. However, H₂Se gas is highly toxic for health and environment. Also, selenium is wasted during selenization process. As the other drawback, this process is difficult to control the composition which can influence the band gap of CIGS film because the composition of CIGS film can be changed after selenization. Therefore, to overcome these drawbacks, one-step fabrication of CIGS absorber layer without selenization is needed. Until now, however, the efficiency of the CIGS solar cell fabricated via one-step process without selenization has been rarely reported [10-11], which motivated present study.

In this study, CIGS absorber layers were fabricated via RF magnetron sputtering employing single quaternary CIGS targets with various compositions without selenization. The phases and microstructures of the CIGS absorber layers were investigated and the performance of the CIGS solar cell fabricated by applying these absorber layers is examined.

4.2. Experimental

Various single CIGS sputtering targets with the nominal compositions of Cu_x(In_{0.7}Ga_{0.3})Se_y (where x=0.95 and 1, y=2 to 2.5) were fabricated by conventional solid state reaction using CIGS powder synthesized by planetary ball milling. Employing these targets, CIGS absorbers were deposited on Mo coated soda lime glass (SLG) substrates by RF magnetron

sputtering without selenization. Base pressure of vacuum chamber before deposition was approximately 3.0×10^{-6} Torr. Substrate rotation was carried out at 3 rpm for film uniformity.

First, properties of the CIGS films fabricated via the single CIGS sputtering target with the nominal composition of $\text{Cu}(\text{In}_{0.7}\text{Ga}_{0.3})\text{Se}_2$ were investigated. The CIGS films were deposited with RF power of 190W under argon gas pressure of 10mTorr at room temperature (R.T.), and then post- annealed in Ar atmosphere. Also, CIGS films were deposited at various temperatures ranging from 300 to 450 °C.

Second, properties of the CIGS films fabricated via single CIGS sputtering targets with the nominal compositions of $\text{Cu}_{0.95}(\text{In}_{0.7}\text{Ga}_{0.3})\text{Se}_{2.5}$ and $\text{Cu}_{0.95}(\text{In}_{0.7}\text{Ga}_{0.3})\text{Se}_{2.1}$ were investigated. The CIGS films were deposited at various temperatures under argon gas pressure of 10mTorr with RF power of 190W and 120W, respectively.

Finally, properties of the CIGS films prepared via the single target of $\text{Cu}(\text{In}_{0.7}\text{Ga}_{0.3})\text{Se}_{2.5}$ powder were investigated. The CIGS films were deposited with RF power of 120W under argon gas pressure of 10mTorr at the temperatures ranging from room temperature (R.T.) to 500 °C. After deposition, the CIGS films were annealed at 450 °C for 30min in Ar atmosphere with Se.

Using the fabricated CIGS absorber layers, the CIGS thin film solar cells with the structure of Al/AZO/i-ZnO/CdS/CIGS/Mo/SLG were fabricated to measure the conversion efficiency. A 50nm-thick CdS layer was coated by chemical bath deposition. A 50nm-thick intrinsic ZnO and a 400nm-thick Al-doped ZnO (2 wt% Al_2O_3) layers were sequentially deposited by using RF

magnetron sputtering. Al grids for the enhancement of carrier collection were deposited by thermal evaporation. The cell area defined by mechanical scribing was approximately 0.36 cm².

Crystal structures of the CIGS films were investigated by x-ray diffraction (XRD) with Cu-K α radiation. Surface morphologies and cross-sectional images were observed via field emission scanning electron microscopy (FESEM). Compositional analysis of CIGS films was performed by inductively coupled plasma (ICP) spectrometer. Resistivity and Hall resistance are measured by Hall effect measurement system. Conversion efficiency of the CIGS thin film solar cell was measured by a solar simulator under AM 1.5 illumination.

4.3. Results and discussion

4.3.1. CIGS layers prepared using the single CIGS targets of various compositions

Fig. 4.1 (a) shows the surface morphology of the CIGS film deposited at room temperature by using a stoichiometric CIGS (Cu(In_{0.7}Ga_{0.3})Se₂) target. And Figs. 4.1 (b), (c) and (d) show the surface morphologies of the CIGS films annealed in an Ar atmosphere at the temperatures of 400, 500 and 600 °C, respectively. As can be seen in figures, grain growth did not occur regardless of the annealing temperature when the CIGS precursor film was annealed in an Ar atmosphere. Therefore, the CIGS films were deposited at various temperatures ranging from 300 to 450 °C. As shown in Fig. 4.2, grain

size was increased with increasing a deposition temperature. However, rough and porous surface morphology with the faceted grains was obtained. Using these CIGS films, the CIGS thin film solar cells with the structure of Al/AZO/i-ZnO/CdS/CIGS/Mo/SLG were fabricated. Fig. 4.3 shows the current-voltage characteristics under AM 1.5 illumination. Very low efficiencies were obtained from the CIGS solar cells fabricated using a stoichiometric CIGS target.

For enhancing the efficiency and obtaining the smooth surface morphology, various CIGS targets with the nominal compositions of $\text{Cu}_{0.95}(\text{In}_{0.7}\text{Ga}_{0.3})\text{Se}_{2.5}$ and $\text{Cu}_{0.95}(\text{In}_{0.7}\text{Ga}_{0.3})\text{Se}_{2.1}$ were used. Figs. 4.4 and 4.5 show the CIGS films fabricated by using $\text{Cu}_{0.95}(\text{In}_{0.7}\text{Ga}_{0.3})\text{Se}_{2.5}$ and $\text{Cu}_{0.95}(\text{In}_{0.7}\text{Ga}_{0.3})\text{Se}_{2.1}$ target. As can be seen in Fig. 4.4 (a) and Fig. 4.5 (a), grain size of these films was smaller than that of the CIGS film fabricated using a stoichiometric CIGS target. This result is thought to be caused by Cu-poor composition of these CIGS targets. A smaller quantity of copper in the CIGS film can suppress the formation of the Cu_{2-x}Se phase which is known to increase grain size. Therefore, the CIGS films with a smoother surface morphology can be obtained by using Cu-poor CIGS targets. However, surface morphology becomes rough with increasing deposition temperature as shown in Fig. 4.5 (b), (c) and (d). And all of the films showed the faceted grains similar to those of the CIGS film fabricated using a stoichiometric CIGS target although grain size is smaller.

Meanwhile, XRD patterns of these CIGS films were investigated. As shown in Fig. 4.6, the CIGS films were crystalized to a random orientation. And the second phase of $(\text{In,Ga})_2\text{Se}_3$ was detected in all of the CIGS films. Peak

intensity of the second phase was decreased with increasing deposition temperature. Eventually, the diffraction peak of $(\text{In,Ga})_2\text{Se}_3$ phase almost disappeared and the CIGS film shows chalcopyrite structure which can be characterized by peaks such as (101), (103), (211), (213)/(105) and (301).

Conversion efficiency of the CIGS solar cells fabricated by using these CIGS absorber layers was measured. Although the CIGS films have chalcopyrite structure with high crystallinity, very low conversion efficiencies were achieved. As shown in Fig. 4.7, the highest conversion efficiency of about 2% was obtained from the CIGS solar cell fabricated using the $\text{Cu}_{0.95}(\text{In}_{0.7}\text{Ga}_{0.3})\text{Se}_{2.5}$ target. However, the CIGS solar cells fabricated using the $\text{Cu}_{0.95}(\text{In}_{0.7}\text{Ga}_{0.3})\text{Se}_{2.1}$ target, containing the smaller quantity of Se, showed the lower conversion efficiency as shown in Fig. 4.7.

Low conversion efficiency of these solar cells is thought to be caused by Se-poor composition of these CIGS films as well as rough surface morphology. Fig. 4.8 shows the ternary phase diagram of the CIGS films fabricated in this study. Comparing with initial composition of CIGS targets, selenium was rather decreased. This means that supplement of additional selenium is needed for the stoichiometric a-CIS phase

4.3.2 CIGS layers prepared using the single target of $\text{Cu}(\text{In}_{0.7}\text{Ga}_{0.3})\text{Se}_{2.5}$ powder

For reducing a Se loss and increasing a Se amount of CIGS film, the CIGS films were prepared by using the single target of $\text{Cu}(\text{In}_{0.7}\text{Ga}_{0.3})\text{Se}_{2.5}$ powder. The CIGS target did not go through sintering process to impede a vaporation

of Se. Fig. 4.9 shows the SEM images of the CIGS films deposited at various temperatures. As shown in figures, grain size was increased with increasing deposition temperature. Especially, abrupt grain growth was occurred at the deposition temperature of 400 °C. However, the CIGS films show still rough and porous surface morphology. Meanwhile, after annealing in Ar atmosphere with selenium, that is to say a selenization, grain size of all of the CIGS films was increased and denser CIGS films were obtained as shown in Fig. 4.10. XRD patterns of these CIGS films were investigated. Fig. 4.11 (a) and (b) show the XRD patterns of the CIGS film before and after selenization, respectively. All of the CIGS films deposited above 350 °C had the second phase of $(\text{In,Ga})_2\text{Se}_3$ as well as the CIGS phase. And the CIGS films showed a (220)/(204) preferred orientation. This can be caused by Se-rich composition of the CIGS film. After selenization, the second phase of $(\text{In,Ga})_2\text{Se}_3$ disappeared and the intensity of (112) orientation was increased. This means that the CIGS films had been recrystallized by the incorporation of selenium. On the other hand, the MoSe_2 layer was created. A MoSe_2 layer is known to enhance the efficiency by forming the ohmic contact between the CIGS layer and the Mo electrode layer [12,13]. However, very thick MoSe_2 layer is detrimental to the conversion efficiency [14].

Resistivity and Hall resistance are measured by Hall effect measurement system. Fig. 4.12 (a) shows the resistivity before and after selenization of the CIGS film as a function of deposition temperature. Before selenization, the CIGS films have high resistivity. After selenization, however, resistivity of the films was greatly decreased. And Figs 4.12 (b) and (c) show the Hall resistance after selenization of the CIGS films deposited at 400 and 450 °C,

respectively. All of the CIGS films show the positive slope in the properties of Hall resistance versus magnetic field. This means that the CIGS films have the p-type conductivity.

Conversion efficiency of the CIGS solar cells fabricated by using these CIGS absorber layers was measured. Fig. 4.13 shows the current-voltage characteristics of the CIGS solar cells. And their conversion efficiencies were summarized in the table 4.1. After selenization, the highest conversion efficiency of about 3.3% was obtained from the CIGS solar cell fabricated using the CIGS film deposited at 400 °C.

Consequently, selenization process is beneficial to efficiency enhancement because of improvement of structural and electrical properties.

4.4. Summary

Various single CIGS sputtering targets with the nominal compositions of $\text{Cu}_x(\text{In}_{0.7}\text{Ga}_{0.3})\text{Se}_y$ ($x=0.95\sim 1$, $y=2\sim 2.5$) were fabricated. Employing these targets, CIGS films were deposited on Mo coated soda lime glass (SLG) substrates by using RF magnetron sputtering. In the case of CIGS film fabricated using a stoichiometric CIGS target, grain growth of the CIGS film deposited at room temperature did not occur regardless of the annealing temperature when the CIGS precursor film was annealed in an Ar atmosphere. Grain size of the CIGS films deposited at various temperatures was increased with increasing a deposition temperature. However, rough and porous surface morphology with the faceted grains was obtained and therefore very low efficiencies were achieved. For enhancing the efficiency and obtaining the

smooth surface morphology, various CIGS targets with the nominal compositions of $\text{Cu}_{0.95}(\text{In}_{0.7}\text{Ga}_{0.3})\text{Se}_{2.5}$ and $\text{Cu}_{0.95}(\text{In}_{0.7}\text{Ga}_{0.3})\text{Se}_{2.1}$ were used to fabricate CIGS absorber layer. Grain size of these films was smaller than that of the CIGS film fabricated using a stoichiometric CIGS target. This result is thought to be caused by Cu-poor composition of these CIGS targets. Although the CIGS films with a smoother surface morphology can be obtained by using Cu-poor CIGS targets, surface morphology becomes rough with increasing deposition temperature. Conversion efficiency of about 2% was obtained from the CIGS solar cell fabricated using the $\text{Cu}_{0.95}(\text{In}_{0.7}\text{Ga}_{0.3})\text{Se}_{2.5}$ target. However, the CIGS solar cells fabricated using the $\text{Cu}_{0.95}(\text{In}_{0.7}\text{Ga}_{0.3})\text{Se}_{2.1}$ target, containing the smaller quantity of Se, showed the lower conversion efficiency. Meanwhile, for supplement of selenium, CIGS films fabricated by using the single target of $\text{Cu}(\text{In}_{0.7}\text{Ga}_{0.3})\text{Se}_{2.5}$ powder were annealed in Ar atmosphere with selenium. These films showed the densely packed surface morphology. Conversion efficiency of the solar cells fabricated using these CIGS films was enhanced. Consequentially, selenization process is beneficial to improvement of structural and electrical properties. Hence, in the next study, the effect of selenization of CIGS precursor film was systematically investigated.

References

- [1] I. Repins, M. A. Contreras, B. Egaas, C. DeHart, J. Scharf, C. L. Perkins, B. To, R. Noufi, *Prog. Photovolt: Res. Appl.* 16 (2008) 235.
- [2] P. Jackson, D. Hariskos, E. Lotter, S. Paetel, R. Wuerz, R. Menner, W. Wischmann, M. Powalla, *Prog. Photovolt. Res. Appl.* 19 (2011) 894.
- [3] M. A. Green, K. Emery, Y. Hishikawa, W. Warta, E. D. Dunlop, *Prog. Photovolt. Res. Appl.* 22 (2014) 1.
- [4] S.D. Kim, H.J. Kim, K.H. Yoon, J. Song, *Sol. Energy Mater. Sol. Cells* 62 (2000) 357.
- [5] D.G. Moon, S. Ahn, J.H. Yun, A. Cho, J. Gwak, S. Ahn, K. Shin, K. Yoon, H.D. Lee, H. Pak, S. Kwon, *Sol. Energy Mater. Sol. Cells* 95 (2011) 2786.
- [6] M. Marudachalam, H. Hichri, R. Klenk, R.W. Birkmire, W.N. Shafarman, *Appl. Phys. Lett.* 67 (1995) 3978.
- [7] T. Nakada, A. Kunioka, *Jpn. J. Appl. Phys.* 37 (1998) L1065.
- [8] W. Li, Y. Sun, W. Liu, L. Zhou, *Solar Energy* 80 (2006) 191.
- [9] J.H. Shi, Z.Q. Li, D.W. Zhang, Q.Q. Liu, Z. Sun, S.M. Huang, *Prog. Photovolt. Res. Appl.* 19 (2011) 160.
- [10] J.A. Frantz, R.Y. Bekele, V.Q. Nguyen, J.S. Sanghera, A. Bruce, S.V. Frolov, M. Cyrus, I.D. Aggarwal, *Thin Solid Films* 519 (2011) 7763.
- [11] C.H. Chen, W.C. Shih, C.Y. Chien, C.H. Hsu, Y.H. Wu, C.H. Lai, *Sol. Energy Mater. Sol. Cells* 103 (2012) 25.
- [12] T. Wada, N. Kohara, S. Nishiwaki, T. Negami, *Thin Solid Films* 387 (2001) 118.
- [13] L. Assmann, J. C. Bernede, A. Drici, C. Amory, E. Halgand, M. Morsli, *Appl. Surf. Sci.* 171 (2001) 15.
- [14] X. Zhu, Z. Zhou, Y. Wang, L. Zhang, A. Li, F. Huang, *Sol. Energy Mater. Sol. Cells* 101 (2012) 57.

Table. 4.1. Summary of conversion efficiencies shown in Fig. 4.13.

Sample	Deposition temperature (°C)	V_{oc} (V)	J_{sc} (mA/cm ²)	FF (%)	η (%)
A	R. T.	0.164	15.15	26.7	0.67
B	350	0.085	16.44	25.9	0.36
C	400	0.339	21.40	45.3	3.29
D	450	0.325	17.21	36.1	2.02
E	500	0.307	20.38	35.4	2.21

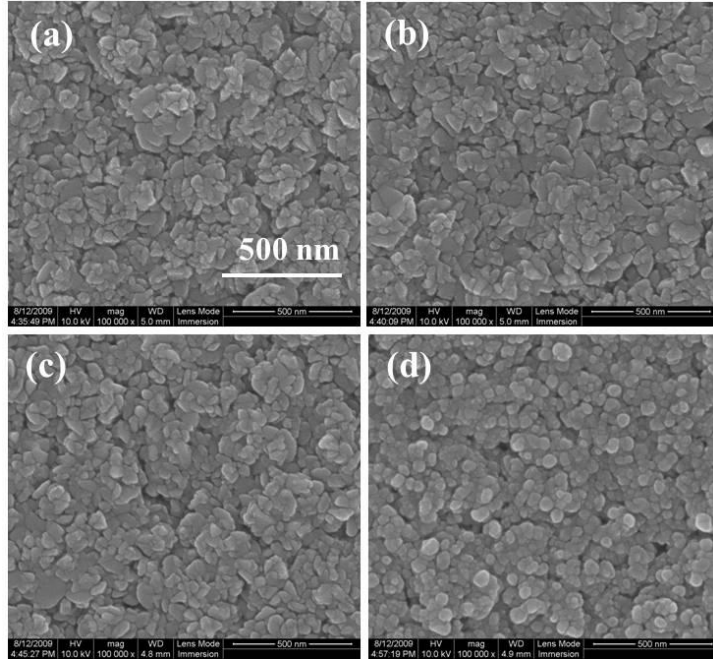


Fig. 4.1. Surface morphology of the CIGS film deposited at (a) room temperature and the CIGS films annealed at (b) 400 °C (c) 500 °C and (d) 600 °C in an Ar atmosphere. The CIGS film was fabricated using a stoichiometric CIGS ($\text{Cu}(\text{In}_{0.7}\text{Ga}_{0.3})\text{Se}_2$) target.

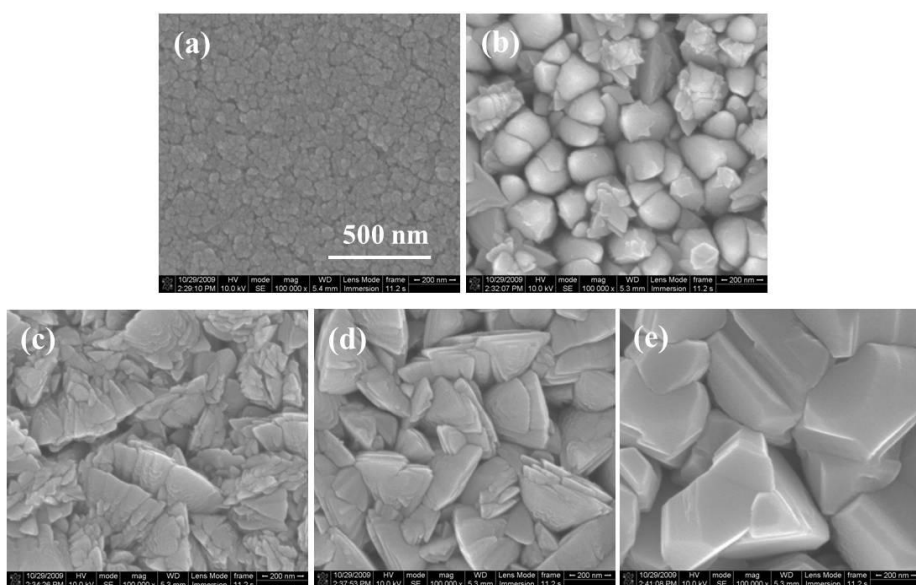


Fig. 4.2. Surface morphology of the CIGS films deposited at (a) room temperature, (b) 300 °C, (c) 350 °C, (d) 400 °C and (e) 450 °C. The CIGS film was fabricated using a stoichiometric CIGS ($\text{Cu}(\text{In}_{0.7}\text{Ga}_{0.3})\text{Se}_2$) target.

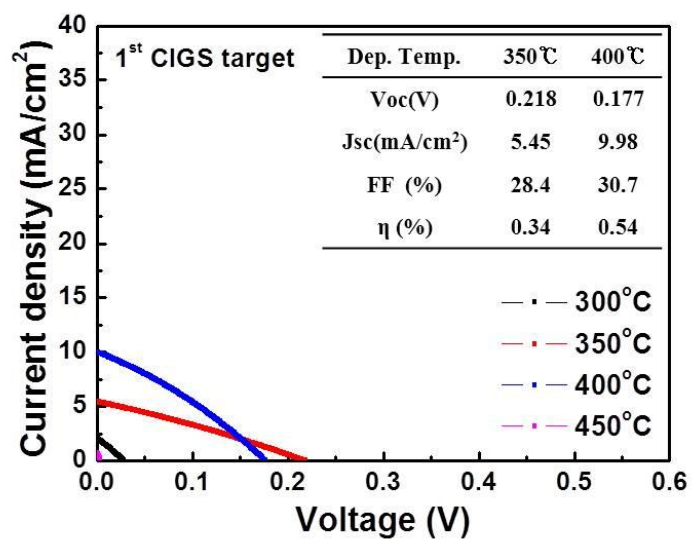


Fig. 4.3. Current-voltage characteristics of the CIGS solar cells fabricated using a stoichiometric CIGS ($\text{Cu}(\text{In}_{0.7}\text{Ga}_{0.3})\text{Se}_2$) target. The CIGS absorber layers were deposited at the temperatures of 300, 350, 400 and 450 °C, respectively.

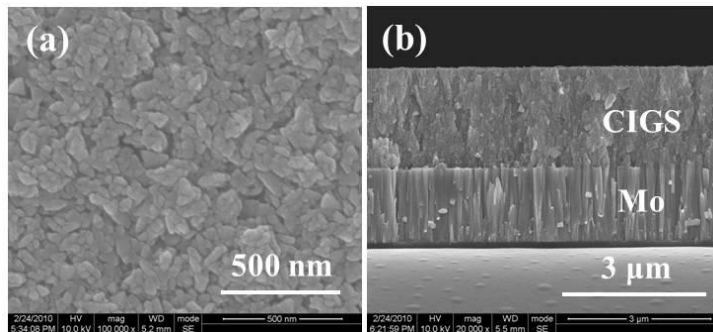


Fig. 4.4. Surface morphology and cross-sectional image of the CIGS films fabricated using a $\text{Cu}_{0.95}(\text{In}_{0.7}\text{Ga}_{0.3})\text{Se}_{2.5}$ target. The CIGS film was deposited at 300 °C.

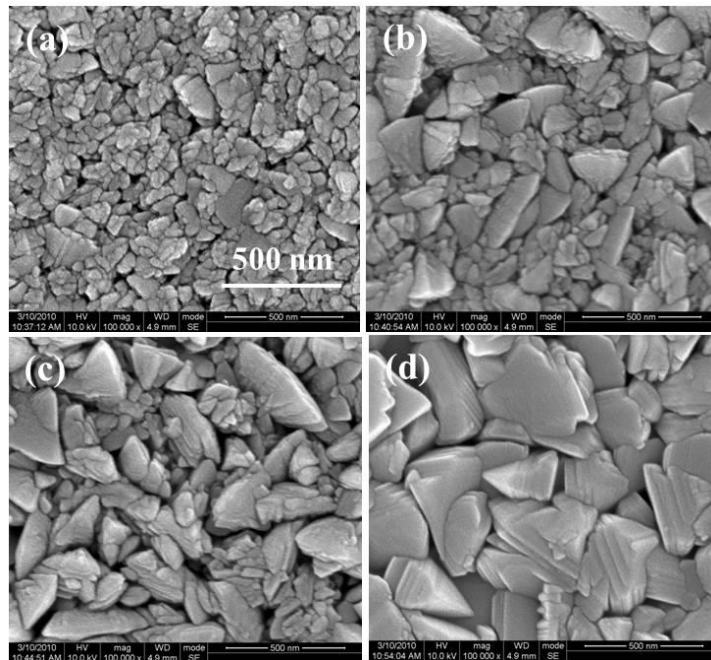


Fig. 4.5. Surface morphology of the CIGS films deposited at (a) 300 °C, (b) 350 °C, (c) 400 °C and (d) 450 °C. The CIGS film was fabricated using a $\text{Cu}_{0.95}(\text{In}_{0.7}\text{Ga}_{0.3})\text{Se}_{2.1}$ target.

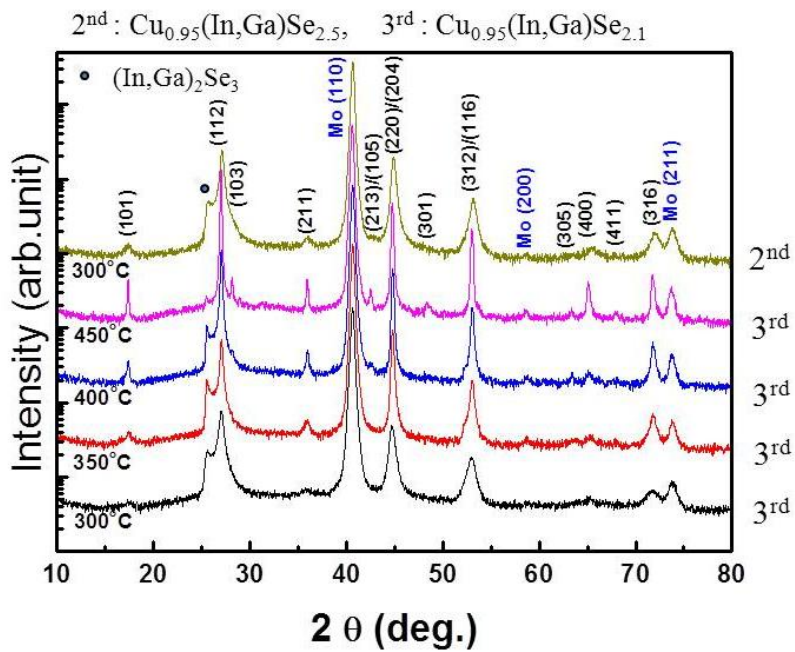


Fig. 4.6. XRD patterns of the CIGS films fabricated using $\text{Cu}_{0.95}(\text{In}_{0.7}\text{Ga}_{0.3})\text{Se}_{2.5}$ and $\text{Cu}_{0.95}(\text{In}_{0.7}\text{Ga}_{0.3})\text{Se}_{2.1}$ target.

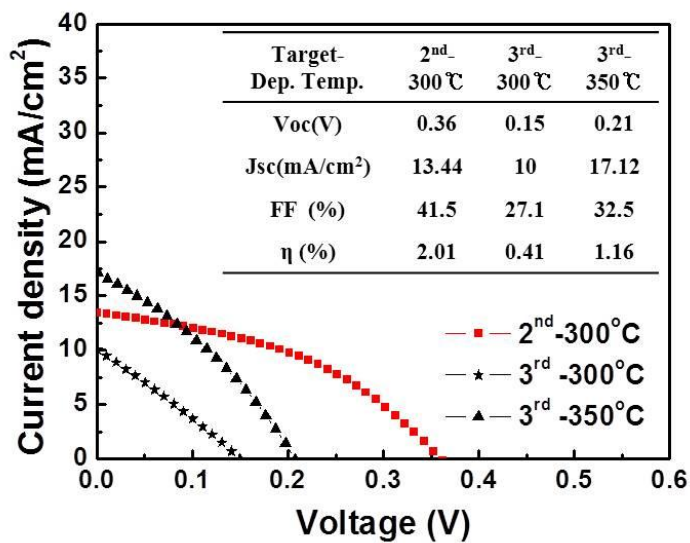


Fig. 4.7. Current-voltage characteristics of the CIGS solar cells fabricated using the $\text{Cu}_{0.95}(\text{In}_{0.7}\text{Ga}_{0.3})\text{Se}_{2.5}$ and $\text{Cu}_{0.95}(\text{In}_{0.7}\text{Ga}_{0.3})\text{Se}_{2.1}$ target. The CIGS absorber layers were deposited at the temperatures of 300 °C and 350 °C, respectively.

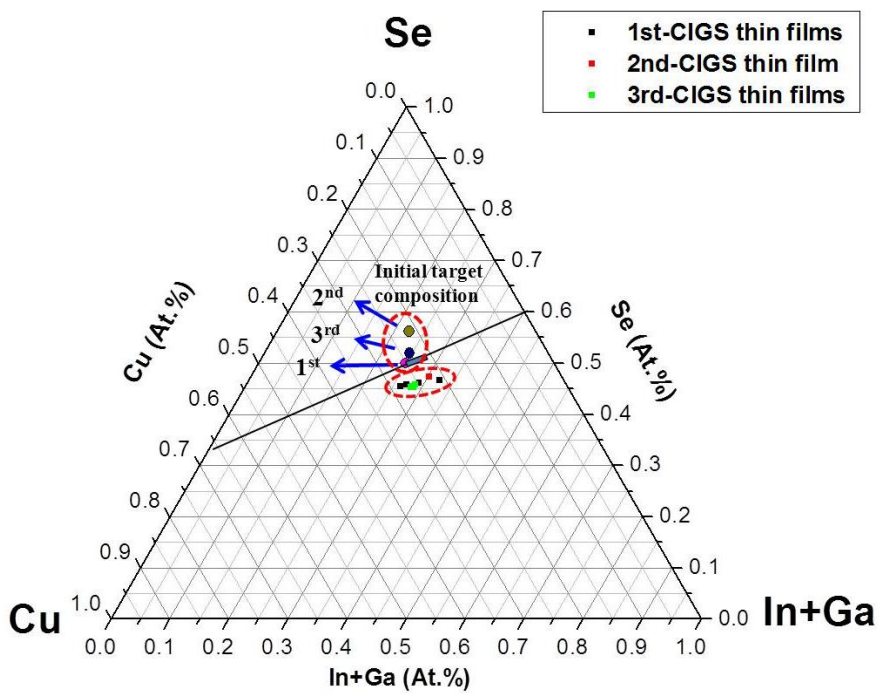


Fig. 4.8. Ternary phase diagram of the CIGS targets and the CIGS films fabricated using these CIGS targets

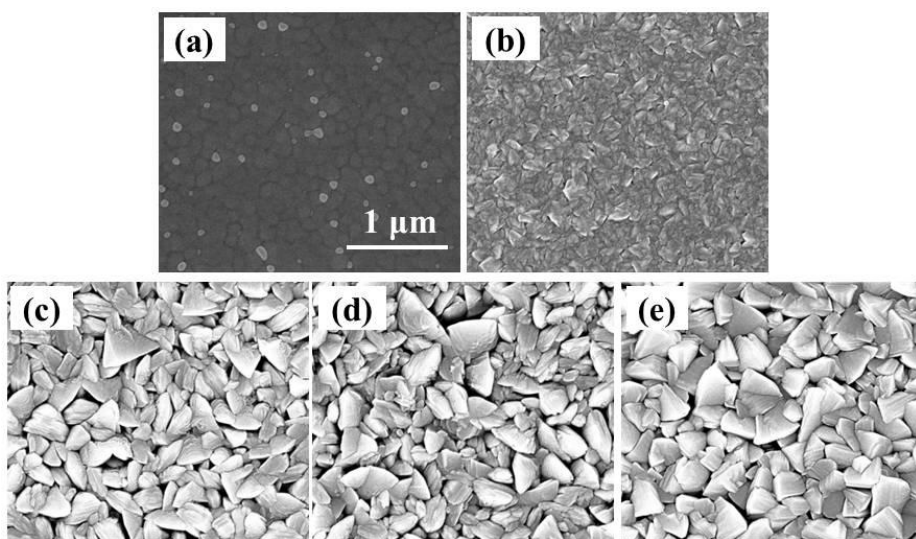


Fig. 4.9. Surface morphology of the CIGS films deposited at (a) room temperature (b) 350 °C, (c) 400 °C, (d) 450 °C and (e) 500 °C. The CIGS film was fabricated using the single target of $\text{Cu}(\text{In}_{0.7}\text{Ga}_{0.3})\text{Se}_{2.5}$ powder.

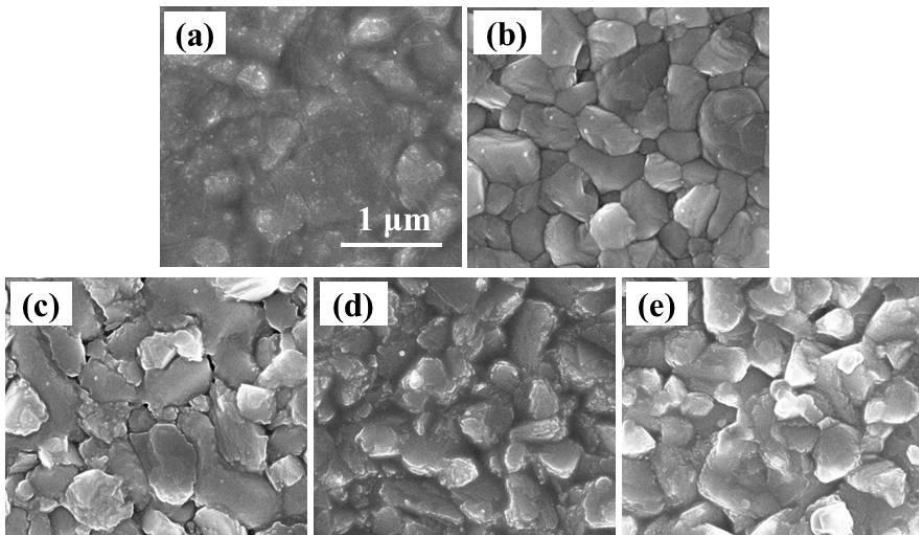


Fig. 4.10. Surface morphology after selenization of the CIGS films deposited at (a) room temperature (b) 350 °C, (c) 400 °C, (d) 450 °C and (e) 500 °C. The CIGS film was fabricated using the single target of $\text{Cu}(\text{In}_{0.7}\text{Ga}_{0.3})\text{Se}_{2.5}$ powder.

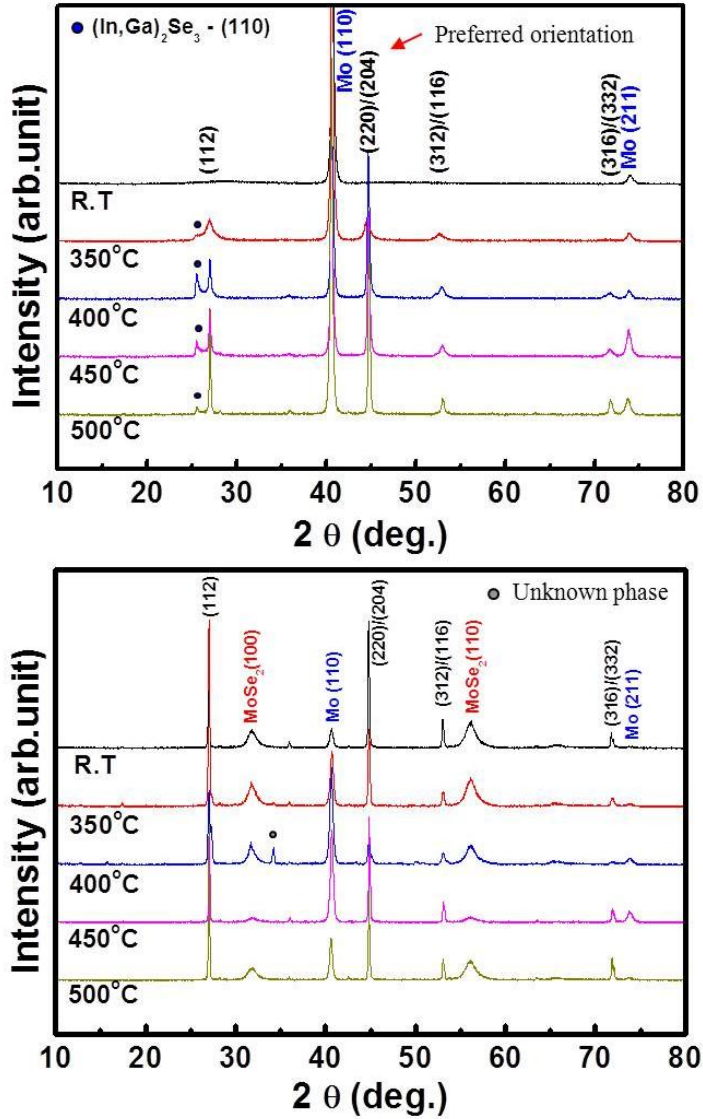


Fig. 4.11. XRD patterns (a) before and (b) after selenization of the CIGS films deposited at room temperature, 350, 400, 450 and 500 °C. The CIGS film was fabricated using the single target of $\text{Cu}(\text{In}_{0.7}\text{Ga}_{0.3})\text{Se}_{2.5}$ powder.

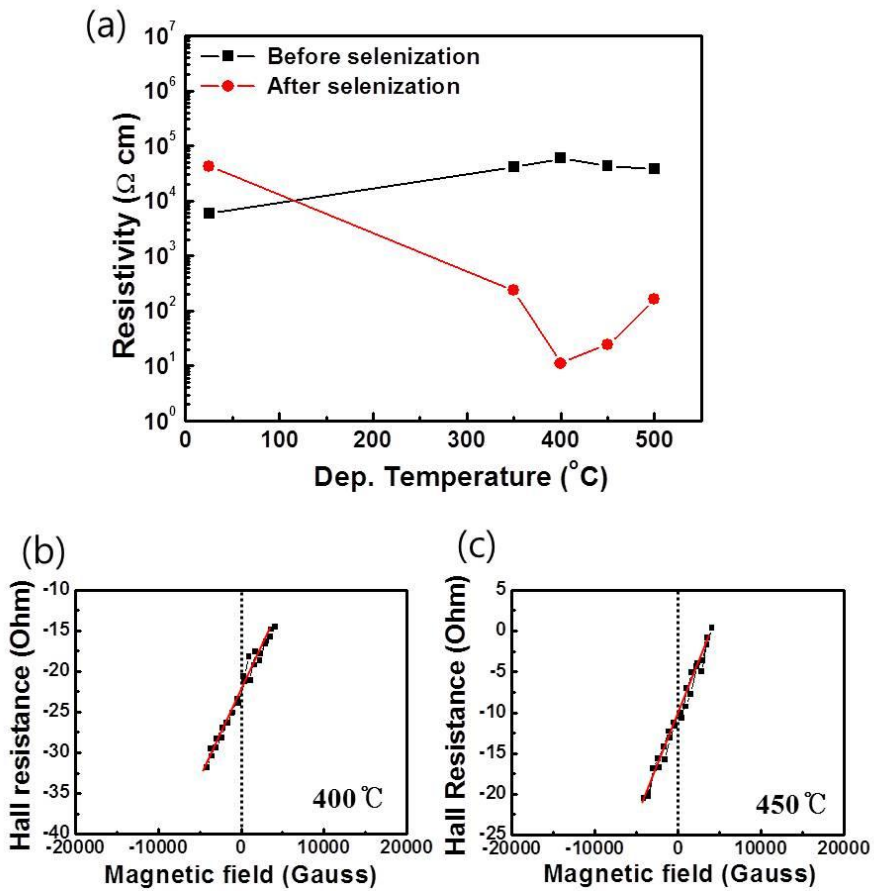


Fig. 4.12. (a) Resistivity before and after selenization of the CIGS film as a function of deposition temperature. And Hall resistance after selenization of the CIGS films deposited at (b) 400 $^{\circ}\text{C}$ and (c) 450 $^{\circ}\text{C}$.

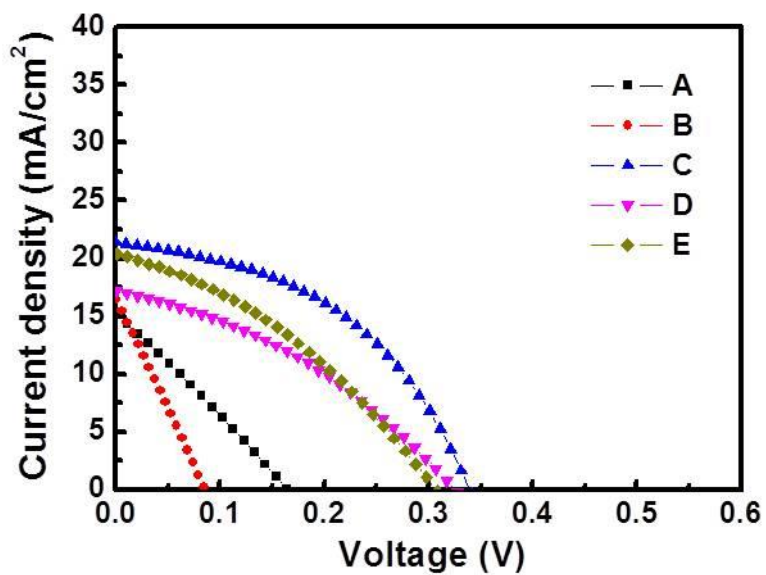


Fig. 4.13. Current-voltage characteristics of the CIGS solar cells fabricated using the single target of $\text{Cu}(\text{In}_{0.7}\text{Ga}_{0.3})\text{Se}_{2.5}$ powder. The solar cell A, B, C, D and E are fabricated after selenization CIGS precursor films deposited at the temperatures of 400, 450, 475 and 500 °C, respectively.

Chapter 5. CIGS absorber layers prepared by RF sputtering with selenization for CIGS solar cells

5.1. Introduction

Thin film solar cells have been extensively investigated to provide a low-cost solar energy because these require small consumption of raw materials. Among them, Cu(In,Ga)Se₂ (CIGS) solar cell has attracted great attention mainly due to its high conversion efficiency which can be achieved via direct band gap characteristics, high absorption coefficient and ease in band gap engineering of CIGS film. It also has the advantages of excellent resistance to high energy radiation and long-term outdoor stability. The highest conversion efficiency of ~20% has been obtained from CIGS thin films deposited by a three-stage co-evaporation method [1]. This method is very complicated and large-area film with uniform composition is difficult to obtain; hence, it is difficult to realize mass production of CIGS thin films. Meanwhile, a two-step process, which includes deposition of the metal precursor film by sputtering and selenization, has been studied by many research groups since uniform films with large area can be fabricated through this process. To date, various sputtering methods such as co-sputtering [2, 3] and sequential sputtering [4-6] using separate elemental

targets or metal alloy targets have been used for preparing the metal precursor films.

Recently, single quaternary CIGS target has been used for fabricating the CIGS precursor layer [7] or CIGS absorber layer [8, 9] via one-step process. This one-step process is very easy to obtain large-area CIGS films with uniform composition. The properties of CIGS films prepared by the one-step process using the single CIGS target are highly dependent on the characteristics of the single CIGS target. In particular, the composition of the target can affect the properties of the CIGS film because the CIGS compound is a self-doping semiconductor by point defects with low formation energy [10] and has many kinds of the second phases [11, 12]. Until now, however, the effect of composition of the single CIGS target on the properties of CIGS films and CIGS thin film solar cells has been rarely reported. Therefore, in this chapter, characteristics of the CIGS film and device fabricated using single quaternary CIGS targets with various compositions were firstly investigated. Also, in general, properties of CIGS film are greatly influenced by selenium. Therefore, characteristics of the CIGS films selenized using powders with various Se ratios were secondly examined. Based on above results, nano-crystalline CIGS precursor film was proposed to enhance the CIGS solar cell performance. Finally, the properties of the CIGS film and device fabricated using nano-crystalline CIGS precursor film were systematically investigated.

For these studies, CIGS precursor films were deposited via RF magnetron sputtering employing single quaternary CIGS targets and then selenized under Se atmosphere. The phases and microstructures of CIGS absorber

layers and their effects on the CIGS solar cell performance have been systematically investigated.

5.2. Experimental

Various single CIGS sputtering targets with the nominal compositions of $\text{Cu}_x(\text{In}_{0.7}\text{Ga}_{0.3})\text{Se}_y$ (where $x=0.9$ and 1 , $y=2$ to 2.5) were fabricated via conventional solid state reaction using CIGS powder synthesized by a planetary ball milling. Employing these targets, the CIGS precursor films were deposited on the Mo-coated soda lime glass (SLG) substrates by using RF magnetron sputtering. Base pressure of vacuum chamber was approximately 3.0×10^{-6} Torr. The CIGS precursor films were deposited with RF power of 150W under argon gas pressure of 10 mTorr at room temperature. Substrate rotation was carried out at 3 rpm for film uniformity. After deposition, these CIGS precursor films were selenized under Se atmosphere using Se powder during 30 minutes in a tube furnace at various temperatures. The CIGS precursor films fabricated by using a stoichiometric CIGS ($\text{Cu}(\text{In}_{0.7}\text{Ga}_{0.3})\text{Se}_2$) target were selenized at the temperatures ranging from 300 °C to 450 °C to investigate grain growth behavior. Other CIGS precursor films deposited by using a Cu-poor CIGS ($\text{Cu}_{0.9}(\text{In}_{0.7}\text{Ga}_{0.3})\text{Se}_2$) target or Se-excess targets with Cu-poor compositions ($\text{Cu}_{0.9}(\text{In}_{0.7}\text{Ga}_{0.3})\text{Se}_{2.2}$ and $\text{Cu}_{0.9}(\text{In}_{0.7}\text{Ga}_{0.3})\text{Se}_{2.5}$) were selenized at temperatures between 400 °C and 500 °C.

And, to investigate the effect of selenium on the properties of CIGS film and CIGS solar cell, CIGS precursor films were selenized at 475 °C during

30 minutes in various Se atmospheres controlled by mixing powders with various weight ratios of alumina to selenium of 4:1, 6:1, 8:1 and 12:1. The weight of each mixing powder was 0.6g.

Also, to fabricate the nano-crystalline CIGS precursor film, the CIGS films were deposited at the various substrate temperatures ranging from room temperature (R.T.) to 150 °C. Among these CIGS precursor films, the nano-crystalline CIGS precursor film was selected by results of XRD patterns and TEM images. Nano-crystalline CIGS precursor films were selenized at 475 °C during 30 minutes.

After selenization process, the CIGS thin film solar cells with the structure of Al/AZO/i-ZnO/CdS/CIGS/Mo/SLG were fabricated to measure the conversion efficiency. A 50 nm-thick CdS layer was coated by chemical bath deposition. A 50 nm-thick intrinsic ZnO and a 400 nm-thick Al-doped ZnO (2 wt% Al₂O₃) layers were sequentially deposited by using RF magnetron sputtering. Al grids for the enhancement of carrier collection were deposited by thermal evaporation. The cell area defined by mechanical scribing was approximately 0.36 cm².

Crystal structures of the CIGS films were investigated by x-ray diffraction (XRD) with Cu-K α radiation. Surface morphologies and cross-sectional images were observed via field emission scanning electron microscopy (FESEM) and surface roughness was investigated by atomic force microscope (AFM). Compositional analysis of CIGS films was performed by energy dispersive X-ray spectroscopy (EDS). Electron probe micro analyzer (EPMA) was used to investigate the composition mapping of a cross-section of the CIGS film. Transmission electron microscope (TEM) was used for phase analysis of nanocrystalline CIGS film. The conversion

efficiency of the CIGS thin film solar cell was measured by a solar simulator under AM 1.5 illumination at 25 °C. External quantum efficiency (EQE) of the CIGS thin film solar cell was measured to study spectral response in the wavelength ranging from 300 nm to 1200 nm.

5.3. Results and discussion

5.3.1. CIGS layers prepared using the single CIGS targets of various compositions

5.3.1.1. A CIGS target with the nominal composition of $\text{Cu}(\text{In}_{0.7}\text{Ga}_{0.3})\text{Se}_2$

Fig. 5.1 shows the surface and cross-sectional SEM images of the CIGS films fabricated by using a stoichiometric CIGS target. The as-deposited CIGS film before selenization (Fig. 5.1 (a)) showed almost featureless microstructure. After selenization, grain growth occurred and grain size was increased with increasing selenization temperature. An abrupt grain growth can be obviously noticed when the CIGS film was selenized at 425 °C, as shown in Fig. 5.1 (e). In our previous experiment (not shown here), grain growth did not occur when the CIGS film was annealed in an Ar atmosphere without Se at the same temperature as that of selenization. These results show that Se incorporation into the CIGS film plays an important role in grain growth of the CIGS precursor film. After selenization process, the MoSe_2 layer was also formed between the CIGS and the Mo layer and its thickness was increased with increasing selenization temperature.

The XRD patterns of as-deposited and selenized CIGS films fabricated by using a stoichiometric CIGS target were also investigated. As seen in Fig. 5.2, the as-deposited CIGS film is amorphous. After selenization, all of the CIGS films showed chalcopyrite structure as characterized by presence of peaks at (101), (103), (211), (213)/(105), (301), and so on. Elemental selenium peaks were simultaneously detected in the CIGS films selenized below 400 °C but disappeared when the films were selenized at higher temperatures of 425 °C and 450 °C. Crystallinity of the selenized CIGS film was enhanced with increasing selenization temperature.

Based on the results of SEM and XRD measurements shown in Figs. 5.1 and 5.2, respectively, selenization process should be performed at a temperature above 425 °C to instigate grain growth through full reaction between the Se and CIGS precursor film. Consequently, sufficient thermal energy and Se atmosphere are prerequisites to grain growth of the CIGS precursor film .

Although grain size and crystallinity of the CIGS film for solar cell application are thought to be achieved by selenization process, very low conversion efficiency of less than 0.1% was obtained. This is observed in Fig. 5.3 where the current-voltage characteristics of the CIGS solar cells were determined. This can be attributed to the inappropriate composition and rough and porous surface morphology with microscopic voids. Table 5.1 shows the composition of the CIGS films fabricated by using a stoichiometric CIGS target before and after selenization. In these films, the value of Cu/(In+Ga) was larger than that of device-quality stoichiometry ratio which is approximately 0.69~0.98 [13].

Compared to device-quality stoichiometry ratio, a larger quantity of copper

can make Cu_{2-x}Se phase which is formed from the Cu_xSe liquid phase although these phases are not detected by XRD. Therefore, grain growth could be enhanced due to the existence of Cu_xSe liquid phase [14, 15]. In general, defects responsible for recombination are much more likely to occur at surfaces and interfaces [16]. Hence, large grain size can enhance the performance of solar cell by reducing grain boundary recombination. However, the large fraction of copper in the CIGS film can easily make a p-type semi-metallic compound of Cu_{2-x}Se with high hole concentration, resulting in exceeding the optimum carrier concentration of $10^{16} \sim 10^{17}/\text{cm}^3$ [17, 18]. As a result, the CIGS film has too low resistivity and thus the cell performance is deteriorated. Therefore, very low short-circuit current density (J_{sc}) and fill factor can be caused by improper composition of the CIGS film. Also, very rough and porous surface morphology of the CIGS film can result to low open-circuit voltage (V_{oc}) and fill factor in the CIGS solar cell because of increased localized shunt path [19], which can be also affected by composition of the film.

5.3.1.2 A Cu-poor CIGS target with the nominal composition of $\text{Cu}_{0.9}(\text{In}_{0.7}\text{Ga}_{0.3})\text{Se}_2$

Therefore, the Cu-poor CIGS ($\text{Cu}_{0.9}(\text{In}_{0.7}\text{Ga}_{0.3})\text{Se}_2$) target was used to suppress the formation of Cu-Se related compounds in the CIGS film and to make a smooth surface morphology which can be achieved by using a Cu-poor composition [20]. Table 5.2 shows the composition of the CIGS films deposited by using a Cu-poor CIGS target before and after selenization. As

expected, the Cu content was decreased and the Se content was increased in these films compared to those in the films fabricated by using a stoichiometric CIGS target. In these films, the values of $\text{Cu}/(\text{In}+\text{Ga})$ were between 0.76 and 0.88 which are in the regime of device-quality stoichiometry ratio, while the values of $\text{Ga}/(\text{In}+\text{Ga})$ were identical to the films fabricated via stoichiometric CIGS target.

Fig. 5.4 shows the surface and cross-sectional SEM images of as-deposited and selenized CIGS films fabricated by using a Cu-poor CIGS target. In this case, higher selenization temperature was applied due to the result that grain growth was clearly observed above the selenization temperature of 400 °C in the case of the stoichiometric target. Compared with the case of the stoichiometric target as shown in Fig. 5.1, smaller grain size was observed when selenized at the same temperature. When selenized at 450 °C, the surface morphology was still rough and porous. However, when selenized at 475 °C and above, dense and smooth surface morphology was obtained. In this case, very thick MoSe_2 layer, detrimental to the conversion efficiency, was observed between the CIGS film and the Mo electrode layer [21]. As a whole, compared with the case of the stoichiometric target, the thicker MoSe_2 layer was formed when selenized at the same temperature. This is because the Se amount in the as-deposited film fabricated by using a Cu-poor CIGS target is relatively larger than that in the as-deposited film fabricated by using a stoichiometric CIGS target as presented in Tables 5.1 and 5.2. Therefore, the formation of MoSe_2 layer becomes easier due to short diffusion length of selenium atoms to form a MoSe_2 layer. The thickness of a MoSe_2 layer is increased with increasing selenization temperature because large thermal

energy increases the selenium mobility and reactivity to molybdenum.

Fig. 5.5 shows the XRD patterns of the CIGS films fabricated by using a Cu-poor CIGS target as a function of selenization temperature. Chalcopyrite CIGS films without the second phases were obtained at the selenization temperatures above 450 °C. However, elemental selenium peaks appeared again in the CIGS film selenized at 400 °C. Meanwhile, in the cross-sectional image of this film as shown in Fig. 5.4 (b), the thickness of the CIGS film was slightly increased. The Se content at this condition was exceptionally high as shown in Table 5.2. From these results, it is supposed that the CIGS film is not fully selenized. In other words, although selenium atoms are incorporated into the CIGS precursor film during selenization process, the reaction for crystallization and grain growth could not occur at the selenization temperature of 400 °C due to insufficient thermal energy. So, to find where the unreacted selenium atoms are, elemental distribution across cross-section of the CIGS film selenized at 400 °C was investigated. As a result, all the measured elements except Se exhibited uniform distribution along the thickness of the film. In the case of Se, a little different distribution was observed; unexpectedly, more selenium inside the film is observed compared to surrounding surface region (~200nm), as shown in Fig. 5.6. These results reveal that selenium atoms are easily diffused into the internals of the CIGS film even at 400 °C. However, as mentioned before, more thermal energy is needed to give rise to crystallization and grain growth through the reaction between Se atoms and CIGS precursor film.

Although the MoSe₂ layer in the case of a Cu-poor CIGS target was thicker than that of a stoichiometric CIGS target, the conversion efficiency was

increased by enhancement of the open-circuit voltage and short-circuit current density. This may be due to the decreased hole concentration by suppressing the formation of Cu-Se related phases and the decreased leakage current by increasing density of the CIGS film. A conversion efficiency of ~3.54% was achieved from the CIGS film selenized at 475 °C as shown in Fig. 5.7. The resulting open-circuit voltage of 0.343 V is still too low in comparison with the V_{oc} derived from the band gap (E_g) of this CIGS film of which band gap is about 1.14 eV leading to the V_{oc} of approximately 0.64 V in the solar cell with good performance, as will be described later. Lower V_{oc} of solar cell devices can be attributed to many defects and the shunting path in the CIGS film. Meanwhile, selenium atom in the CIGS film is known to decrease the defects [22, 23] and reduce the formation of the second phases composed of Cu-Se related compound when the CIGS film has a larger amount of In and Ga compared to Cu. It has been reported that the addition of selenium increases the band gap of the CIGS film [23]. Therefore, Se-excess CIGS targets with a Cu-poor composition ($Cu_{0.9}(In_{0.7}Ga_{0.3})Se_{2.2}$ and $Cu_{0.9}(In_{0.7}Ga_{0.3})Se_{2.5}$) were prepared and used to fabricate CIGS precursor films to enhance the conversion efficiency.

5.3.1.3 A Cu-poor and a Se-excess CIGS targets with the nominal compositions of $Cu_{0.9}(In_{0.7}Ga_{0.3})Se_{2.2}$ and $Cu_{0.9}(In_{0.7}Ga_{0.3})Se_{2.5}$

Figs. 5.8. (b) and 5.8. (c) show the surface morphologies of the selenized CIGS films fabricated by employing Se-excess CIGS targets with a Cu-poor composition. All films showed the faceted grains and where the grain size

was increased with increasing Se content in the CIGS target. However, grain size of these films was smaller than that of the film fabricated by employing the stoichiometric CIGS target. This result can be attributed to the Cu-poor composition of the CIGS precursor film. As mentioned above, Cu-poor composition suppresses the formation of copper selenide phase which can enhance grain growth [20].

Fig. 5.9 (a) shows the conversion efficiency of the CIGS solar cells fabricated by using Se-excess CIGS targets with a Cu-poor composition. The open-circuit voltage was increased with increasing selenium content of the CIGS target, which is due to the increased band gap of the CIGS film as shown in Fig. 5.9 (c) [23]. Among them, the highest efficiency of 6.88% was achieved from the CIGS solar cell fabricated by using the $\text{Cu}_{0.9}(\text{In}_{0.7}\text{Ga}_{0.3})\text{Se}_{2.2}$ target having an open-circuit voltage of 0.463 V, short-circuit current density of 27.95 mA/cm^2 and fill factor of 53.13%.

Spectral response, the external quantum efficiencies (EQE) of these CIGS solar cells, were measured in the wavelength ranging from 300 to 1200 nm as shown in Fig. 5.9 (b). Each spectrum was normalized with the highest value of EQE for comparison. For wavelength larger than 650 nm, relatively large EQE loss occurred in the solar cell fabricated by using the $\text{Cu}_{0.9}(\text{In}_{0.7}\text{Ga}_{0.3})\text{Se}_2$ target. This loss can be attributed to the recombination caused by defects in the CIGS absorber layer. To determine the band gap from the EQE spectrum, the relationship of $[E \ln(1-\text{EQE})]^2$ versus E is used near the band edge, where $E=h\nu$ [24]. As shown in Fig. 5.9 (c), the CIGS films fabricated by using $\text{Cu}_{0.9}(\text{In}_{0.7}\text{Ga}_{0.3})\text{Se}_2$ and $\text{Cu}_{0.9}(\text{In}_{0.7}\text{Ga}_{0.3})\text{Se}_{2.2}$ targets have very similar E_g values of 1.14 and 1.15 eV, respectively, but the CIGS film fabricated by

using $\text{Cu}_{0.9}(\text{In}_{0.7}\text{Ga}_{0.3})\text{Se}_{2.5}$ target has a higher value of 1.19 eV. Using the band gaps of the CIGS film, open-circuit voltages were calculated using $V_{oc} = E_g/q - 0.5\text{V}$ which was derived from the experimental results of V_{oc} versus E_g using the CIGS solar cells with good performance [25]. As a result, the measured V_{oc} 's were lower than the calculated ones.

To investigate the lower values of the V_{oc} in these solar cells compared to the calculated ones using the band gap, open-circuit voltages were plotted as a function of band gap as shown in Fig. 5.9 (d). Dotted line was plotted via $V_{oc} = E_g/q - 0.5\text{V}$. The CIGS solar cells fabricated in this work showed smaller V_{oc} values (0.16 ~ 0.297 V) in comparison to the calculated ones. The difference between the measured V_{oc} and the calculated one using E_g was very large in the CIGS solar cell fabricated by using the $\text{Cu}_{0.9}(\text{In}_{0.7}\text{Ga}_{0.3})\text{Se}_2$ target, but decreased with increasing the selenium content in the CIGS target.

Furthermore, the XRD patterns after selenization of the CIGS precursor films fabricated by using the three targets were investigated. As shown in Fig. 5.10, all films had the CIGS phase with chalcopyrite structure but the ordered vacancy compound (OVC) phase ($\text{Cu}(\text{In,Ga})_3\text{Se}_5$) co-existed in the CIGS films fabricated by using Se-excess CIGS targets with a Cu-poor composition. The peak intensity of the OVC phase was increased with increasing Se content in the CIGS target. The content of the OVC phase can be inferred by checking the composition of CIGS films as shown in Table 5.3. The quantity of (In+Ga) was increased and the quantity of Cu was decreased with increasing Se content in the CIGS target. This result reveals that the content of the OVC phase, consisting of smaller amount of Cu and larger amount of (In+Ga) than those of $\text{Cu}(\text{In,Ga})\text{Se}_2$ phase, is increased. The OVC phase is

well-known to have a larger band gap than that of CIS compound [26]. Therefore, coexistence of the OVC phase can increase the band gap of the CIGS absorber layer although the ratio of Ga/(In+Ga), which is a critical parameter to determine band gap, is identical. Having this in consideration, the results on the band gap obtained in this work are acceptable.

The OVC phase also plays a key role in reducing interface recombination at the interface between the CdS layer and the CIGS layer by lowering the valence band maximum (VBM) [10]. In this case, the limiting factor for the open-circuit voltage is mainly the recombination in the bulk of the absorber material [27]. Therefore, as per experimental results, decrease of the difference between the measured V_{oc} and the calculated one as shown in Fig. 5.9 (d) may be due to the fact that the OVC phase increases the band gap by lowering the VBM resulting to suppressed interface recombination.

5.3.2 Effect of selenization condition on the CIGS layers

In this chapter, the characteristics before and after selenization of the CIGS precursor films deposited using the single CIGS targets with the nominal compositions of $Cu_{0.9}(In,Ga)Se_2$ and $Cu_{0.9}(In,Ga)Se_{2.5}$ were investigated. The CIGS precursor films were selenized using mixing powders with various weight ratios of alumina to selenium. Fig. 5.11 shows SEM images before and after selenization of the CIGS films fabricated using a single quaternary CIGS target with the nominal compositions of $Cu_{0.9}(In_{0.7}Ga_{0.3})Se_2$. As shown in Fig. 5.11 (b), grain growth did not occur when the CIGS precursor film was annealed in an Ar atmosphere without Se. However, when annealed with a

small quantity of selenium, grain growth occurred and grain size was increased with increasing the Se ratio of mixing powder. These results show that Se incorporation into the CIGS film plays an important role in grain growth of the CIGS precursor film. Also, after selenization process, the MoSe₂ layer was formed between the CIGS and the Mo layer and its thickness was increased with increasing the Se ratio of mixing powder. These tendencies are similar to those of increase of selenization temperature in the previous chapter. And also, the microstructure before and after selenization of the CIGS precursor films fabricated using a single quaternary CIGS target with the nominal compositions of Cu_{0.9}(In_{0.7}Ga_{0.3})Se_{2.5} was investigated. The results are in Fig. 5.12. As can be seen in Fig. 5.12 (b), grain growth also did not occur when the CIGS precursor film was annealed in an Ar atmosphere without Se. However, when annealed with a small quantity of selenium, grain growth occurred and grain size was increased with increasing the Se ratio of mixing powder. These results are similar to those of the CIGS films fabricated using the CIGS target with the nominal compositions of Cu_{0.9}(In_{0.7}Ga_{0.3})Se₂. However, in the case of the CIGS films fabricated using the Cu_{0.9}(In_{0.7}Ga_{0.3})Se_{2.5} target, the porous and rough surface morphology was observed and the pores were increased with increasing a selenium ratio in the mixing powder. And the thickness of the MoSe₂ layer of these films was thicker than that of the films fabricated using the Cu_{0.9}(In_{0.7}Ga_{0.3})Se₂ target.

Table 5.5 (a) and (b) show the composition of the CIGS films deposited using the single CIGS targets with the nominal compositions of Cu_{0.9}(In,Ga)Se₂ and Cu_{0.9}(In,Ga)Se_{2.5}, respectively. In the case of the CIGS films fabricated using the Cu_{0.9}(In_{0.7}Ga_{0.3})Se_{2.5} target, when the CIGS

precursor film was annealed in an Ar atmosphere without Se (0:0 in table 5.5 (b)), the Se amount of the CIGS film was significantly decreased. This result is thought to be related to the thickness reduction of the CIGS film shown in Fig. 5.12 (b). In other words, most of the selenium in the CIGS precursor film is not employed for grain growth of the CIGS film although the precursor film contains a large quantity of Se. Extra selenium atoms excepting Se used for forming the CIGS related phases are evaporated to the outside of the CIGS film. On the other hand, supplement of selenium atoms around the CIGS precursor film can induce grain growth of the CIGS film because of impeding the evaporation of selenium atoms in the CIGS precursor film. Additional selenium atoms around the CIGS precursor film are rather incorporated into the inside of the CIGS film. Hence, grain size of the CIGS film is increased with increasing the Se ratio of mixing powder. However, all CIGS films had the similar composition after selenization regardless the Se ratio of mixing powder. This means that the composition of CIGS film is influenced by the composition of the precursor film rather than selenization process. Also, the thickness of the MoSe₂ layer is increased with increasing the Se ratio of mixing powder. And the MoSe₂-layer thickness of the CIGS film fabricated using the Cu_{0.9}(In_{0.7}Ga_{0.3})Se_{2.5} target is thicker than that of the CIGS film fabricated using the Cu_{0.9}(In_{0.7}Ga_{0.3})Se₂ target because of a large amount of Se in the CIGS film fabricated using the Cu_{0.9}(In_{0.7}Ga_{0.3})Se_{2.5} target.

Fig. 5.13 (a) and (b) shows the XRD patterns of the CIGS films fabricated using the single quaternary CIGS targets with the nominal compositions of Cu_{0.9}(In_{0.7}Ga_{0.3})Se₂ and Cu_{0.9}(In_{0.7}Ga_{0.3})Se_{2.5}, respectively. In the case of the CIGS films fabricated using the Cu_{0.9}(In_{0.7}Ga_{0.3})Se₂ target, XRD patterns

revealed that all of the CIGS films after selenization consisted of the chalcopyrite structure without secondary phases and were crystallized to a random orientation. However, the full width at half maximum (FWHM) of the CIGS film annealed in an Ar atmosphere without Se was wider than that of selenized CIGS films. This result is attributed to the low crystallinity of the CIGS film annealed in an Ar atmosphere without Se. Meanwhile, all of the CIGS films fabricated using the $\text{Cu}_{0.9}(\text{In}_{0.7}\text{Ga}_{0.3})\text{Se}_{2.5}$ target exhibited the chalcopyrite structure including the ordered vacancy compound (OVC) phase regardless of the Se ratio of mixing powders used for selenization. This result reveals that the occurrence of the OVC phase is decided by the value of $\text{Cu}/(\text{In}+\text{Ga})$ rather than a quantity of selenium. The CIGS precursor film with the small value of $\text{Cu}/(\text{In}+\text{Ga})$ is easy to form the OVC phase during selenization.

To clarify the existence of the OVC phase, Raman spectra of the CIGS films were investigated. As shown in Fig. 5.14, the CIGS films fabricated using the single quaternary CIGS targets with the nominal compositions of $\text{Cu}_{0.9}(\text{In}_{0.7}\text{Ga}_{0.3})\text{Se}_2$ and $\text{Cu}_{0.9}(\text{In}_{0.7}\text{Ga}_{0.3})\text{Se}_{2.5}$ showed the single CIGS phase and the CIGS phase including an OVC phase, respectively. And it is found that these phases in each CIGS film are evenly distributed. Fig. 5.15 (a) and (b) show the auger electron spectroscopy (AES) depth profiles after selenization of the CIGS films fabricated using the single quaternary CIGS targets with the nominal compositions of $\text{Cu}_{0.9}(\text{In}_{0.7}\text{Ga}_{0.3})\text{Se}_2$ and $\text{Cu}_{0.9}(\text{In}_{0.7}\text{Ga}_{0.3})\text{Se}_{2.5}$, respectively. As can be seen in figures, each element of the CIGS film was evenly distributed in the CIGS films without grading of elements. It means that the single CIGS phase in the CIGS film fabricated

using the $\text{Cu}_{0.9}(\text{In}_{0.7}\text{Ga}_{0.3})\text{Se}_2$ target and the CIGS phase including the OVC phase in the CIGS film fabricated using $\text{Cu}_{0.9}(\text{In}_{0.7}\text{Ga}_{0.3})\text{Se}_{2.5}$ target are evenly distributed.

Meanwhile, the CIGS films fabricated using the two different CIGS targets showed the different photoluminescence(PL) spectrum as shown in Fig. 5.16. In the case of the CIGS films fabricated using the $\text{Cu}_{0.9}(\text{In}_{0.7}\text{Ga}_{0.3})\text{Se}_{2.5}$ target, PL spectrum of the CIGS film exhibited doublet peak and its position shifted to higher energy level. This is thought to be attributed to the existence of the OVC phase with the CIGS phase. The OVC phase is well-known to have the larger band gap than that of CIS compound [26]. Therefore, a coexistence of the OVC phases can increase the band gap of the CIGS absorber layer. In this point of view, doublet peak and its position at higher energy level of the CIGS film fabricated using the $\text{Cu}_{0.9}(\text{In}_{0.7}\text{Ga}_{0.3})\text{Se}_{2.5}$ target are acceptable.

Fig. 5.17. (a) and (b) shows the current-voltage characteristics of the CIGS solar cells fabricated using the single CIGS targets with the nominal compositions of $\text{Cu}_{0.9}(\text{In,Ga})\text{Se}_2$ and $\text{Cu}_{0.9}(\text{In,Ga})\text{Se}_{2.5}$, respectively. And the conversion efficiencies of these solar cells were summarized in the table 5.6. The open-circuit voltages of the CIGS solar cells fabricated using the $\text{Cu}_{0.9}(\text{In}_{0.7}\text{Ga}_{0.3})\text{Se}_{2.5}$ target were generally higher than those of solar cells fabricated using the $\text{Cu}_{0.9}(\text{In}_{0.7}\text{Ga}_{0.3})\text{Se}_2$ target. This result can be caused by effect of OVC phase in the CIGS film considering the results of the band gap in chapter 5.3.1 and PL spectrum in this study. However, the open-circuit voltage of the CIGS solar cells fabricated using the $\text{Cu}_{0.9}(\text{In}_{0.7}\text{Ga}_{0.3})\text{Se}_{2.5}$ target was decreased with decreasing Se ratio of mixing powder used for selenization. The defect density in the CIGS film can be increased with

decreasing the Se ratio in a furnace during selenization, which can lead to reduce the V_{oc} . Among them, the best efficiency was achieved from the CIGS solar cell fabricated using the $Cu_{0.9}(In_{0.7}Ga_{0.3})Se_{2.5}$ target and its value is 6.70 % with the open-circuit voltage of 0.530V, short-circuit current density of 23.97 mA/cm² and the fill factor of 52.67%. Considering the results of this study, Se-excess CIGS target with a Cu-poor composition is beneficial to the enhancement of efficiency of the solar cell fabricated using the single CIGS target.

5.3.3 CIGS layers prepared using nanocrystalline precursor film

X-ray diffraction pattern was used to select the nanocrystalline CIGS film among fabricated ones. Fig. 5.18 shows XRD patterns of the as-deposited CIGS films deposited at various temperatures using the single CIGS sputtering target with the nominal composition of $Cu_{0.9}(In_{0.7}Ga_{0.3})Se_{2.5}$. As seen in Fig. 5.18, the CIGS film deposited at room temperature is amorphous. And also, XRD patterns of CIGS films deposited at the temperatures ranging from 60 °C to 120 °C have no particular distinguishing features and are similar to that of CIGS film deposited at room temperature. However, when deposited at 130 °C, the CIGS film is crystallized to the (112) orientation, which is known as the main peak of CIGS compound, although full width at half maximum (FWHM) is wide. And the intensity of the (112) peak is increased when the film is deposited at 140 °C. However, intensity of the (112) peak is decreased in the as-deposited film deposited at the higher temperature of 150 °C. This is thought to be involved in growth of another

phase. In other words, the intensity of the (112) peak is decreased with growth of (220)/(204) and (312)/(116) peaks. In our previous study, not shown here, this tendency had also been observed in the film deposited by using the CIGS sputtering target with the nominal composition of $\text{Cu}(\text{In}_{0.7}\text{Ga}_{0.3})\text{Se}_2$.

Based on the results of XRD patterns, as-deposited CIGS films fabricated at the temperatures of 120 °C and 130 °C were considered as the nanocrystalline CIGS precursor films. To clarify the formation of the nanocrystalline CIGS precursor film, phases of the CIGS film deposited at 120 °C and 130 °C were investigated by TEM. Fig. 5.19 shows TEM images of the CIGS precursor films deposited at 120 °C and 130 °C. As shown in Fig. 5.19, nanocrystalline CIGS films were successfully fabricated at these temperatures. It was found that the CIGS film was composed of the mixed phases of amorphous phases and nanocrystalline phases.

These CIGS precursor films were selenized at the temperature of 475 °C for 30 min, which is optimum condition in our previous study. Fig. 5.20 shows XRD patterns of selenized CIGS films. The CIGS films after selenization of nanocrystalline CIGS precursor films deposited at 120 °C and 130 °C showed a (112) preferred orientation. However, intensity ratio of (112) to (220)/(204) was decreased with decreasing the deposition temperature and in the end the CIGS film deposited at room temperature showed a random orientation. Table 5.7 shows the intensity ratio of (112) to (220)/(204). In general, the intensity ratio of (112) to (220)/(204) of $\text{Cu}(\text{In}_{0.7}\text{Ga}_{0.3})\text{Se}_2$ powder (PDF #35-1102) is 2.5. This value is similar to that after selenization of the CIGS films deposited at room temperature. Therefore, it is found that CIGS films deposited at room temperature and higher temperatures (120 and 130 °C) are crystallized to a

random orientation and a (112) preferred orientation, respectively.

Table 5.8 shows the composition before and after selenization of the CIGS precursor films deposited at various temperatures. In the case of the as-deposited film, the CIGS film deposited at room temperature has the smaller amount of Cu and the larger amount of Se compared to the CIGS film deposited at 120 and 130 °C. However, after selenization of these as-deposited CIGS precursor films, the difference of the Cu and Se amount between them is decreased. In other words, after selenization of the CIGS film deposited at room temperature, Cu content is increased and Se content is decreased. And in the case of the CIGS film deposited at 120 and 130 °C, Cu content is slightly decreased and Se content is almost same. Finally, all of the selenized CIGS films have the similar composition, consisted of the smaller amount of Cu and the larger amount of (In+Ga) than those of stoichiometric Cu(In,Ga)Se_2 phase, regardless of deposition temperature although Cu contents in the films are slightly different. However, XRD patterns of the CIGS films showed some different characteristics even if the CIGS films had the similar compositions. After selenization, distinguishable peaks between ordered vacancy compound (OVC) phase and CIGS phase were observed in the CIGS film deposited at room temperature. However, these peaks were disappeared in the CIGS film deposited at 130 °C. This result is thought to be attributed to the preferred orientation of CIGS phase and OVC phase. The main peak position of CIGS ($\text{Cu(In}_{0.7}\text{Ga}_{0.3}\text{)Se}_2$, PDF#35-1102) phase is similar to that of OVC ($\text{Cu(In,Ga}_3\text{)Se}_5$, PDF #51-1222) phase. Therefore, if the OVC phase also has the (112) preferred orientation it is difficult to distinguish an existence of the OVC phase from the XRD pattern.

So, Raman spectra of the CIGS films were investigated to clarify the existence of an OVC phase. Figs. 5.21 (a) and (b) shows the raman spectra of the CIGS films selenized using mixing powders with the weight ratios of alumina to selenium of 8:1 and 4:1, respectively. As shown in figures, all of the films contained the OVC phase. Therefore, it is clear that the OVC phase also has the (112) preferred orientation. As a result, all of the CIGS films fabricated in this study have the OVC phase which can lead to decrease of open-circuit voltage loss as discussed in chapter 5.3.1.

Meanwhile, the microstructure of these CIGS films showed the different morphology. Figs. 5.22, 23 and 24 show SEM images of the CIGS films before and after selenization of the CIGS precursor films deposited at room temperature, 120 and 130 °C, respectively. As can be seen in figures, all of the as-deposited CIGS films show almost featureless microstructure. After selenization, grain growth occurred and grain size was increased with increasing a selenium ratio in a tube furnace. This tendency appeared in all of the selenized CIGS films regardless of deposition temperature of the CIGS precursor film. However, after selenization of the CIGS precursor film deposited at room temperature, the porous and rough surface morphology was observed and the pores were increased with increasing a selenium ratio in the mixed powder used for selenization. This surface morphology was improved to the dense surface morphology by selenization of the nano-crystalline CIGS precursor film. Finally, the CIGS film with the densely packed surface morphology as well as the large grain size was obtained by increase of Se ratio in a tube furnace and using the nano-crystalline CIGS precursor film. Root mean square (RMS) roughness of the CIGS films was investigated. As

shown in Fig. 5. 25. and Table 5.9, for the CIGS film deposited at room temperature, the RMS roughness of the selenized CIGS film was increased with increasing a selenium ratio in the mixed powder. However, the RMS roughness was decreased when the nano-crystalline CIGS precursor films were selenized. Dense and smooth surface morphology of the CIGS film is important to improve device performance because the surface of the CIGS film is the contact surface for the p-n junction. Hence, this result is meaningful for enhancement of device performance.

Meanwhile, in the cross-sectional SEM images, thickness of the CIGS film after selenization of the CIGS precursor film deposited at room temperature is greatly decreased. However, the ratio of thickness reduction from the as-deposited CIGS film is decreased with increasing deposition temperature. This is thought to be caused by difference of the film density between the as-deposited films. In other words, the thickness reduction of the amorphous CIGS film containing many pores is larger than that of the nano-crystalline CIGS film composed of relatively high density.

Also, the MoSe₂ layer was checked. A MoSe₂ layer is known to enhance the efficiency by forming the ohmic contact between the CIGS layer and the Mo electrode layer [28, 29]. However, very thick MoSe₂ layer is detrimental to the conversion efficiency [30]. In this experiment, the thickness of the MoSe₂ layer was decreased after selenization of the nano-crystalline CIGS precursor film compared to that of the amorphous CIGS precursor film. This is because the Se amount in the CIGS precursor film deposited at room temperature is larger than that in the CIGS precursor films deposited at 120 and 130 °C as shown in table 5.8. Hence, the formation of a MoSe₂ layer becomes easier in

the as-deposited CIGS film deposited at room temperature due to short diffusion length of selenium atoms to form a MoSe₂ layer. Also, compared with the film deposited at 120 °C, the thinner MoSe₂ layer was formed when deposited at 130 °C although the Se amount of these films is similar. This result shows that the density of the CIGS precursor film affects the formation of a MoSe₂ layer. This can be understood in the way that Se incorporation into the inside of the CIGS film during selenization is more difficult in the denser film. As a result, film density and Se amount of the CIGS precursor film have an important effect on the formation of the MoSe₂ layer. Therefore, the use of the nano-crystalline CIGS precursor film is beneficial to the improvement of the solar cell performance by reducing the thickness of a MoSe₂ layer.

By using these CIGS films, the CIGS thin film solar cells with the structure of Al/AZO/i-ZnO/CdS/CIGS/Mo/SLG were fabricated to measure the conversion efficiency. Fig. 5.26 (a), (b) and (c) show the current-voltage characteristics of the CIGS solar cells fabricated by using the CIGS precursor films deposited at room temperature, 120 and 130 °C, respectively. And the conversion efficiencies of these solar cells are summarized in the table 5.10. The open-circuit voltage was increased with increasing a selenium ratio of the mixed powder used for selenization although the short-circuit current density between them was similar. Lower V_{oc} of solar cell devices can be attributed to many defects and shunting paths in the CIGS film. Meanwhile, selenium has been known to decrease the defects in the CIGS film. Therefore, it is possible that defect density in the CIGS film can be increased with decreasing the Se ratio in a furnace during selenization, which can lead to reduction of the V_{oc} . Among them, the best efficiency was achieved from the CIGS solar cell

fabricated by using the CIGS precursor film deposited at 130 °C and its value is 8.09 % with the open-circuit voltage of 0.571V, short-circuit current density of 26.58 mA/cm² and the fill factor of 53.28%. This value is higher than that of the CIGS solar cell fabricated using amorphous CIGS precursor film. This result is thought to be achieved by the beneficial factors such as the existence of an OVC phase, the thickness reduction of a MoSe₂ layer, smooth surface morphology and the decrease of defect density achieved by dense CIGS film with large grain.

5.4. Summary

The characteristics of the CIGS thin film solar cells fabricated via single CIGS targets with various compositions were investigated. By employing the stoichiometric CIGS target, the Cu-rich CIGS film was obtained and very low conversion efficiency was achieved due to inappropriate composition and porous surface morphology. CIGS films with device-quality stoichiometry ratio were achieved from the Cu-poor CIGS target. This film showed a densely packed morphology and chalcopyrite structure without the second phases. A conversion efficiency of 3.54% was achieved from the CIGS film selenized at 475 °C. However, the open-circuit voltage (V_{oc}) of this solar cell was too low compared to V_{oc} derived from the band gap (E_g) of CIGS compound. The difference could be decreased with increasing Se contents in the CIGS target. Increase of the Se content in the CIGS target led to decrease of the Cu content and increase of the (In+Ga) content in the CIGS film, which created the ordered vacancy compound

(OVC) phase. As a result, the CIGS thin films fabricated by employing the Se-excess CIGS targets with a Cu-poor composition showed the chalcopyrite CIGS phase including an OVC phase. The OVC phase in the CIGS film was increased with increasing the Se content in the CIGS target. The difference between $E_g/q - 0.5V$ and V_{oc} was remarkably decreased with the formation of the OVC phases. The highest efficiency of 6.88% has been achieved from the CIGS solar cell fabricated using the $Cu_{0.9}(In_{0.7}Ga_{0.3})Se_{2.2}$ target. The performance of the CIGS solar cells fabricated in this study was summarized in the Table 5.4. This study reveals that the selenium content in the single CIGS target plays a key role in structural and electrical properties.

Characteristics of CIGS films selenized using mixing powders with various weight ratios of alumina to selenium was investigated. For this experiment, the CIGS precursor films were deposited using the single CIGS targets with the nominal compositions of $Cu_{0.9}(In,Ga)Se_2$ and $Cu_{0.9}(In,Ga)Se_{2.5}$. As the results, regardless of target composition, grain size was increased with increasing the Se ratio of mixing powder. The $MoSe_2$ layer was formed between the CIGS and the Mo layer and its thickness was also increased with increasing the Se ratio of mixing powder. The $MoSe_2$ -layer thickness of the CIGS film fabricated using the $Cu_{0.9}(In_{0.7}Ga_{0.3})Se_{2.5}$ target is thicker than that of the CIGS film fabricated using the $Cu_{0.9}(In_{0.7}Ga_{0.3})Se_2$ target because of larger amount of Se in the CIGS film fabricated using the $Cu_{0.9}(In_{0.7}Ga_{0.3})Se_{2.5}$ target. From the auger electron spectroscopy (AES) depth profiles after selenization of the CIGS films, it was found that each element of the CIGS film was evenly distributed in the CIGS films without grading of elements. This means that the CIGS phases including the OVC

phase in the CIGS film fabricated using $\text{Cu}_{0.9}(\text{In}_{0.7}\text{Ga}_{0.3})\text{Se}_{2.5}$ target are evenly distributed. The open-circuit voltages of the CIGS solar cells fabricated using the $\text{Cu}_{0.9}(\text{In}_{0.7}\text{Ga}_{0.3})\text{Se}_{2.5}$ target were generally higher than those of solar cells fabricated using the $\text{Cu}_{0.9}(\text{In}_{0.7}\text{Ga}_{0.3})\text{Se}_2$ target. However, the open-circuit voltage of the CIGS solar cells fabricated using the $\text{Cu}_{0.9}(\text{In}_{0.7}\text{Ga}_{0.3})\text{Se}_{2.5}$ target was decreased with decreasing Se ratio of mixing powder used for selenization.

Also, characteristics of the CIGS films selenized using nanocrystalline precursor film were investigated. The CIGS films were deposited at various temperatures using a single quaternary $\text{Cu}_{0.9}(\text{In}_{0.7}\text{Ga}_{0.3})\text{Se}_{2.5}$ target. Based on the results of XRD patterns, as-deposited CIGS films fabricated at the temperatures of 120 °C and 130 °C were considered as the nano-crystalline CIGS precursor films and selenized at 475 °C for 30min. The CIGS films showed a (112) preferred orientation. All of the selenized CIGS films have the similar composition regardless of deposition temperature although Cu content in the film is slightly different. From the Raman spectra of the CIGS films, the existence of OVC phase which can lead to decrease of open-circuit voltage loss was identified. The CIGS film with dense surface morphology as well as the large grain size was obtained by increase of Se ratio in a tube furnace and using the nano-crystalline CIGS precursor film. And the thickness of the MoSe_2 layer was decreased after selenization of the nano-crystalline CIGS precursor film compared to that of the amorphous CIGS precursor film. The highest efficiency was achieved from the CIGS solar cell fabricated using the nanocrystalline CIGS precursor film deposited at 130 °C and its value is 8.09 % with the open-circuit voltage of 0.571V, short-circuit

current density of 26.58 mA/cm^2 and the fill factor of 53.28%. This result is thought to be achieved by the beneficial factors such as the existence of an OVC phase, the thickness reduction of a MoSe_2 layer, smooth surface morphology and the decrease of defect density achieved by dense CIGS film with large grain.

References

- [1] P. Jackson, D. Hariskos, E. Lotter, S. Paetel, R. Wuerz, R. Menner, W. Wischmann, M. Powalla, *Prog. Photovolt. Res. Appl.* 19 (2011) 894.
- [2] S.D. Kim, H.J. Kim, K.H. Yoon, J. Song, *Sol. Energy Mater. Sol. Cells* 62 (2000) 357.
- [3] D.G. Moon, S. Ahn, J.H. Yun, A. Cho, J. Gwak, S. Ahn, K. Shin, K. Yoon, H.D. Lee, H. Pak, S. Kwon, *Sol. Energy Mater. Sol. Cells* 95 (2011) 2786.
- [4] M. Marudachalam, H. Hichri, R. Klenk, R.W. Birkmire, W.N. Shafarman, *Appl. Phys. Lett.* 67 (1995) 3978.
- [5] T. Nakada, A. Kunioka, *Jpn. J. Appl. Phys.* 37 (1998) L1065.
- [6] W. Li, Y. Sun, W. Liu, L. Zhou, *Solar Energy* 80 (2006) 191.
- [7] J.H. Shi, Z.Q. Li, D.W. Zhang, Q.Q. Liu, Z. Sun, S.M. Huang, *Prog. Photovolt. Res. Appl.* 19 (2011) 160.
- [8] J.A. Frantz, R.Y. Bekele, V.Q. Nguyen, J.S. Sanghera, A. Bruce, S.V. Frolov, M. Cyrus, I.D. Aggarwal, *Thin Solid Films* 519 (2011) 7763.
- [9] C.H. Chen, W.C. Shih, C.Y. Chien, C.H. Hsu, Y.H. Wu, C.H. Lai, *Sol. Energy Mater. Sol. Cells* 103 (2012) 25.
- [10] S.B. Zhang, S.H. Wei, A. Zunger, H. K. Yoshida, *Phys. Rev. B* 57 (1998) 9642.
- [11] L. Zhang, Q. He, W.L. Jiang, F.F. Liu, C.J. Li, Y. Sun, *Sol. Energy Mater. Sol. Cells* 93 (2009) 114.
- [12] T. Yamaguchi, T. Kobata, S. Niiyama, T. Nakamura, A. Yoshida, *Sol. Energy Mater. Sol. Cells* 75 (2003) 87.
- [13] P. Jackson, R. Wurz, U. Rau, J. Mattheis, M. Kurth, T. Schlotzer, G. Bilger, J.H. Werner, *Prog. Photovolt. Res. Appl.* 15 (2007) 507.
- [14] J.R. Tuttle, M. Contreras, M.H. Bode, D. Nilas, D.S. Albin, R. Matson, A.M. Gabor, A. Tennant, A. Duda, R. Noufi, *J. Appl. Phys.* 77 (1995) 153.
- [15] R. Klenk, T. Walter, H. W. Schock, D. Cahen, *Adv. Mater.* 5 (1993) 114.
- [16] J. Nelson, *The physics of solar cells*, 2004, p110.

- [17] W. Liu, J.G. Tian, Q. He, F.Y. Li, C.J. Li, Y. Sun, *Thin Solid Films* 519 (2010) 244.
- [18] R. Noufi, R. Axton, C. Herrington, and S. K. Deb, *Appl. Phys. Lett.* 45 (1984) 668.
- [19] S. Dongaonkar, J. D. Servaites, G. M. Ford, S. Loser, J. Moore, R. M. Gelfand, H. Mohseni, H. W. Hillhouse, R. Agrawal, M. A. Ratner, T. J. Marks, M. S. Lundstrom, and M. A. Alam, *J. Appl. Phys.* 108 (2010) 124509.
- [20] T. Walter, H. W. Schock, *Thin Solid Films* 224 (1993) 74.
- [21] X. Zhu, Z. Zhou, Y. Wang, L. Zhang, A. Li, F. Huang, *Sol. Energy Mater. Sol. Cells* 101 (2012) 57.
- [22] T. Sakurai, M.M. Islam, H. Uehigashi, S. Ishizuka, A. Yamada, K. Matsubara, S. Niki, K. Akimoto, *Sol. Energy Mater. Sol. Cells* 95 (2011) 227.
- [23] R. Caballero, C. Maffiotte, C. Guillen, *Thin Solid Films* 474 (2005) 70.
- [24] G. Zoppi, I. Forbes, R. W. Miles, P. J. Dale, J. J. Scragg, L. M. Peter, *Prog. Photovolt.: Res. Appl.* 17 (2009) 315.
- [25] S. R. Kodigala, *Thin films and nanostructures*, vol. 35 “Cu(In_{1-x}Ga_x)Se₂ based thin film solar cells”, 2010, p11.
- [26] T. Negami, N. Kohara, M. Nishitani, T. Wada, T. Hirao, *Appl. Phys. Lett.* 67 (1995) 825.
- [27] M. Turcu, O. Pakma, U. Rau, *Appl. Phys. Lett.* 80 (2002) 2598.
- [28] T. Wada, N. Kohara, S. Nishiwaki, T. Negami, *Thin Solid Films* 387 (2001) 118.
- [29] L. Assmann, J. C. Bernede, A. Drici, C. Amory, E. Halgand, M. Morsli, *Appl. Surf. Sci.* 171 (2001) 15.
- [30] X. Zhu, Z. Zhou, Y. Wang, L. Zhang, A. Li, F. Huang, *Sol. Energy Mater. Sol. Cells* 101 (2012) 57.

Table 5.1. Composition of the CIGS films fabricated using a stoichiometric CIGS target.

	Sel.temp. (°C)	Cu (%)	In (%)	Ga (%)	Se (%)	Cu/ (In+Ga)	Ga/ (In+Ga)
Batch		25	17.5	7.5	50	1	0.30
	As-dep.	24.3	16.5	7.2	52.0	1.03	0.30
	350	24.8	15.5	6.5	53.2	1.13	0.30
Film	375	24.4	16.3	7.3	52.0	1.03	0.31
	400	24.9	17.2	7.3	50.6	1.02	0.30
	425	25.6	17.3	7.0	50.1	1.05	0.29
	450	24.9	17.1	7.5	50.5	1.01	0.30

Table 5.2. Composition of the CIGS films fabricated using a Cu-poor CIGS target ($\text{Cu}_{0.9}(\text{In}_{0.7}\text{Ga}_{0.3})\text{Se}_2$).

	Sel.temp. (°C)	Cu (%)	In (%)	Ga (%)	Se (%)	Cu/ (In+Ga)	Ga/ (In+Ga)
Batch		23.08	17.95	7.69	51.28	0.90	0.30
	As-dep.	20.2	17.6	7.4	54.8	0.81	0.30
	400	17	15.9	6.2	60.9	0.77	0.28
Film	450	20.7	19.3	7.8	52.2	0.76	0.29
	475	20.5	18.6	8.0	52.9	0.77	0.30
	500	22.7	18.3	7.5	51.5	0.88	0.29

Table 5.3. Composition of the CIGS films fabricated using Se-excess CIGS targets with a Cu-poor composition.

Composition	Sample	Cu (%)	In (%)	Ga (%)	Se (%)	Cu/(In+Ga)	Ga/(In+Ga)
$\text{Cu}_{0.9}(\text{In,Ga})\text{Se}_{2.2}$	As-dep.	16.7	16.6	6.7	60.0	0.72	0.29
	After sel.	18.0	18.7	8.7	54.6	0.66	0.32
$\text{Cu}_{0.9}(\text{In,Ga})\text{Se}_{2.5}$	As-dep.	12.6	17.6	7.4	62.4	0.50	0.30
	After sel.	13.1	22.4	9.8	54.7	0.41	0.30

Table 5.4. Summary of efficiency of the CIGS solar cells fabricated in this study. (As a function of target composition and selenization temperature)

Sample	Nominal target composition	Selenization temperature (°C)	V_{oc} (V)	J_{sc} (mA/cm ²)	FF (%)	η (%)	E_g (eV)	$(\frac{E_g}{q} - 0.5V) - V_{oc}(sample)$ (V)
A	$Cu(In_{0.7}Ga_{0.3})Se_2$	400	0.090	1.70	35.1	0.05		
B	$Cu(In_{0.7}Ga_{0.3})Se_2$	450	0.163	1.89	31.2	0.10		
C	$Cu_{0.9}(In_{0.7}Ga_{0.3})Se_2$	400	0.267	2.35	43.5	0.27		
D	$Cu_{0.9}(In_{0.7}Ga_{0.3})Se_2$	450	0.284	12.50	44.0	1.57		
E	$Cu_{0.9}(In_{0.7}Ga_{0.3})Se_2$	475	0.343	22.33	46.1	3.54	1.14	0.297
F	$Cu_{0.9}(In_{0.7}Ga_{0.3})Se_2$	500	0.269	20.72	36.8	2.05		
G	$Cu_{0.9}(In_{0.7}Ga_{0.3})Se_{2.2}$	475	0.463	27.95	53.1	6.88	1.15	0.187
H	$Cu_{0.9}(In_{0.7}Ga_{0.3})Se_{2.5}$	475	0.530	23.97	52.7	6.70	1.19	0.160

Table 5.5. Composition before and after selenization of CIGS precursor films deposited using the single CIGS targets with the nominal compositions of (a) $\text{Cu}_{0.9}(\text{In,Ga})\text{Se}_2$ and (b) $\text{Cu}_{0.9}(\text{In,Ga})\text{Se}_{2.5}$. The CIGS films were selenized using mixing powders with various weight ratios of alumina to selenium.

(a)	$\text{Al}_2\text{O}_3:\text{Se}$ ratio	Cu (%)	In (%)	Ga (%)	Se (%)	Cu/ (In+Ga)	Ga/ (In+Ga)
	As-dep.	20.7	17.7	7.5	54.1	0.82	0.30
	4:1	23.3	17.9	7.6	51.2	0.91	0.30
	6:1	23.1	18.3	7.3	51.3	0.90	0.29
	8:1	22.8	18.4	7.4	51.4	0.88	0.29
	12:1	23.1	18.5	7.5	50.9	0.89	0.29
	0:0	23.3	19.1	7.7	49.9	0.87	0.29

(b)	$\text{Al}_2\text{O}_3:\text{Se}$ ratio	Cu (%)	In (%)	Ga (%)	Se (%)	Cu/ (In+Ga)	Ga/ (In+Ga)
	As-dep.	11	18	7.5	63.5	0.43	0.29
	4:1	13	22.5	9.3	55.2	0.41	0.29
	6:1	13	21.9	8.8	56.3	0.42	0.29
	8:1	13.1	22.7	9.3	54.9	0.41	0.29
	12:1	13.5	22.7	8.4	55.4	0.43	0.27
	0:0	13.8	23.1	9.4	53.6	0.42	0.29

Table 5.6. Summary of the conversion efficiencies shown in Fig. 5.17.

Sample	Nominal target composition	Al ₂ O ₃ : Se ratio	V _{oc} (V)	J _{sc} (mA/cm ²)	FF (%)	η (%)
A	Cu _{0.9} (In,Ga)Se ₂	4:1	0.277	28.87	42.7	3.42
B	Cu _{0.9} (In,Ga)Se ₂	6:1	0.347	24.94	43.9	3.80
C	Cu _{0.9} (In,Ga)Se ₂	8:1	0.340	18.48	38.3	2.40
D	Cu _{0.9} (In,Ga)Se ₂	12:1	0.283	25.13	35.9	2.56
E	Cu _{0.9} (In,Ga)Se _{2.5}	4:1	0.530	23.97	52.7	6.70
F	Cu _{0.9} (In,Ga)Se _{2.5}	6:1	0.514	21.90	39.3	4.43
G	Cu _{0.9} (In,Ga)Se _{2.5}	8:1	0.499	22.56	47.8	5.38
H	Cu _{0.9} (In,Ga)Se _{2.5}	12:1	0.364	20.02	34.6	2.52

Table 5.7. Intensity ratio of the CIGS films shown in Fig 5.20.

Sample	Dep. Temp. (°C)	Al ₂ O ₃ :Se ratio	I (112)/ I(220)(204)
A	R. T.	8:1	2.6
B	R. T.	6:1	2.3
C	R. T.	4:1	2.5
D	120	8:1	81
E	120	6:1	125
F	120	4:1	73
G	130	8:1	223
H	130	6:1	129
I	130	4:1	77

Table 5.8. Composition before and after selenization of the CIGS precursor films deposited at (a) room temperature, (b) 120 and (c) 130 °C

(a)	Al ₂ O ₃ :Se ratio	Cu (%)	In (%)	Ga (%)	Se (%)	Cu/ (In+Ga)	Ga/ (In+Ga)
	As-dep.	11	18	7.5	63.5	0.43	0.29
	8:1	13.1	22.7	9.3	54.9	0.41	0.29
	6:1	13	21.9	8.8	56.3	0.42	0.29
	4:1	13	22.5	9.3	55.2	0.41	0.29

(b)	Al ₂ O ₃ :Se ratio	Cu (%)	In (%)	Ga (%)	Se (%)	Cu/ (In+Ga)	Ga/ (In+Ga)
	As-dep.	16.4	20.4	8.5	54.7	0.57	0.29
	8:1	14.7	21.2	9.4	54.7	0.48	0.31
	6:1	14.5	23.6	8.4	53.5	0.45	0.26
	4:1	15.5	23.0	8.0	53.5	0.50	0.26

(c)	Al ₂ O ₃ :Se ratio	Cu (%)	In (%)	Ga (%)	Se (%)	Cu/ (In+Ga)	Ga/ (In+Ga)
	As-dep.	16.8	21.3	8.4	53.5	0.57	0.28
	8:1	14.9	21.9	9.1	54.1	0.48	0.29
	6:1	15.6	23.5	8.2	52.7	0.49	0.26
	4:1	15.2	23.4	7.8	53.6	0.49	0.25

Table 5.9. RMS roughness of the CIGS films shown in Fig. 5.25.

Dep. Temp. & Al₂O₃ : Se ratio	RMS roughness (nm)	Standard deviation (nm)
R.T. – 8:1	38.8	0.65
R.T. – 6:1	70.5	1.86
R.T. – 4:1	73.1	1.12
120 °C – 4:1	66.0	4.01
130 °C – 4:1	42.5	2.15

Table 5.10. Summary of the conversion efficiencies shown in Fig. 5.26.

Sample	Dep. Temp. (°C)	Al ₂ O ₃ : Se ratio	V _{oc} (V)	J _{sc} (mA/cm ²)	FF (%)	η (%)
A	R.T.	8:1	0.499	22.56	47.8	5.38
B	R.T.	6:1	0.514	21.90	39.3	4.43
C	R.T.	4:1	0.530	23.97	52.7	6.70
D	120	8:1	0.418	24.28	44.1	4.48
E	120	6:1	0.494	22.23	46.3	5.09
F	120	4:1	0.537	23.59	54.5	6.90
G	130	8:1	0.427	26.32	47.6	5.34
H	130	6:1	0.537	21.72	45.6	5.23
I	130	4:1	0.571	26.58	53.3	8.09

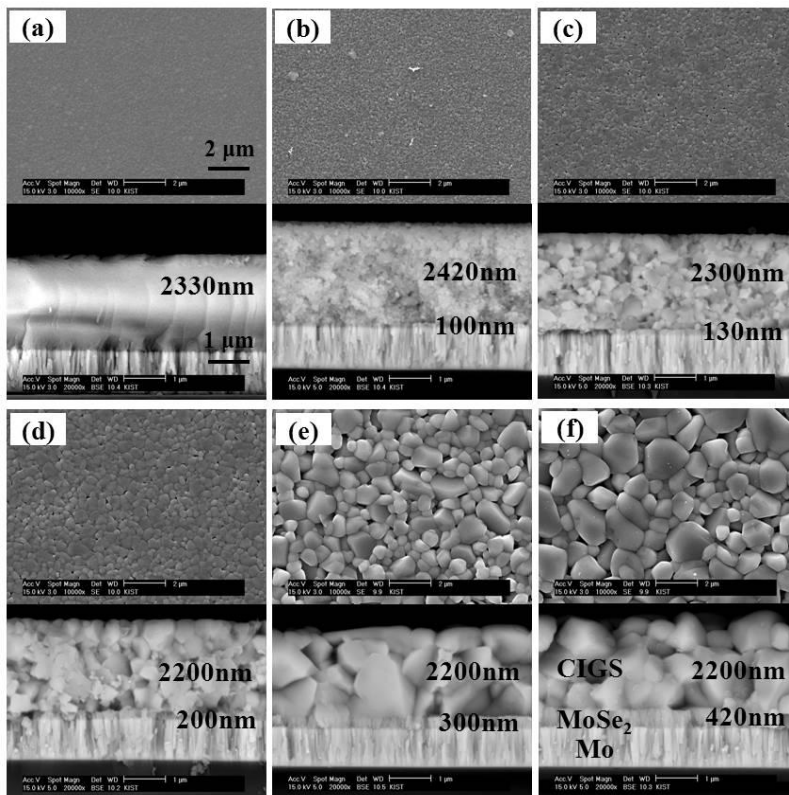


Fig. 5.1. FE-SEM images of the CIGS films (a) as-deposited and selenized at (b) 350 °C, (c) 375 °C, (d) 400 °C, (e) 425 °C and (f) 450 °C. CIGS precursor films were fabricated using a stoichiometric CIGS target and then selenized at various temperatures.

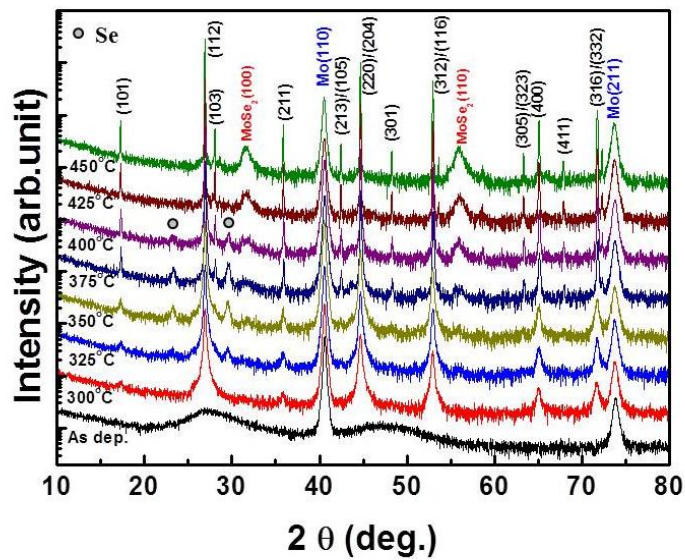


Fig. 5.2. XRD patterns of as-deposited and selenized CIGS films. CIGS precursor films were fabricated using a stoichiometric CIGS target and then selenized at the temperatures from 300 to 450 °C.

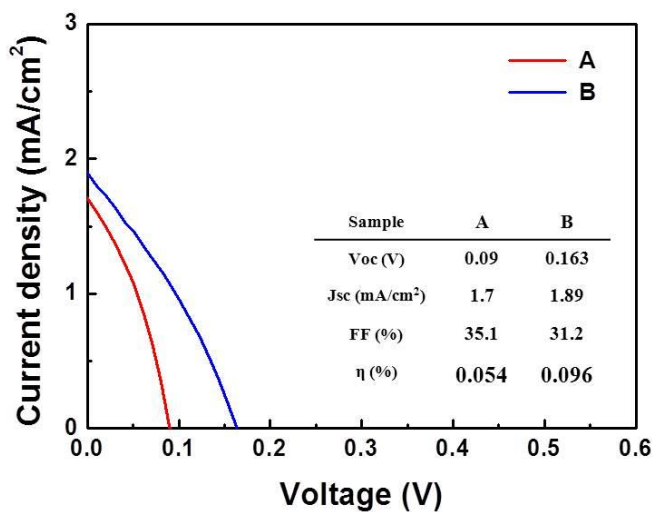


Fig. 5.3. Current-voltage characteristics of the CIGS solar cells fabricated using a stoichiometric CIGS target. The solar cell A and B are fabricated using the CIGS absorber layers selenized at the temperatures of 400 and 450 °C, respectively.

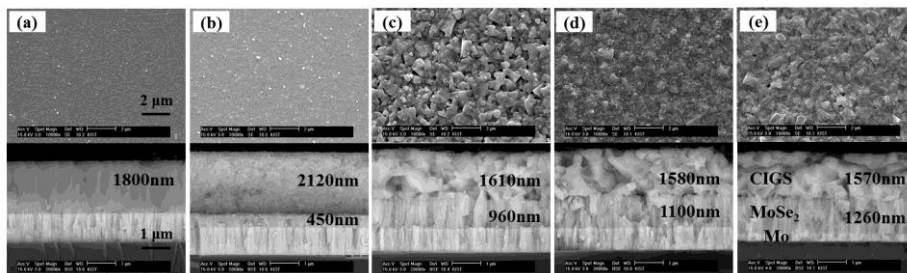


Fig. 5.4. FE-SEM images of the CIGS films (a) as-deposited and selenized at (b) 400 °C, (c) 450 °C, (d) 475 °C and (e) 500 °C. CIGS precursor films were fabricated using a Cu-poor CIGS target and then selenized at various temperatures.

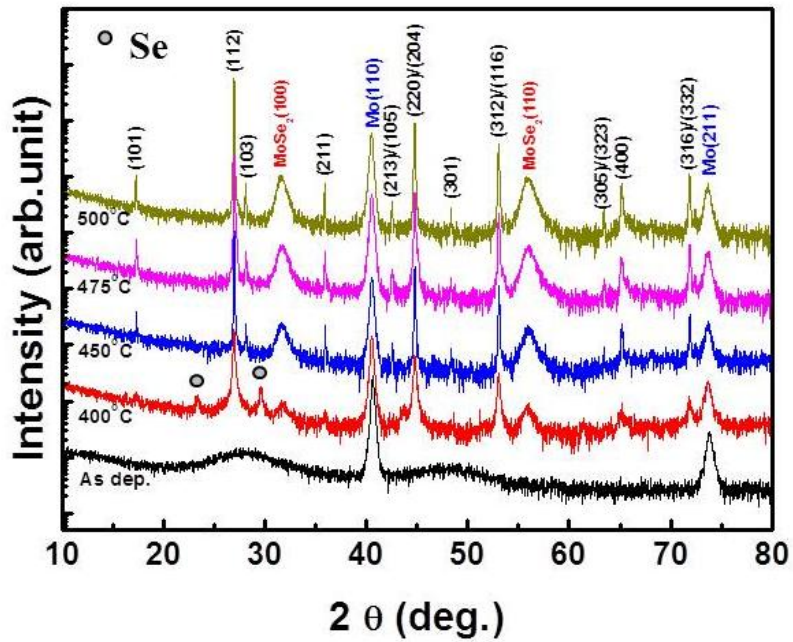


Fig. 5.5. XRD patterns of as-deposited and selenized CIGS films. CIGS precursor films were fabricated using a Cu-poor CIGS target and then selenized at the temperatures from 400 to 500 °C.

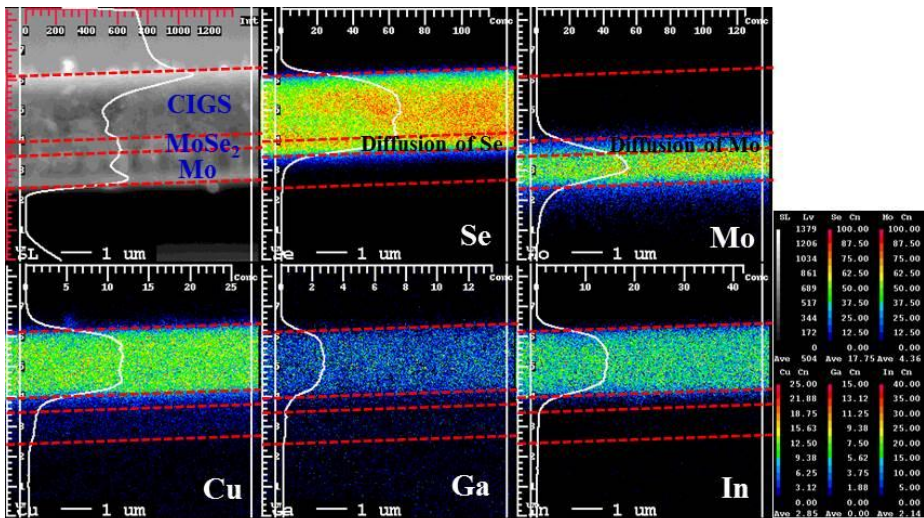


Fig. 5.6. Composition mapping images of the CIGS film selenized at the temperature of 400 °C.

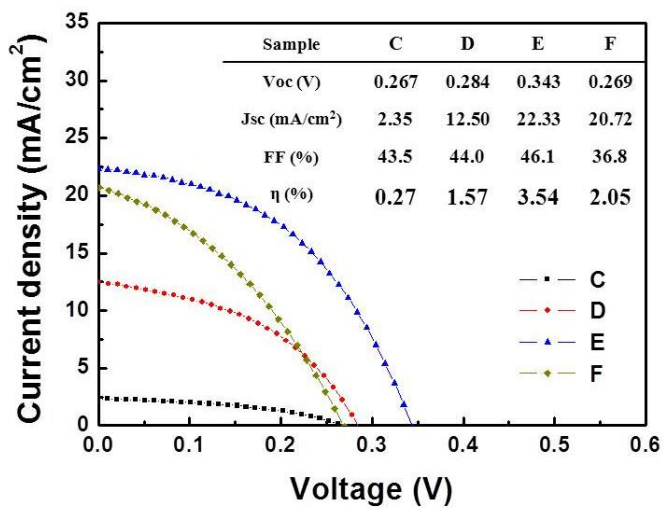


Fig. 5.7. Current-voltage characteristics of the CIGS solar cells fabricated using a Cu-poor CIGS target. The solar cell C, D, E and F are fabricated using the CIGS absorber layers selenized at the temperatures of 400, 450, 475 and 500 °C, respectively.

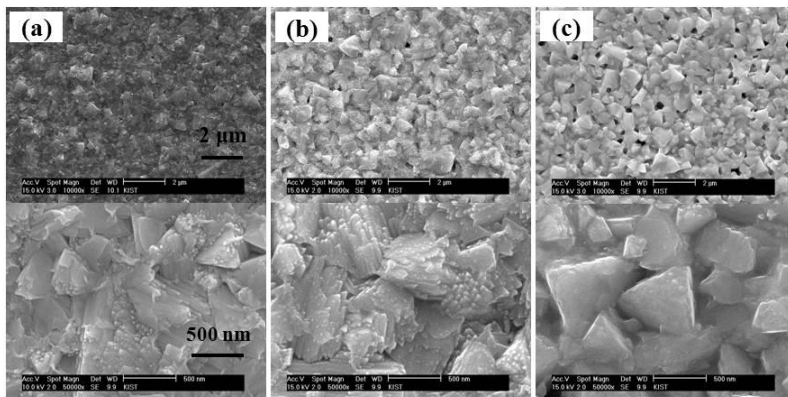


Fig. 5.8. FE-SEM images after selenization of the CIGS precursor films fabricated using (a) $\text{Cu}_{0.9}(\text{In}_{0.7}\text{Ga}_{0.3})\text{Se}_2$, (b) $\text{Cu}_{0.9}(\text{In}_{0.7}\text{Ga}_{0.3})\text{Se}_{2.2}$ and (c) $\text{Cu}_{0.9}(\text{In}_{0.7}\text{Ga}_{0.3})\text{Se}_{2.5}$ targets. All of the films are selenized at the temperature of 475°C for 30minutes.

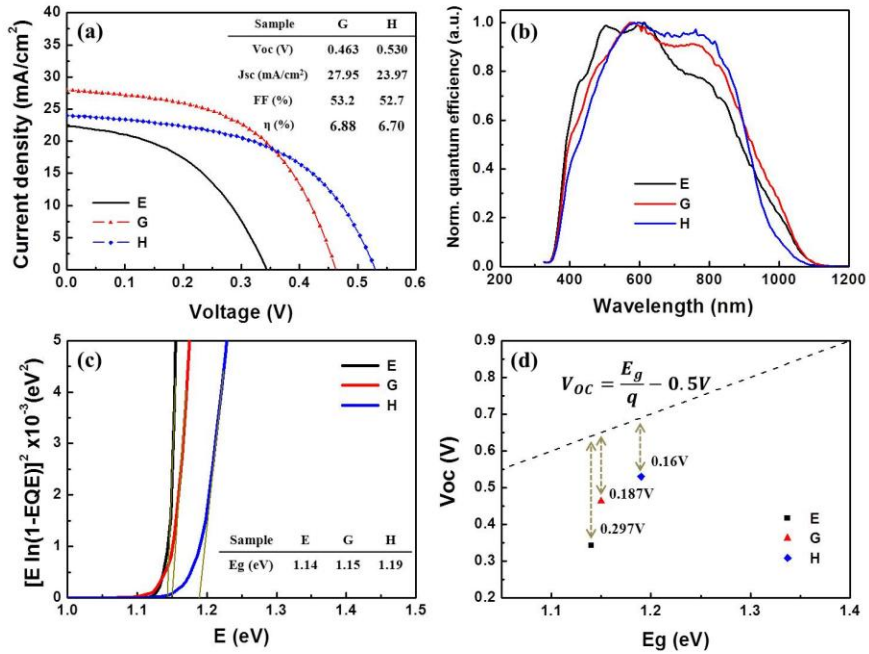


Fig. 5.9. (a) Current-voltage characteristics and (b) normalized quantum efficiency of the CIGS solar cells fabricated using various CIGS targets. (c) Band gap determination from EQE data. (d) A plot of V_{oc} versus band gap (E_g). The solar cell E, G and H are fabricated by using $Cu_{0.9}(In,Ga)Se_2$, $Cu_{0.9}(In,Ga)Se_{2.2}$ and $Cu_{0.9}(In,Ga)Se_{2.5}$ target, respectively.

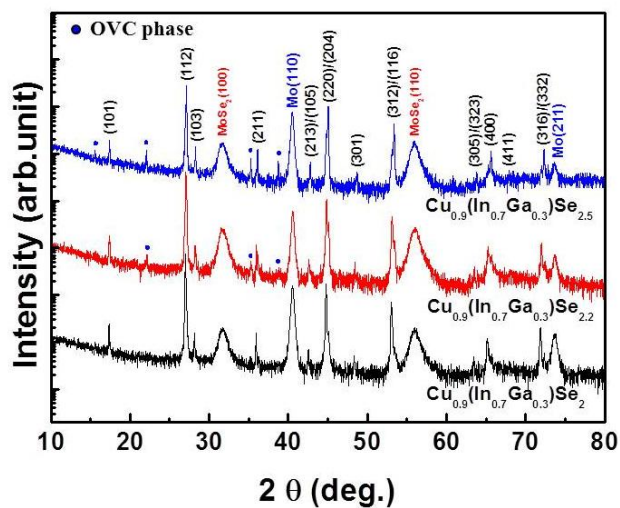


Fig. 5.10. XRD patterns after selenization of the CIGS precursor films fabricated using $\text{Cu}_{0.9}(\text{In}_{0.7}\text{Ga}_{0.3})\text{Se}_2$, $\text{Cu}_{0.9}(\text{In}_{0.7}\text{Ga}_{0.3})\text{Se}_{2.2}$ and $\text{Cu}_{0.9}(\text{In}_{0.7}\text{Ga}_{0.3})\text{Se}_{2.5}$ targets. All of the films are selenized at the temperature of 475°C for 30minutes.

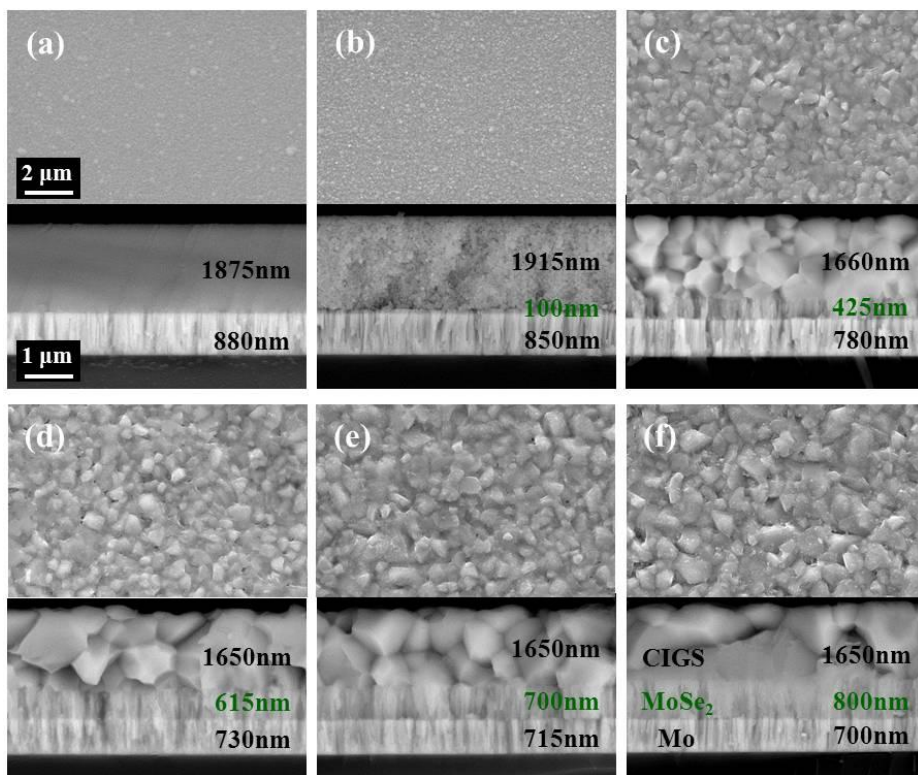


Fig. 5.11. FE-SEM images of the (a) as-deposited CIGS film and the CIGS films selenized using mixing powders with weight ratios of alumina to selenium of (b) 0:0, (c) 12:1, (d) 8:1, (e) 6:1 and (f) 4:1. The CIGS precursor film was fabricated using a single quaternary CIGS target with the nominal compositions of $\text{Cu}_{0.9}(\text{In}_{0.7}\text{Ga}_{0.3})\text{Se}_2$.

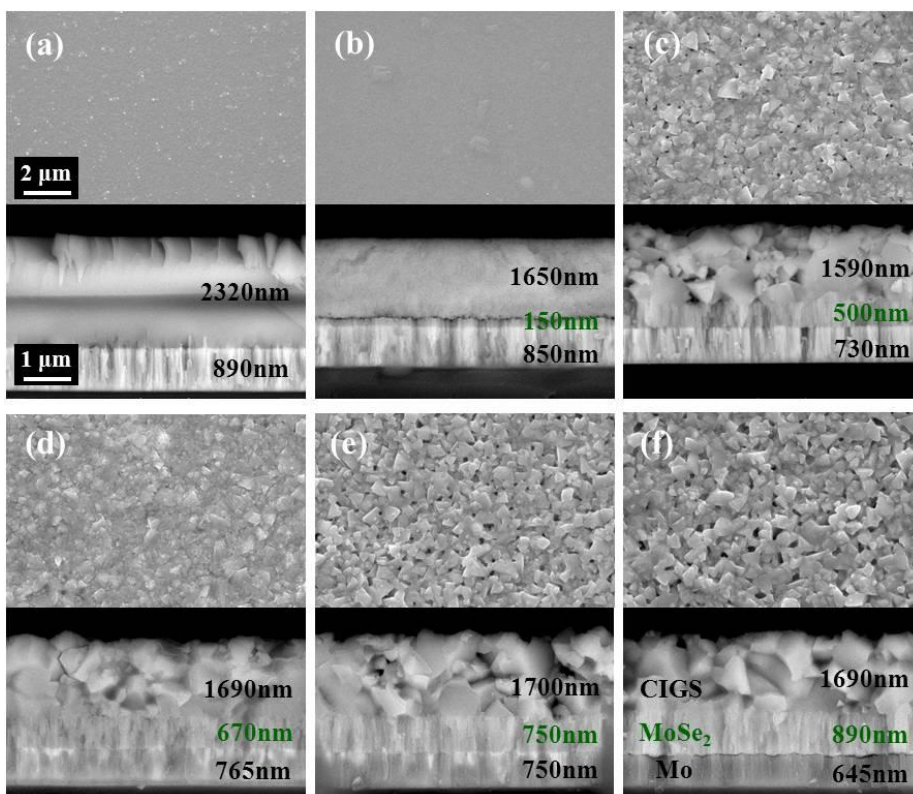


Fig. 5.12. FE-SEM images of the (a) as-deposited CIGS film and the CIGS films selenized using mixing powders with weight ratios of alumina to selenium of (b) 0:0, (c) 12:1, (d) 8:1, (e) 6:1 and (f) 4:1. The CIGS precursor film was fabricated using a single quaternary CIGS target with the nominal compositions of $\text{Cu}_{0.9}(\text{In}_{0.7}\text{Ga}_{0.3})\text{Se}_{2.5}$.

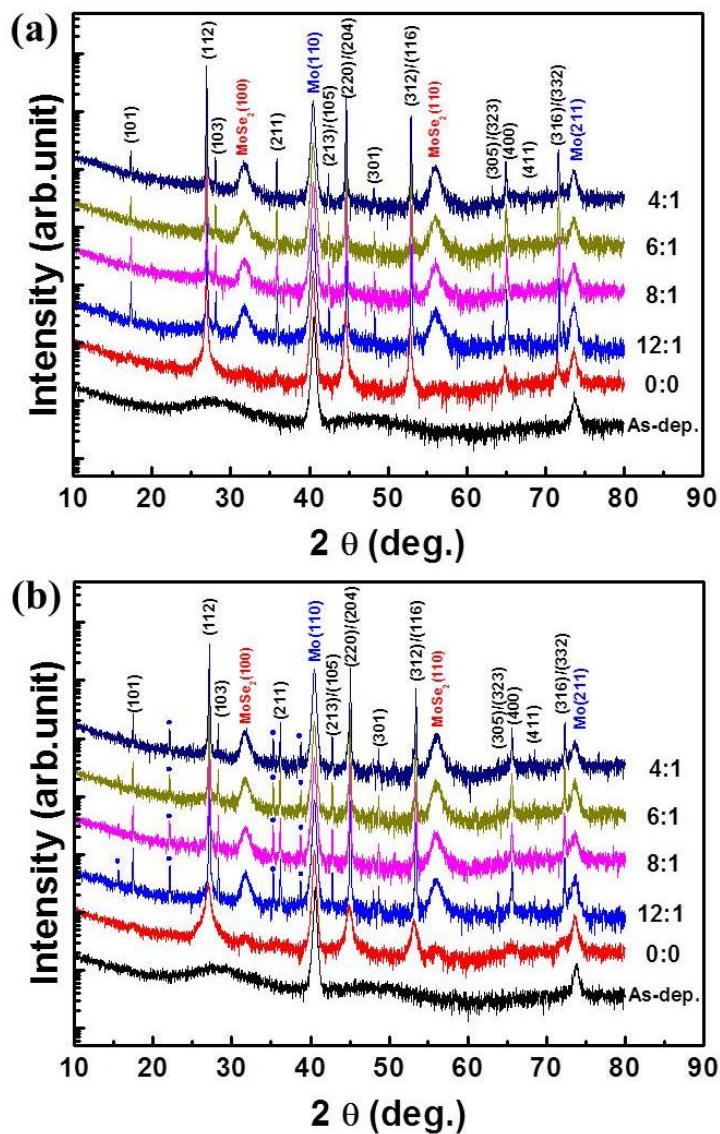


Fig. 5.13. XRD patterns before and after selenization of the CIGS precursor films fabricated using the single quaternary CIGS targets with the nominal compositions of (a) $\text{Cu}_{0.9}(\text{In}_{0.7}\text{Ga}_{0.3})\text{Se}_2$ and (b) $\text{Cu}_{0.9}(\text{In}_{0.7}\text{Ga}_{0.3})\text{Se}_{2.5}$. The CIGS films were selenized using mixing powders with the weight ratios of alumina to selenium of 0:0, 12:1, 8:1, 6:1 and 4:1, respectively.

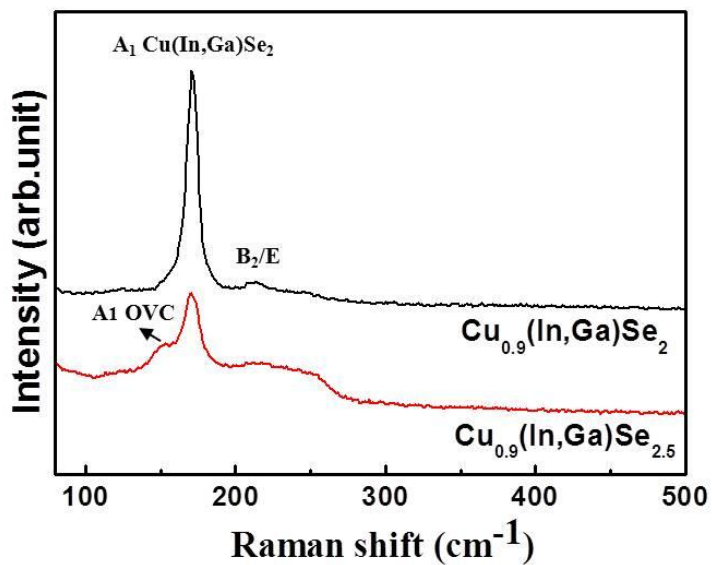


Fig. 5.14. Raman spectra after selenization of the CIGS films fabricated using the single quaternary CIGS targets with the nominal compositions of $\text{Cu}_{0.9}(\text{In}_{0.7}\text{Ga}_{0.3})\text{Se}_2$ and $\text{Cu}_{0.9}(\text{In}_{0.7}\text{Ga}_{0.3})\text{Se}_{2.5}$. The CIGS films were selenized using mixing powders with the weight ratio of alumina to selenium of 8:1.

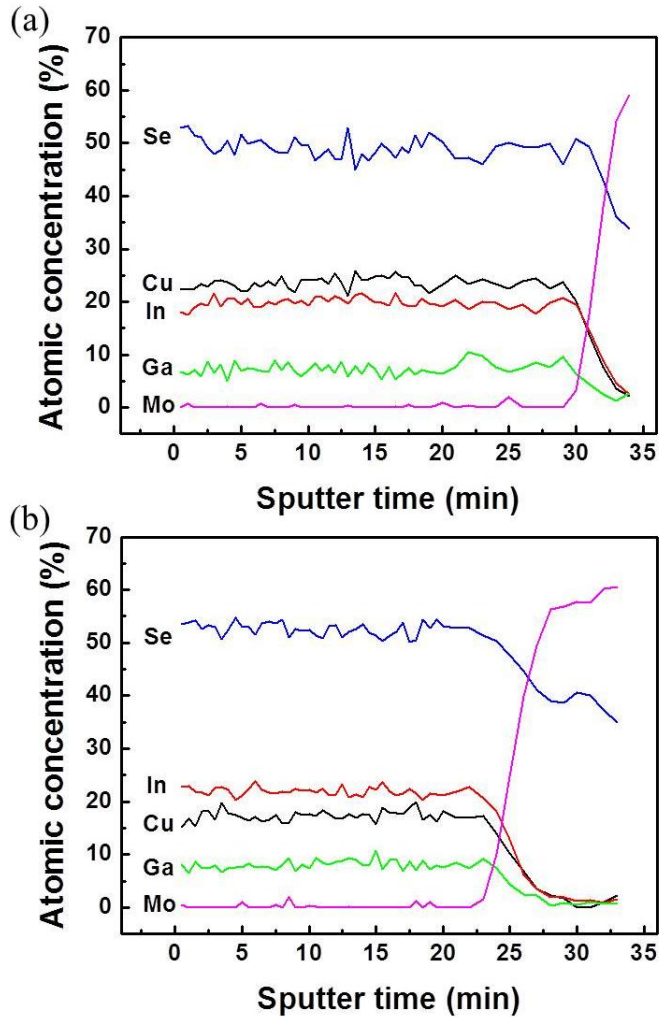


Fig. 5.15. Auger electron spectroscopy (AES) depth profiles after selenization of the CIGS films fabricated using the single quaternary CIGS targets with the nominal compositions of (a) $\text{Cu}_{0.9}(\text{In}_{0.7}\text{Ga}_{0.3})\text{Se}_2$ and (b) $\text{Cu}_{0.9}(\text{In}_{0.7}\text{Ga}_{0.3})\text{Se}_{2.5}$. The CIGS films were selenized using mixing powders with the weight ratio of alumina to selenium of 8:1.

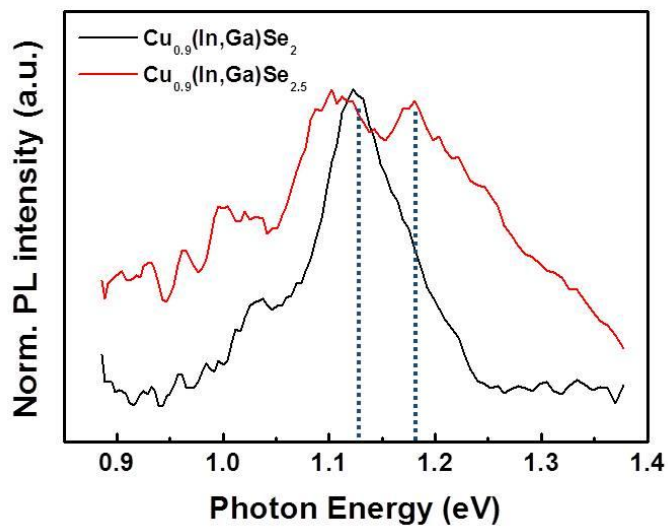


Fig. 5.16. Photoluminescence (PL) spectra after selenization of the CIGS films fabricated using the single quaternary CIGS targets with the nominal compositions of $\text{Cu}_{0.9}(\text{In}_{0.7}\text{Ga}_{0.3})\text{Se}_2$ and $\text{Cu}_{0.9}(\text{In}_{0.7}\text{Ga}_{0.3})\text{Se}_{2.5}$. The CIGS films were selenized using mixing powders with the weight ratio of alumina to selenium of 8:1.

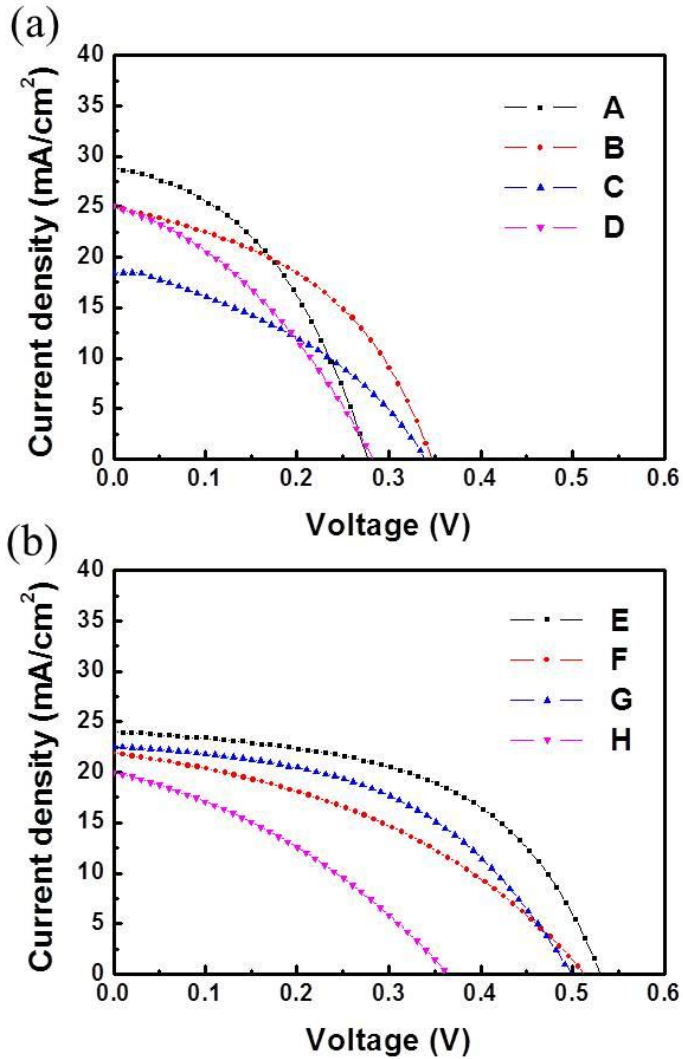


Fig. 5.17. Current-voltage characteristics of the CIGS solar cells fabricated using the single CIGS targets with the nominal compositions of (a) $\text{Cu}_{0.9}(\text{In,Ga})\text{Se}_2$ and (b) $\text{Cu}_{0.9}(\text{In,Ga})\text{Se}_{2.5}$. Detail conditions and values of the sample A to H are in table 5.6.

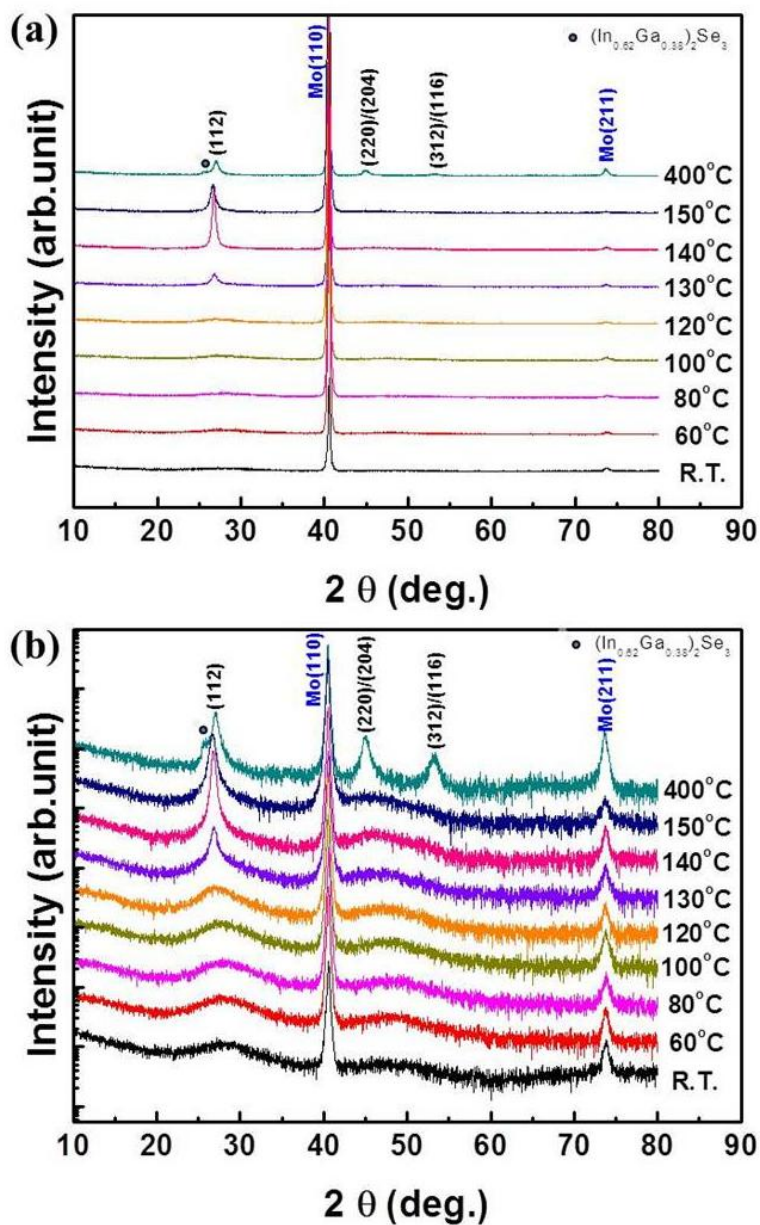


Fig. 5.18. (a) Linear scale and (b) logarithmic scale XRD patterns of the as-deposited CIGS films deposited at various temperatures using a single quaternary $\text{Cu}_{0.9}(\text{In}_{0.7}\text{Ga}_{0.3})\text{Se}_{2.5}$ target.

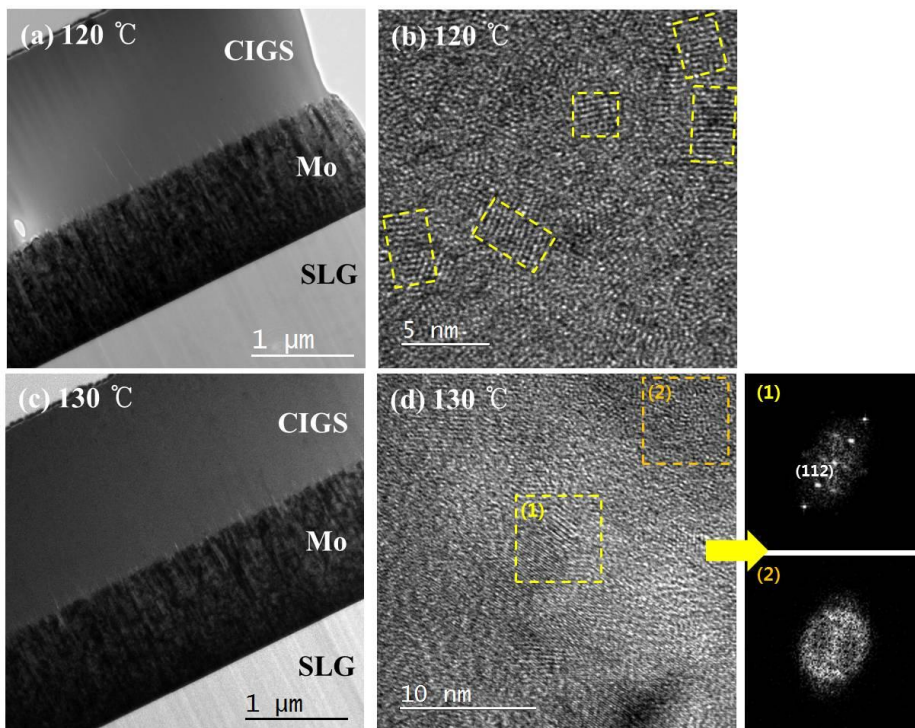


Fig. 5.19. (a), (c) TEM bright-field images and (b), (d) high resolution TEM images of the CIGS precursor films deposited at 120 and 130 °C. And Fast Fourier Transformation (FFT) patterns of region (1) and (2) in figure (d).

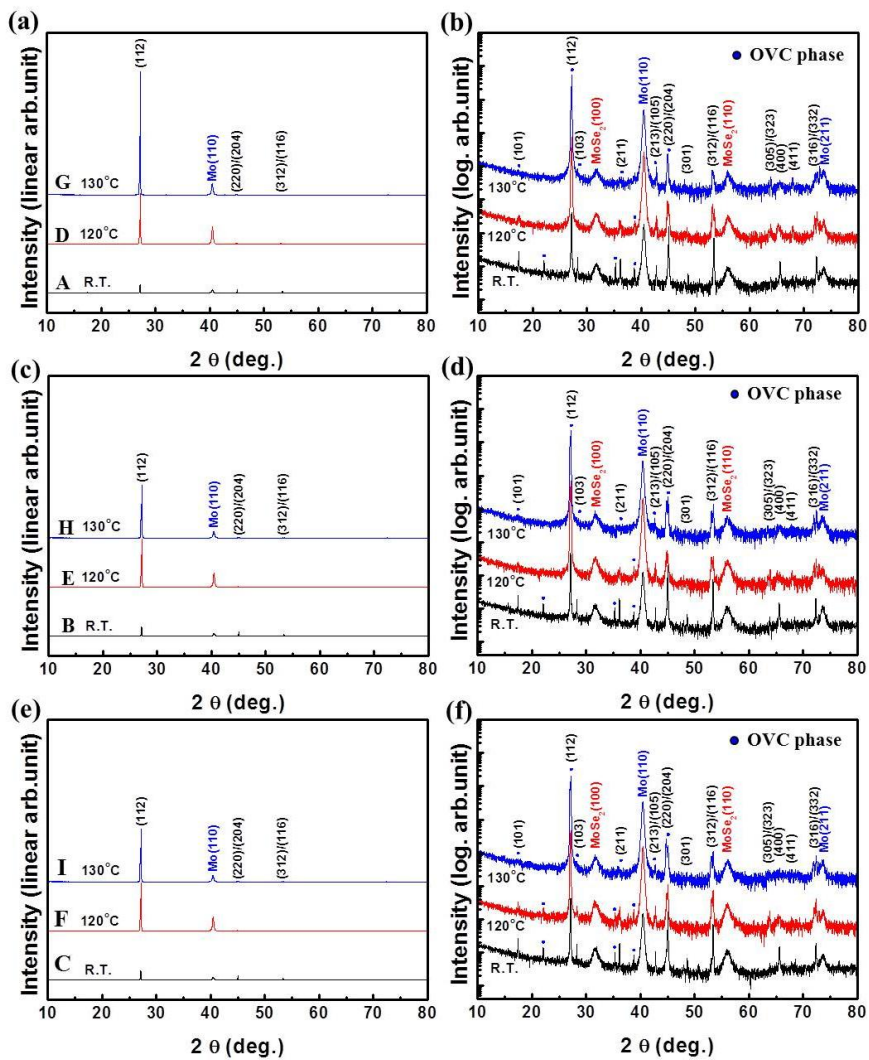


Fig. 5.20. XRD patterns of the CIGS films selenized using mixing powders with the weight ratios of alumina to selenium of (a)(b) 8:1, (c)(d) 6:1 and (e)(f) 4:1.

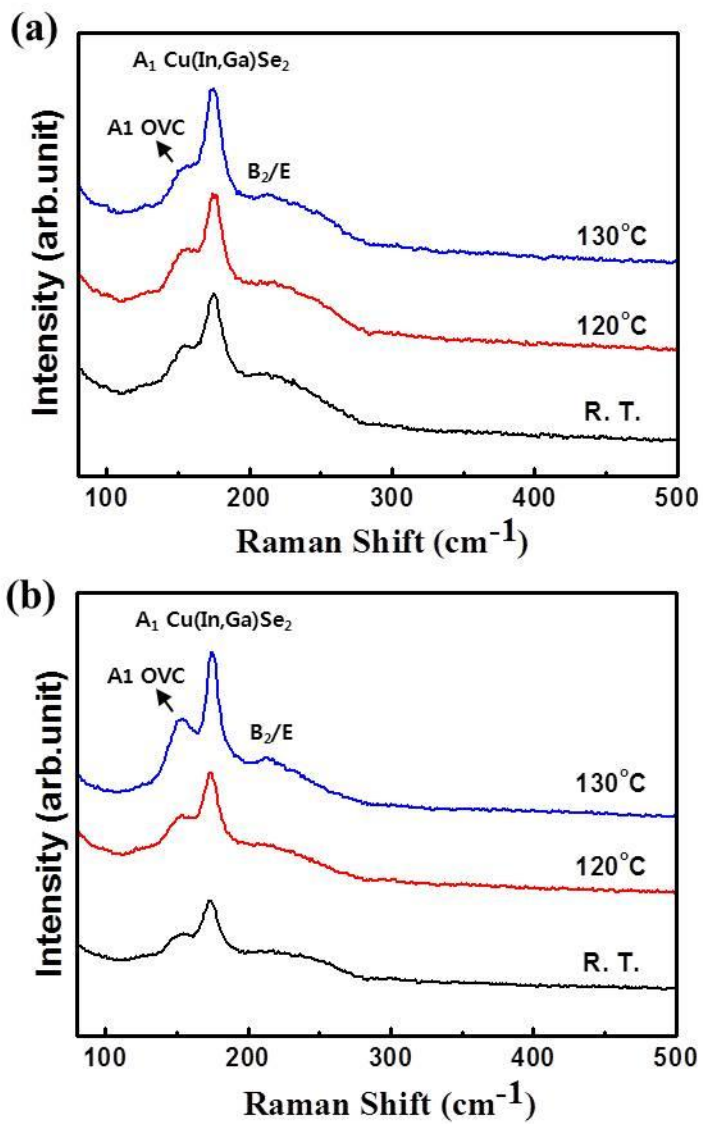


Fig. 5.21. Raman spectra of the CIGS films selenized using mixing powders with the weight ratios of alumina to selenium of (a) 8:1 and (b) 4:1

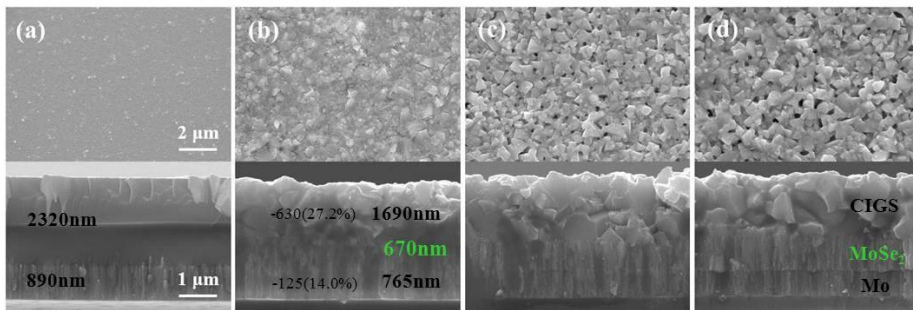


Fig. 5.22. FE-SEM images of the (a) as-deposited CIGS film deposited at room temperature and the CIGS films selenized using mixing powders with weight ratios of alumina to selenium of (b) 8:1, (c) 6:1 and (d) 4:1. CIGS precursor films were fabricated using a single quaternary CIGS target with the nominal composition of $\text{Cu}_{0.9}(\text{In}_{0.7}\text{Ga}_{0.3})\text{Se}_{2.5}$.

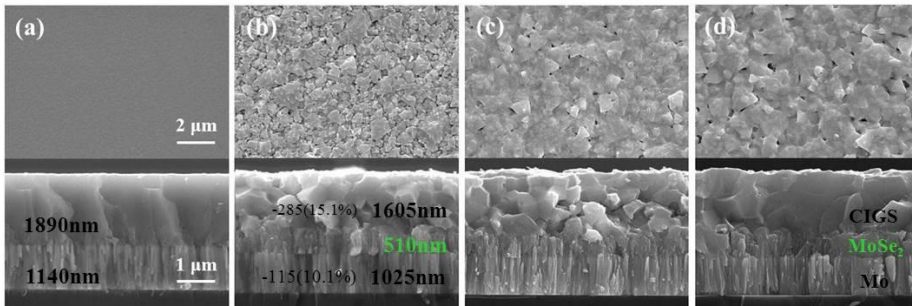


Fig. 5.23. FE-SEM images of the (a) as-deposited CIGS film deposited at 120 °C and the CIGS films selenized using mixing powders with weight ratios of alumina to selenium of (b) 8:1, (c) 6:1 and (d) 4:1. CIGS precursor films were fabricated using a single quaternary CIGS target with the nominal composition of $\text{Cu}_{0.9}(\text{In}_{0.7}\text{Ga}_{0.3})\text{Se}_{2.5}$.

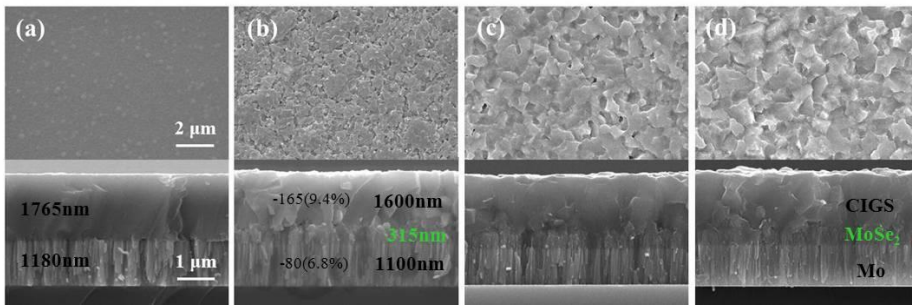


Fig. 5.24. FE-SEM images of the (a) as-deposited CIGS film deposited at 130 °C and the CIGS films selenized using mixing powders with weight ratios of alumina to selenium of (b) 8:1, (c) 6:1 and (d) 4:1. CIGS precursor films were fabricated using a single quaternary CIGS target with the nominal composition of $\text{Cu}_{0.9}(\text{In}_{0.7}\text{Ga}_{0.3})\text{Se}_{2.5}$.

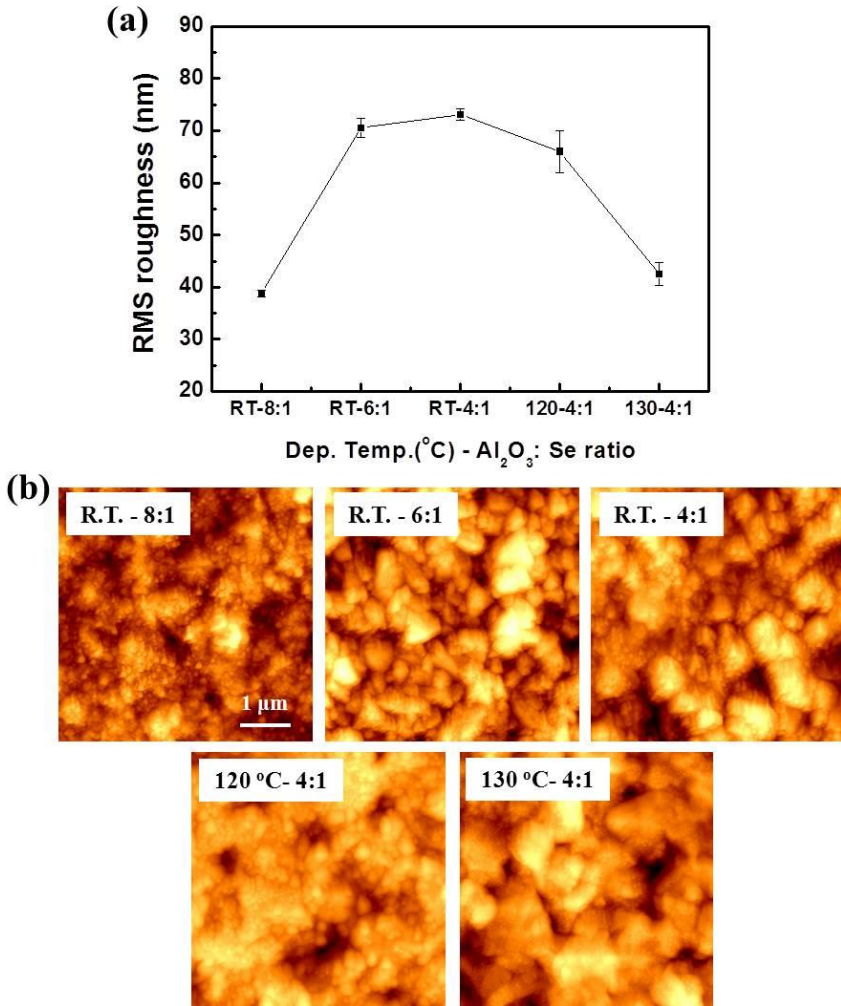


Fig. 5.25. (a) RMS roughness and (b) AFM image of the CIGS films as a function of deposition temperature and selenization condition with various weight ratios of alumina to selenium. Details for the deposition temperature and weight ratio of alumina to selenium are given in the figure.

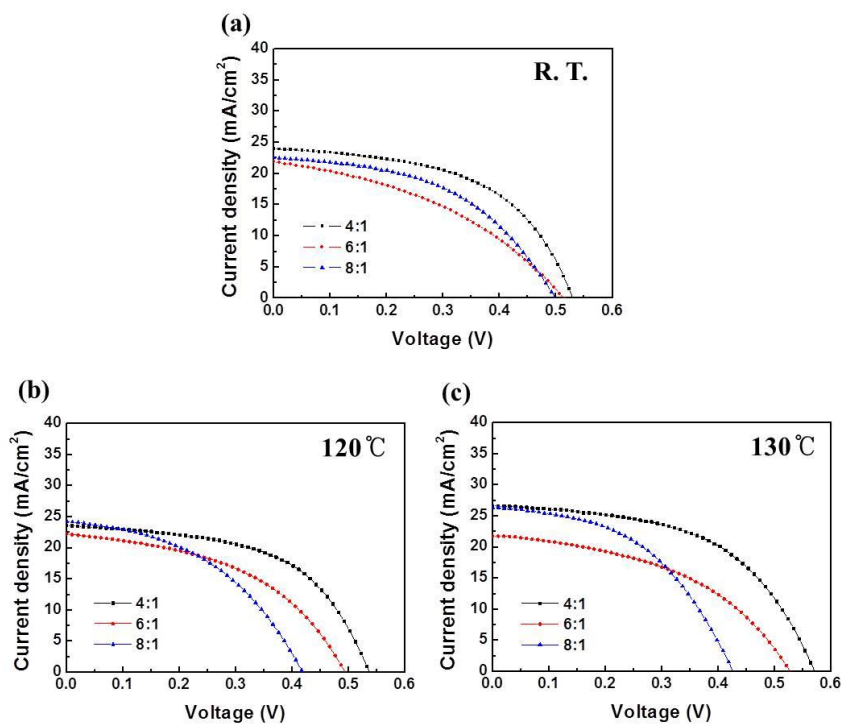


Fig. 5.26. Current-voltage characteristics of the CIGS solar cells fabricated using the CIGS precursor films deposited at (a) room temperature, (b) 120 °C and (c) 130 °C. The CIGS precursor films were selenized using mixing powders with weight ratios of alumina to selenium of 8:1, 6:1 and 4:1, respectively.

Chapter 6. Summary

In this thesis, the properties of CIGS films and CIGS solar cells prepared by RF sputtering of single CIGS targets were investigated. In addition, antireflection (AR) coating and transparent conducting Al-doped ZnO (AZO) films was studied, which are necessary to enhance conversion efficiency.

First, multi-layer antireflection (AR) coatings were investigated. For this study, ZnS and ZnS-MgF₂ composite films were prepared on soda-lime glass substrates and their optical constants were determined by envelope method. And MgF₂ film was deposited on GaAs substrate by rf magnetron sputtering and their optical constants were determined by spectroscopic ellipsometry. In particular, ZnS-MgF₂ composite films were fabricated by co-sputtering of ZnS and MgF₂ target to obtain intermediate refractive index material for a middle layer in the triple-layer AR coating and these films exhibited the desired intermediate refractive index. All films were highly transparent in the range from visible and near-infrared (IR). Based on the extracted optical constants, single-, double- and triple-layer AR coatings on GaAs substrates were designed by using a quarter-wave thickness at a normal incidence and fabricated by rf magnetron sputtering. The experimental results of AR coating were compared to simulated results. Experimental result was consistent with the simulated result. Low reflectance could be obtained from single-layer AR coating only at a specific wavelength and could be obtained from multi-layer AR coating at wide wavelength regime.

Second, the characteristics of the transparent conducting Al-doped ZnO

(AZO) films were investigated. AZO films were deposited on soda-lime glass substrates by using dc magnetron sputtering as a function of argon gas pressure, O₂/Ar gas ratio and substrate temperature, and their electrical and optical properties were investigated. As a result, the resistivity of the AZO films decreased with decreasing argon gas pressure or O₂/Ar gas ratio. As the substrate temperature was increased, resistivity decreased continuously and the lowest value of resistivity was obtained at the temperature of 250 °C in pure Ar and 250-300 °C in O₂/Ar ratio of 1.23%, respectively. The higher substrate temperature increased the resistivity a little. The transmittance was found to be very sensitive to O₂/Ar gas ratio and substrate temperature. Addition of a very small amount of oxygen to argon (1.23% of O₂/Ar ratio) or slight increase of the substrate temperature from room temperature to 150 °C enhanced the transmittance in visible region remarkably. Conclusively, the AZO films with low resistivity of order of 10⁻⁴ Ωcm and high transparency in visible region could be prepared at the substrate temperatures of above 150 °C (the lowest resistivity of 3.19 × 10⁻⁴ Ωcm at 250 °C) by dc magnetron sputtering.

Third, the properties of CIGS absorber layers prepared by RF sputtering without selenization were investigated. Employing various single CIGS sputtering targets with the nominal compositions of Cu_x(In_{0.7}Ga_{0.3})Se_y (where x=0.95 and 1, y=2 to 2.5), CIGS films were deposited on Mo coated soda lime glass (SLG) substrates by using RF magnetron sputtering. When the CIGS precursor film deposited at room temperature using a stoichiometric CIGS target was annealed in an Ar atmosphere, grain growth of the CIGS film did not occur regardless of the post-annealing temperature. Grain size of the CIGS

films was increased with increasing a deposition temperature. However, rough and porous surface morphology with the faceted grains was obtained and therefore very low efficiencies were achieved. For enhancing the efficiency and obtaining the smooth surface morphology, various CIGS targets with the nominal compositions of $\text{Cu}_{0.95}(\text{In}_{0.7}\text{Ga}_{0.3})\text{Se}_{2.5}$ and $\text{Cu}_{0.95}(\text{In}_{0.7}\text{Ga}_{0.3})\text{Se}_{2.1}$ were used to fabricate CIGS absorber layer. Grain size of these films was smaller than that of the CIGS film fabricated using a stoichiometric CIGS target. This result is thought to be caused by the Cu-poor composition of these CIGS targets. Although the CIGS films with a smoother surface morphology can be obtained by using Cu-poor CIGS targets, surface morphology becomes rough with increasing deposition temperature. And the films showed the Se-deficient composition. Conversion efficiency of about 2% was obtained from the CIGS solar cell fabricated using the $\text{Cu}_{0.95}(\text{In}_{0.7}\text{Ga}_{0.3})\text{Se}_{2.5}$ target. Meanwhile, for supplement of selenium, CIGS films fabricated by using the single target of $\text{Cu}(\text{In}_{0.7}\text{Ga}_{0.3})\text{Se}_{2.5}$ powder were annealed in Ar atmosphere with selenium. These films showed the densely packed surface morphology. Conversion efficiency was enhanced. Consequentially, selenization process is beneficial to improvement of structural and electrical properties. Hence, in the next study, the effect of selenization of CIGS precursor film was systematically investigated.

Finally, the characteristics of CIGS absorber layers after selenization of CIGS precursor film deposited at room temperature were systematically investigated. In this study, the CIGS targets with various compositions of $\text{Cu}_x(\text{In}_{0.7}\text{Ga}_{0.3})\text{Se}_y$ (where $x=0.9, 1$; $y=2, 2.2, 2.5$) were fabricated. Utilizing these targets, the CIGS precursor films were deposited by RF magnetron

sputtering and then selenized in a tube furnace under Se atmosphere using Se powder. From the stoichiometric CIGS target, Cu-rich CIGS films were obtained and very low conversion efficiencies were obtained due to inappropriate composition and porous and rough surface morphology with large grains. In contrast, the CIGS films fabricated by using the Cu-poor CIGS target showed the device-quality stoichiometry ratio and densely packed surface morphology with small grains, as well as the chalcopyrite structure without the second phases. Increase of the Se content in the single CIGS target led to decrease of the Cu content and increase of the (In+Ga) content in the CIGS film, which created the ordered vacancy compound (OVC) phases and increased the band gap (E_g) of the CIGS film resulting in increase of the open-circuit voltage (V_{oc}). The difference between $E_g/q - 0.5V$ and V_{oc} was remarkably decreased with the formation of the OVC phases. The highest efficiency of 6.88% could be achieved from the CIGS solar cell fabricated by using the Cu-poor and Se-excess target with the nominal composition of $Cu_{0.9}(In_{0.7}Ga_{0.3})Se_{2.2}$. Consequently, the composition of the single CIGS target was found to play a key role in the structural and electrical properties of the CIGS film and CIGS thin film solar cell efficiency.

Characteristics of CIGS films selenized using mixing powders with various weight ratios of alumina to selenium were investigated. For this experiment, the CIGS precursor films were deposited using the single CIGS targets with the nominal compositions of $Cu_{0.9}(In,Ga)Se_2$ and $Cu_{0.9}(In,Ga)Se_{2.5}$. As the results, regardless of target composition, grain size was increased with increasing the Se ratio of mixing powder. The $MoSe_2$ layer was formed between the CIGS and the Mo layer and its thickness was also increased with

increasing the Se ratio of mixing powder. The MoSe₂-layer thickness of the CIGS film fabricated using the Cu_{0.9}(In_{0.7}Ga_{0.3})Se_{2.5} target is thicker than that of the CIGS film fabricated using the Cu_{0.9}(In_{0.7}Ga_{0.3})Se₂ target because of larger amount of Se in the CIGS film fabricated using the Cu_{0.9}(In_{0.7}Ga_{0.3})Se_{2.5} target. From the auger electron spectroscopy (AES) depth profiles, it was found that each element of the CIGS film was evenly distributed in the CIGS films without grading of elements. This means that the CIGS phases including the OVC phase are evenly distributed. The open-circuit voltages of the CIGS solar cells fabricated using the Cu_{0.9}(In_{0.7}Ga_{0.3})Se_{2.5} target were commonly higher than those of the solar cells fabricated using the Cu_{0.9}(In_{0.7}Ga_{0.3})Se₂ target. The open-circuit voltage of the CIGS solar cells fabricated using the Cu_{0.9}(In_{0.7}Ga_{0.3})Se_{2.5} target was decreased with decreasing Se ratio of mixing powder used for selenization.

Also, characteristics of CIGS films selenized using nanocrystalline precursor film were investigated. CIGS precursor films were deposited at various temperatures using a single quaternary Cu_{0.9}(In_{0.7} Ga_{0.3})Se_{2.5} target. Base on the results of XRD patterns and TEM images, as-deposited CIGS films fabricated at the substrate temperatures of 120 °C and 130 °C were considered as the nano-crystalline CIGS precursor films. The CIGS films were selenized at 475 °C for 30min. The CIGS films showed a (112) preferred orientation. All of the selenized CIGS films had the similar composition regardless of deposition temperature although Cu content in the film was slightly different. From the Raman spectra of the CIGS films, the existence of OVC phase which can lead to decrease of open-circuit voltage loss was identified. The CIGS film with smooth and dense surface

morphology as well as the large grain size was obtained by increase of Se ratio in a tube furnace and using the nano-crystalline CIGS precursor film. And the thickness of the MoSe₂ layer was decreased after selenization of the nano-crystalline CIGS precursor film compared to that of the amorphous CIGS precursor film. The highest efficiency was achieved from the CIGS solar cell fabricated using the nanocrystalline CIGS precursor film deposited at 130 °C and its value is 8.09 % with the open-circuit voltage of 0.571V, short-circuit current density of 26.58 mA/cm² and the fill factor of 53.28%. This result is thought to be achieved by the beneficial factors such as the existence of an OVC phase, the thickness reduction of a MoSe₂ layer, smooth surface morphology and the decrease of defect density achieved by dense CIGS film with large grain.

Publications

Papers (SCI journals)

1. Sung-Mok Jung, Bong-Geun Song, Young-Hwan Kim, Jong-Ku Park, Seong-Il Kim, and Sang-Im Yoo, Cu(In,Ga)Se₂ thin film solar cells fabricated via RF sputter method using single CIGS targets, to be submitted.
2. Sung-Mok Jung, Young-Hwan Kim, Jong-Ku Park, Seong-Il Kim, and Sang-Im Yoo, Characteristics of CIGS absorber layers and devices fabricated using nanocrystalline CIGS precursor film, to be submitted.
3. Sung-Mok Jung, Young-Hwan Kim, Seong-Il Kim, and Sang-Im Yoo, Characteristics of transparent conducting Al-doped ZnO films prepared by dc magnetron sputtering, Current Applied Physics 11 (2011) S191.
4. Sung-Mok Jung, Young-Hwan Kim, Seong-Il Kim, and Sang-Im Yoo, Design and fabrication of multi-layer antireflection coating for III-V solar cell, Current Applied Physics 11 (2011) 538.
5. Sung-Mok Jung, Sang-Im Yoo, Young-Hwan Kim, Yong Tae Kim and Suk-Kyoung Hong, Characteristics of Sol-Gel Derived Bi_{3.15}Nd_{0.85}Ti₃O₁₂ Thin Films on Al₂O₃/Si for Metal-Ferroelectric-Insulator-Semiconductor Structure, Journal of the Korean Physical Society 49 (2006) S552.

Contributed papers (SCI journals)

6. Sung-Yun Lee, Young-Hwan Kim, Kyoung Jin Choi, Sung-Mok Jung and Sang-Im Yoo, Effect of copper-oxide segregation on the dielectric properties of $\text{CaCu}_3\text{Ti}_4\text{O}_{12}$ thin films fabricated by pulsed-laser deposition, *Thin Solid Films* 518 (2010) 5711.
7. D. S. Kim, C. E. Lee, Y. H. Kim, S. M. Jung, and Y. T. Kim, Growth and characterization of $\text{Pr}_{0.7}\text{Ca}_{0.3}\text{MnO}_3$ thin films for resistance random access memory, *Journal of the Korean Physical Society* 49 (2006) S557.

초 록

태양전지는 에너지 위기와 환경오염과 같은 문제들이 대두됨에 따라 많은 관심을 받아 왔다. 특히, 박막형 태양전지는 원료절감과 경량으로 만들 수 있다는 장점들 때문에 널리 연구되어 왔으며, 이중 CIGS (Cu(In,Ga)Se_2) 태양전지는 높은 광전변환효율과 안정성이 우수하다는 장점들 때문에 전 세계적인 관심을 받아 왔다. 하지만, 20% 이상의 고효율을 달성한 CIGS 태양전지 제조방법은 비교적 공정이 복잡한 삼단계 동시증발법(three-stage co-evaporation process)에 의해 달성 되어왔으며, 이 방법은 대면적에서 균일한 조성을 가진 박막을 제조하기가 어렵다는 단점을 갖는다. 따라서 본 학위 논문에서는 대면적에서 균일한 조성을 얻기 용이하며, 공정을 간략화 할 수 있는 방법을 채택 하였으며, 이를 위해 다양한 조성의 CIGS 단일 타겟들을 사용하여 RF(radio frequency) 스퍼터링 법으로 제조한 CIGS 박막과 CIGS 태양전지의 특성에 대해 살펴보았다. 추가적으로, 효율 향상을 위해 반드시 필요한 무반사 코팅 및 AZO(Al-doped ZnO) 투명전극층의 박막 특성에 대해 살펴보았다. 본 연구의 주요결과들은 다음과 같다.

첫째, ZnS 와 MgF_2 를 이용하여 제조한 이중 및 삼층 구조 등의 다층 무반사 코팅들의 특성에 대해 살펴보았다. 이 연구를 위해, ZnS와 ZnS- MgF_2 혼합 박막을 각각 소다라임유리(soda-lime glass) 기판 위에 증착하여 포락선 방법(envelope method)에 의해 광학상수들을 결정하였으며, 또한 GaAs 기판위에 MgF_2 박막을 증착하여 분광 타원계측법(spectroscopic ellipsometry)에 의해

광학상수들을 결정하였다. 특히, 삼층 구조 무반사 코팅의 중간층에 필요한 ZnS와 MgF₂ 사이의 중간 값의 굴절률을 가진 박막을 얻기 위해 ZnS와 MgF₂ 타겟을 동시 스퍼터링(co-sputtering)하였고, ZnS-MgF₂ 혼합 박막을 제조하여 중간 값의 굴절률을 가진 박막을 성공적으로 제조 할 수 있었다. 제조된 모든 박막들은 가시광 및 근적외선 범위에서 투명했다. ZnS-MgF₂ 혼합 박막의 경우, Mg와 F의 양이 증가함에 따라 광 흡수단은 단파장쪽으로 이동하였으며, 굴절률은 감소했다. 본 실험을 통해 구한 광학 상수들을 사용하여, GaAs에 대한 단층, 이중 및 삼층의 무반사 코팅은 설계 되었으며, 이것을 바탕으로하여 각 코팅층들을 RF 스퍼터링에 의해 제조하였고, 실험결과들을 설계된 결과들과 비교하였다. 단층 무반사 코팅을 통해 특정 파장에서 낮은 반사율을 얻을 수 있었으며, 다층 무반사 코팅을 통해 넓은 범위의 파장에서 낮은 반사율을 얻을 수 있었다. 추가적으로, 다층 무반사 코팅의 반사율에 대한 입사각 의존성을 살펴보았으며, 코팅 층의 수에 따라 다른 특성들을 나타냈다.

둘째, AZO 투명전극을 DC(direct current) 스퍼터링법으로 제조함 있어서, Ar 가스 압력, O₂/Ar 가스 비율 및 기판온도 등의 공정변수들이 AZO 투명전극의 전기적, 광학적 특성에 미치는 영향들을 살펴보았다. Ar 가스 압력 및 O₂/Ar 가스 비율이 작아 질수록 AZO 박막의 비저항은 감소했다. 또한, 기판 온도를 상온으로부터 증가시킬수록 비저항 값은 감소 하였으며, 250℃에서 가장 작은 비저항값을 얻을 수 있었으나, 기판 온도를 더욱 증가시켰을 때 비저항 값은 다소 증가하였다. 투과도는 O₂/Ar 가스 비율 및 기판 온도에 민감 했으며, Ar에 산소(1.23% 의 O₂/Ar

비율)를 다소 추가하거나, 상온으로부터 150℃까지 기판온도를 증가시켰을 때 가시광 영역에서의 투과도를 향상시킬 수 있었다. 결론적으로, 150℃ 이상의 기판 온도에서 AZO 박막을 증착했을 때, $\sim 10^{-4} \Omega\text{cm}$ 크기의 낮은 비저항과 가시광 영역에서 높은 투과도를 갖는 AZO 박막을 제조할 수 있었다.

셋째, 셀렌화 공정없이 CIGS 단일 타겟의 RF 스퍼터링에 의해 제조된 CIGS 흡수층의 특성에 대해 살펴보았다. 본 연구를 위해, $\text{Cu}_x(\text{In}_{0.7}\text{Ga}_{0.3})\text{Se}_y$ ($x=0.95\sim 1$, $y=2\sim 2.5$)의 공칭 조성들을 가진 다양한 CIGS 단일 타겟들을 제조하였으며, 이 CIGS 타겟들을 사용하여 Mo이 코팅된 소다라미유리 기판위에 RF 스퍼터링법을 통해 CIGS 박막을 제조하였다. 먼저, 정량 조성의 CIGS 타겟을 사용하여 상온에서 박막을 증착하였고, 이 CIGS 박막은 Ar 분위기에서 후 열처리 했을 때 열처리 온도와 상관없이 결정립 성장은 일어나지 않았으나, 증착 온도를 증가시켜 감에 따라 결정립의 크기는 증가하였다. 그러나 면들로 구성된 형상의 결정립들(the faceted grains)로 이루어진 거칠고 공극이 많은 표면 형상의 박막이 제조되었고, 따라서 효율은 매우 낮았다. 고른(평탄한) 표면 형상 및 효율 향상을 달성하기 위해 $\text{Cu}_{0.95}(\text{In}_{0.7}\text{Ga}_{0.3})\text{Se}_{2.5}$ 와 $\text{Cu}_{0.95}(\text{In}_{0.7}\text{Ga}_{0.3})\text{Se}_{2.1}$ 의 공칭조성을 가진 타겟들을 사용하여 CIGS 흡수층을 제조하였다. 이러한 타겟들을 사용하여 제조된 박막의 결정립 크기는 정량 조성타겟을 사용하여 제조한 박막의 결정립보다 작았으며, 이것은 위의 CIGS 타겟들의 Cu 부족한 조성에 의해 야기된 결과라 사료된다. 비록 Cu가 부족한 CIGS 타겟을 사용 하여 더 고른 표면 형상을 가진 CIGS 박막을 제조할 수 있었지만, 표면 형상은 증착온도를 증가 시켜 감에 따라 거칠어 졌다. 결과적으로,

$\text{Cu}_{0.95}(\text{In}_{0.7}\text{Ga}_{0.3})\text{Se}_{2.5}$ 타겟을 사용하여 제조된 태양전지로부터 약 2%의 광전 변환 효율을 달성 할 수 있었으나, 더욱 적은 양의 Se을 함유하고 있는 $\text{Cu}_{0.95}(\text{In}_{0.7}\text{Ga}_{0.3})\text{Se}_{2.1}$ 타겟을 사용해서 제조된 태양전지는 더욱 낮은 효율을 나타냈으며, 위의 세 가지 타겟으로 제조된 모든 CIGS 박막들은 공통적으로 Se이 부족한 조성을 가졌다. 그러므로 Se의 보충을 위해 타겟의 소결공정을 생략하고 $\text{Cu}(\text{In}_{0.7}\text{Ga}_{0.3})\text{Se}_{2.5}$ 의 공칭조성을 가진 파우더의 압착에 의해 제조한 타겟을 이용하여 CIGS 박막을 제조하였다. 결과적으로 CIGS 박막 내의 Se 함유량은 증가하였으나, 위의 경우와 마찬가지로 거칠고 공극이 많은 표면 형상을 나타냈으며, 효율은 매우 낮았다. 그러나 이 박막들은 Se 분위기에서 열처리 했을 때, 밀도가 높은 표면 형상을 가진 박막으로 바뀌었으며, 광전변환 효율은 3.3%까지 향상되었다. 이러한 결과들을 고려해 볼 때, 셀렌화 공정은 단일 CIGS 타겟을 사용하여 제조된 CIGS 박막의 구조적, 전기적 특성들을 개선시키며, 따라서 다음의 연구들을 통해 CIGS 박막의 셀렌화 후 특성들에 대해 체계적으로 살펴 보았다.

이 연구를 위해 우선, 상온에서 증착한 CIGS 전구체 박막의 셀렌화 후 특성에 대해 체계적으로 살펴보았다. $\text{Cu}_x(\text{In}_{0.7}\text{Ga}_{0.3})\text{Se}_y$ ($x=0.9, 1; y=2, 2.2, 2.5$)로 구성된 다양한 공칭 조성을 가진 단일 타겟들을 제조하였으며, 이러한 조성의 타겟들을 RF 마그네트론 스퍼터링에 의해 증착하여 CIGS 전구체 박막을 제조하였다. 제조된 CIGS 전구체 박막은 셀레늄 파우더를 사용하여 조성한 셀레늄 분위기의 튜브퍼니스 안에서 셀렌화 하였다. 정량조성의 CIGS 타겟을 사용하여 제조한 CIGS 전구체 박막은 셀렌화 후 Cu가 과량 함유된 CIGS 박막을 형성 했으며, 이것은 산발적으로 Cu_{2-x}Se 상을

형성시켰다. 또한 큰 결정립의 형성과 함께 거칠고 공극이 많은 표면 형상을 나타냈다. 결과적으로 이 박막을 사용하여 제조된 태양전지는 이러한 부적합한 표면 형상과 조성 때문에 매우 낮은 광전변환효율을 나타냈다. 이와 대조적으로, Cu-poor한 CIGS ($\text{Cu}_{0.9}(\text{In}_{0.7}\text{Ga}_{0.3})\text{Se}_2$) 타겟을 사용하여 제조된 CIGS 박막은 태양전지 소자에 적합한 화학량론비율(device-quality stoichiometry ratio)의 조성을 나타냈으며, 작은 결정립들로 구성된 밀도가 높은 표면 형상뿐 만 아니라 이차상이 없는 chalcopyrite CIGS 구조를 나타냈다. Cu-poor한 타겟에 Se의 함량을 증가시키기에 따라 CIGS 박막 내의 Cu 함량은 감소되었으며, (In+Ga) 함량은 증가 되었다. 이러한 박막 조성의 변화는 ordered vacancy compound (OVC) 상을 형성시켰고 CIGS 박막의 밴드갭을 증가시켜, 결국 개방전압(V_{oc} , open-circuit voltage)을 증가 시켰다. 특히, $E_g/q - 0.5V$ 와 V_{oc} 사이의 차이는 OVC 상의 형성과 함께 두드러지게 감소하였다. 결과적으로 $\text{Cu}_{0.9}(\text{In}_{0.7}\text{Ga}_{0.3})\text{Se}_{2.2}$ 의 공칭 조성 타겟을 사용하여 제조한 CIGS 태양전지로부터 6.88%의 광전 변환 효율을 달성 하였다. 위의 결과들을 미루어 볼 때, CIGS 단일 타겟의 조성은 CIGS 박막의 구조적, 전기적 특성 및 CIGS 태양전지 효율에 중요한 역할을 함을 알 수 있었다.

다음으로 셀렌화 분위기의 셀레늄 함량을 다양하게 변화시켜 셀렌화한 CIGS 박막들의 특성을 살펴보았다. 본 실험을 위해 $\text{Cu}_{0.9}(\text{In,Ga})\text{Se}_2$ 와 $\text{Cu}_{0.9}(\text{In,Ga})\text{Se}_{2.5}$ 의 공칭 조성을 가진 타겟들을 사용하였다. 타겟조성에 상관없이 셀렌화시 사용된 혼합 파우더의 Se 비율이 증가함에 따라(셀렌화 분위기의 셀레늄 함량증가) 결정립 크기는 증가 되었으며, CIGS 와 Mo층 사이에 형성된 MoSe_2

층의 두께 또한 증가하였다. 형성된 MoSe_2 층의 두께는 $\text{Cu}_{0.9}(\text{In}_{0.7}\text{Ga}_{0.3})\text{Se}_{2.5}$ 타겟을 사용했을 때 CIGS 전구체 박막이 더 많은 양의 Se을 함유 함으로 인해 $\text{Cu}_{0.9}(\text{In}_{0.7}\text{Ga}_{0.3})\text{Se}_2$ 타겟을 사용한 경우보다 더 두꺼웠다. 셀렌화 된 CIGS 박막의 깊이방향의 조성분석을 오제 전자 분광법(auger electron spectroscopy)으로 실시하였으며, CIGS 박막의 각 원소들은 조성의 변화 없이 고르게 분포하였다. 이것은 $\text{Cu}_{0.9}(\text{In}_{0.7}\text{Ga}_{0.3})\text{Se}_{2.5}$ 타겟을 사용하여 제조한 CIGS 전구체 박막을 셀렌화 했을 때 박막내에 CIGS 상과 OVC 상이 고르게 분포하고 있음을 나타낸다. 셀렌화 분위기의 셀레늄 함량과 상관없이, 일반적으로 $\text{Cu}_{0.9}(\text{In}_{0.7}\text{Ga}_{0.3})\text{Se}_{2.5}$ 타겟을 사용해서 제조한 CIGS 태양전지의 개방 전압은 $\text{Cu}_{0.9}(\text{In}_{0.7}\text{Ga}_{0.3})\text{Se}_2$ 타겟을 사용하여 제조한 CIGS 태양전지의 개방 전압보다 컸다. 하지만 셀렌화 분위기의 셀레늄 함량을 감소시킴에 따라 $\text{Cu}_{0.9}(\text{In}_{0.7}\text{Ga}_{0.3})\text{Se}_{2.5}$ 타겟을 사용해서 제조한 CIGS 태양전지의 개방전압은 감소 하는 경향을 나타냈다.

마지막으로 나노결정 CIGS 전구체 박막을 셀렌화 했을 때의 CIGS 박막 특성들을 살펴 보았다. 본 실험에서는 선행실험에서 큰 개방전압이 달성되어 고효율이 기대되는 $\text{Cu}_{0.9}(\text{In}_{0.7}\text{Ga}_{0.3})\text{Se}_{2.5}$ 의 공칭 조성 타겟을 사용 하였으며, 60°C 부터 150°C 까지의 다양한 온도에서 CIGS 전구체 박막을 증착하였다. 증착된 박막의 XRD 패턴과 TEM 사진 분석을 통해 나노결정 CIGS 박막이 120°C 와 130°C 에서 형성 되었음을 확인하였다. 이러한 나노결정 CIGS 전구체 박막들을 475°C 에서 30분 동안 셀렌화 하였고, 셀렌화 후 박막들은 (112) 우선 배향성을 나타냈다. 전구체 박막의 증착 온도에 상관없이, 셀렌화된 CIGS 박막들은 모두 비슷한 조성을

가졌으며, 정량 조성에 비해 Cu 함량이 적고, (In+Ga) 함량이 많았다. 다만 분광법에 의해 이 CIGS 박막들은 모두 개방전압의 손실을 줄일 것으로 기대되는 OVC 상을 포함 하고 있음을 확인 하였다. 특히, 나노결정 CIGS 전구체 박막을 셀레늄 함량을 증가시킨 분위기에서 셀렌화 하였을 때, 결정립이 크며 평탄하고 밀도가 높은 표면 형상을 나타냈다. 또한 상온에서 증착된 비정질 CIGS 전구체 박막의 경우 보다 나노 결정 CIGS 전구체 박막을 사용했을 때 더욱 얇은 MoSe₂층이 형성되었다. 본 연구에서 가장 높은 광전변환 효율은 130℃ 에서 증착된 나노결정 CIGS 전구체 박막을 사용해서 제조한 CIGS 태양전지로부터 달성되었으며, 0.571V 의 개방전압, 26.58 mA/cm² 의 단락전류밀도, 53.28%의 충전율과 함께 8.09%의 광전변환효율이 달성되었다. 이러한 결과는 OVC 상의 존재, MoSe₂ 층의 감소, 평탄한 표면 형상 및 큰 결정립들로 이루어진 밀도가 높은 박막 형성에 의한 결합 밀도의 감소 등이 태양전지 효율을 향상시키는 이로운 요인들로 작용했기 때문으로 사료된다.

주요어: CIGS 박막형 태양전지, 단일 사성분계 CIGS 타겟, 셀렌화, 나노결정 CIGS 전구체 박막, ordered vacancy compound (OVC) 상, ZnS, MgF₂, 무반사 코팅, 광학 상수, RF 마그네트론 스퍼터링, Al-doped ZnO, 기판온도, 산소분압, DC 마그네트론 스퍼터링.

학 번 : 2007-30808



저작자표시-비영리-동일조건변경허락 2.0 대한민국

이용자는 아래의 조건을 따르는 경우에 한하여 자유롭게

- 이 저작물을 복제, 배포, 전송, 전시, 공연 및 방송할 수 있습니다.
- 이차적 저작물을 작성할 수 있습니다.

다음과 같은 조건을 따라야 합니다:



저작자표시. 귀하는 원저작자를 표시하여야 합니다.



비영리. 귀하는 이 저작물을 영리 목적으로 이용할 수 없습니다.



동일조건변경허락. 귀하가 이 저작물을 개작, 변형 또는 가공했을 경우에는, 이 저작물과 동일한 이용허락조건하에서만 배포할 수 있습니다.

- 귀하는, 이 저작물의 재이용이나 배포의 경우, 이 저작물에 적용된 이용허락조건을 명확하게 나타내어야 합니다.
- 저작권자로부터 별도의 허가를 받으면 이러한 조건들은 적용되지 않습니다.

저작권법에 따른 이용자의 권리는 위의 내용에 의하여 영향을 받지 않습니다.

이것은 [이용허락규약\(Legal Code\)](#)을 이해하기 쉽게 요약한 것입니다.

[Disclaimer](#)

공학박사 학위논문

**Characteristics of Cu(In,Ga)Se₂
Thin Film Solar Cells Fabricated by
RF Sputtering of Single CIGS Targets**

**CIGS 단일 타겟의 RF 스퍼터링에 의해 제조된
Cu(In,Ga)Se₂ 박막형 태양전지의 특성**

2014년 2월

서울대학교 대학원

재료공학부

정 성 목

Characteristics of Cu(In,Ga)Se_2 Thin Film Solar Cells Fabricated by RF Sputtering of Single CIGS Targets

CIGS 단일 타겟의 RF 스퍼터링에 의해 제조된
 Cu(In,Ga)Se_2 박막형 태양전지의 특성

지도 교수 유 상 임

이 논문을 공학박사 학위논문으로 제출함
2014 년 2 월

서울대학교 대학원
재료공학부
정 성 목

정성목의 박사 학위논문을 인준함
2014 년 2 월

위 원 장 박 병 우 (인)

부위원장 유 상 임 (인)

위 원 박 찬 (인)

위 원 김 영 환 (인)

위 원 조 소 혜 (인)

Abstract

Characteristics of Cu(In,Ga)Se₂ Thin Film Solar Cells Fabricated by RF Sputtering of Single CIGS Targets

Sung-Mok Jung

Department of Materials Science and Engineering

The Graduate School

Seoul National University

Solar cells have attracted great attention with the increase of problems such as an energy crisis and an environmental pollution. Particularly, thin film solar cells have been extensively investigated due to their small consumption of raw materials and possibility of lightweight. Among them, Cu(In,Ga)Se₂ (CIGS) solar cell has attracted worldwide attention due to its merits of high conversion efficiency and stability. However, a very complicated fabrication process, so-called three-stage co-evaporation process, is required for the achievement of the highest conversion efficiency of ~20%. In addition, this method has a difficulty to produce large-area film with uniform composition.

In this thesis, the properties of CIGS films and CIGS solar cells prepared by RF sputtering of single CIGS targets were investigated. In addition, antireflection (AR) coating and transparent conducting Al-doped ZnO (AZO) films was studied, which are necessary to enhance efficiency. The major

results are as in the following.

First, multi-layer antireflection (AR) coatings such as double- and triple-layer with ZnS and MgF₂ were investigated. For this study, ZnS and ZnS-MgF₂ composite films were prepared on soda-lime glass substrates and their optical constants were determined by envelope method. And MgF₂ film was deposited on GaAs substrate by rf magnetron sputtering and their optical constants were determined by spectroscopic ellipsometry. In particular, ZnS-MgF₂ composite films were fabricated by co-sputtering of ZnS and MgF₂ target to obtain intermediate refractive index material for a middle layer in the triple-layer AR coating and these films exhibited the desired intermediate refractive index. All films were highly transparent in the range from visible and near-infrared (IR). In the case of ZnS-MgF₂ composite film, optical absorption edge was continuously shifted to short wavelength and refractive index decreased with increasing concentration of Mg and F. Based on the extracted optical constants, single-, double- and triple-layer AR coatings on GaAs substrates were designed by using a quarter-wave thickness at a normal incidence and fabricated by rf magnetron sputtering. The experimental results of AR coating were compared to simulated results. Low reflectance could be obtained from single-layer AR coating only at a specific wavelength and could be obtained from multi-layer AR coating at wide wavelength regime. Additionally, incident angle dependence of the reflectance of the multi-layer AR coatings was also investigated and showed different behavior according to a number of layers.

Second, the characteristics of the transparent conducting Al-doped ZnO (AZO) films were investigated. Al-doped ZnO films were deposited on soda-

lime glass substrates by using dc magnetron sputtering as a function of argon gas pressure, O₂/Ar gas ratio and substrate temperature, and their electrical and optical properties were investigated. As a result, the resistivity of the AZO films decreased with decreasing argon gas pressure or O₂/Ar gas ratio. As the substrate temperature was increased, resistivity decreased continuously and the lowest value of resistivity was obtained at the temperature of 250 °C in pure Ar and 250-300 °C in O₂/Ar ratio of 1.23%, respectively. The higher substrate temperature increased the resistivity a little. The transmittance was found to be very sensitive to O₂/Ar gas ratio and substrate temperature. Addition of a very small amount of oxygen to argon (1.23% of O₂/Ar ratio) or slight increase of the substrate temperature from room temperature to 150 °C enhanced the transmittance in visible region remarkably. Conclusively, the AZO films with low resistivity of order of 10⁻⁴ Ωcm and high transparency in visible region could be prepared at the substrate temperatures of above 150 °C (the lowest resistivity of 3.19 × 10⁻⁴ Ωcm at 250 °C) by dc magnetron sputtering and these films are applicable to various fields which require transparent conducting oxide films as well as solar cell field.

Third, the properties of CIGS absorber layers prepared by RF sputtering without selenization were investigated. For this study, various single CIGS sputtering targets with the nominal compositions of Cu_x(In_{0.7}Ga_{0.3})Se_y (x=0.95~1, y=2~2.5) were fabricated. Employing these targets, CIGS films were deposited on Mo coated soda lime glass (SLG) substrates by using RF magnetron sputtering. When the CIGS precursor film deposited at room temperature using a stoichiometric CIGS target was annealed in an Ar atmosphere, grain growth of the CIGS film did not occur regardless of the

post-annealing temperature. Grain size of the CIGS films was increased with increasing a deposition temperature. However, rough and porous surface morphology with the faceted grains was obtained and therefore very low efficiencies were achieved. For enhancing the efficiency and obtaining the smooth surface morphology, various CIGS targets with the nominal compositions of $\text{Cu}_{0.95}(\text{In}_{0.7}\text{Ga}_{0.3})\text{Se}_{2.5}$ and $\text{Cu}_{0.95}(\text{In}_{0.7}\text{Ga}_{0.3})\text{Se}_{2.1}$ were used to fabricate CIGS absorber layer. Grain size of these films was smaller than that of the CIGS film fabricated using a stoichiometric CIGS target. This result is thought to be caused by Cu-poor composition of these CIGS targets. Although the CIGS films with a smoother surface morphology can be obtained by using Cu-poor CIGS targets, surface morphology becomes rough with increasing deposition temperature. Conversion efficiency of about 2% was obtained from the CIGS solar cell fabricated using the $\text{Cu}_{0.95}(\text{In}_{0.7}\text{Ga}_{0.3})\text{Se}_{2.5}$ target. However, the CIGS solar cells fabricated using the $\text{Cu}_{0.95}(\text{In}_{0.7}\text{Ga}_{0.3})\text{Se}_{2.1}$ target, containing the smaller quantity of Se, showed the lower conversion efficiency. Meanwhile, for supplement of selenium, CIGS films fabricated by using the single target of $\text{Cu}(\text{In}_{0.7}\text{Ga}_{0.3})\text{Se}_{2.5}$ powder were annealed in Ar atmosphere with selenium. These films showed the densely packed surface morphology. Conversion efficiency of the solar cells fabricated using these CIGS films was enhanced. Consequentially, selenization process is beneficial to improvement of structural and electrical properties. Hence, in the next study, the effect of selenization of CIGS precursor film was systematically investigated.

Finally, the characteristics of CIGS absorber layers after selenization of CIGS precursor film deposited at room temperature were systematically investigated. In this study, the CIGS targets with various compositions of

$\text{Cu}_x(\text{In}_{0.7}\text{Ga}_{0.3})\text{Se}_y$ (where $x=0.9, 1; y=2, 2.2, 2.5$) were fabricated. Utilizing these targets, the CIGS precursor films were produced by RF magnetron sputtering at room temperature. The CIGS precursor films were then selenized in a tube furnace under Se atmosphere using Se powder. From the stoichiometric CIGS target, Cu-rich CIGS films were obtained and very low conversion efficiencies were achieved due to inappropriate composition and porous and rough surface morphology with large grains. In contrast, the CIGS films fabricated by using the Cu-poor CIGS target showed the device-quality stoichiometry ratio and densely packed surface morphology with small grains, as well as the chalcopyrite structure without the second phases. Increase of the Se content in the single CIGS target led to decrease of the Cu content and increase of the (In+Ga) content in the CIGS film, which created the ordered vacancy compound (OVC) phases and increased the band gap (E_g) of the CIGS film resulting in increase of the open-circuit voltage (V_{oc}). The difference between $E_g/q - 0.5\text{V}$ and V_{oc} was remarkably decreased with the formation of the OVC phases. The highest efficiency of 6.88% could be achieved from the CIGS solar cell fabricated by using the Cu-poor and Se-excess target with the nominal composition of $\text{Cu}_{0.9}(\text{In}_{0.7}\text{Ga}_{0.3})\text{Se}_{2.2}$. Consequently, the composition of the single CIGS target was found to play a key role in the structural and electrical properties of the CIGS film and CIGS thin film solar cell efficiency.

Characteristics of CIGS films selenized using mixing powders with various weight ratios of alumina to selenium were investigated. For this experiment, the CIGS precursor films were deposited using the single CIGS targets with the nominal compositions of $\text{Cu}_{0.9}(\text{In,Ga})\text{Se}_2$ and $\text{Cu}_{0.9}(\text{In,Ga})\text{Se}_{2.5}$. As the

results, regardless of target composition, grain size was increased with increasing the Se ratio of mixing powder. The MoSe₂ layer was formed between the CIGS and the Mo layer and its thickness was also increased with increasing the Se ratio of mixing powder. The MoSe₂-layer thickness of the CIGS film fabricated using the Cu_{0.9}(In_{0.7}Ga_{0.3})Se_{2.5} target is thicker than that of the CIGS film fabricated using the Cu_{0.9}(In_{0.7}Ga_{0.3})Se₂ target because of larger amount of Se in the CIGS film fabricated using the Cu_{0.9}(In_{0.7}Ga_{0.3})Se_{2.5} target. From the auger electron spectroscopy (AES) depth profiles after selenization of the CIGS films, it was found that each element of the CIGS film was evenly distributed in the CIGS films without grading of elements. This means that the CIGS phases including the OVC phase in the CIGS film fabricated using Cu_{0.9}(In_{0.7}Ga_{0.3})Se_{2.5} target are evenly distributed. The open-circuit voltages of the CIGS solar cells fabricated using the Cu_{0.9}(In_{0.7}Ga_{0.3})Se_{2.5} target were generally higher than those of solar cells fabricated using the Cu_{0.9}(In_{0.7}Ga_{0.3})Se₂ target. However, the open-circuit voltage of the CIGS solar cells fabricated using the Cu_{0.9}(In_{0.7}Ga_{0.3})Se_{2.5} target was decreased with decreasing Se ratio of mixing powder used for selenization.

Also, characteristics of CIGS films selenized using nanocrystalline precursor film were investigated. CIGS films were deposited at various temperatures using a single quaternary Cu_{0.9}(In_{0.7}Ga_{0.3})Se_{2.5} target. Based on the results of XRD patterns and TEM images, as-deposited CIGS films fabricated at the temperatures of 120 °C and 130 °C were considered as the nano-crystalline CIGS precursor films and selenized at 475 °C for 30min. The CIGS films showed a (112) preferred orientation. All of the selenized CIGS films had the

similar composition regardless of deposition temperature although Cu content in the film was slightly different. From the Raman spectra of the CIGS films, the existence of OVC phase which can lead to decrease of open-circuit voltage loss was identified. The CIGS film with smooth and dense surface morphology as well as the large grain size was obtained by increase of Se ratio in a tube furnace and using the nano-crystalline CIGS precursor film. And the thickness of the MoSe₂ layer was decreased after selenization of the nano-crystalline CIGS precursor film compared to that of the amorphous CIGS precursor film. The highest efficiency was achieved from the CIGS solar cell fabricated using the nanocrystalline CIGS precursor film deposited at 130 °C and its value is 8.09 % with the open-circuit voltage of 0.571V, short-circuit current density of 26.58 mA/cm² and the fill factor of 53.28%. This result is thought to be achieved by the beneficial factors such as the existence of an OVC phase, the thickness reduction of a MoSe₂ layer, smooth surface morphology and the decrease of defect density achieved by dense CIGS film with large grain.

Keywords: CIGS thin film solar cell, single quaternary CIGS target, selenization, nanocrystalline CIGS precursor film, Orderd vacancy compound, Zinc sulfide, Magnesium fluoride, Antireflection coating, Optical constants, RF magnetron sputtering, Al-doped ZnO, Substrate temperature, Oxygen partial pressure, DC magnetron sputtering

Student Number: 2007-30808

Contents

List of Tables and Figures	xi
Chapter 1 General Background.....	1
1.1 Historical reviews on solar cells.....	1
1.2 CIGS thin film solar cell.....	2
1.2.1 Growth process of CIGS film	2
1.2.1.1 Three-stage co-evaporation process	2
1.2.1.2 Two step process	4
1.2.1.3 Other deposition processes.....	4
1.3 Architecture of CIGS solar cells.....	5
1.3.1 Architecture	5
1.3.1.1 CIGS absorber layer	5
1.3.1.2 Buffer layer.....	6
1.3.1.3 Window layer.....	7
1.3.1.4 Electrode (bottom, top).....	8
Chapter 2 Design and fabrication of multi-layer antireflection coating for III-V solar cell	20
2.1 Introduction	20
2.2 Experimental.....	21
2.3 Results and discussion.....	23
2.4 Summary.....	26
Chapter 3 Characteristics of transparent conducting Al-doped ZnO films prepared by dc magnetron sputtering....	36

2.1	Introduction	36
2.2	Experimental	37
2.3	Results and discussion.....	38
2.4	Summary.....	43
Chapter 4	CIGS absorber layers prepared by RF sputtering without selenization for CIGS solar cells.....	59
4.1	Introduction	59
4.2	Experimental.....	59
4.3	Results and discussion.....	62
4.3.1	CIGS layers prepared using the single CIGS targets of various compositions.....	62
4.3.2	CIGS layers prepared using the single target of Cu(In _{0.7} Ga _{0.3})Se _{2.5} powder.....	64
4.4	Summary.....	66
Chapter 5	CIGS absorber layers prepared by RF sputtering with selenization for CIGS solar cells	83
5.1	Introduction	83
5.2	Experimental.....	85
5.3	Results and discussion.....	87
5.3.1	CIGS layers prepared using the single CIGS targets of various compositions	87
5.3.1.1	A CIGS target with the nominal composition of Cu(In _{0.7} Ga _{0.3})Se ₂	87
5.3.1.2	A Cu-poor CIGS target with the nominal composition of Cu _{0.9} (In _{0.7} Ga _{0.3})Se ₂	89

5.3.1.3 A Cu-poor and a Se-excess CIGS targets with the nominal compositions of $\text{Cu}_{0.9}(\text{In}_{0.7}\text{Ga}_{0.3})\text{Se}_{2.2}$ and $\text{Cu}_{0.9}(\text{In}_{0.7}\text{Ga}_{0.3})\text{Se}_{2.5}$	92
5.3.2 Effect of selenization condition on the CIGS layers	95
5.3.3 CIGS layers prepared using nanocrystalline precursor film	100
5.4 Summary.....	106
Chapter 6 Summary.....	148
Publications.....	154
Abstract in Korean.....	156

List of Tables

Table. 1.1. Experimental details for coating of CdS layer.....	15
Table. 3.1. Optical band gap values of the AZO films deposited at various process parameters.	47
Table. 4.1. Summary of conversion efficiencies shown in Fig. 4.13.....	69
Table 5.1. Composition of the CIGS films fabricated using a stoichiometric CIGStarget.	112
Table 5.2. Composition of the CIGS films fabricated using a Cu-poor CIGS target ($\text{Cu}_{0.9}(\text{In}_{0.7}\text{Ga}_{0.3})\text{Se}_2$).	113
Table 5.3. Composition of the CIGS films fabricated using Se-excess CIGS targets with a Cu-poor composition.	114
Table 5.4. Summary of efficiency of the CIGS solar cells fabricated in this study. (As a function of target composition and selenization temperature). .	115
Table 5.5. Composition before and after selenization of CIGS precursor films deposited using the single CIGS targets with the nominal compositions of (a) $\text{Cu}_{0.9}(\text{In,Ga})\text{Se}_2$ and (b) $\text{Cu}_{0.9}(\text{In,Ga})\text{Se}_{2.5}$. The CIGS films were selenized using mixing powders with various weight ratios of alumina to selenium... .	116
Table 5.6. Summary of the conversion efficiencies shown in Fig. 5.17.....	117

Table 5.7. Intensity ratio of the CIGS films shown in Fig. 5.19.	118
Table 5.8. Composition before and after selenization of the CIGS precursor films deposited at (a) room temperature, (b) 120 and (c) 130 °C.....	119
Table 5.9. RMS roughness of the CIGS films shown in Fig. 5.25.....	120
Table 5.10. Summary of the conversion efficiencies shown in Fig. 5.26.....	121

List of Figures

Fig. 1.1. Best research-cell efficiencies chart for various photovoltaic technologies, which is compiled by National Renewable Energy Laboratory (NREL).....	16
Fig. 1.2. Schematic of three-stage co-evaporation process.....	17
Fig. 1.3. Cross-sectional schematic of a CIGS solar cell.....	18
Fig. 1.4. Experimental procedure for coating of the CdS layer.....	19
Fig. 2.1. Transmittance spectra of ZnS and ZnS-MgF ₂ films on SLG substrates depending on wavelength.....	30
Fig. 2.2. (a) Refractive index and (b) extinction coefficient of ZnS-MgF ₂ composite films depending on rf power applied to MgF ₂ . Optical constants of pure ZnS and MgF ₂ were also exhibited.....	31
Fig. 2.3. EPMA results and refractive index variation at the wavelength of 632 nm for ZnS-MgF ₂ composite films depending on rf power applied to MgF ₂	32
Fig. 2.4. Simulated reflectance spectra of GaAs substrate with single-, double- and triple-layer antireflection coating depending on wavelength. All structures are designed by quarter-wave coating at a reference wavelength of 600 nm. Reflectance spectra were theoretically calculated by Essential Macleod program.....	33
Fig. 2.5. Measured (solid line) and simulated (dash line) reflectance spectra of	

GaAs substrate with (a) single-layer (b) double-layer and (c) triple-layer antireflection coating. ZnS50W-MgF₂140W composite film was used as intermediate refractive index material in triple-layer AR coating..... 34

Fig. 2.6. Simulated reflectance spectra of (a) double-layer and (b) triple-layer AR coating as a function of incident angle. 35

Fig. 3.1. (a) Resistivity, (b) carrier concentration and Hall mobility of the AZO films deposited at various argon gas pressures. 48

Fig. 3.2. FE-SEM images of the AZO films deposited at argon gas pressures of (a) 3 mTorr, (b) 5 mTorr, (c) 10 mTorr and (d) 15 mTorr..... 49

Fig. 3.3. Optical transmittance spectra of the AZO films depending on argon gas pressure in the visible and near-infrared wavelength region. 50

Fig. 3.4. (a) Resistivity and (b) transmittance of the AZO films deposited at room temperature with various O₂/Ar gas ratios..... 51

Fig. 3.5. XRD patterns of the AZO films deposited at room temperature with various O₂/Ar gas ratios. 52

Fig. 3.6. (a) Resistivity, (b) carrier concentration and Hall mobility of the AZO films depending on the substrate temperature..... 53

Fig. 3.7. FE-SEM images of the AZO films deposited at substrate temperature of (a) room temperature, (b) 150 °C, (c) 200 °C, (d) 250 °C, (e) 300 °C and (f) 350 °C under pure argon gas pressure..... 54

Fig. 3.8. Transmittance spectra of the AZO films deposited at various temperatures in (a) pure Ar and (b) O ₂ /Ar gas ratio of 1.23%	55
Fig. 3.9. (a) Resistivity, (b) carrier concentration and Hall mobility of the AZO films deposited at 250 °C with various O ₂ /Ar gas ratios.	56
Fig. 3.10. Transmittance spectra of the AZO films deposited at 250 °C with various O ₂ /Ar gas ratios.	57
Fig. 3.11. Optical band gap of the AZO films deposited at various substrate temperatures in (a) pure Ar and (b) O ₂ /Ar gas ratio of 1.23%	58
Fig. 4.1. Surface morphology of the CIGS film deposited at (a) room temperature and the CIGS films annealed at (b) 400 °C (c) 500 °C and (d) 600 °C in an Ar atmosphere. The CIGS film was fabricated using a stoichiometric CIGS (Cu(In _{0.7} Ga _{0.3})Se ₂) target.	70
Fig. 4.2. Surface morphology of the CIGS films deposited at (a) room temperature, (b) 300 °C, (c) 350 °C, (d) 400 °C and (e) 450 °C. The CIGS film was fabricated using a stoichiometric CIGS (Cu(In _{0.7} Ga _{0.3})Se ₂) target.	71
Fig. 4.3. Current-voltage characteristics of the CIGS solar cells fabricated using a stoichiometric CIGS (Cu(In _{0.7} Ga _{0.3})Se ₂) target. The CIGS absorber layers were deposited at the temperatures of 300, 350, 400 and 450 °C, respectively.	72
Fig. 4.4. Surface morphology and cross-sectional image of the CIGS films fabricated using a Cu _{0.95} (In _{0.7} Ga _{0.3})Se _{2.5} target. The CIGS film was deposited at 300 °C.	73

Fig. 4.5. Surface morphology of the CIGS films deposited at (a) 300 °C, (b) 350 °C, (c) 400 °C and (d) 450 °C. The CIGS film was fabricated using a $\text{Cu}_{0.95}(\text{In}_{0.7}\text{Ga}_{0.3})\text{Se}_{2.1}$ target.....	74
Fig. 4.6. XRD patterns of the CIGS films fabricated using $\text{Cu}_{0.95}(\text{In}_{0.7}\text{Ga}_{0.3})\text{Se}_{2.5}$ and $\text{Cu}_{0.95}(\text{In}_{0.7}\text{Ga}_{0.3})\text{Se}_{2.1}$ target.	75
Fig. 4.7. Current-voltage characteristics of the CIGS solar cells fabricated using the $\text{Cu}_{0.95}(\text{In}_{0.7}\text{Ga}_{0.3})\text{Se}_{2.5}$ and $\text{Cu}_{0.95}(\text{In}_{0.7}\text{Ga}_{0.3})\text{Se}_{2.1}$ target. The CIGS absorber layers were deposited at the temperatures of 300 °C and 350 °C, respectively.	76
Fig. 4.8. Ternary phase diagram of the CIGS targets and the CIGS films fabricated using these CIGS targets	77
Fig. 4.9. Surface morphology of the CIGS films deposited at (a) room temperature (b) 350 °C, (c) 400 °C, (d) 450 °C and (e) 500 °C. The CIGS film was fabricated using the single target of $\text{Cu}(\text{In}_{0.7}\text{Ga}_{0.3})\text{Se}_{2.5}$ powder.....	78
Fig. 4.10. Surface morphology after selenization of the CIGS films deposited at (a) room temperature (b) 350 °C, (c) 400 °C, (d) 450 °C and (e) 500 °C. The CIGS film was fabricated using the single target of $\text{Cu}(\text{In}_{0.7}\text{Ga}_{0.3})\text{Se}_{2.5}$ powder.	79
Fig. 4.11. XRD patterns (a) before and (b) after selenization of the CIGS films deposited at room temperature, 350, 400, 450 and 500 °C. The CIGS film was fabricated using the single target of $\text{Cu}(\text{In}_{0.7}\text{Ga}_{0.3})\text{Se}_{2.5}$ powder.	80

Fig. 4.12. (a) Resistivity before and after selenization of the CIGS film as a function of deposition temperature. And Hall resistance after selenization of the CIGS films deposited at (b) 400 °C and (c) 450 °C. 81

Fig. 4.13. Current-voltage characteristics of the CIGS solar cells fabricated using the single target of $\text{Cu}(\text{In}_{0.7}\text{Ga}_{0.3})\text{Se}_{2.5}$ powder. The solar cell A, B, C, D and E are fabricated after selenization CIGS precursor films deposited at the temperatures of 400, 450, 475 and 500 °C, respectively. 82

Fig. 5.1. FE-SEM images of the CIGS films (a) as-deposited and selenized at (b) 350 °C, (c) 375 °C, (d) 400 °C, (e) 425 °C and (f) 450 °C. CIGS precursor films were fabricated using a stoichiometric CIGS target and then selenized at various temperatures. 122

Fig. 5.2. XRD patterns of as-deposited and selenized CIGS films. CIGS precursor films were fabricated using a stoichiometric CIGS target and then selenized at the temperatures from 300 to 450 °C..... 123

Fig. 5.3. Current-voltage characteristics of the CIGS solar cells fabricated using a stoichiometric CIGS target. The solar cell A and B are fabricated using the CIGS absorber layers selenized at the temperatures of 400 and 450 °C, respectively..... 124

Fig. 5.4. FE-SEM images of the CIGS films (a) as-deposited and selenized at (b) 400 °C, (c) 450 °C, (d) 475 °C and (e) 500 °C. CIGS precursor films were fabricated using a Cu-poor CIGS target and then selenized at various temperatures. 125

Fig. 5.5. XRD patterns of as-deposited and selenized CIGS films. CIGS

precursor films were fabricated using a Cu-poor CIGS target and then selenized at the temperatures from 400 to 500 °C..... 126

Fig. 5.6. Composition mapping images of the CIGS film selenized at the temperature of 400 °C. 127

Fig. 5.7. Current-voltage characteristics of the CIGS solar cells fabricated using a Cu-poor CIGS target. The solar cell C, D, E and F are fabricated using the CIGS absorber layers selenized at the temperatures of 400, 450, 475 and 500 °C, respectively. 128

Fig. 5.8. FE-SEM images after selenization of the CIGS precursor films fabricated using (a) $\text{Cu}_{0.9}(\text{In}_{0.7}\text{Ga}_{0.3})\text{Se}_2$, (b) $\text{Cu}_{0.9}(\text{In}_{0.7}\text{Ga}_{0.3})\text{Se}_{2.2}$ and (c) $\text{Cu}_{0.9}(\text{In}_{0.7}\text{Ga}_{0.3})\text{Se}_{2.5}$ targets. All of the films are selenized at the temperature of 475 °C for 30minutes. 129

Fig. 5.9. (a) Current-voltage characteristics and (b) normalized quantum efficiency of the CIGS solar cells fabricated using various CIGS targets. (c) Band gap determination from EQE data. (d) A plot of V_{oc} versus band gap (E_g). The solar cell E, G and H are fabricated by using $\text{Cu}_{0.9}(\text{In,Ga})\text{Se}_2$, $\text{Cu}_{0.9}(\text{In,Ga})\text{Se}_{2.2}$ and $\text{Cu}_{0.9}(\text{In,Ga})\text{Se}_{2.5}$ target, respectively. 130

Fig. 5.10. XRD patterns after selenization of the CIGS precursor films fabricated using $\text{Cu}_{0.9}(\text{In}_{0.7}\text{Ga}_{0.3})\text{Se}_2$, $\text{Cu}_{0.9}(\text{In}_{0.7}\text{Ga}_{0.3})\text{Se}_{2.2}$ and $\text{Cu}_{0.9}(\text{In}_{0.7}\text{Ga}_{0.3})\text{Se}_{2.5}$ targets. All of the films are selenized at the temperature of 475 °C for 30minutes. 131

Fig. 5.11. FE-SEM images of the (a) as-deposited CIGS film and the CIGS films selenized using mixing powders with weight ratios of alumina to

selenium of (b) 0:0, (c) 12:1, (d) 8:1, (e) 6:1 and (f) 4:1. The CIGS precursor film was fabricated using a single quaternary CIGS target with the nominal compositions of $\text{Cu}_{0.9}(\text{In}_{0.7}\text{Ga}_{0.3})\text{Se}_2$ 132

Fig. 5.12. FE-SEM images of the (a) as-deposited CIGS film and the CIGS films selenized using mixing powders with weight ratios of alumina to selenium of (b) 0:0, (c) 12:1, (d) 8:1, (e) 6:1 and (f) 4:1. The CIGS precursor film was fabricated using a single quaternary CIGS target with the nominal compositions of $\text{Cu}_{0.9}(\text{In}_{0.7}\text{Ga}_{0.3})\text{Se}_{2.5}$ 133

Fig. 5.13. XRD patterns before and after selenization of the CIGS precursor films fabricated using the single quaternary CIGS targets with the nominal compositions of (a) $\text{Cu}_{0.9}(\text{In}_{0.7}\text{Ga}_{0.3})\text{Se}_2$ and (b) $\text{Cu}_{0.9}(\text{In}_{0.7}\text{Ga}_{0.3})\text{Se}_{2.5}$. The CIGS films were selenized using mixing powders with the weight ratios of alumina to selenium of 0:0, 12:1, 8:1, 6:1 and 4:1, respectively. 134

Fig. 5.14. Raman spectra after selenization of the CIGS films fabricated using the single quaternary CIGS targets with the nominal compositions of $\text{Cu}_{0.9}(\text{In}_{0.7}\text{Ga}_{0.3})\text{Se}_2$ and $\text{Cu}_{0.9}(\text{In}_{0.7}\text{Ga}_{0.3})\text{Se}_{2.5}$. The CIGS films were selenized using mixing powders with the weight ratio of alumina to selenium of 8:1 ... 135

Fig. 5.15. Auger electron spectroscopy (AES) depth profiles after selenization of the CIGS films fabricated using the single quaternary CIGS targets with the nominal compositions of (a) $\text{Cu}_{0.9}(\text{In}_{0.7}\text{Ga}_{0.3})\text{Se}_2$ and (b) $\text{Cu}_{0.9}(\text{In}_{0.7}\text{Ga}_{0.3})\text{Se}_{2.5}$. The CIGS films were selenized using mixing powders with the weight ratio of alumina to selenium of 8:1. 136

Fig. 5.16. Photoluminescence (PL) spectra after selenization of the CIGS films fabricated using the single quaternary CIGS targets with the nominal

compositions of $\text{Cu}_{0.9}(\text{In}_{0.7}\text{Ga}_{0.3})\text{Se}_2$ and $\text{Cu}_{0.9}(\text{In}_{0.7}\text{Ga}_{0.3})\text{Se}_{2.5}$. The CIGS films were selenized using mixing powders with the weight ratio of alumina to selenium of 8:1. 137

Fig. 5.17. Current-voltage characteristics of the CIGS solar cells fabricated using the single CIGS targets with the nominal compositions of (a) $\text{Cu}_{0.9}(\text{In,Ga})\text{Se}_2$ and (b) $\text{Cu}_{0.9}(\text{In,Ga})\text{Se}_{2.5}$. Detail conditions and values of the sample A to H are in table 5.6. 138

Fig. 5.18. (a) Linear scale and (b) logarithmic scale XRD patterns of the as-deposited CIGS films deposited at various temperatures using a single quaternary $\text{Cu}_{0.9}(\text{In}_{0.7}\text{Ga}_{0.3})\text{Se}_{2.5}$ target. 139

Fig. 5.19. (a), (c) TEM bright-field images and (b), (d) high resolution TEM images of the CIGS precursor films deposited at 120 and 130 °C. And Fast Fourier Transformation (FFT) patterns of region (1) and (2) in figure (d). .. 140

Fig. 5.20. XRD patterns of the CIGS films selenized using mixing powders with the weight ratios of alumina to selenium of (a)(b) 8:1, (c)(d) 6:1 and (e)(f) 4:1. 141

Fig. 5.21. Raman spectra of the CIGS films selenized using mixing powders with the weight ratios of alumina to selenium of (a) 8:1 and (b) 4:1 142

Fig. 5.22. FE-SEM images of the (a) as-deposited CIGS film deposited at room temperature and the CIGS films selenized using mixing powders with weight ratios of alumina to selenium of (b) 8:1, (c) 6:1 and (d) 4:1. CIGS precursor films were fabricated using a single quaternary CIGS target with the nominal composition of $\text{Cu}_{0.9}(\text{In}_{0.7}\text{Ga}_{0.3})\text{Se}_{2.5}$ 143

Fig. 5.23. FE-SEM images of the (a) as-deposited CIGS film deposited at 120 °C and the CIGS films selenized using mixing powders with weight ratios of alumina to selenium of (b) 8:1, (c) 6:1 and (d) 4:1. CIGS precursor films were fabricated using a single quaternary CIGS target with the nominal composition of $\text{Cu}_{0.9}(\text{In}_{0.7}\text{Ga}_{0.3})\text{Se}_{2.5}$ 144

Fig. 5.24. FE-SEM images of the (a) as-deposited CIGS film deposited at 130 °C and the CIGS films selenized using mixing powders with weight ratios of alumina to selenium of (b) 8:1, (c) 6:1 and (d) 4:1. CIGS precursor films were fabricated using a single quaternary CIGS target with the nominal composition of $\text{Cu}_{0.9}(\text{In}_{0.7}\text{Ga}_{0.3})\text{Se}_{2.5}$ 145

Fig. 5.25. (a) RMS roughness and (b) AFM image of the CIGS films as a function of deposition temperature and selenization condition with various weight ratios of alumina to selenium. Details for the deposition temperature and weight ratio of alumina to selenium are given in the figure. 146

Fig. 5.26. Current-voltage characteristics of the CIGS solar cells fabricated using the CIGS precursor films deposited at (a) room temperature, (b) 120 °C and (c) 130 °C. The CIGS precursor films were selenized using mixing powders with weight ratios of alumina to selenium of 8:1, 6:1 and 4:1, respectively..... 147

Chapter 1. General background

1.1. Historical reviews on solar cells

Recently, solar cells have attracted great attention with the increase of problems such as an energy crisis and an environmental pollution caused by overuse of fossil fuels. The photovoltaic effect was first discovered in an electrolyte solution by Becquerel in 1839. In 1954, the first silicon solar cell with an efficiency of 6% was developed at Bell Labs by Chapin et al. [1]. In the same year, Reynolds et al. [2] reported the solar cell based on $\text{Cu}_2\text{S}/\text{CdS}$ with an efficiency of 6%. GaAs pn junction solar cell of 6% was reported in 1956 by Jenny et al. [3]. Meanwhile, CuInSe_2 (CIS) solar cell, basis of CIGS solar cell, was first fabricated using p-type single crystals of CuInSe_2 in 1974 by Wagner et al. [4]. And first CIS thin film solar cell was reported by Kazmerski et al. using films fabricated by evaporation of CuInSe_2 powder in 1976 [5]. With achieving a conversion efficiency of 9.4% by Boeing in 1981, CIS thin film solar cell began to receive great attention. The efficiencies of these many kinds of solar cells have been gradually enhanced up to the present time. Fig. 1.1 shows the different photovoltaic cell technologies and their respective growth in highest efficiencies from 1977 to 2013. As shown in Fig. 1.1, among all kinds of solar cell, the highest conversion efficiency of 44% has been achieved from the multijunction cells by using $\text{InGaP}/\text{GaAs}/\text{InGaAs}$. Also, from the crystalline Si solar cell, high conversion efficiency of about 25% has been achieved. However, these solar cells are fabricated by using a crystalline substrate and therefore consume

the large amount of raw materials. Solar cells are generally classified as a crystalline solar cell and a thin film solar cell. Especially, thin film solar cells have been extensively investigated by many researchers due to their merits such as small consumption of raw materials and possibility of lightweight. Among thin film solar cells, Cu(In,Ga)Se_2 (CIGS) solar cell has achieved the highest conversion efficiency of ~20% as shown in Fig. 1.1.

1.2. CIGS thin film solar cells

1.2.1 Growth process of CIGS film

The CIGS absorber layers have been grown by using various vacuum and nonvacuum processes. Vacuum processes such as three-stage co-evaporation process and two-step (stage) process have been widely used and the highest conversion efficiency of ~20% has been achieved from CIGS films deposited by a three-stage co-evaporation method. Meanwhile, nonvacuum processes such as electrodeposition and ink-based deposition have been studied due to its merit in terms of cost. Details for the fabrication method of CIGS film are as in the following.

1.2.1.1 Three-stage co-evaporation process

Three-stage co-evaporation method has been extensively studied [7-14] and the high conversion efficiencies above 20% have been achieved from the CIGS solar cell fabricated by using this method [13-15].

This method consists of three stages. First, In-Ga-Se layer is deposited on

Mo coated substrates at substrate temperature of 300~400 °C. Second, Cu-Se layer is deposited on In-Ga-Se layer at substrate temperature of 500~600 °C. In the third stage, In-Ga-Se layer is additionally deposited at the substrate temperature similar to second stage. Finally, the CIGS film with desired composition is formed [8, 12, 13]. In brief, the CIGS compound formation is represented by following equations.

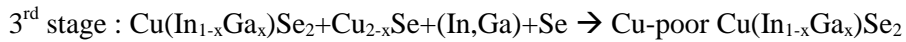
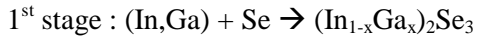


Fig. 1.1 shows the schematic of three-stage co-evaporation process developed by NREL group. The advantage of this method is its considerable flexibility to choose the process specifics and to control film composition and bandgap, allowing solar cells to achieve high efficiency [16]. Also, the CIGS films fabricated using this method show band gap grading caused by graded Ga incorporation as a function of depth [7, 8, 17-19], which lead to enhancement of conversion efficiency. However, good control of the elemental fluxs from each evaporation source is required for obtaining reproducibility. Although CIGS films are deposited by monitoring of flux, film thickness, composition, etc. during deposition, this method may give the difficulty in control. Also this method is difficult to obtain large-area film with uniform composition due to its complicated process and the lack of commercial equipment for large-area thermal evaporation [16].

1.2.1.2 Two-step process

Two-step process consists of deposition of metal precursor film and selenization of the precursor film. Although metal precursor films can be deposited by evaporation [20-23], the precursor films is commonly deposited by sputtering [24-29] such as co-sputtering [24, 25] and sequential sputtering [26-29] using separate elemental targets or metal alloy targets. Also, Cu-In-Ga ternary sputtering target can be used for fabrication of the precursor film [30]. After deposition of the metal precursor film, the film is selenized by using H_2Se gas or Se vapor in the furnace. As another method, after depositing Se onto the metal precursor film, the film is annealed by rapid thermal process (RTP). This two-step process is very attractive because this process enables to obtain the uniform film over large areas although this process has the limited ability to control composition and to increase band gap [31].

1.2.1.3 Other deposition processes (nonvacuum)

Nonvacuum processes have been studied due to its merit in terms of cost. These processes also consist of deposition of precursor film and selenization of the precursor film similar to two step in vacuum process. However, the precursor film is deposited by nonvacuum processes such as electrodeposition [32-34] and ink-based deposition [35-38]. Although these methods have the advantage in terms of reducing material waste, the maximum efficiency of the solar cell fabricated by nonvacuum processes is

lower than that of the solar cell fabricated by vacuum process.

1.3. Architecture of CIGS solar cell

1.3.1 Architecture

CIGS solar cell is composed of various thin film layers as shown in Fig. 1.3. Soda-lime glass (SLG) is commonly used as a substrate. Molybdenum (Mo) and ZnO is used as a bottom electrode and a transparent electrode at front of CIGS solar cell, respectively. CIGS is used as an absorber layer and CdS is used as a buffer layer between CIGS absorber layer and ZnO layer. For the measurement of the solar cell with a small area, metal electrode consisted of Ni and Al is generally used. Details for the each layer are as in the following.

1.3.1.1 CIGS absorber layer

As mentioned in chapter 1.2, the CIGS absorber layer has been generally deposited by a three-stage co-evaporation method. This method is very complicated and uniform film with large area is difficult to obtain; hence, it is not adequate for mass production of CIGS thin films.

In this study, the single quaternary CIGS targets with various compositions were used for fabricating the CIGS absorber layer or CIGS precursor layer by one-step process. This one-step process is very easy to obtain uniformly large-area CIGS films. The CIGS absorber layer was deposited at various temperatures by one-step process without selenization. And also, the CIGS

precursor films were deposited at room temperature and were selenized at various temperatures under Se atmosphere using Se powder.

1.3.1.2 Buffer layer

There is a large difference in a lattice constant and a band gap between the CIGS thin film and the ZnO thin film. Also, CIGS absorber layer can be damaged by the high-energy plasma during deposition of the ZnO layer. Hence, various buffer layers such as CdS, ZnS and InS have been applied between them. Among them, cadmium sulphide (CdS) is mainly used as a buffer layer. CdS has a band gap of 2.46eV and shows the n-type semiconducting property.

In this experiment, the cadmium sulphide was coated on a CIGS absorber layer. As shown in table 1.1, the solution was composed of 355 ml of deionized (D.I.) water (H_2O), 69.5 ml of ammonium hydroxide (NH_4OH), 50 ml of cadmium sulphate hydrate ($0.015\text{ M CdSO}_4 \cdot 8H_2O$) and 25ml of thiourea ($1.5\text{ M NH}_2\text{SCNH}_2$) [39]. These solution components were mixed in a bath at room temperature. And the CIGS film is immersed in the bath containing the solution. The bath containing the CIGS film was placed into a water-heated vessel of $78\text{ }^\circ\text{C}$ during 12 min. After deposition, the substrates were rinsed with D.I. water and dried at $60\text{ }^\circ\text{C}$ for 10min. Fig. 1.4 shows the experimental procedure for coating the CdS layer.

1.3.1.3 Window layer

In general, the ZnO bilayer (i-ZnO and n-ZnO) is used as a window layer. The i-ZnO layer with a high resistivity (HR) of 1~100 Ωcm is deposited on the CdS layer. This layer is necessary to improve the performance of the CIGS solar cell. For large area and polycrystalline devices like CIGS thin film solar cells, the same electronic quality over the entire area cannot be expected. Instead, the recombination can be occurred at grain boundaries or by local shunting paths, which deteriorates the cell performance. The influence of these regions on the cell performance can be reduced by using the i-ZnO layer. The high-resistivity ZnO film provides a local series resistance which prevents electrical inhomogeneities, e.g. sites of locally enhanced recombination, of the CIGS film. As a result, the improvement of the fill factor as well as the open circuit voltage can be achieved by using the i-ZnO layer [40]. Another role of the i-ZnO layer is for the protection from the high-energy plasma damage induced to the CIGS absorber surface and the CdS layer during deposition of the n-type ZnO layer [41]. The thickness of the i-ZnO layer has to be adjusted between about 50nm and 70nm. If i-ZnO layer thickness is greater than these thicknesses, the short circuit current density decreases because of an increase in series resistance of the solar cell. And the fill factor becomes worse due to an increase of leakage current for less than these thicknesses [42].

Meanwhile, in the CIGS solar cell, world record efficiencies have been achieved by using the CdS buffer layer among various buffer layers such as CdS, ZnS and InS. However, the thick CdS buffer layer absorbs short

wavelength light ($< 510\text{nm}$). So, any photocurrent can not be generated in the short wavelength region. Photocurrent in this region can be generated by increasing the band gap of the contact layer. And the contact layer must have high conductivity for lateral current collection. Hence, transparent conducting oxide (TCO) film onto the thin CdS layer has been applied because TCO film has the high conductivity as well as the wide band gap. Low deposition temperature of $<150\text{ }^\circ\text{C}$ should be concerned to apply TCO films to CIGS solar cells. Among the TCO films, ZnO based TCO film has been widely used due to its merits such as non-toxicity, abundance of element, use of inexpensive material and very low resistivity by doping. Low resistivity of the ZnO based TCO film can be also achieved at relatively low deposition temperature by sputtering.

In this study, the bilayered-ZnO film was applied to CIGS solar cells. A 50nm-thick i-ZnO film and a 400nm-thick Al-doped ZnO (2wt% Al_2O_3) film were sequentially deposited at room temperature on the CdS layer by using RF magnetron sputtering.

1.3.1.4 Metal electrode (bottom, top)

- Bottom electrode

In general, molybdenum (Mo) has been used as a bottom electrode of the CIGS solar cell among Ni, Al, and Au because which withstands corrossions against from Se and S, whereas Al or Au diffuses fast into CIGS layer and Ni reacts with CIGS. And the thermal expansion coefficient of Mo is similar to that of CIS [43]. Also, molybdenum allows Na diffusion from a soda lime

glass (SLG) substrate to a CIGS layer [44], which is beneficial to a conversion efficiency of CIGS solar cell. Characteristics of the Mo layer are strongly affected by process parameters such as sputtering power and working gas pressure. The Mo layer deposited at low Ar gas pressure shows densely packed microstructure and has low resistivity. However, the adhesion to SLG substrate is poor. On the contrary, the Mo film deposited at high Ar gas pressure has the good adhesion although the film has a high resistivity [45-49]. Therefore, the Mo bilayer film with the bottom layer sputtered at high pressure and the top layer sputtered at low pressure has been recommended [45, 48] and normally used as the bottom electrode of CIGS solar cell.

Meanwhile, the MoSe₂ layer is formed between the CIGS and the Mo layer when the CIGS precursor film is selenized. The MoSe₂ layer has a wider band gap (~1.4eV) than that of Cu(In_{1-x}Ga_x)Se ($x < \sim 0.6$) absorber layer, which would form the back surface field to avoid recombination of charge carriers at back [50]. And also, the MoSe₂ layer formed at the CIGS/Mo interface changes its contact type from a Schottky- to an ohmic-type contact [50, 51], which is beneficial to conversion efficiency. However, very thick MoSe₂ layer is detrimental to the conversion efficiency [52]. Therefore, it is important to obtain the MoSe₂ layer with an adequate thickness. The thickness of the MoSe₂ layer is affected by Mo layer properties such as microstructure, grain size and film density. For example, the Mo layer deposited at a low pressure has a thinner MoSe₂ layer [53]. And the growth rate of a MoSe₂ layer and the adhesion to the Mo layer is also dependent on growth orientation of the MoSe₂ grains. If the c-axis of the MoSe₂ grains is parallel to the Mo surface, thick MoSe₂ layer is easily formed and adhesion of MoSe₂ is much stronger

[53, 54]. In this experiment, the Mo electrode layer was deposited onto the soda lime glass substrate by the DC magnetron sputtering method. As mentioned above, properties of the Mo electrode layer are greatly influenced by deposition conditions. Therefore, to utilize the Mo layer as a bottom electrode of the CIGS solar cell, electrical and mechanical properties of the Mo electrode layer had been investigated through a preliminary experiment (not shown here). As a result, the Mo layer was deposited with RF power of 150watt under argon gas pressure of 5mTorr at 200 °C for 50min. The approximately 1um thick Mo film was deposited. The Mo film showed a low sheet resistance below 0.2 Ω /sq and good adhesion without peeling off.

- Top electrode (grid)

For the measurement of a solar cell with a small area, normally $\sim 1\text{cm}^2$, the bilayer-top metal electrode consisted of Ni and Al has been applied to a CIGS solar cell. First, several tens of nanometers of Ni are deposited on the TCO layer to prevent the formation of an oxide layer with high resistivity. And a few micrometers of Al are deposited on the Ni layer. The top electrode has to be designed as a grid with a small area to allow much light. This grid layer is generally deposited by evaporation through a metal shadow mask. In this experiment, Al grids for the enhancement of current collection were deposited by thermal evaporation.

References

- [1] D. M. Chapin, C.S. Fuller, G. L. Pearson, *J. Appl. Phys.* 25 (1954) 676.
- [2] D. C. Reynolds, G. Leies, L. L. Antes, R.E. Marberger, *Phys. Rev.* 96 (1954) 533.
- [3] D. Jenny, J. Loferski, P. Rappaport, *Phys. Rev.* 101 (1956) 1208.
- [4] S. Wagner, J. Shay, P. Migliorato, H. Kasper, *Appl. Phys. Lett.* 25 (1974) 434.
- [5] L. Kazmerski, F. White, G. Morgan, *Appl. Phys. Lett.* 29 (1976) 268.
- [6] http://www.nrel.gov/ncpv/images/efficiency_chart.jpg
- [7] A. M. Gabor, J. R. Tuttle, D. S. Albin, M. A. Contreras, R. Noufi, A. M. Hermann, *Appl. Phys. Lett.* 65 (1994) 198.
- [8] M. A. Contreras, J. R. Tuttle, A. M. Gabor, A. Tennant, K. Ramanathan, S. Asher, A. Franz, J. Keane, L. Wang, J. Scofield, R. Noufi, First WCPEC; Dec. 5-9, 1994; Hawaii, p68.
- [9] N. Kohara, T. Negami, M. Nishitani, T. Wada, *Jpn. J. Appl. Phys.* 34 (1995) L1141.
- [10] M. A. Contreras, B. Egaas, K. Ramanathan, J. Hiltner, A. Swartzlander, F. Hasoon, R. Noufi, *Pro. Photovolt: Res. Appl.* 7 (1999) 311.
- [11] T. Nakada, A. Kunioka, *Appl. Phys. Lett.* 74 (1999) 2444.
- [12] S. Chaisitsak, A. Yamada, M. Konagai, *Jpn. J. Appl. Phys.* 41 (2002) 507.
- [13] I. Repins, M. A. Contreras, B. Egaas, C. DeHart, J. Scharf, C. L. Perkins, B. To, R. Noufi, *Pro. Photovolt: Res. Appl.* 16 (2008) 235.
- [14] P. Jackson, D. Hariskos, E. Lotter, S. Paetel, R. Wuerz, R. Menner, W. Wischmann, M. Powalla, *Prog. Photovolt. Res. Appl.* 19 (2011) 894.
- [15] M. A. Green, K. Emery, Y. Hishikawa, W. Warta, E. D. Dunlop, *Prog. Photovolt. Res. Appl.* 22 (2014) 1.
- [16] A. Luque, S. Hegedus, *Handbook of Photovoltaic science and*

engineering, wiley, 2003, p583.

- [17] K. Ramanathan, M. A. Contreras, C. L. Perkins, S. Asher, F. S. Hasoon, J. Keane, D. Young, M. Romero, W. Metzger, R. Noufi, J. Ward, A. Duda, *Prog. Photovolt. Res. Appl.* 11 (2003) 225.
- [18] A. M. Gabor, J. R. Tuttle, M. H. Bode, A. Franz, A. L. Tennant, M. A. Contreras, R. Noufi, D. G. Jensen, A. M. Hermann, *Sol. Energy Mater. Sol. Cells* 41 (1996) 247.
- [19] P. Jackson, R. Wuerz, U. Rau, J. Mattheis, M. Kurth, T. Schlotzer, G. Bilger, J. H. Werner, *Prog. Photovolt. Res. Appl.* 15 (2007) 507.

Two-step process

- [20] B. M. Basol, V. K. Kapur, *Appl. Phys. Lett.* 54 (1989) 1918.
- [21] K. Kushiya, A. Shimizu, A. Yamada, M. Konagai, *Jpn. J. Appl. Phys.* 34 (1995) 54.
- [22] S. Nishiwaki, T. Satoh, S. Hayashi, Y. Hashimoto, S. Shimakawa, T. Negami, T. Wada, *Sol. Energy Mater. Sol. Cells* 67 (2001) 217.
- [23] R. Caballero, C. Guillen, *Sol. Energy Mater. Sol. Cells* 86 (2005) 1.
- [24] S.D. Kim, H.J. Kim, K.H. Yoon, J. Song, *Sol. Energy Mater. Sol. Cells* 62 (2000) 357.
- [25] D.G. Moon, S. Ahn, J.H. Yun, A. Cho, J. Gwak, S. Ahn, K. Shin, K. Yoon, H.D. Lee, H. Pak, S. Kwon, *Sol. Energy Mater. Sol. Cells* 95 (2011) 2786.
- [26] M. Marudachalam, H. Hichri, R. Klenk, R. W. Birkmire, W. N. Shafarman, J. M. Schultz, *Appl. Phys. Lett.* 67 (1995) 3978.
- [27] T. Nakada, A. Kunioka, *Jpn. J. Appl. Phys.* 37 (1998) L1065.
- [28] W. Li, Y. Sun, W. Liu, L. Zhou, *Solar Energy* 80 (2006) 191.
- [29] N. G. Dhere, K. W. Lynn, *Sol. Energy Mater. Sol. Cells* 41 (1996) 271.
- [30] G. S. Chen, J. C. Yang, Y. C. Chan, L. C. Yang, W. Huang, *Sol. Energy Mater. Sol. Cells* 93 (2009) 1351.
- [31] A. Luque, S. Hegedus, *Handbook of Photovoltaic science and engineering*, wiley, 2003, p584.

- [32] V. K. Kapur, B. M. Basol, E. S. Tseng, *Solar Cells* 21 (1987) 65.
- [33] M. Ganchev, J. Kois, M. Kaelin, S. Bereznev, E. Tzvetkova, O. Volobujeva, N. Stratieva, A. Tiwari, *Thin Solid Films* 511 (2006) 325.
- [34] D. Wang, L. Wan, Z. Bai, Y. Cao, *Appl. Phys. Lett.* 92 (2008) 211912.
- [35] C. R. Abernathy, C. W. Bates, A. A. Anani, B. Haba, G. Smestad, *Appl. Phys. Lett.* 45 (1984) 980.
- [36] S. J. Ahn, K. H. Kim, J. H. Yun, K. H. Yoon, *J. Appl. Phys.* 105 (2009) 113533.
- [37] W. Liu, D. B. Mitzi, M. Yuan, A. J. Kellock, S. J. Chey, O. Gunawan, *Chem. Mater.* 22 (2010) 1010.
- [38] E. J. Lee, S. J. Park, J. W. Cho, J. Gwak, M. K. Oh, B. K. Min, *Sol. Energy Mater. Sol. Cells* 95 (2011) 2928.
- [39] M. A. Contreras, M. J. Romero, B. To, F. Hasoon, R. Noufi, S. Ward, K. Ramanathan, *Thin Solid Films* 403 (2002) 204.
- [40] U. Rau, M. Schmidt, *Thin Solid Films* 387 (2001) 141.
- [41] N.F. Cooray, K. Kushiya, A. Fujimaki, D. Okumura, M. Sato, M. Ooshita, O. Yamase, *Jpn. J. Appl. Phys.* 38 (1999) 6213.
- [42] S. R. Kodigala, *Thin films and nanostructures*, vol. 35 “Cu(In_{1-x}Ga_x)Se₂ based thin film solar cells”, 2010, p606.
- [43] S. R. Kodigala, *Thin films and nanostructures*, vol. 35 “Cu(In_{1-x}Ga_x)Se₂ based thin film solar cells”, 2010, p630.
- [44] S. S. Wang, C. Y. Hsu, F. J. Shiou, P. C. Huang, D. C. Wen, *J. Electron. Mater.* 42 (2013) 71.
- [45] J. H. Scofield, A. Duda, D. Albin, B. L. Ballard, P. K. Predecki, *Thin Solid Films* 260 (1995) 26.
- [46] H. Khatri, S. Marsillac, *J. Phys.: Condens. Matter* 20 (2008) 055206.
- [47] S. A. Pethe, E. Takahashi, A. Kaul, N. G. Dhere, *Sol. Energy Mater. Sol. Cells* 100 (2012) 1.
- [48] H. M. Wu, S. C. Liang, Y. L. Lin, C. Y. Ni, H. Y. Bor, D. C. Tsai, F. S. Shieu, *Vacuum* 86 (2012) 1916.

- [49] C. H. Huang, H. L. Cheng, W. E. Chang, M. Y. Huang, Y. J. Chien, *Semicond. Sci. Technol.* 27 (2012) 115020.
- [50] T. Wada, N. Kohara, S. Nishiwaki, T. Negami, *Thin Solid Films* 387 (2001) 118.
- [51] L. Assmann, J. C. Bernede, A. Drici, C. Amory, E. Halgand, M. Morsli, *Appl. Surf. Sci.* 171 (2001) 15.
- [52] X. Zhu, Z. Zhou, Y. Wang, L. Zhang, A. Li, F. Huang, *Sol. Energy Mater. Sol. Cells* 101 (2012) 57.
- [53] T. Wada, N. Kohara, T. Negami, M. Nishitani, *Jpn. J. Appl. Phys.* 35 (1996) L1253.
- [54] D. Abou-Ras, G. Kostorz, D. Bremaud, M. Kalin, F.V. Kurdesau, A.N. Tiwari, M. Dobeli, *Thin Solid Films* 480 (2005) 433.

Table. 1.1. Experimental details for coating of CdS layer

Material		Molecular weight	Experimental detail		
			Concentration (M)	Material weight (g)	D.I. water (ml)
Deionized water	H ₂ O	18			355.5ml
Cadmium sulfate hydrate	CdSO ₄ ·8H ₂ O	769.55	0.015	0.194	50ml
Thiourea	NH ₂ SCNH ₂	76.12	1.5	2.883	25ml
Ammonium hydroxide	NH ₄ OH	35.03	1		69.5ml

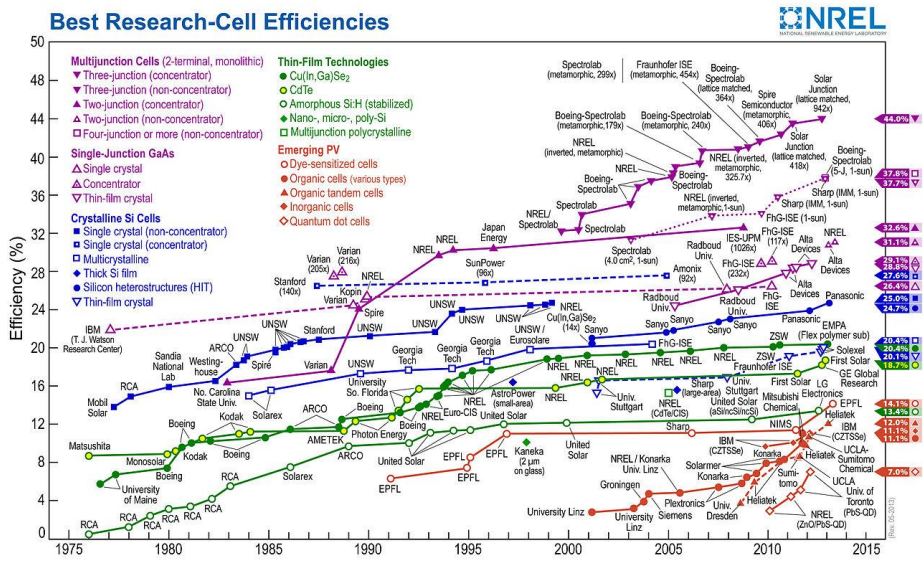


Fig 1.1 Best research-cell efficiencies chart for various photovoltaic technologies, which is compiled by National Renewable Energy Laboratory (NREL) [6]

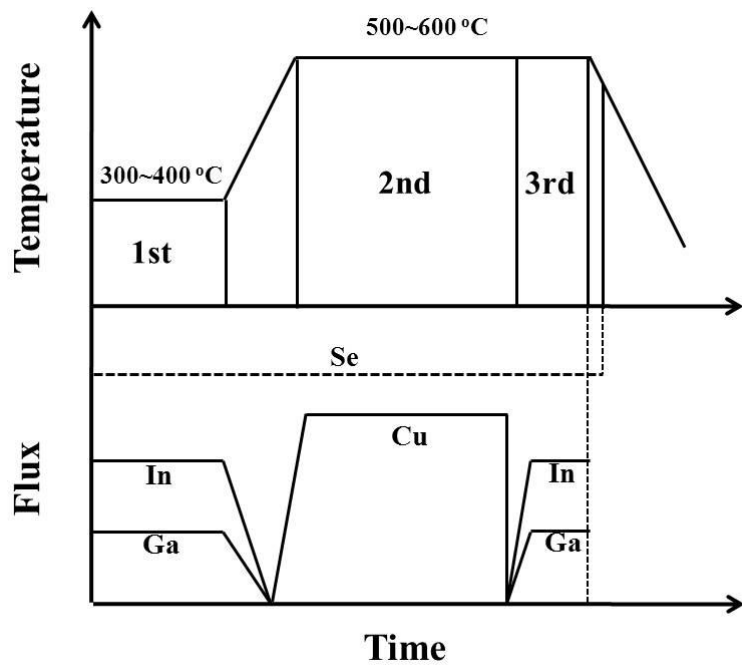


Fig. 1.2. Schematic of three-stage co-evaporation process. (Redrawn from ref. [8, 12, 13])

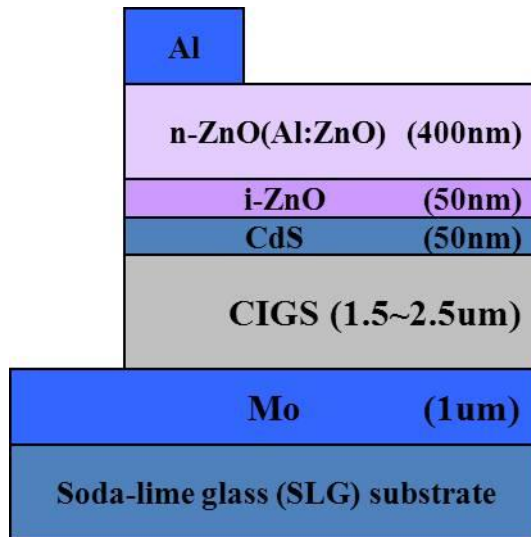


Fig. 1.3. Cross-sectional schematic of a CIGS solar cell.

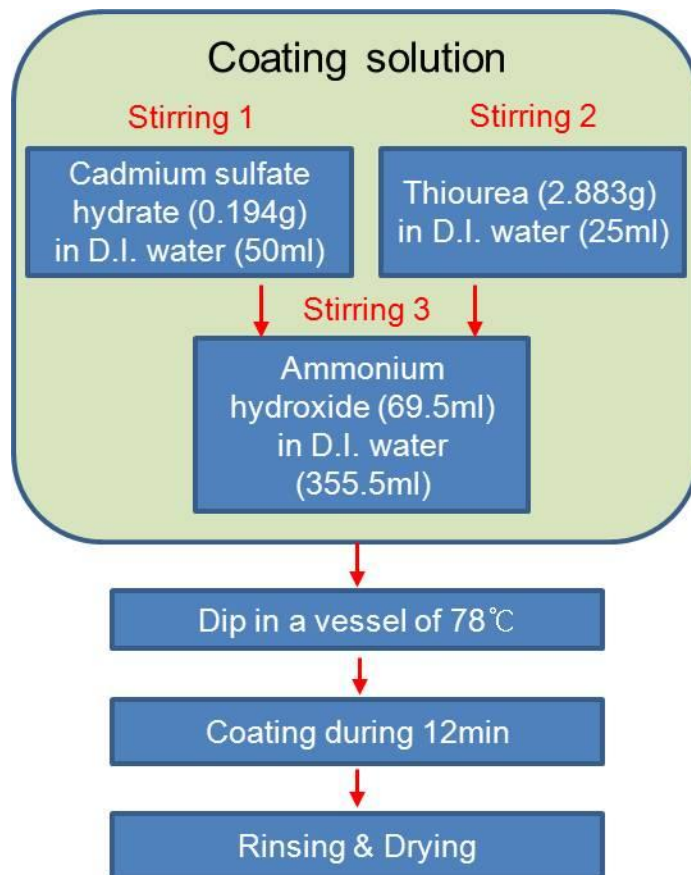


Fig. 1.4. Experimental procedure for coating of the CdS layer

Chapter 2. Design and fabrication of multi-layer antireflection coating for III-V solar cell

2.1. Introduction

Semiconductor materials such as GaAs and Si are known to have high reflectivity of about 30-40%. If these materials are applied to solar cells, high reflectivity has a harmful effect on solar cell efficiency. To reduce reflectivity and enhance solar cell efficiency, antireflection (AR) coating layer should be deposited on the solar cell surface. AR coatings have been studied in various optical fields for increasing transmittance and decreasing reflectance. Low reflectance can be obtained from a single-layer antireflection coating only at a specific wavelength. However, for a practical application to solar cells, low reflectance at wide wavelength regime from visible to near-infrared is required and can be achieved by a multi-layer antireflection coating such as double-layer and triple-layer antireflection coating. For the multi-layer antireflection coating, various materials with different refractive indices are necessary to achieve low reflectance.

Generally, ZnS, TiO₂ and CeO₂ are used as high refractive index material and MgF₂ and SiO₂ are used as low refractive index material in the AR coating. ZnS is very interesting material in the optical fields because it has a direct and wide band gap of 3.5-3.8 eV and transmits high energy photons [1-4]. And also MgF₂ has been universally used due to low refractive index and high transmittance in ultraviolet region [5]. Therefore, ZnS with a high

refractive index and MgF_2 with a low refractive index are commonly used for single- or double-layer AR coatings. Generally, refractive indices of ZnS and MgF_2 are known to be 2.354 and 1.377 at 630 nm, respectively [6,7]. However, refractive index is dependent on deposition method [8], deposition temperature [9,10], porosity [11-14] and stoichiometry [4], etc. Therefore, it is very important to look for the optimal deposition conditions irrespective of deposition method.

In this work, multi-layer AR coating such as double- and triple-layer was investigated with ZnS and MgF_2 . For a triple-layer AR coating, another material with an intermediate refractive index between those of ZnS and MgF_2 is needed and ZnS- MgF_2 composite film was suggested. ZnS, MgF_2 and ZnS- MgF_2 composite films were deposited by rf magnetron sputtering and their optical properties were examined. Based on the optical constants of each material, single-layer, double-layer and triple-layer AR coatings were designed and fabricated on the GaAs substrate. Especially, optical properties of co-sputtered ZnS- MgF_2 composite films were systematically investigated as a function of concentration of MgF_2 and ZnS in order to apply them to intermediate refractive index layer of triple-layer AR coating. And also experimental results of AR coating were compared to simulated results.

2.2. Experimental

ZnS and ZnS- MgF_2 composite films were prepared on soda-lime glass (SLG) substrates with optical grade by rf magnetron sputtering. Base pressure of vacuum chamber before deposition was approximately 3.0×10^{-6} Torr. ZnS

and MgF_2 target with a 99.99% high purity were used in this work. ZnS films were deposited with rf power of 50W under a working pressure of 5 mTorr. Substrate rotation was carried out at 3 rpm for film uniformity. ZnS- MgF_2 composite films were deposited by co-sputtering of ZnS and MgF_2 targets. To control the composition, rf power applied to MgF_2 target was varied with a fixed rf power to ZnS target. Thicknesses of ZnS film and ZnS- MgF_2 films were adjusted to be 600-800 nm, which is need to determine optical constants by using envelope method.

Transmittance of the ZnS and ZnS- MgF_2 composite films was measured in the wavelength range of 300-1500 nm by using UV-VIS-NIR spectrophotometer (Varian model, Cary 5000). Refractive indices (n), extinction coefficient (k) and thicknesses (d) of the ZnS film and ZnS- MgF_2 films were determined by envelope method. Additionally, optical constant of MgF_2 film was analyzed. Actually, it is difficult to determine optical constants of MgF_2 by envelope method due to small discrepancy of refractive index between glass substrate and MgF_2 . Therefore, in this experiment, MgF_2 film with a thickness needed for AR coating was deposited on GaAs substrates with rf power of 200W under Ar gas pressure of 10 mTorr and their optical constants were obtained by using spectroscopic ellipsometry (SE) at wide wavelength region. Quantitative analysis of ZnS- MgF_2 films was investigated by electron probe microanalyser (EPMA) for studying a relation between relative atomic concentration and refractive index of the film.

By using the extracted optical constant, single-, double-, and triple-layer AR coatings were designed and fabricated on GaAs substrate by rf magnetron sputtering and their reflectance were measured by using spectrophotometer.

Finally, reflectance spectra obtained by experiment were fitted and analyzed by computation of Essential Macleod program.

In the design of AR coatings, optical constants of the top layer of the III-V solar cell are important. In III-V solar cells, the top layer, on which AR coating is fabricated, is AlGaAs in the single-junction cell or InGaP(or AlGaP) in the multi-junction cells. In this work, we focused to investigate the characteristics of AR coatings depending on the number of AR coating layer, namely, single-, double- and triple-layer AR coating. For this purpose, GaAs single crystal substrates were used because they have uniform surface properties enough to compare the characteristics of AR coatings depending on the number of AR coating layer and also have similar optical constants to those of the top layers of III-V solar cells (refractive indices of GaAs and InGaP are ~ 3.85 and ~ 3.6 [15], respectively). Therefore, those results obtained in this work are very helpful to optimization of AR coatings for III-V solar cells.

2.3. Results and discussion

Fig. 2.1 shows the transmittance spectra of ZnS and ZnS-MgF₂ composite films on SLG substrates as a function of wavelength and also rf power dependence of transmittance of ZnS-MgF₂ films. It can be seen that all of the ZnS and ZnS-MgF₂ films were highly transparent in the wide wavelength region. The optical absorption edge shifted continuously toward short wavelength with increasing rf power to MgF₂. From these transmittance spectra, optical constants of ZnS and ZnS-MgF₂ films with wavelength could

be calculated by using envelope method. The refractive index (n) and extinction coefficient (k) were calculated using Swanepoel's method [16] which is based on the idea of Manifacier et al. [17].

Fig. 2.2 shows the refractive indices and extinction coefficients of ZnS-MgF₂ composite films depending on rf power to MgF₂ and those of ZnS and MgF₂ films. This figure indicates that all of the ZnS-MgF₂ composite films have intermediate refractive indices between those of ZnS and MgF₂, implying that these ZnS-MgF₂ composite films could be used as a middle layer of triple-layer AR coating. Refractive index of ZnS-MgF₂ composite film slightly decreased with increasing rf power to MgF₂. However, extinction coefficients of these films were similar and almost zero in visible region as well as infrared region. This result also indicates that all of these films are highly transparent between visible and infrared region.

In order to elucidate the origin of the variation of refractive index of the ZnS-MgF₂ composite film, film composition was investigated by EPMA. Fig. 2.3 shows the EPMA results of ZnS-MgF₂ films depending on rf power to MgF₂. As shown in Fig. 2.3, atomic concentrations of zinc and sulfur were slightly decreased with increasing the rf power up to 230W and then decreased abruptly at the rf power of 250W. This behavior is similar to that of refractive index as shown in this figure. This result indicates that refractive index of the ZnS-MgF₂ composite film is dependent on the film composition, namely, amount of ZnS with a high refractive index or MgF₂ with a low one is important to determine refractive index of ZnS-MgF₂ composite film. The more the amount of MgF₂ with a low refractive index, the lower the refractive index of ZnS-MgF₂ composite film and *vice versa*. As a result, ZnS-MgF₂

composite films having an intermediate refractive index for triple-layer AR coating could be successfully fabricated by co-sputtering of ZnS and MgF₂.

By using the optical constants of upper results, single (ZnS)-, double (ZnS/MgF₂)- and triple (ZnS/ZnS-MgF₂/MgF₂)-layer antireflection coatings were designed with a quarter-wave thickness at the reference wavelength of 600 nm for normal incidence. Therefore, the thickness of each layer could be calculated by using the equation of $nd = \lambda/4$ (n: refractive index, d: thickness, λ : wavelength). The thicknesses of MgF₂, ZnS-MgF₂ and ZnS layers, which used in three types of AR coatings, were 109.7, 81.2 and 64.6 nm, respectively. Fig. 2.4 presents the simulated reflectance spectra depending on the wavelength by using Essential Macleod program. As shown in Fig. 2.4, reflectance was dramatically changed according to a number of coating layers. However, in the triple-layer AR coating, although refractive index of ZnS-MgF₂ middle layer was changed from 1.842 to 1.654 at 632 nm, reflectance spectra were almost similar irrespective of refractive index. These results indicate that reflectance of AR coating is affected by a number of coating layers and a small change in the refractive index of the middle layer of triple-layer AR coating did not lead to a remarkable change in the reflectance of the triple-layer AR coating.

Based on designs of Fig. 2.4, single and multiple layers were coated on GaAs substrate. Fig. 2.5(a), (b) and (c) show reflectance spectra of GaAs substrate with single-, double- and triple-layer AR coating, respectively. ZnS 50W-MgF₂ 140W composite film was used as a middle layer with intermediate refractive index in triple layer AR coating. As shown in Fig. 2.5, as was expected, low reflectance could be obtained from a single-layer

antireflection coating only at a specific wavelength and could be obtained from double- and triple-layer antireflection coating at wide wavelength regime from visible to near-infrared. Especially, in the case of multi-layer AR coating, low reflectance was achieved by double-layer antireflection coating in the visible region and achieved by triple-layer antireflection coating in the near-UV and near-IR region. Reflectance spectra obtained by experiment were fitted by simulation by Essential Macleod. Solid line and dashed line indicate experimental results and simulated results, respectively. In the case of single-layer AR coating, experimental result was nicely consistent with the simulated result. However, reflectance of multi-layer AR coating had a small discrepancy between experimental result and simulated result, which can be caused by optical inhomogeneity [18] and difference between designed thickness and deposited one of each layer.

The effect of incident angle on the reflectance of multi-layer AR coating was investigated. Fig. 2.6 shows the simulated reflectance spectra of double- and triple-layer AR coating as a function of incident angle. As shown in Fig. 2.6, reflectance of double-layer increased gradually above 600 nm with increasing incident angle. On the other hand, reflectance of triple-layer decreased with increasing incident angle. It indicates that the triple-layer AR coating is efficient at the wavelength of above 600 nm in the case that incident angle is varied.

2.4. Summary

ZnS and MgF₂ film were fabricated on soda-lime glass substrate and GaAs

substrate and their optical constants were determined by envelope method and spectroscopic ellipsometry, respectively. Co-sputtered ZnS-MgF₂ composite films for applying to triple-layer AR coating were prepared on SLG substrate depending on rf power applied to MgF₂ and their optical constants were determined by envelope method. All films were highly transparent in the range from visible and near-IR. In the case of ZnS-MgF₂ composite film, optical absorption edge was continuously shifted to short wavelength and refractive index decreased with increasing concentration of Mg and F. Based on these optical constants, single-layer and multi-layer AR coatings were designed by using a quarter-wave thickness at a normal incidence and fabricated by using rf magnetron sputtering. Low reflectance could be obtained from a single-layer antireflection coating only at a specific wavelength and from multi-layer antireflection coating at wide wavelength region. However, range of low reflectance of double- and triple-layer AR coating was different although multilayer AR coating showed low reflectance at wide wavelength range. Double-layer AR coating showed low reflectance mainly in the visible region, which is important for solar cell application, and triple-layer AR coating showed low reflectance mainly in the near-UV and near-IR region. Incident angle dependence of reflectance of multi-layer AR coating showed different behavior according to a number of layers. So, before application of multi-layer AR coatings, their characteristics and application field should be considered to be used to the proper place.

References

- [1] R. Menner, B. Dimmler, R.H. Mauch, H.W. Schock, *J. Crystal Growth* 86 (1988) 906.
- [2] R. Nomura, T. Murai, T. Toyosaki, H. Matsuda, *Thin Solid Films* 271 (1995) 4.
- [3] Y.-Z. Yoo, T. Chikyow, P. Ahmet, Z.W. Jin, M. Kawasaki, H. Koinuma, *J. Crystal Growth* 237 (2002) 1594.
- [4] Y.P. Venkata Subbaiah, P. Prathap, K.T. Ramakrishna Reddy, *Appl. Surf. Sci.* 253 (2006) 2409.
- [5] T. Yoshida, K. Nishimoto, K. Sekine, K. Etoh, *Appl. Opt.* 45 (2006) 1375.
- [6] E.D. Palik, *Handbook of Optical Constants of Solids*. Academic, San Diego, 1998.
- [7] E.D. Palik, *Handbook of Optical Constants of Solids II*. Academic, San Diego, 1998.
- [8] T.D. Radjabov, I.E. Djamaletdinova, A.V. Sharudo, H. Hamidova, *Surf. Coat. Technol.* 72 (1995) 99.
- [9] F. Huang, Q. Song, M. Li, B. Xie, H. Wang, Y. Jiang, Y. Song, *Appl. Surf. Sci.* 255 (2008) 2006.
- [10] H. Yu, H. Qi, Y. Cui, Y. Shen, J.D. Shao, Z.X. Fan, *Appl. Surf. Sci.* 253 (2007) 6113.
- [11] S. Strehlke, S. Bastide, J. Guillet, C. Levy-Clement, *Mater. Sci. Eng. B* 69 (2000) 81.
- [12] V.M. Aroutiounian, K.R. Maroutyan, A.L. Zatikyan, K.J. Touryan, *Thin Solid Films* 403 (2002) 517.
- [13] S.H. Woo, Y.J. Park, D.H. Chang, K.M.A. Sobahan, C.K. Hwangbo, *J. Korean Phys. Soc.* 51 (2007) 1501.
- [14] J.-Q. Xi, J. Kim, E.F. Schubert, D. Ye, T.-M. Lu, S. Lin, *Opt. Lett.* 31 (2006) 601.

- [15] W. Yuan, Master thesis, Univ. of Notre Dame, Indiana, USA, Dec. 2009.
- [16] R. Swanepoel, J. Phys. E: Sci. Instrum. 16 (1983) 1214.
- [17] J.C. Manificier, J. Gasiot, J.P. Fillard, J. Phys. E: Sci. Instrum. 9 (1976) 1002.
- [18] X. Wu, F. Lai, L. Lin, J. Lv, B. Zhuang, Q. Yan, Z. Huang, Appl. Surf. Sci. 254 (2008) 6455.

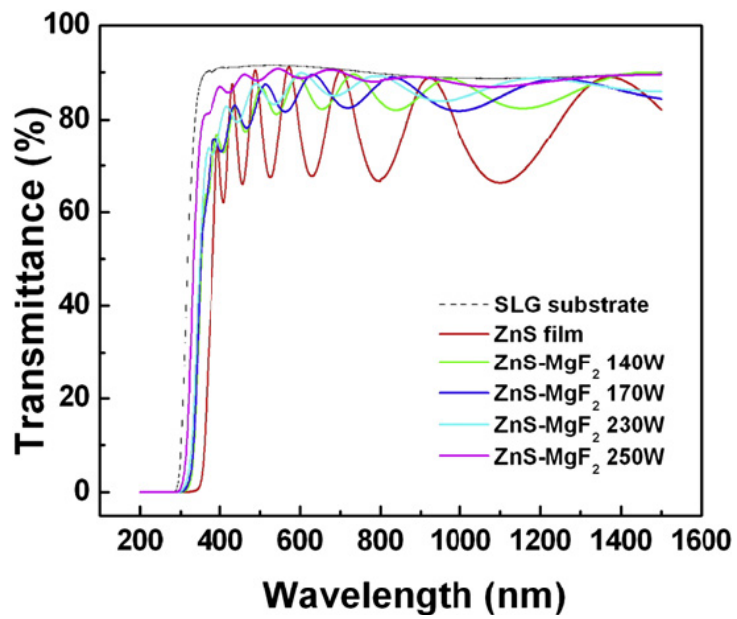


Fig. 2.1. Transmittance spectra of ZnS and ZnS-MgF₂ films on SLG substrates depending on wavelength.

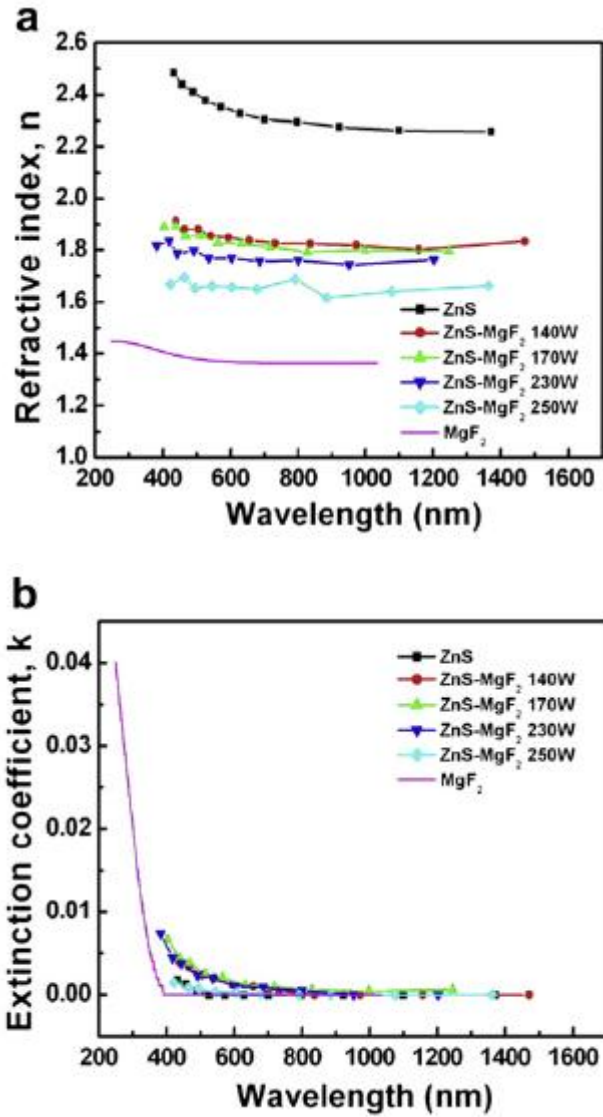


Fig. 2.2. (a) Refractive index and (b) extinction coefficient of ZnS-MgF₂ composite films depending on rf power applied to MgF₂. Optical constants of pure ZnS and MgF₂ were also exhibited.

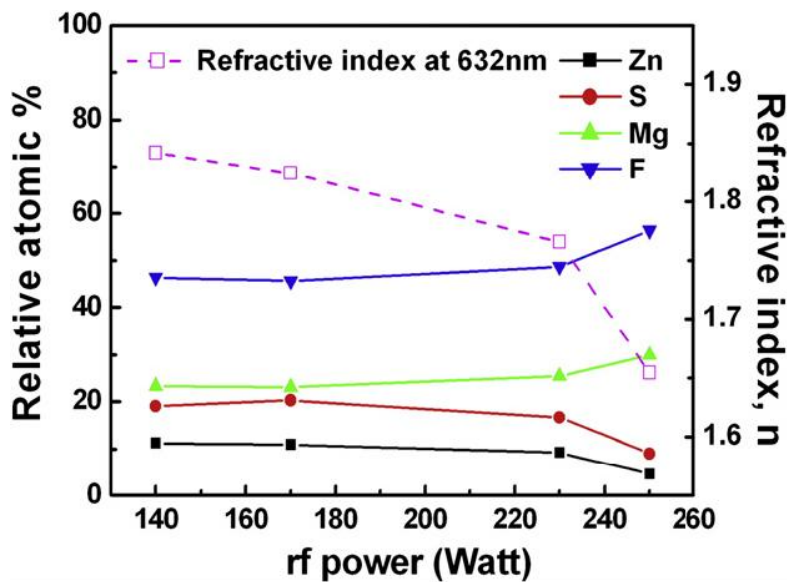


Fig. 2.3. EPMA results and refractive index variation at the wavelength of 632 nm for ZnS-MgF₂ composite films depending on rf power applied to MgF₂.

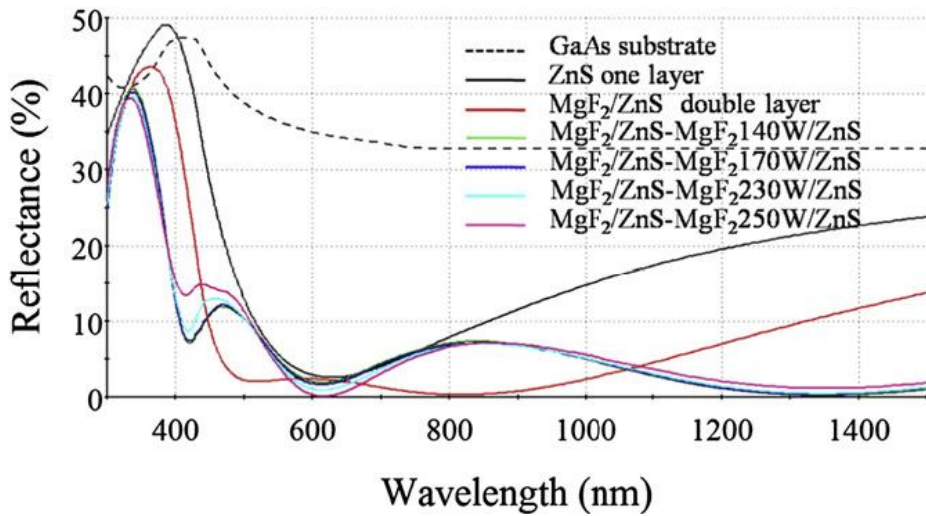


Fig. 2.4. Simulated reflectance spectra of GaAs substrate with single-, double- and triple-layer antireflection coating depending on wavelength. All structures are designed by quarter-wave coating at a reference wavelength of 600 nm. Reflectance spectra were theoretically calculated by Essential Macleod program.

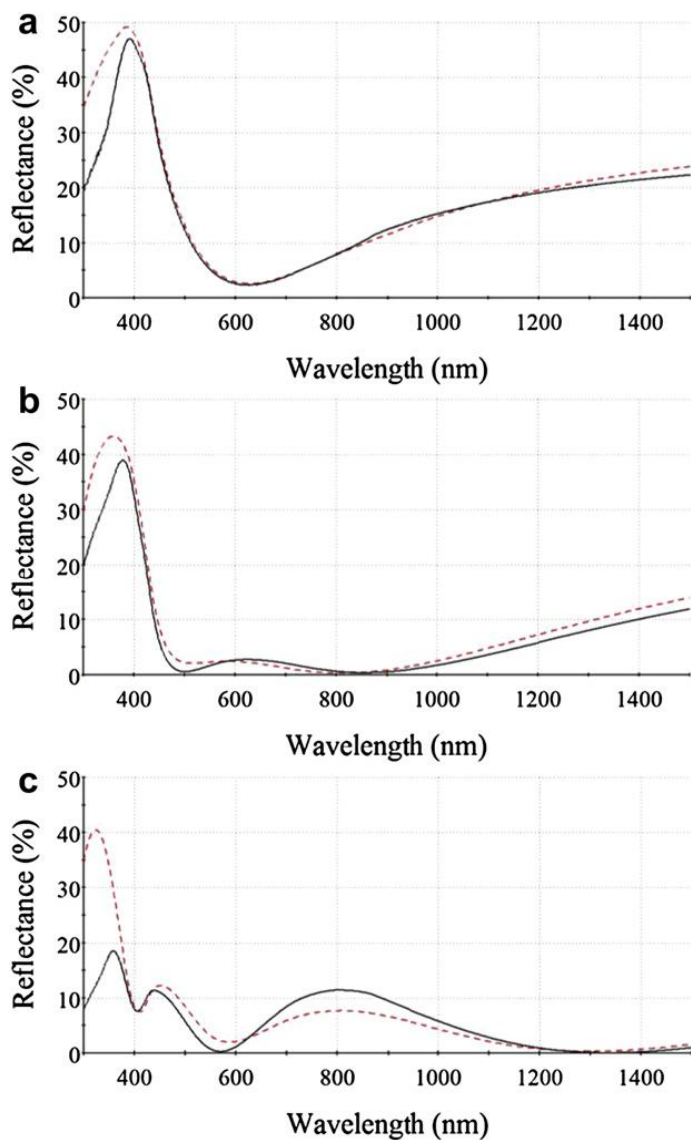


Fig. 2.5. Measured (solid line) and simulated (dash line) reflectance spectra of GaAs substrate with (a) single-layer (b) double-layer and (c) triple-layer antireflection coating. ZnS50W-MgF₂140W composite film was used as intermediate refractive index material in triple-layer AR coating.

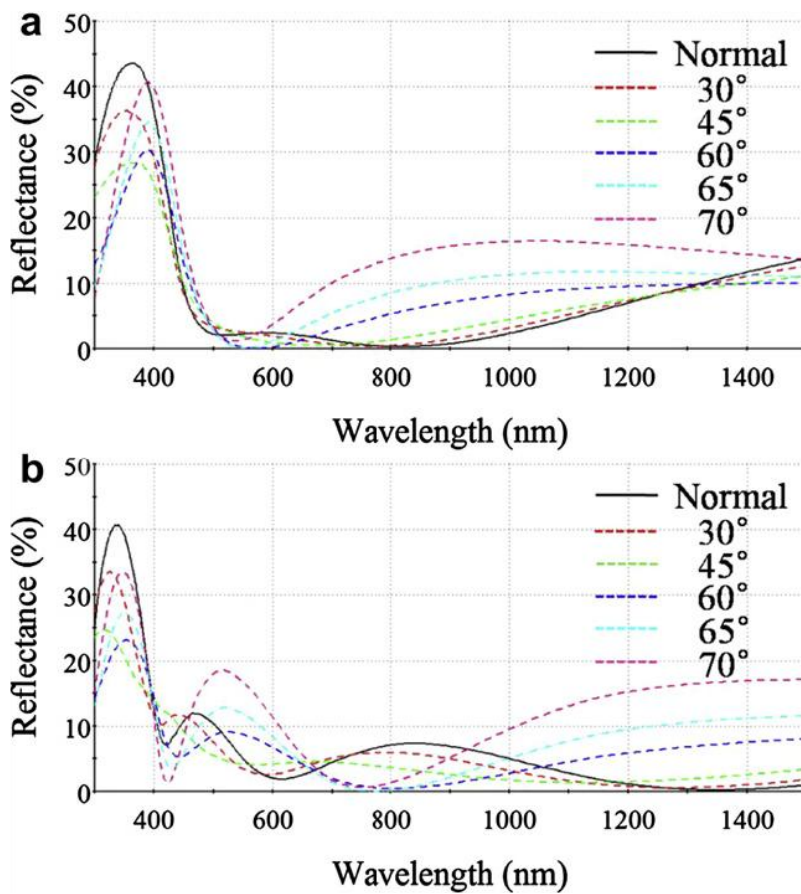


Fig. 2.6. Simulated reflectance spectra of (a) double-layer and (b) triple-layer AR coating as a function of incident angle.

Chapter 3. Characteristics of transparent conducting Al-doped ZnO films prepared by dc magnetron sputtering

3.1. Introduction

Transparent conducting oxide (TCO) films have been studied for various photo-electronic devices such as displays and solar cells. Indium tin oxide (ITO) is the most commonly-used TCO material because of its high conductivity and high transmittance. However, ITO has some demerits such as thermal instability and the high-cost of indium. On the other hand, zinc oxide (ZnO) based transparent conducting oxide has been investigated because of its various merits such as non-toxicity, abundance of element, use of inexpensive material, very low resistivity by doping and usefulness of various dopants. For obtaining ZnO-based TCO films, various processing methods such as sputtering [1-4], PLD [5,6], CVD [7], PECVD [8], MOCVD [9] sol-gel [10,11] and spray pyrolysis [12,13] have been extensively studied. Among them, sputtering method is generally used because it is simple process and is possible to fabricate the films with uniform surface over large area, dense structure and high crystallinity.

Meanwhile, the effects of various processing parameters such as substrate temperature [14], oxygen partial pressure [15] and doping material [16] have been investigated to improve electrical and optical properties of ZnO-based

TCO films. And it is revealed that these parameters have a significant effect on properties of ZnO-based TCO film. Recently, the flexible optoelectronic devices have attracted much attention and therefore it is important to decrease the substrate temperature to obtain TCO films with low resistivity and high transparency. In addition, in case of CIGS solar cells, low substrate temperature is very important to protect the underneath device structure of p-n junction. The substrate temperature below 200 °C is required to not deteriorate the p-n junction [17].

In this work, Al-doped ZnO (AZO) films were fabricated by using dc magnetron sputtering as a function of Ar gas pressure, O₂/Ar gas ratio and substrate temperature and their electrical, optical and structural properties were systematically investigated to obtain AZO films with both low resistivity of order of 10⁻⁴ Ωcm and high transparency in visible region. Especially, low substrate temperature of ≤ 200 °C was concerned to apply AZO films to CIGS solar cells.

3.2. Experimental

Al-doped ZnO films were deposited on soda-lime glass substrates with optical grade by using dc magnetron sputtering. Base pressure of vacuum chamber before deposition was approximately 3.0 × 10⁻⁶ Torr. 2 wt%-Al₂O₃ doped ZnO target with a high purity (99.99%) and low resistivity (below 1 Ωcm) was used in this work. AZO films were deposited with dc power of 100W under argon gas pressure of 3-15 mTorr at room temperature (R.T.). Substrate rotation was carried out at 3 rpm for film uniformity.

In order to obtain the AZO films with both high transparency and low resistivity for practical applications, the effects of substrate temperature and oxygen partial pressure on the properties of AZO films were systematically investigated. For this purpose, substrate temperature (T_s) was varied from R.T. to 350 °C and O_2/Ar gas ratio from 1.23 to 9.09 % at $T_s =$ R.T. and 250 °C. In these cases, working pressure and dc power were fixed at 5 mTorr and 100 W, respectively.

The AZO films were characterized with investigation of their electrical, optical and structural properties. Resistivity, carrier concentration and Hall mobility of the AZO films were measured by using Hall measurement system. Transmittance was measured in the wavelength range of 200-1500 nm by using UV-VIS-NIR spectrophotometer (Varian model, Cary 5000). Crystal structures and surface morphologies of the AZO films were investigated by using x-ray diffraction (XRD) with Cu-K α radiation and field emission scanning electron microscopy (FESEM), respectively.

3.3. Results and discussion

AZO films were deposited at room temperature with various argon gas pressures to investigate the effect of argon gas pressure on the properties of them. Fig. 3.1 shows the resistivity, carrier concentration and Hall mobility of the AZO films deposited at various argon gas pressures. As shown in Fig. 3.1, the resistivity increased with increasing argon gas pressure. On the contrary, carrier concentration and Hall mobility decreased with increasing argon gas pressure. Fig. 3.2 shows the surface morphologies of the AZO films

depending on argon gas pressure. With increasing argon gas pressure, the AZO films became less dense with larger grains due to the decreased deposition rate and growth attribute of ZnO. In general, ZnO film is known to grow preferentially with c-axis due to its lowest surface energy and it was confirmed by XRD measurement (not shown here) that all the AZO films were grown mainly with (001) preferred orientation irrespective of argon pressure. The deposition rate was almost linearly decreased with increasing argon gas pressure (21.8 nm/min for 3 mTorr to 13.3 nm/min for 15 mTorr) due to scattering effect. The increase of resistivity of the AZO films could be related to the change of surface morphology depending on the argon gas pressure. As shown in Fig. 3.2, with increasing argon gas pressure, the AZO film became less dense, that is, porous with larger grains, resulting in decrease of the mobility due to grain boundary scattering of charge carrier [18]. Therefore, the increase of resistivity with increasing argon gas pressure could be explained by the decrease of mobility due to grain boundary scattering of charge carrier as well as decrease of carrier concentration. Although the resistivity of the AZO films decreased with decreasing argon gas pressure and low resistivity of $\sim 10^{-3} \Omega\text{cm}$ could be obtained at room temperature, the transparency of them decreased, too. Fig. 3.3 shows the transmittance spectra of the AZO films depending on the argon gas pressure. As mentioned before, transmittance decreased with decreasing argon gas pressure. Especially, the AZO films deposited at 3 mTorr had light grey color, indicating that it was excessively lack of oxygen and had metallic properties in part, resulting in low resistivity and low transmittance. Therefore, to enhance the transmittance with sustaining low resistivity, a small amount of oxygen was mixed with

argon during sputtering.

Fig. 3.4 shows resistivity and transmittance of the AZO films deposited at R.T. depending on the O₂/Ar gas ratio of 1.23-9.09%. The transmittance of the AZO film was greatly enhanced with nearly sustaining low resistivity when a very small amount of oxygen (1.23%) was mixed. However, further increase of O₂/Ar gas ratio increased the resistivity as well as the transmittance, implying that oxygen content (or oxygen vacancy) plays a key role in resistivity of AZO film and careful control of oxygen content is needed for both low resistivity and high transmittance of the AZO films. Fig. 3.5 shows XRD patterns of the AZO films depending on O₂/Ar gas ratio. This figure indicates that growth behavior of the AZO film is dependent on O₂/Ar gas ratio. When O₂/Ar gas ratio was below 1.64%, the AZO films were grown with random orientation; however, texturing with preferential orientation of (001) appeared when O₂/Ar gas ratio was above 3.23%. Interestingly, resistivity of the AZO film showed dependency of growth orientation. The AZO films grown with random orientation had resistivity of order of 10⁻³ Ωcm, however, the resistivity increased abruptly to order of 10⁻¹ Ωcm or above when the AZO films were grown with preferential orientation. Further study is needed to know the precise transition point of O₂/Ar gas ratio from random to preferential growth of the AZO film and its effect on the resistivity.

In order to decrease the resistivity of the AZO film down to order of 10⁻⁴ Ωcm with high transmittance for a practical application, the AZO films were deposited at the substrate temperature of R.T.~350 °C with a step of 50 °C under pure argon gas and O₂/Ar gas ratio of 1.23%. Fig. 3.6 shows resistivity, carrier concentration and Hall mobility of the AZO films deposited at various

substrate temperatures. With increasing the substrate temperature up to 250 °C, resistivity was continuously decreased, however, further increase of the substrate temperature increased the resistivity slightly due to decrease of the mobility as shown in Fig. 3.6 (b). The decrease of the mobility at the substrate temperature above 300 °C may be explained by thickness effect. The mobility of Al(or Ga)-doped ZnO film was reported to decrease with decreasing film thickness [19,20]. At the substrate temperature above 300 °C, deposition rate decreased with increasing the substrate temperature and thus the film thickness decreased to 235 and 180 nm at 300 and 350 °C, respectively while it was 330 nm at 250 °C. Therefore, the decrease of the mobility of the AZO films deposited at 300 and 350 °C is attributable to the decreased film thickness.

Fig. 3.7 shows the surface morphologies of the AZO films deposited at various substrate temperatures under pure argon gas. It was observed that the AZO films became more compact and denser and grain boundary became vague with increasing substrate temperature. These results are in agreement with a modified Thornton model which was proposed by Kluth et al. [21] to describe structural changes of the RF sputtered AZO film. From the surface morphology change as shown in Fig. 3.2 and 3.7, the mobility of the AZO films is related to the film structure, namely, grain boundary scattering of charge carrier plays an important role in the mobility of the AZO film.

Resistivity of order of 10^{-4} Ωcm could be achieved by increasing the substrate temperature above 150 °C under pure argon gas and above 250 °C under O₂/Ar gas ratio of 1.23%, respectively. In this work, the AZO film deposited at $T_s = 250$ °C under pure argon gas exhibited the lowest resistivity

of $3.19 \times 10^{-4} \Omega\text{cm}$. Fig. 3.8 shows the transmittance spectra of the AZO films deposited at various substrate temperatures. As shown in Fig. 3.8, except the AZO film deposited at R.T. under pure argon gas, all the films exhibited transparent characteristics in visible region. Especially, transmittance in visible region was greatly enhanced with increasing the substrate temperature in the case of pure argon gas as shown in Fig. 3.8(a). As shown in Fig. 3.4, transmittance was also enhanced by adding a small amount of oxygen to argon gas, indicating that transmittance of the AZO film is very sensitive to the substrate temperature and oxygen content in the sputtering gas. In near-infrared wavelength region, the transmittance decreased with decrease of resistivity of the AZO film because transmittance in the near-infrared region is affected by free carrier absorption.

The effect of O_2/Ar gas ratio at the substrate temperature of 250°C was also investigated. Fig. 3.9 shows resistivity, carrier concentration and Hall mobility of the AZO film deposited at $T_s = 250^\circ\text{C}$ depending on O_2/Ar gas ratio. As shown in Fig. 3.9, with increasing O_2/Ar gas ratio, resistivity increased and carrier concentration, Hall mobility decreased. This tendency is consistent with that of the AZO films deposited at room temperature, implying that oxygen content in the sputtering gas is critical to the electrical properties of the AZO film, irrespective of substrate temperature. Fig. 3.10 shows the transmittance spectra of the AZO films according to O_2/Ar gas ratio. As can be expected from the results shown in Fig. 3.8, all the AZO films without exception showed high transparency in the visible region due to high substrate temperature of 250°C . The decrease of transmittance in near-infrared wavelength region was also observed with decrease of resistivity.

Optical band gap of AZO films was investigated. Fig. 3.11 shows the optical band gap (E_g) of the AZO films deposited at various substrate temperatures under pure argon gas and O_2/Ar gas ratio of 1.23 %. As shown in Fig. 3.11, optical band gap increased with increasing substrate temperature up to 250 °C and further increase of the substrate temperature decreased E_g . It has a maximum value of 3.7 eV at the substrate temperature of 250 °C under pure argon gas. It was found that the optical band gap increased with decreasing O_2/Ar gas ratio and it showed similar tendency depending on the O_2/Ar gas ratio regardless substrate temperature although its value was different. Table 3.1 shows the optical band gap values of the AZO films depending on the substrate temperatures and the O_2/Ar gas ratios. As a whole, the optical band gap of the AZO film was closely related to the carrier concentration, namely, it was increased with increasing carrier concentration. This is consistent with Burstein-Moss effect [22].

3.4. Summary

AZO films were deposited on soda-lime glass substrates by dc magnetron sputtering as a function of argon gas pressure, O_2/Ar gas ratio and substrate temperature, and their electrical, optical and structural properties were systematically investigated. When the AZO films were deposited at room temperature, both resistivity and transmittance decreased with decreasing argon gas pressure. Small addition of oxygen to argon (O_2/Ar ratio of 1.23 %) enhanced the transmittance greatly with sustaining low resistivity, however, further addition increased the resistivity. This dependency of resistivity on the

O₂/Ar ratio was exhibited irrespective of the substrate temperature. As the substrate temperature was increased, resistivity decreased continuously and the lowest value of resistivity was obtained at the temperature of 250 °C in pure Ar and 250-300 °C in O₂/Ar ratio of 1.23 %, respectively. Further increase of the substrate temperature increased the resistivity slightly due to decrease of the Hall mobility at higher temperature. All of the AZO films were transparent in visible region except for AZO films deposited at room temperature in pure Ar. These results indicate that increase of temperature also enhances transparency of the AZO film in visible wavelength region. On the other hand, transmittance in near-infrared wavelength region gradually decreased with increasing the substrate temperature up to 250-300 °C because of free carrier absorption loss caused by high carrier concentration. Conclusively, the AZO films with low resistivity of order of 10⁻⁴ Ωcm and high transparency in visible region could be prepared at the substrate temperatures of above 150 °C (the lowest resistivity of 3.19 × 10⁻⁴ Ωcm at 250 °C) by dc magnetron sputtering and these films are applicable to various fields which require transparent conducting oxide films.

References

- [1] T. Minami, K. Oohashi, S. Takata, T. Mouri, N. Ogawa, *Thin Solid Films* 193-194 (1990) 721.
- [2] B.H. Choi, H.B. Im, J.S. Song, K.H. Yoon, *Thin Solid Films* 193-194 (1990) 712.
- [3] X. Yu, J. Ma, F. Ji, Y. Wang, X. Zhang, C. Cheng, H. Ma, *Appl. Surf. Sci.* 239 (2005) 222.
- [4] X. Bie, J.G. Lu, L. Gong, L. Lin, B.H. Zhao, Z.Z. Ye, *Appl. Surf. Sci.* 256 (2009) 289.
- [5] H. Kim, A. Piqué, J.S. Horwitz, H. Murata, Z.H. Kafafi, C.M. Gilmore, D.B. Chrisey, *Thin Solid Films* 377-378 (2000) 798.
- [6] S.M. Park, T. Ikegami, K. Ebihara, *Thin Solid Films* 513 (2006) 90.
- [7] T. Minami, H. Sato, H. Sonohara, S. Takata, T. Miyata, I. Fukuda, *Thin Solid Films* 253 (1994) 14.
- [8] J.J. Robbins, J. Harvey, J. Leaf, C. Fry, C.A. Wolden, *Thin Solid Films* 473 (2005) 35.
- [9] A.R. Kaul, O.Yu. Gorbenko, A.N. Botev, L.I. Burova, *Superlattices Microstruct.* 38 (2005) 272.
- [10] K.Y. Cheong, N. Muti, S.R. Ramanan, *Thin Solid Films* 410 (2002) 142.
- [11] R.F. Silva, M.E.D. Zaniquelli, *Thin Solid Films* 449 (2004) 86.
- [12] K.T.R. Reddy, T.B.S. Reddy, I. Forbes, R.W. Miles, *Surf. Coat. Technol.* 151-152 (2002) 110.
- [13] A. Mosbah, A. Moustaghfir, S. Abed, N. Bouhssira, M.S. Aida, E. Tomasella, M. Jacquet, *Surf. Coat. Technol.* 200 (2005) 293.
- [14] J. Mass, P. Bhattacharya, R.S. Katiyar, *Mater. Sci. Eng. B.* 103 (2003) 9.
- [15] K. Ellmer, F. Kudella, R. Mientus, R. Schieck, S. Fiechter, *Thin Solid Films* 247 (1994) 15.
- [16] T. Minami, *Thin Solid Films* 516 (2008) 1314.
- [17] O. Kluth, G. Schöpe, B. Rech, R. Menner, M. Oertel, K. Orgassa, H.W.

- Schock, *Thin Solid Films* 502 (2006) 311.
- [18] Q.B. Ma, Z.Z. Ye, H.P. He, S.H. Hu, J.R. Wang, L.P. Zhu, Y.Z. Zhang, B.H. Zhao, *J. Cryst. Growth* 304 (2007) 64.
- [19] X. Yu, J. Ma, F. Ji, Y. Wang, C. Cheng, H. Ma, *Appl. Surf. Sci.* 245 (2005) 310.
- [20] W.J. Jeong, S.K. Kim, G.C. Park, *Thin Solid Films* 506 (2006) 180.
- [21] O. Kluth, G. Schöpe, J. Hüpkes, C. Agashe, J. Müller, B. Rech, *Thin Solid Films* 442 (2003) 80.
- [22] E. Burstein, *Physiol. Rev.* 93 (1954) 632.

Table. 3.1. Optical band gap values of the AZO films deposited at various process parameters.

Temperature (°C)	Optical band gap (eV)				
	Pure Ar	O ₂ /Ar=1.23%	O ₂ /Ar=1.64%	O ₂ /Ar=3.23%	O ₂ /Ar-9.09%
RT	3.36	3.40	3.36	3.28	3.28
150	3.60	3.49			
200	3.66	3.60			
250	3.70	3.68	3.57	3.49	3.30
300	3.67	3.67			
350	3.61	3.56			

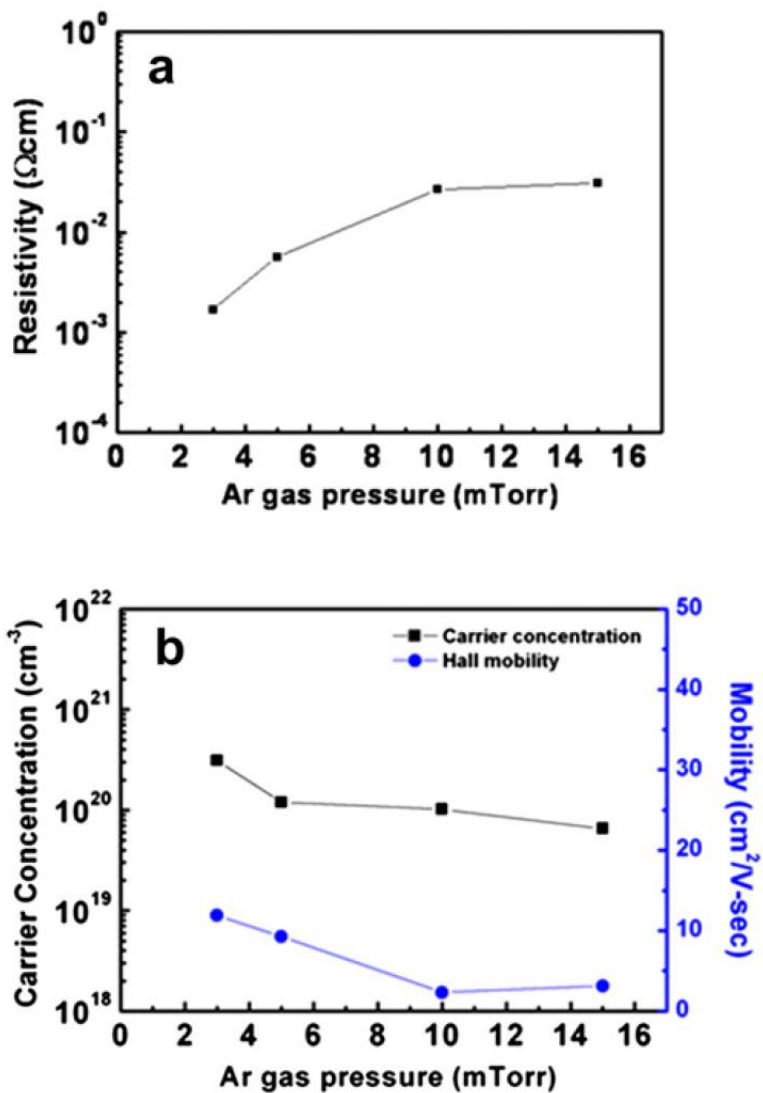


Fig. 3.1. (a) Resistivity, (b) carrier concentration and Hall mobility of the AZO films deposited at various argon gas pressures.

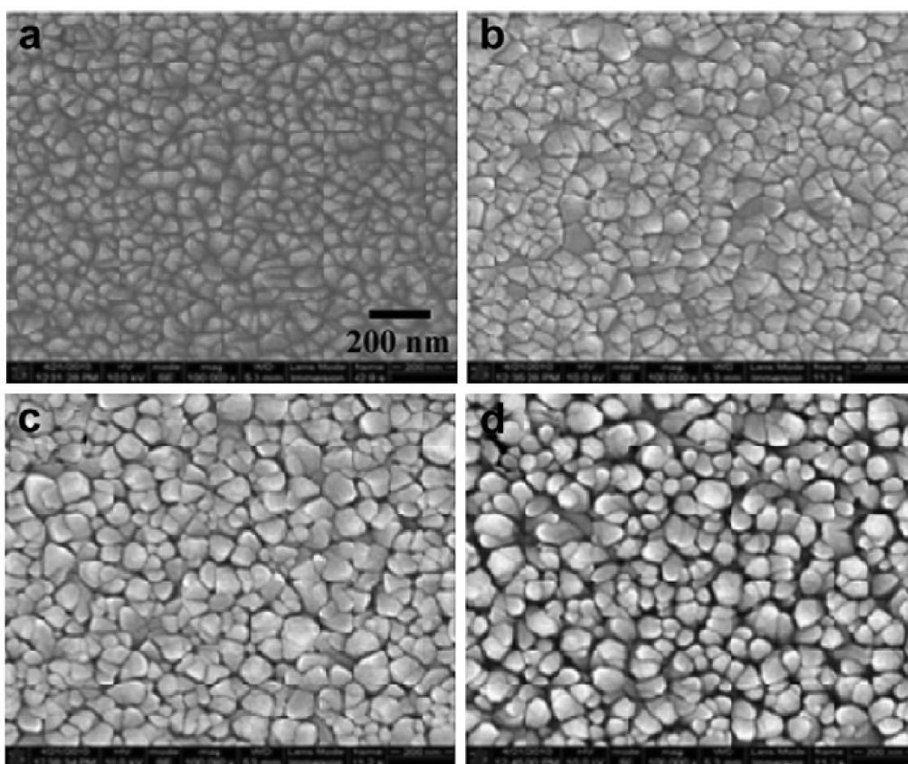


Fig. 3.2. FE-SEM images of the AZO films deposited at argon gas pressures of (a) 3 mTorr, (b) 5 mTorr, (c) 10 mTorr and (d) 15 mTorr.

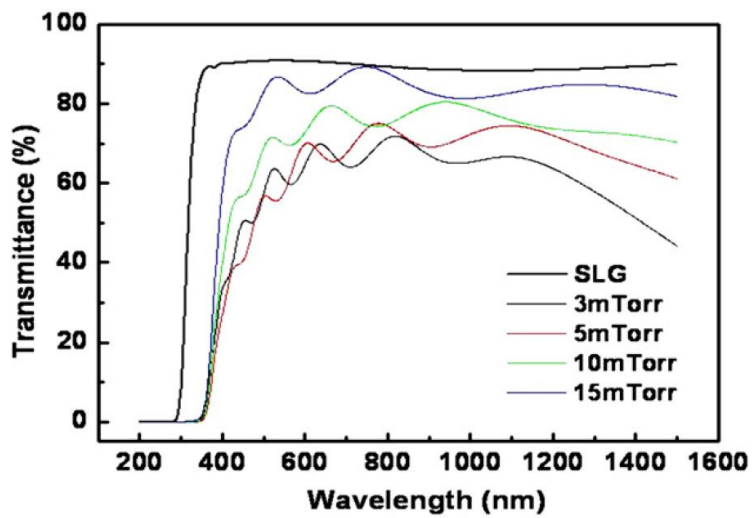


Fig. 3.3. Optical transmittance spectra of the AZO films depending on argon gas pressure in the visible and near-infrared wavelength region.

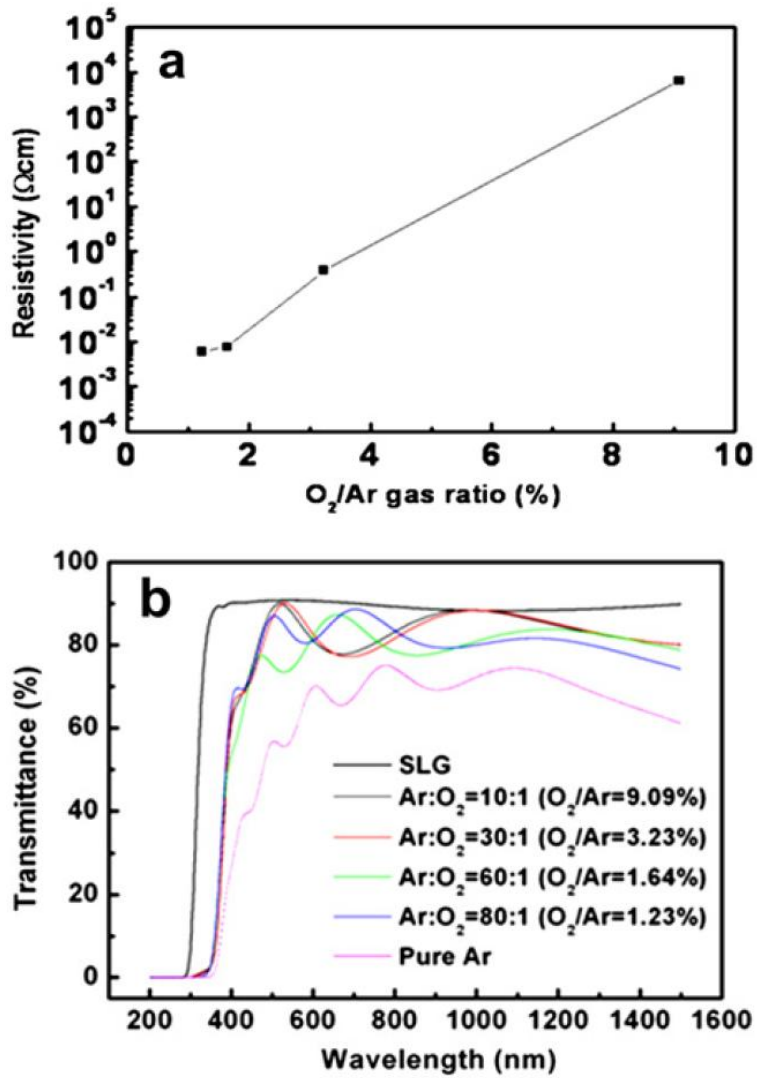


Fig. 3.4. (a) Resistivity and (b) transmittance of the AZO films deposited at room temperature with various O₂/Ar gas ratios.

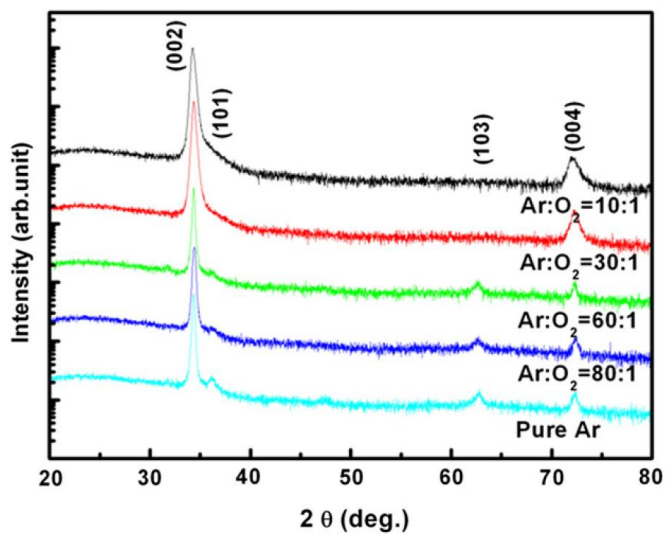


Fig. 3.5. XRD patterns of the AZO films deposited at room temperature with various O₂/Ar gas ratios.

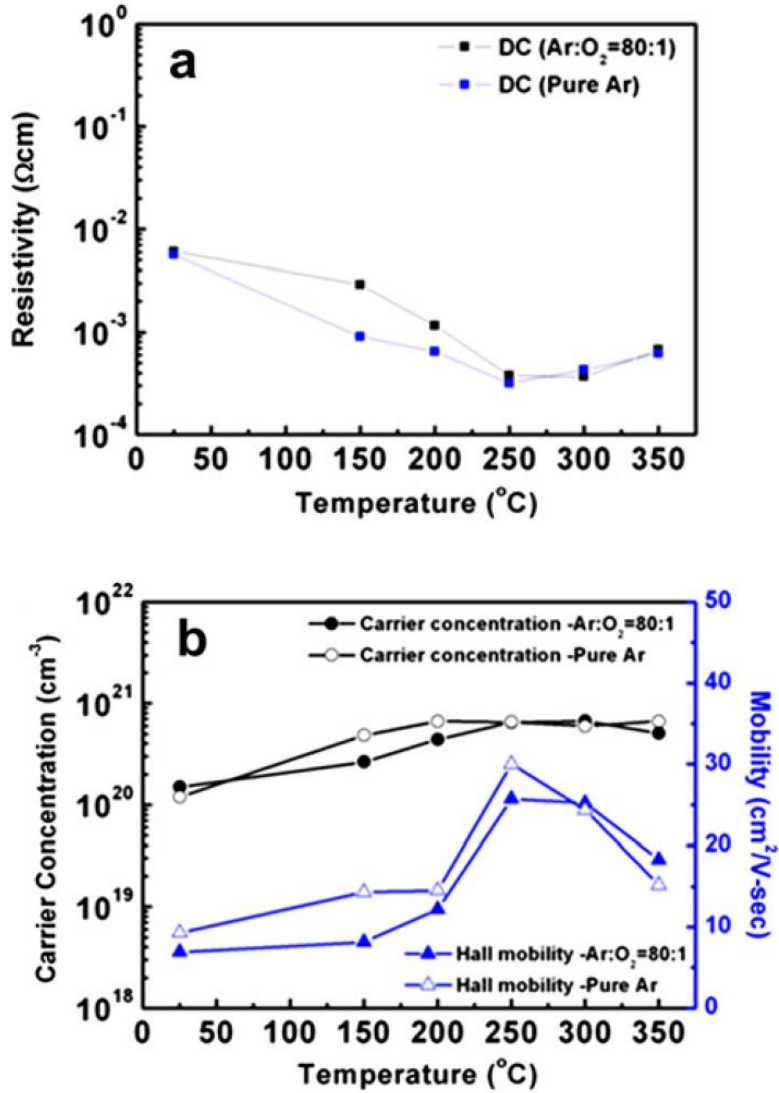


Fig. 3.6. (a) Resistivity, (b) carrier concentration and Hall mobility of the AZO films depending on the substrate temperature.

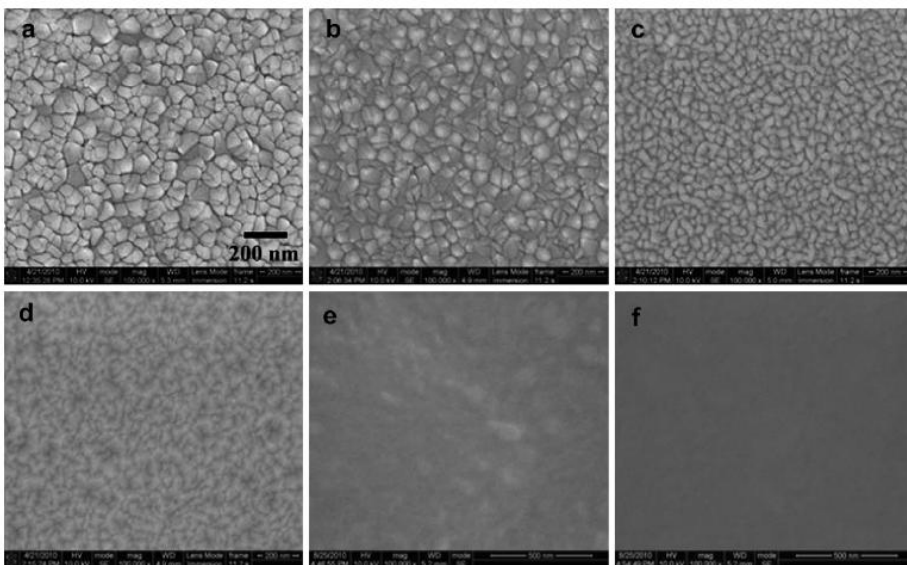


Fig. 3.7. FE-SEM images of the AZO films deposited at substrate temperature of (a) room temperature, (b) 150 °C, (c) 200 °C, (d) 250 °C, (e) 300 °C and (f) 350 °C under pure argon gas pressure.

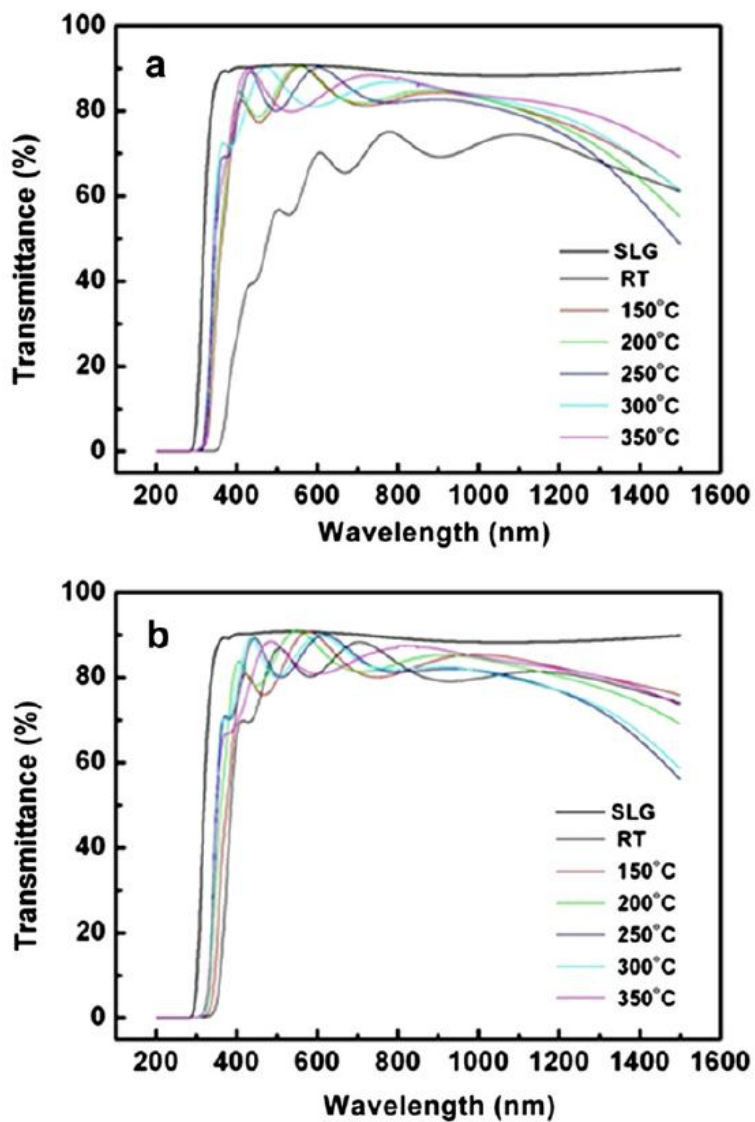


Fig. 3.8. Transmittance spectra of the AZO films deposited at various temperatures in (a) pure Ar and (b) O₂/Ar gas ratio of 1.23%.

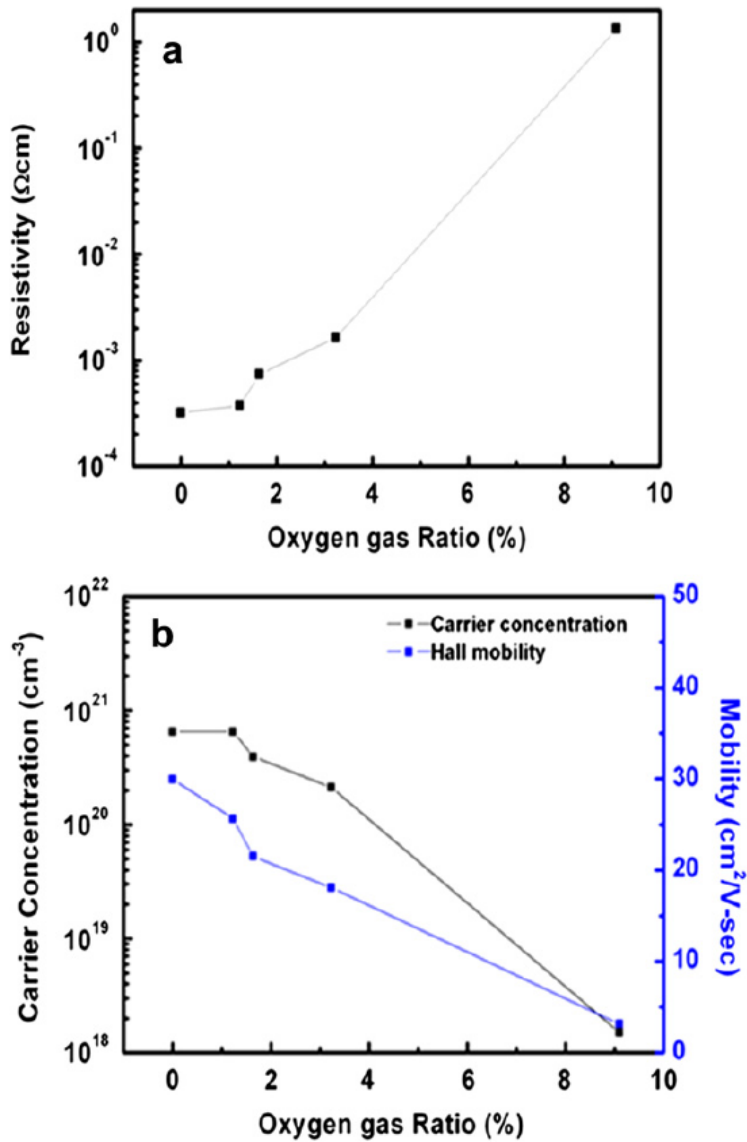


Fig. 3.9. (a) Resistivity, (b) carrier concentration and Hall mobility of the AZO films deposited at 250 °C with various O₂/Ar gas ratios.

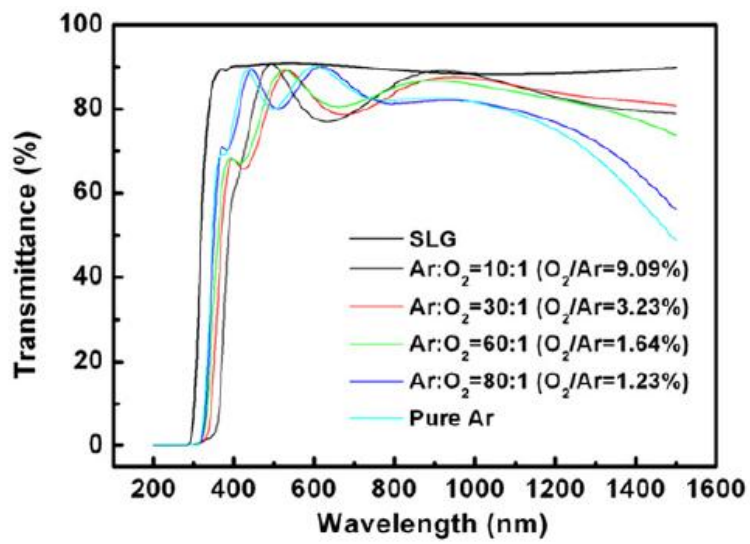


Fig. 3.10. Transmittance spectra of the AZO films deposited at 250 °C with various O₂/Ar gas ratios.

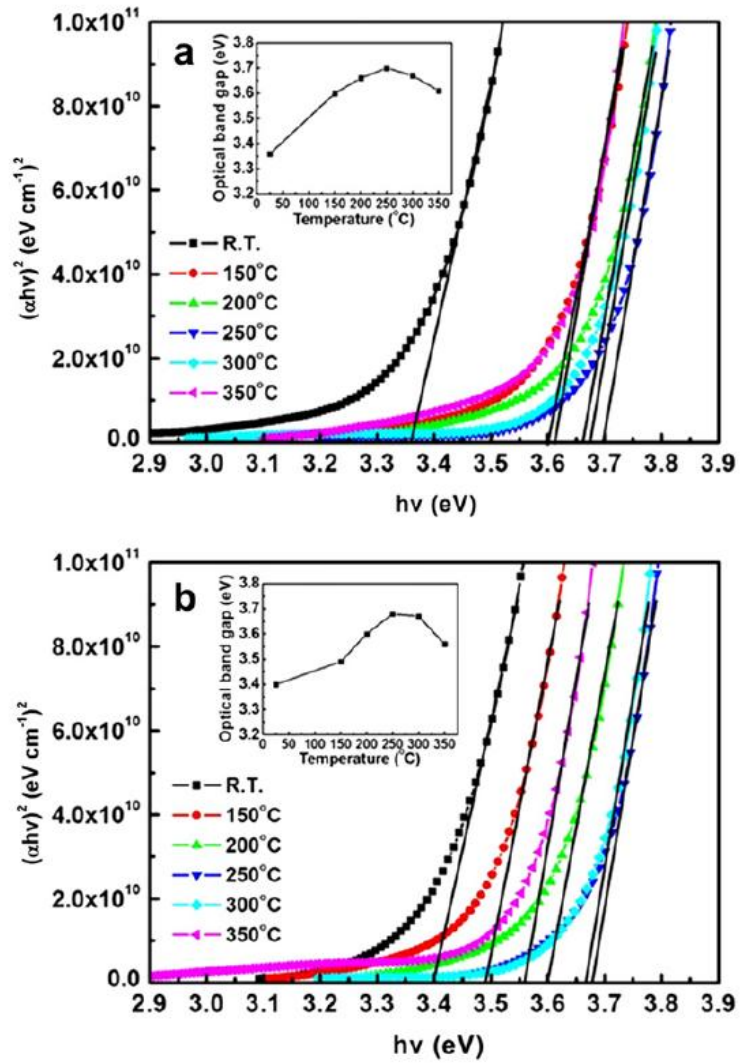


Fig. 3.11. Optical band gap of the AZO films deposited at various substrate temperatures in (a) pure Ar and (b) O₂/Ar gas ratio of 1.23%.

Chapter 4. CIGS absorber layers prepared by RF sputtering without selenization for CIGS solar cells

4.1. Introduction

Cu(In_{1-x}Ga_x)Se₂ (CIGS) thin film solar cell has attracted great attention as one of the most promising solar cells mainly due to its high conversion efficiency which can be achieved via direct band gap characteristics, high absorption coefficient, and ease in band gap engineering of CIGS film. It also has the advantages of excellent resistance to high energy radiation and long-term outdoor stability. However, a very complicated fabrication process, so-called three-stage co-evaporation process, is required for the achievement of the highest conversion efficiency of ~20% [1-3]. In addition, this method has a difficulty to produce large-area film with uniform composition. Meanwhile, a two-step process, which includes deposition of the metal precursor film by sputtering and selenization process, has been studied by many research groups since uniform films with large area can be fabricated through this process. To date, various sputtering methods such as co-sputtering [4, 5] and sequential sputtering [6-8] using separate elemental targets or metal alloy targets have been used for preparing the metal precursor films. And also, single quaternary CIGS target has been recently used for fabricating the CIGS precursor film [9] via one-step process. This one-step process is very easy to obtain large-area

CIGS films with uniform composition because this process simplifies the fabrication process by reducing the number of targets. However, this method still needs the post-selenization process. In general, H₂Se gas is used as a Se source for selenization. However, H₂Se gas is highly toxic for health and environment. Also, selenium is wasted during selenization process. As the other drawback, this process is difficult to control the composition which can influence the band gap of CIGS film because the composition of CIGS film can be changed after selenization. Therefore, to overcome these drawbacks, one-step fabrication of CIGS absorber layer without selenization is needed. Until now, however, the efficiency of the CIGS solar cell fabricated via one-step process without selenization has been rarely reported [10-11], which motivated present study.

In this study, CIGS absorber layers were fabricated via RF magnetron sputtering employing single quaternary CIGS targets with various compositions without selenization. The phases and microstructures of the CIGS absorber layers were investigated and the performance of the CIGS solar cell fabricated by applying these absorber layers is examined.

4.2. Experimental

Various single CIGS sputtering targets with the nominal compositions of Cu_x(In_{0.7}Ga_{0.3})Se_y (where x=0.95 and 1, y=2 to 2.5) were fabricated by conventional solid state reaction using CIGS powder synthesized by planetary ball milling. Employing these targets, CIGS absorbers were deposited on Mo coated soda lime glass (SLG) substrates by RF magnetron

sputtering without selenization. Base pressure of vacuum chamber before deposition was approximately 3.0×10^{-6} Torr. Substrate rotation was carried out at 3 rpm for film uniformity.

First, properties of the CIGS films fabricated via the single CIGS sputtering target with the nominal composition of $\text{Cu}(\text{In}_{0.7}\text{Ga}_{0.3})\text{Se}_2$ were investigated. The CIGS films were deposited with RF power of 190W under argon gas pressure of 10mTorr at room temperature (R.T.), and then post- annealed in Ar atmosphere. Also, CIGS films were deposited at various temperatures ranging from 300 to 450 °C.

Second, properties of the CIGS films fabricated via single CIGS sputtering targets with the nominal compositions of $\text{Cu}_{0.95}(\text{In}_{0.7}\text{Ga}_{0.3})\text{Se}_{2.5}$ and $\text{Cu}_{0.95}(\text{In}_{0.7}\text{Ga}_{0.3})\text{Se}_{2.1}$ were investigated. The CIGS films were deposited at various temperatures under argon gas pressure of 10mTorr with RF power of 190W and 120W, respectively.

Finally, properties of the CIGS films prepared via the single target of $\text{Cu}(\text{In}_{0.7}\text{Ga}_{0.3})\text{Se}_{2.5}$ powder were investigated. The CIGS films were deposited with RF power of 120W under argon gas pressure of 10mTorr at the temperatures ranging from room temperature (R.T.) to 500 °C. After deposition, the CIGS films were annealed at 450 °C for 30min in Ar atmosphere with Se.

Using the fabricated CIGS absorber layers, the CIGS thin film solar cells with the structure of Al/AZO/i-ZnO/CdS/CIGS/Mo/SLG were fabricated to measure the conversion efficiency. A 50nm-thick CdS layer was coated by chemical bath deposition. A 50nm-thick intrinsic ZnO and a 400nm-thick Al-doped ZnO (2 wt% Al_2O_3) layers were sequentially deposited by using RF

magnetron sputtering. Al grids for the enhancement of carrier collection were deposited by thermal evaporation. The cell area defined by mechanical scribing was approximately 0.36 cm².

Crystal structures of the CIGS films were investigated by x-ray diffraction (XRD) with Cu-K α radiation. Surface morphologies and cross-sectional images were observed via field emission scanning electron microscopy (FESEM). Compositional analysis of CIGS films was performed by inductively coupled plasma (ICP) spectrometer. Resistivity and Hall resistance are measured by Hall effect measurement system. Conversion efficiency of the CIGS thin film solar cell was measured by a solar simulator under AM 1.5 illumination.

4.3. Results and discussion

4.3.1. CIGS layers prepared using the single CIGS targets of various compositions

Fig. 4.1 (a) shows the surface morphology of the CIGS film deposited at room temperature by using a stoichiometric CIGS (Cu(In_{0.7}Ga_{0.3})Se₂) target. And Figs. 4.1 (b), (c) and (d) show the surface morphologies of the CIGS films annealed in an Ar atmosphere at the temperatures of 400, 500 and 600 °C, respectively. As can be seen in figures, grain growth did not occur regardless of the annealing temperature when the CIGS precursor film was annealed in an Ar atmosphere. Therefore, the CIGS films were deposited at various temperatures ranging from 300 to 450 °C. As shown in Fig. 4.2, grain

size was increased with increasing a deposition temperature. However, rough and porous surface morphology with the faceted grains was obtained. Using these CIGS films, the CIGS thin film solar cells with the structure of Al/AZO/i-ZnO/CdS/CIGS/Mo/SLG were fabricated. Fig. 4.3 shows the current-voltage characteristics under AM 1.5 illumination. Very low efficiencies were obtained from the CIGS solar cells fabricated using a stoichiometric CIGS target.

For enhancing the efficiency and obtaining the smooth surface morphology, various CIGS targets with the nominal compositions of $\text{Cu}_{0.95}(\text{In}_{0.7}\text{Ga}_{0.3})\text{Se}_{2.5}$ and $\text{Cu}_{0.95}(\text{In}_{0.7}\text{Ga}_{0.3})\text{Se}_{2.1}$ were used. Figs. 4.4 and 4.5 show the CIGS films fabricated by using $\text{Cu}_{0.95}(\text{In}_{0.7}\text{Ga}_{0.3})\text{Se}_{2.5}$ and $\text{Cu}_{0.95}(\text{In}_{0.7}\text{Ga}_{0.3})\text{Se}_{2.1}$ target. As can be seen in Fig. 4.4 (a) and Fig. 4.5 (a), grain size of these films was smaller than that of the CIGS film fabricated using a stoichiometric CIGS target. This result is thought to be caused by Cu-poor composition of these CIGS targets. A smaller quantity of copper in the CIGS film can suppress the formation of the Cu_{2-x}Se phase which is known to increase grain size. Therefore, the CIGS films with a smoother surface morphology can be obtained by using Cu-poor CIGS targets. However, surface morphology becomes rough with increasing deposition temperature as shown in Fig. 4.5 (b), (c) and (d). And all of the films showed the faceted grains similar to those of the CIGS film fabricated using a stoichiometric CIGS target although grain size is smaller.

Meanwhile, XRD patterns of these CIGS films were investigated. As shown in Fig. 4.6, the CIGS films were crystalized to a random orientation. And the second phase of $(\text{In,Ga})_2\text{Se}_3$ was detected in all of the CIGS films. Peak

intensity of the second phase was decreased with increasing deposition temperature. Eventually, the diffraction peak of $(\text{In,Ga})_2\text{Se}_3$ phase almost disappeared and the CIGS film shows chalcopyrite structure which can be characterized by peaks such as (101), (103), (211), (213)/(105) and (301).

Conversion efficiency of the CIGS solar cells fabricated by using these CIGS absorber layers was measured. Although the CIGS films have chalcopyrite structure with high crystallinity, very low conversion efficiencies were achieved. As shown in Fig. 4.7, the highest conversion efficiency of about 2% was obtained from the CIGS solar cell fabricated using the $\text{Cu}_{0.95}(\text{In}_{0.7}\text{Ga}_{0.3})\text{Se}_{2.5}$ target. However, the CIGS solar cells fabricated using the $\text{Cu}_{0.95}(\text{In}_{0.7}\text{Ga}_{0.3})\text{Se}_{2.1}$ target, containing the smaller quantity of Se, showed the lower conversion efficiency as shown in Fig. 4.7.

Low conversion efficiency of these solar cells is thought to be caused by Se-poor composition of these CIGS films as well as rough surface morphology. Fig. 4.8 shows the ternary phase diagram of the CIGS films fabricated in this study. Comparing with initial composition of CIGS targets, selenium was rather decreased. This means that supplement of additional selenium is needed for the stoichiometric a-CIS phase

4.3.2 CIGS layers prepared using the single target of $\text{Cu}(\text{In}_{0.7}\text{Ga}_{0.3})\text{Se}_{2.5}$ powder

For reducing a Se loss and increasing a Se amount of CIGS film, the CIGS films were prepared by using the single target of $\text{Cu}(\text{In}_{0.7}\text{Ga}_{0.3})\text{Se}_{2.5}$ powder. The CIGS target did not go through sintering process to impede a vaporation

of Se. Fig. 4.9 shows the SEM images of the CIGS films deposited at various temperatures. As shown in figures, grain size was increased with increasing deposition temperature. Especially, abrupt grain growth was occurred at the deposition temperature of 400 °C. However, the CIGS films show still rough and porous surface morphology. Meanwhile, after annealing in Ar atmosphere with selenium, that is to say a selenization, grain size of all of the CIGS films was increased and denser CIGS films were obtained as shown in Fig. 4.10. XRD patterns of these CIGS films were investigated. Fig. 4.11 (a) and (b) show the XRD patterns of the CIGS film before and after selenization, respectively. All of the CIGS films deposited above 350 °C had the second phase of $(\text{In,Ga})_2\text{Se}_3$ as well as the CIGS phase. And the CIGS films showed a (220)/(204) preferred orientation. This can be caused by Se-rich composition of the CIGS film. After selenization, the second phase of $(\text{In,Ga})_2\text{Se}_3$ disappeared and the intensity of (112) orientation was increased. This means that the CIGS films had been recrystallized by the incorporation of selenium. On the other hand, the MoSe_2 layer was created. A MoSe_2 layer is known to enhance the efficiency by forming the ohmic contact between the CIGS layer and the Mo electrode layer [12,13]. However, very thick MoSe_2 layer is detrimental to the conversion efficiency [14].

Resistivity and Hall resistance are measured by Hall effect measurement system. Fig. 4.12 (a) shows the resistivity before and after selenization of the CIGS film as a function of deposition temperature. Before selenization, the CIGS films have high resistivity. After selenization, however, resistivity of the films was greatly decreased. And Figs 4.12 (b) and (c) show the Hall resistance after selenization of the CIGS films deposited at 400 and 450 °C,

respectively. All of the CIGS films show the positive slope in the properties of Hall resistance versus magnetic field. This means that the CIGS films have the p-type conductivity.

Conversion efficiency of the CIGS solar cells fabricated by using these CIGS absorber layers was measured. Fig. 4.13 shows the current-voltage characteristics of the CIGS solar cells. And their conversion efficiencies were summarized in the table 4.1. After selenization, the highest conversion efficiency of about 3.3% was obtained from the CIGS solar cell fabricated using the CIGS film deposited at 400 °C.

Consequently, selenization process is beneficial to efficiency enhancement because of improvement of structural and electrical properties.

4.4. Summary

Various single CIGS sputtering targets with the nominal compositions of $\text{Cu}_x(\text{In}_{0.7}\text{Ga}_{0.3})\text{Se}_y$ ($x=0.95\sim 1$, $y=2\sim 2.5$) were fabricated. Employing these targets, CIGS films were deposited on Mo coated soda lime glass (SLG) substrates by using RF magnetron sputtering. In the case of CIGS film fabricated using a stoichiometric CIGS target, grain growth of the CIGS film deposited at room temperature did not occur regardless of the annealing temperature when the CIGS precursor film was annealed in an Ar atmosphere. Grain size of the CIGS films deposited at various temperatures was increased with increasing a deposition temperature. However, rough and porous surface morphology with the faceted grains was obtained and therefore very low efficiencies were achieved. For enhancing the efficiency and obtaining the

smooth surface morphology, various CIGS targets with the nominal compositions of $\text{Cu}_{0.95}(\text{In}_{0.7}\text{Ga}_{0.3})\text{Se}_{2.5}$ and $\text{Cu}_{0.95}(\text{In}_{0.7}\text{Ga}_{0.3})\text{Se}_{2.1}$ were used to fabricate CIGS absorber layer. Grain size of these films was smaller than that of the CIGS film fabricated using a stoichiometric CIGS target. This result is thought to be caused by Cu-poor composition of these CIGS targets. Although the CIGS films with a smoother surface morphology can be obtained by using Cu-poor CIGS targets, surface morphology becomes rough with increasing deposition temperature. Conversion efficiency of about 2% was obtained from the CIGS solar cell fabricated using the $\text{Cu}_{0.95}(\text{In}_{0.7}\text{Ga}_{0.3})\text{Se}_{2.5}$ target. However, the CIGS solar cells fabricated using the $\text{Cu}_{0.95}(\text{In}_{0.7}\text{Ga}_{0.3})\text{Se}_{2.1}$ target, containing the smaller quantity of Se, showed the lower conversion efficiency. Meanwhile, for supplement of selenium, CIGS films fabricated by using the single target of $\text{Cu}(\text{In}_{0.7}\text{Ga}_{0.3})\text{Se}_{2.5}$ powder were annealed in Ar atmosphere with selenium. These films showed the densely packed surface morphology. Conversion efficiency of the solar cells fabricated using these CIGS films was enhanced. Consequentially, selenization process is beneficial to improvement of structural and electrical properties. Hence, in the next study, the effect of selenization of CIGS precursor film was systematically investigated.

References

- [1] I. Repins, M. A. Contreras, B. Egaas, C. DeHart, J. Scharf, C. L. Perkins, B. To, R. Noufi, *Prog. Photovolt: Res. Appl.* 16 (2008) 235.
- [2] P. Jackson, D. Hariskos, E. Lotter, S. Paetel, R. Wuerz, R. Menner, W. Wischmann, M. Powalla, *Prog. Photovolt. Res. Appl.* 19 (2011) 894.
- [3] M. A. Green, K. Emery, Y. Hishikawa, W. Warta, E. D. Dunlop, *Prog. Photovolt. Res. Appl.* 22 (2014) 1.
- [4] S.D. Kim, H.J. Kim, K.H. Yoon, J. Song, *Sol. Energy Mater. Sol. Cells* 62 (2000) 357.
- [5] D.G. Moon, S. Ahn, J.H. Yun, A. Cho, J. Gwak, S. Ahn, K. Shin, K. Yoon, H.D. Lee, H. Pak, S. Kwon, *Sol. Energy Mater. Sol. Cells* 95 (2011) 2786.
- [6] M. Marudachalam, H. Hichri, R. Klenk, R.W. Birkmire, W.N. Shafarman, *Appl. Phys. Lett.* 67 (1995) 3978.
- [7] T. Nakada, A. Kunioka, *Jpn. J. Appl. Phys.* 37 (1998) L1065.
- [8] W. Li, Y. Sun, W. Liu, L. Zhou, *Solar Energy* 80 (2006) 191.
- [9] J.H. Shi, Z.Q. Li, D.W. Zhang, Q.Q. Liu, Z. Sun, S.M. Huang, *Prog. Photovolt. Res. Appl.* 19 (2011) 160.
- [10] J.A. Frantz, R.Y. Bekele, V.Q. Nguyen, J.S. Sanghera, A. Bruce, S.V. Frolov, M. Cyrus, I.D. Aggarwal, *Thin Solid Films* 519 (2011) 7763.
- [11] C.H. Chen, W.C. Shih, C.Y. Chien, C.H. Hsu, Y.H. Wu, C.H. Lai, *Sol. Energy Mater. Sol. Cells* 103 (2012) 25.
- [12] T. Wada, N. Kohara, S. Nishiwaki, T. Negami, *Thin Solid Films* 387 (2001) 118.
- [13] L. Assmann, J. C. Bernede, A. Drici, C. Amory, E. Halgand, M. Morsli, *Appl. Surf. Sci.* 171 (2001) 15.
- [14] X. Zhu, Z. Zhou, Y. Wang, L. Zhang, A. Li, F. Huang, *Sol. Energy Mater. Sol. Cells* 101 (2012) 57.

Table. 4.1. Summary of conversion efficiencies shown in Fig. 4.13.

Sample	Deposition temperature (°C)	V_{oc} (V)	J_{sc} (mA/cm ²)	FF (%)	η (%)
A	R. T.	0.164	15.15	26.7	0.67
B	350	0.085	16.44	25.9	0.36
C	400	0.339	21.40	45.3	3.29
D	450	0.325	17.21	36.1	2.02
E	500	0.307	20.38	35.4	2.21

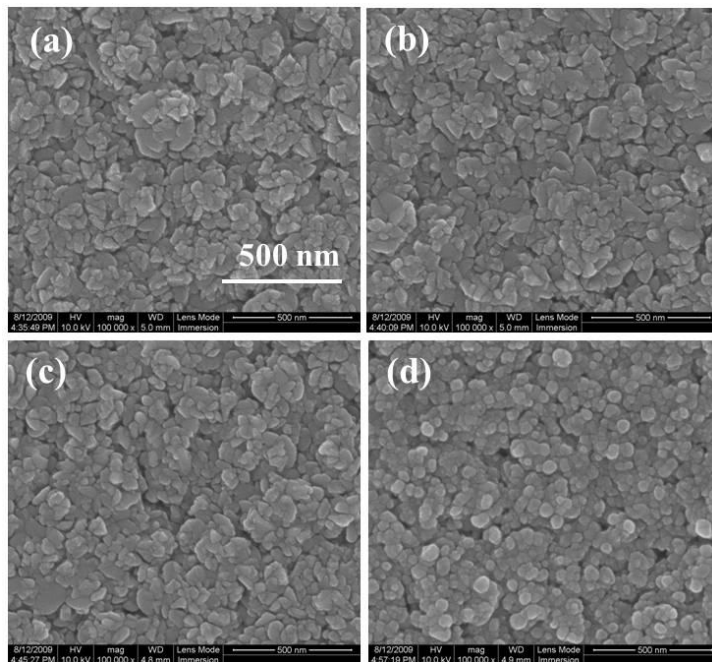


Fig. 4.1. Surface morphology of the CIGS film deposited at (a) room temperature and the CIGS films annealed at (b) 400 °C (c) 500 °C and (d) 600 °C in an Ar atmosphere. The CIGS film was fabricated using a stoichiometric CIGS ($\text{Cu}(\text{In}_{0.7}\text{Ga}_{0.3})\text{Se}_2$) target.

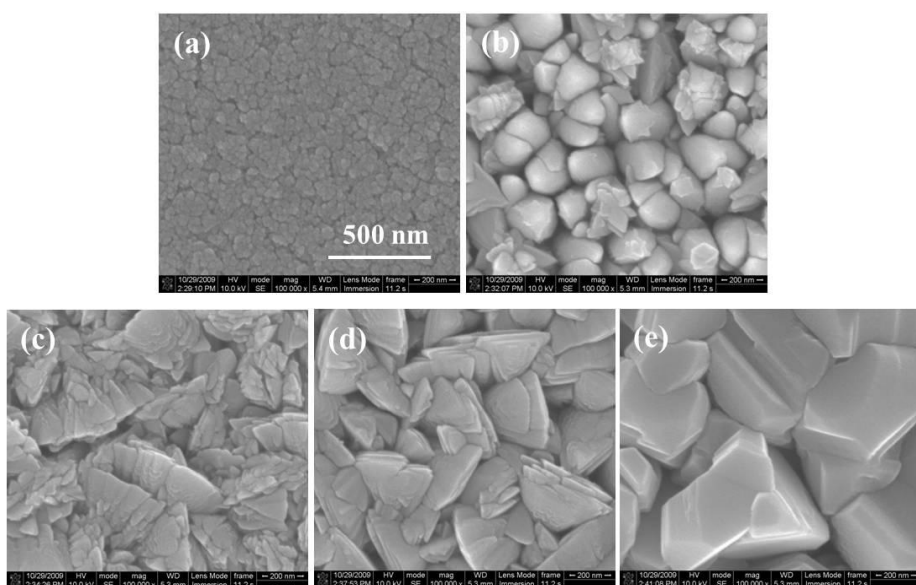


Fig. 4.2. Surface morphology of the CIGS films deposited at (a) room temperature, (b) 300 °C, (c) 350 °C, (d) 400 °C and (e) 450 °C. The CIGS film was fabricated using a stoichiometric CIGS ($\text{CuIn}_{0.7}\text{Ga}_{0.3}\text{Se}_2$) target.

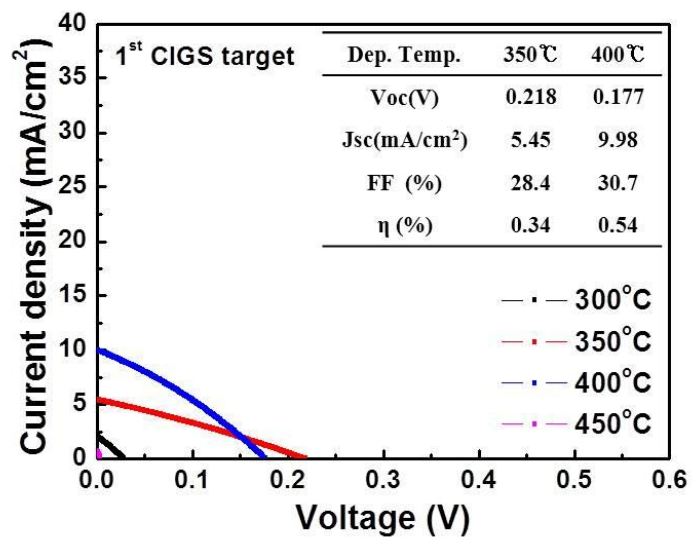


Fig. 4.3. Current-voltage characteristics of the CIGS solar cells fabricated using a stoichiometric CIGS ($\text{Cu}(\text{In}_{0.7}\text{Ga}_{0.3})\text{Se}_2$) target. The CIGS absorber layers were deposited at the temperatures of 300, 350, 400 and 450 °C, respectively.

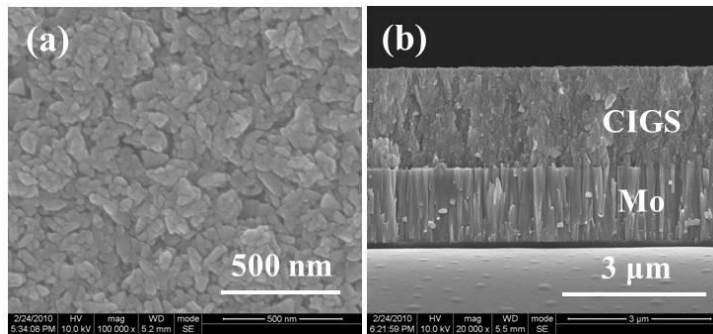


Fig. 4.4. Surface morphology and cross-sectional image of the CIGS films fabricated using a $\text{Cu}_{0.95}(\text{In}_{0.7}\text{Ga}_{0.3})\text{Se}_{2.5}$ target. The CIGS film was deposited at 300 °C.

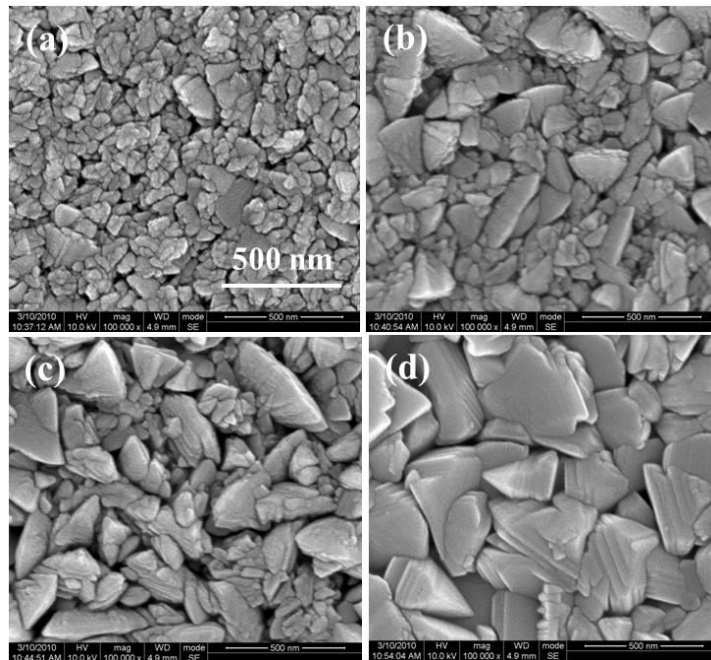


Fig. 4.5. Surface morphology of the CIGS films deposited at (a) 300 °C, (b) 350 °C, (c) 400 °C and (d) 450 °C. The CIGS film was fabricated using a $\text{Cu}_{0.95}(\text{In}_{0.7}\text{Ga}_{0.3})\text{Se}_{2.1}$ target.

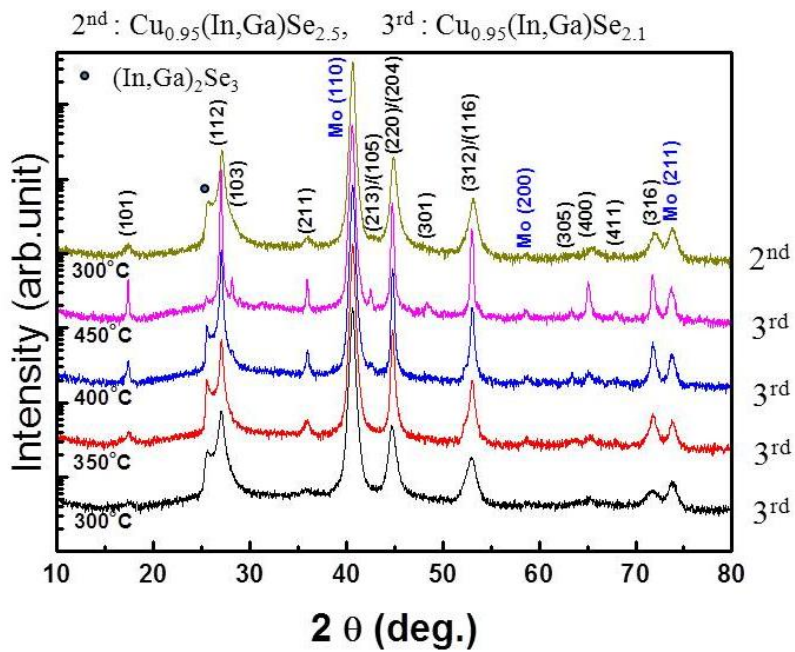


Fig. 4.6. XRD patterns of the CIGS films fabricated using $\text{Cu}_{0.95}(\text{In}_{0.7}\text{Ga}_{0.3})\text{Se}_{2.5}$ and $\text{Cu}_{0.95}(\text{In}_{0.7}\text{Ga}_{0.3})\text{Se}_{2.1}$ target.

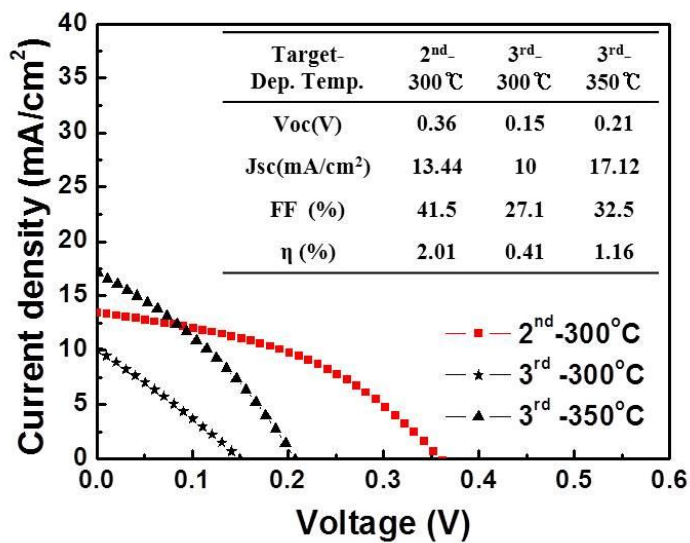


Fig. 4.7. Current-voltage characteristics of the CIGS solar cells fabricated using the $\text{Cu}_{0.95}(\text{In}_{0.7}\text{Ga}_{0.3})\text{Se}_{2.5}$ and $\text{Cu}_{0.95}(\text{In}_{0.7}\text{Ga}_{0.3})\text{Se}_{2.1}$ target. The CIGS absorber layers were deposited at the temperatures of 300 °C and 350 °C, respectively.

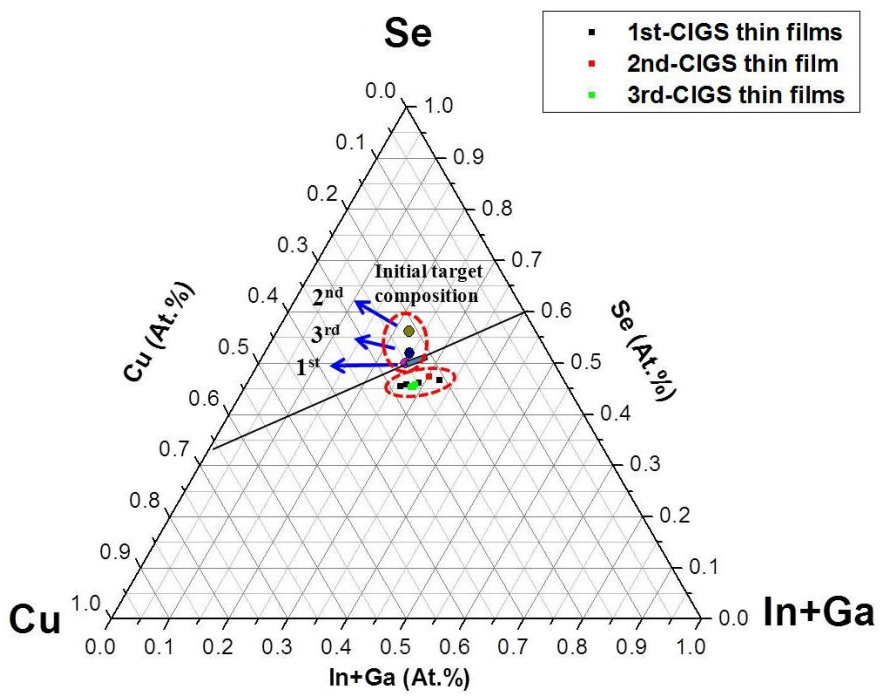


Fig. 4.8. Ternary phase diagram of the CIGS targets and the CIGS films fabricated using these CIGS targets

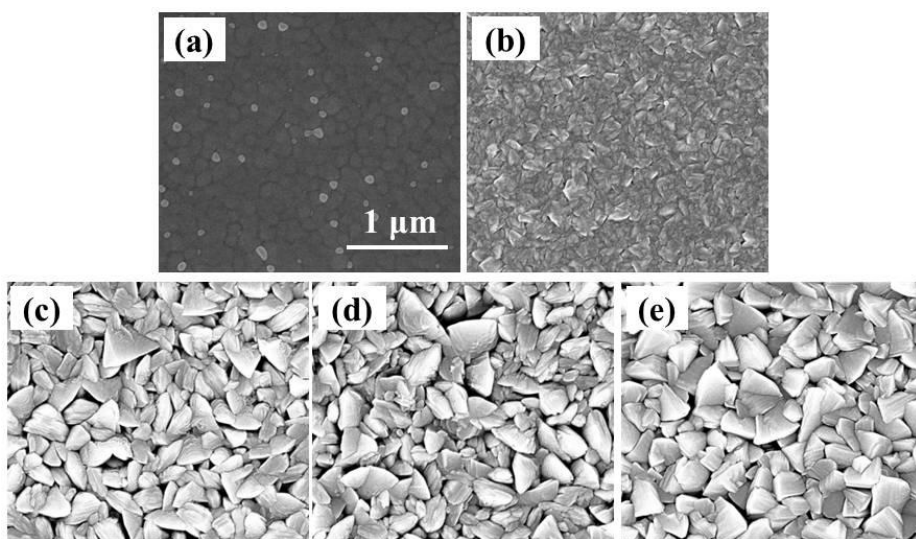


Fig. 4.9. Surface morphology of the CIGS films deposited at (a) room temperature (b) 350 °C, (c) 400 °C, (d) 450 °C and (e) 500 °C. The CIGS film was fabricated using the single target of $\text{Cu}(\text{In}_{0.7}\text{Ga}_{0.3})\text{Se}_{2.5}$ powder.

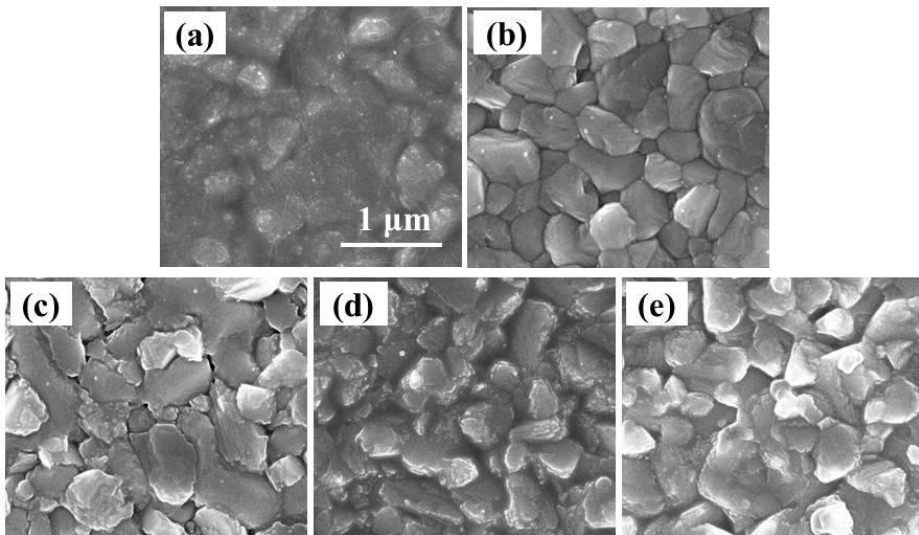


Fig. 4.10. Surface morphology after selenization of the CIGS films deposited at (a) room temperature (b) 350 °C, (c) 400 °C, (d) 450 °C and (e) 500 °C. The CIGS film was fabricated using the single target of $\text{Cu}(\text{In}_{0.7}\text{Ga}_{0.3})\text{Se}_{2.5}$ powder.

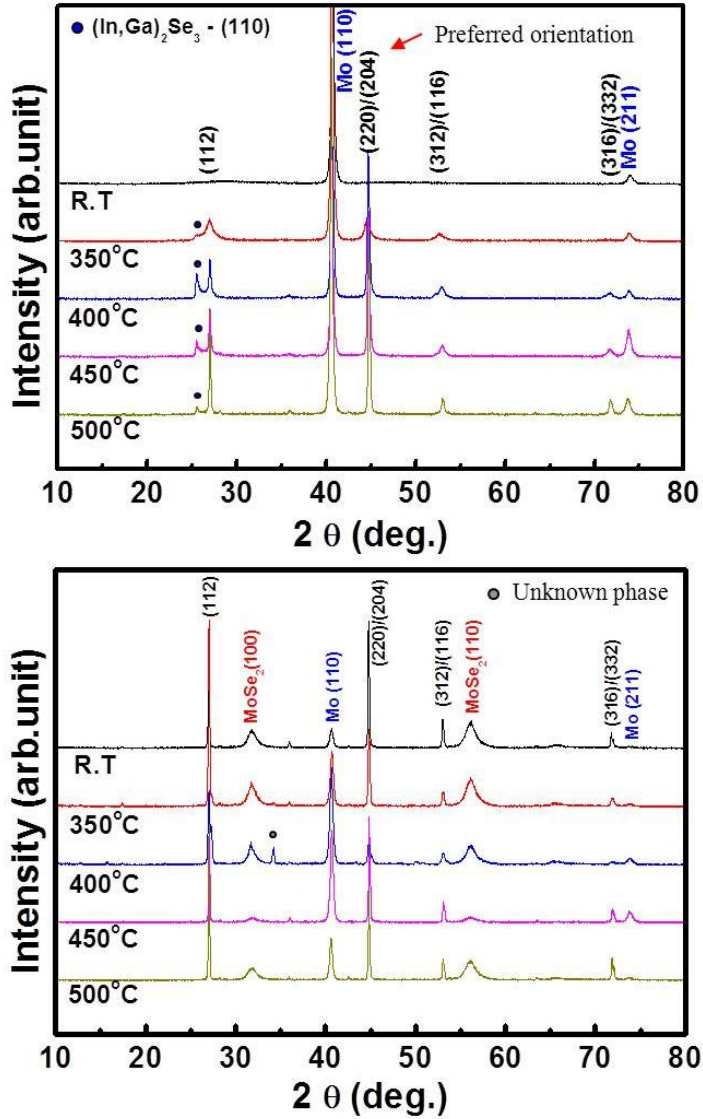


Fig. 4.11. XRD patterns (a) before and (b) after selenization of the CIGS films deposited at room temperature, 350, 400, 450 and 500 °C. The CIGS film was fabricated using the single target of $\text{Cu}(\text{In}_{0.7}\text{Ga}_{0.3})\text{Se}_{2.5}$ powder.

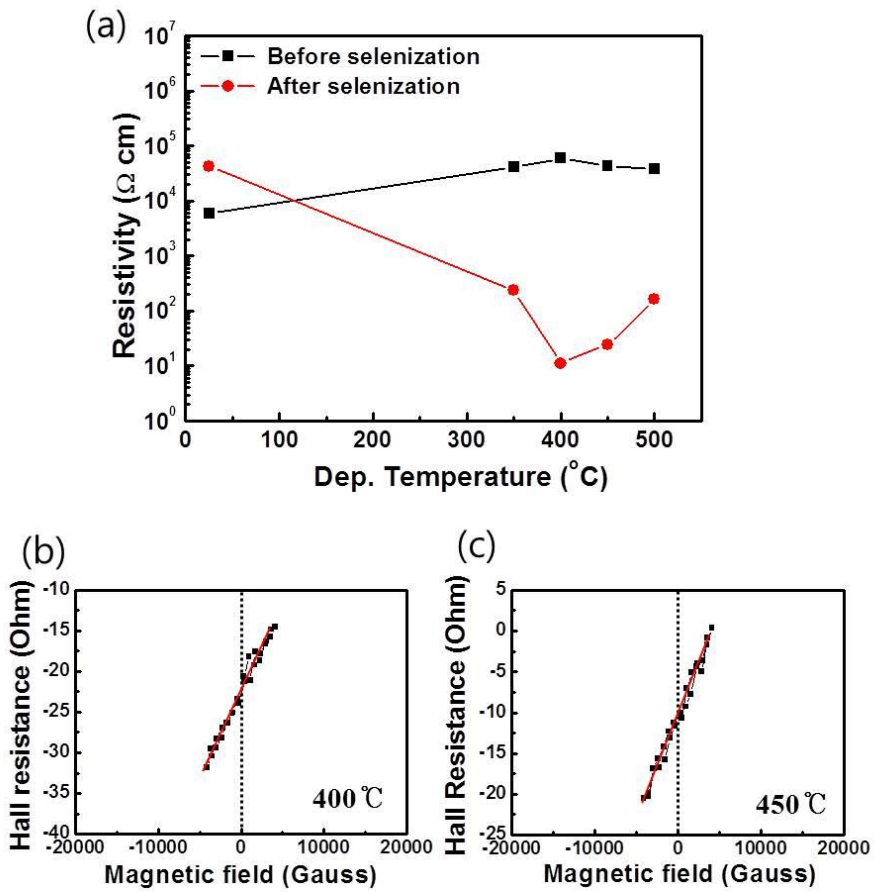


Fig. 4.12. (a) Resistivity before and after selenization of the CIGS film as a function of deposition temperature. And Hall resistance after selenization of the CIGS films deposited at (b) 400 $^{\circ}\text{C}$ and (c) 450 $^{\circ}\text{C}$.

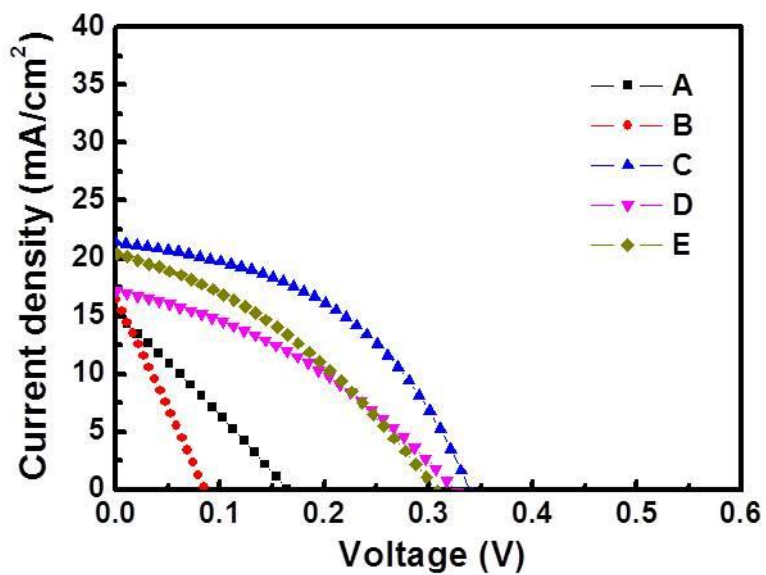


Fig. 4.13. Current-voltage characteristics of the CIGS solar cells fabricated using the single target of $\text{Cu}(\text{In}_{0.7}\text{Ga}_{0.3})\text{Se}_{2.5}$ powder. The solar cell A, B, C, D and E are fabricated after selenization CIGS precursor films deposited at the temperatures of 400, 450, 475 and 500 °C, respectively.

Chapter 5. CIGS absorber layers prepared by RF sputtering with selenization for CIGS solar cells

5.1. Introduction

Thin film solar cells have been extensively investigated to provide a low-cost solar energy because these require small consumption of raw materials. Among them, Cu(In,Ga)Se₂ (CIGS) solar cell has attracted great attention mainly due to its high conversion efficiency which can be achieved via direct band gap characteristics, high absorption coefficient and ease in band gap engineering of CIGS film. It also has the advantages of excellent resistance to high energy radiation and long-term outdoor stability. The highest conversion efficiency of ~20% has been obtained from CIGS thin films deposited by a three-stage co-evaporation method [1]. This method is very complicated and large-area film with uniform composition is difficult to obtain; hence, it is difficult to realize mass production of CIGS thin films. Meanwhile, a two-step process, which includes deposition of the metal precursor film by sputtering and selenization, has been studied by many research groups since uniform films with large area can be fabricated through this process. To date, various sputtering methods such as co-sputtering [2, 3] and sequential sputtering [4-6] using separate elemental

targets or metal alloy targets have been used for preparing the metal precursor films.

Recently, single quaternary CIGS target has been used for fabricating the CIGS precursor layer [7] or CIGS absorber layer [8, 9] via one-step process. This one-step process is very easy to obtain large-area CIGS films with uniform composition. The properties of CIGS films prepared by the one-step process using the single CIGS target are highly dependent on the characteristics of the single CIGS target. In particular, the composition of the target can affect the properties of the CIGS film because the CIGS compound is a self-doping semiconductor by point defects with low formation energy [10] and has many kinds of the second phases [11, 12]. Until now, however, the effect of composition of the single CIGS target on the properties of CIGS films and CIGS thin film solar cells has been rarely reported. Therefore, in this chapter, characteristics of the CIGS film and device fabricated using single quaternary CIGS targets with various compositions were firstly investigated. Also, in general, properties of CIGS film are greatly influenced by selenium. Therefore, characteristics of the CIGS films selenized using powders with various Se ratios were secondly examined. Based on above results, nano-crystalline CIGS precursor film was proposed to enhance the CIGS solar cell performance. Finally, the properties of the CIGS film and device fabricated using nano-crystalline CIGS precursor film were systematically investigated.

For these studies, CIGS precursor films were deposited via RF magnetron sputtering employing single quaternary CIGS targets and then selenized under Se atmosphere. The phases and microstructures of CIGS absorber

layers and their effects on the CIGS solar cell performance have been systematically investigated.

5.2. Experimental

Various single CIGS sputtering targets with the nominal compositions of $\text{Cu}_x(\text{In}_{0.7}\text{Ga}_{0.3})\text{Se}_y$ (where $x=0.9$ and 1 , $y=2$ to 2.5) were fabricated via conventional solid state reaction using CIGS powder synthesized by a planetary ball milling. Employing these targets, the CIGS precursor films were deposited on the Mo-coated soda lime glass (SLG) substrates by using RF magnetron sputtering. Base pressure of vacuum chamber was approximately 3.0×10^{-6} Torr. The CIGS precursor films were deposited with RF power of 150W under argon gas pressure of 10 mTorr at room temperature. Substrate rotation was carried out at 3 rpm for film uniformity. After deposition, these CIGS precursor films were selenized under Se atmosphere using Se powder during 30 minutes in a tube furnace at various temperatures. The CIGS precursor films fabricated by using a stoichiometric CIGS ($\text{Cu}(\text{In}_{0.7}\text{Ga}_{0.3})\text{Se}_2$) target were selenized at the temperatures ranging from 300 °C to 450 °C to investigate grain growth behavior. Other CIGS precursor films deposited by using a Cu-poor CIGS ($\text{Cu}_{0.9}(\text{In}_{0.7}\text{Ga}_{0.3})\text{Se}_2$) target or Se-excess targets with Cu-poor compositions ($\text{Cu}_{0.9}(\text{In}_{0.7}\text{Ga}_{0.3})\text{Se}_{2.2}$ and $\text{Cu}_{0.9}(\text{In}_{0.7}\text{Ga}_{0.3})\text{Se}_{2.5}$) were selenized at temperatures between 400 °C and 500 °C.

And, to investigate the effect of selenium on the properties of CIGS film and CIGS solar cell, CIGS precursor films were selenized at 475 °C during

30 minutes in various Se atmospheres controlled by mixing powders with various weight ratios of alumina to selenium of 4:1, 6:1, 8:1 and 12:1. The weight of each mixing powder was 0.6g.

Also, to fabricate the nano-crystalline CIGS precursor film, the CIGS films were deposited at the various substrate temperatures ranging from room temperature (R.T.) to 150 °C. Among these CIGS precursor films, the nano-crystalline CIGS precursor film was selected by results of XRD patterns and TEM images. Nano-crystalline CIGS precursor films were selenized at 475 °C during 30 minutes.

After selenization process, the CIGS thin film solar cells with the structure of Al/AZO/i-ZnO/CdS/CIGS/Mo/SLG were fabricated to measure the conversion efficiency. A 50 nm-thick CdS layer was coated by chemical bath deposition. A 50 nm-thick intrinsic ZnO and a 400 nm-thick Al-doped ZnO (2 wt% Al₂O₃) layers were sequentially deposited by using RF magnetron sputtering. Al grids for the enhancement of carrier collection were deposited by thermal evaporation. The cell area defined by mechanical scribing was approximately 0.36 cm².

Crystal structures of the CIGS films were investigated by x-ray diffraction (XRD) with Cu-K α radiation. Surface morphologies and cross-sectional images were observed via field emission scanning electron microscopy (FESEM) and surface roughness was investigated by atomic force microscope (AFM). Compositional analysis of CIGS films was performed by energy dispersive X-ray spectroscopy (EDS). Electron probe micro analyzer (EPMA) was used to investigate the composition mapping of a cross-section of the CIGS film. Transmission electron microscope (TEM) was used for phase analysis of nanocrystalline CIGS film. The conversion

efficiency of the CIGS thin film solar cell was measured by a solar simulator under AM 1.5 illumination at 25 °C. External quantum efficiency (EQE) of the CIGS thin film solar cell was measured to study spectral response in the wavelength ranging from 300 nm to 1200 nm.

5.3. Results and discussion

5.3.1. CIGS layers prepared using the single CIGS targets of various compositions

5.3.1.1. A CIGS target with the nominal composition of $\text{Cu}(\text{In}_{0.7}\text{Ga}_{0.3})\text{Se}_2$

Fig. 5.1 shows the surface and cross-sectional SEM images of the CIGS films fabricated by using a stoichiometric CIGS target. The as-deposited CIGS film before selenization (Fig. 5.1 (a)) showed almost featureless microstructure. After selenization, grain growth occurred and grain size was increased with increasing selenization temperature. An abrupt grain growth can be obviously noticed when the CIGS film was selenized at 425 °C, as shown in Fig. 5.1 (e). In our previous experiment (not shown here), grain growth did not occur when the CIGS film was annealed in an Ar atmosphere without Se at the same temperature as that of selenization. These results show that Se incorporation into the CIGS film plays an important role in grain growth of the CIGS precursor film. After selenization process, the MoSe_2 layer was also formed between the CIGS and the Mo layer and its thickness was increased with increasing selenization temperature.

The XRD patterns of as-deposited and selenized CIGS films fabricated by using a stoichiometric CIGS target were also investigated. As seen in Fig. 5.2, the as-deposited CIGS film is amorphous. After selenization, all of the CIGS films showed chalcopyrite structure as characterized by presence of peaks at (101), (103), (211), (213)/(105), (301), and so on. Elemental selenium peaks were simultaneously detected in the CIGS films selenized below 400 °C but disappeared when the films were selenized at higher temperatures of 425 °C and 450 °C. Crystallinity of the selenized CIGS film was enhanced with increasing selenization temperature.

Based on the results of SEM and XRD measurements shown in Figs. 5.1 and 5.2, respectively, selenization process should be performed at a temperature above 425 °C to instigate grain growth through full reaction between the Se and CIGS precursor film. Consequently, sufficient thermal energy and Se atmosphere are prerequisites to grain growth of the CIGS precursor film .

Although grain size and crystallinity of the CIGS film for solar cell application are thought to be achieved by selenization process, very low conversion efficiency of less than 0.1% was obtained. This is observed in Fig. 5.3 where the current-voltage characteristics of the CIGS solar cells were determined. This can be attributed to the inappropriate composition and rough and porous surface morphology with microscopic voids. Table 5.1 shows the composition of the CIGS films fabricated by using a stoichiometric CIGS target before and after selenization. In these films, the value of Cu/(In+Ga) was larger than that of device-quality stoichiometry ratio which is approximately 0.69~0.98 [13].

Compared to device-quality stoichiometry ratio, a larger quantity of copper

can make Cu_{2-x}Se phase which is formed from the Cu_xSe liquid phase although these phases are not detected by XRD. Therefore, grain growth could be enhanced due to the existence of Cu_xSe liquid phase [14, 15]. In general, defects responsible for recombination are much more likely to occur at surfaces and interfaces [16]. Hence, large grain size can enhance the performance of solar cell by reducing grain boundary recombination. However, the large fraction of copper in the CIGS film can easily make a p-type semi-metallic compound of Cu_{2-x}Se with high hole concentration, resulting in exceeding the optimum carrier concentration of $10^{16} \sim 10^{17}/\text{cm}^3$ [17, 18]. As a result, the CIGS film has too low resistivity and thus the cell performance is deteriorated. Therefore, very low short-circuit current density (J_{sc}) and fill factor can be caused by improper composition of the CIGS film. Also, very rough and porous surface morphology of the CIGS film can result to low open-circuit voltage (V_{oc}) and fill factor in the CIGS solar cell because of increased localized shunt path [19], which can be also affected by composition of the film.

5.3.1.2 A Cu-poor CIGS target with the nominal composition of $\text{Cu}_{0.9}(\text{In}_{0.7}\text{Ga}_{0.3})\text{Se}_2$

Therefore, the Cu-poor CIGS ($\text{Cu}_{0.9}(\text{In}_{0.7}\text{Ga}_{0.3})\text{Se}_2$) target was used to suppress the formation of Cu-Se related compounds in the CIGS film and to make a smooth surface morphology which can be achieved by using a Cu-poor composition [20]. Table 5.2 shows the composition of the CIGS films deposited by using a Cu-poor CIGS target before and after selenization. As

expected, the Cu content was decreased and the Se content was increased in these films compared to those in the films fabricated by using a stoichiometric CIGS target. In these films, the values of $\text{Cu}/(\text{In}+\text{Ga})$ were between 0.76 and 0.88 which are in the regime of device-quality stoichiometry ratio, while the values of $\text{Ga}/(\text{In}+\text{Ga})$ were identical to the films fabricated via stoichiometric CIGS target.

Fig. 5.4 shows the surface and cross-sectional SEM images of as-deposited and selenized CIGS films fabricated by using a Cu-poor CIGS target. In this case, higher selenization temperature was applied due to the result that grain growth was clearly observed above the selenization temperature of 400 °C in the case of the stoichiometric target. Compared with the case of the stoichiometric target as shown in Fig. 5.1, smaller grain size was observed when selenized at the same temperature. When selenized at 450 °C, the surface morphology was still rough and porous. However, when selenized at 475 °C and above, dense and smooth surface morphology was obtained. In this case, very thick MoSe_2 layer, detrimental to the conversion efficiency, was observed between the CIGS film and the Mo electrode layer [21]. As a whole, compared with the case of the stoichiometric target, the thicker MoSe_2 layer was formed when selenized at the same temperature. This is because the Se amount in the as-deposited film fabricated by using a Cu-poor CIGS target is relatively larger than that in the as-deposited film fabricated by using a stoichiometric CIGS target as presented in Tables 5.1 and 5.2. Therefore, the formation of MoSe_2 layer becomes easier due to short diffusion length of selenium atoms to form a MoSe_2 layer. The thickness of a MoSe_2 layer is increased with increasing selenization temperature because large thermal

energy increases the selenium mobility and reactivity to molybdenum.

Fig. 5.5 shows the XRD patterns of the CIGS films fabricated by using a Cu-poor CIGS target as a function of selenization temperature. Chalcopyrite CIGS films without the second phases were obtained at the selenization temperatures above 450 °C. However, elemental selenium peaks appeared again in the CIGS film selenized at 400 °C. Meanwhile, in the cross-sectional image of this film as shown in Fig. 5.4 (b), the thickness of the CIGS film was slightly increased. The Se content at this condition was exceptionally high as shown in Table 5.2. From these results, it is supposed that the CIGS film is not fully selenized. In other words, although selenium atoms are incorporated into the CIGS precursor film during selenization process, the reaction for crystallization and grain growth could not occur at the selenization temperature of 400 °C due to insufficient thermal energy. So, to find where the unreacted selenium atoms are, elemental distribution across cross-section of the CIGS film selenized at 400 °C was investigated. As a result, all the measured elements except Se exhibited uniform distribution along the thickness of the film. In the case of Se, a little different distribution was observed; unexpectedly, more selenium inside the film is observed compared to surrounding surface region (~200nm), as shown in Fig. 5.6. These results reveal that selenium atoms are easily diffused into the internals of the CIGS film even at 400 °C. However, as mentioned before, more thermal energy is needed to give rise to crystallization and grain growth through the reaction between Se atoms and CIGS precursor film.

Although the MoSe₂ layer in the case of a Cu-poor CIGS target was thicker than that of a stoichiometric CIGS target, the conversion efficiency was

increased by enhancement of the open-circuit voltage and short-circuit current density. This may be due to the decreased hole concentration by suppressing the formation of Cu-Se related phases and the decreased leakage current by increasing density of the CIGS film. A conversion efficiency of ~3.54% was achieved from the CIGS film selenized at 475 °C as shown in Fig. 5.7. The resulting open-circuit voltage of 0.343 V is still too low in comparison with the V_{oc} derived from the band gap (E_g) of this CIGS film of which band gap is about 1.14 eV leading to the V_{oc} of approximately 0.64 V in the solar cell with good performance, as will be described later. Lower V_{oc} of solar cell devices can be attributed to many defects and the shunting path in the CIGS film. Meanwhile, selenium atom in the CIGS film is known to decrease the defects [22, 23] and reduce the formation of the second phases composed of Cu-Se related compound when the CIGS film has a larger amount of In and Ga compared to Cu. It has been reported that the addition of selenium increases the band gap of the CIGS film [23]. Therefore, Se-excess CIGS targets with a Cu-poor composition ($Cu_{0.9}(In_{0.7}Ga_{0.3})Se_{2.2}$ and $Cu_{0.9}(In_{0.7}Ga_{0.3})Se_{2.5}$) were prepared and used to fabricate CIGS precursor films to enhance the conversion efficiency.

5.3.1.3 A Cu-poor and a Se-excess CIGS targets with the nominal compositions of $Cu_{0.9}(In_{0.7}Ga_{0.3})Se_{2.2}$ and $Cu_{0.9}(In_{0.7}Ga_{0.3})Se_{2.5}$

Figs. 5.8. (b) and 5.8. (c) show the surface morphologies of the selenized CIGS films fabricated by employing Se-excess CIGS targets with a Cu-poor composition. All films showed the faceted grains and where the grain size

was increased with increasing Se content in the CIGS target. However, grain size of these films was smaller than that of the film fabricated by employing the stoichiometric CIGS target. This result can be attributed to the Cu-poor composition of the CIGS precursor film. As mentioned above, Cu-poor composition suppresses the formation of copper selenide phase which can enhance grain growth [20].

Fig. 5.9 (a) shows the conversion efficiency of the CIGS solar cells fabricated by using Se-excess CIGS targets with a Cu-poor composition. The open-circuit voltage was increased with increasing selenium content of the CIGS target, which is due to the increased band gap of the CIGS film as shown in Fig. 5.9 (c) [23]. Among them, the highest efficiency of 6.88% was achieved from the CIGS solar cell fabricated by using the $\text{Cu}_{0.9}(\text{In}_{0.7}\text{Ga}_{0.3})\text{Se}_{2.2}$ target having an open-circuit voltage of 0.463 V, short-circuit current density of 27.95 mA/cm^2 and fill factor of 53.13%.

Spectral response, the external quantum efficiencies (EQE) of these CIGS solar cells, were measured in the wavelength ranging from 300 to 1200 nm as shown in Fig. 5.9 (b). Each spectrum was normalized with the highest value of EQE for comparison. For wavelength larger than 650 nm, relatively large EQE loss occurred in the solar cell fabricated by using the $\text{Cu}_{0.9}(\text{In}_{0.7}\text{Ga}_{0.3})\text{Se}_2$ target. This loss can be attributed to the recombination caused by defects in the CIGS absorber layer. To determine the band gap from the EQE spectrum, the relationship of $[E \ln(1-\text{EQE})]^2$ versus E is used near the band edge, where $E=h\nu$ [24]. As shown in Fig. 5.9 (c), the CIGS films fabricated by using $\text{Cu}_{0.9}(\text{In}_{0.7}\text{Ga}_{0.3})\text{Se}_2$ and $\text{Cu}_{0.9}(\text{In}_{0.7}\text{Ga}_{0.3})\text{Se}_{2.2}$ targets have very similar E_g values of 1.14 and 1.15 eV, respectively, but the CIGS film fabricated by

using $\text{Cu}_{0.9}(\text{In}_{0.7}\text{Ga}_{0.3})\text{Se}_{2.5}$ target has a higher value of 1.19 eV. Using the band gaps of the CIGS film, open-circuit voltages were calculated using $V_{oc} = E_g/q - 0.5\text{V}$ which was derived from the experimental results of V_{oc} versus E_g using the CIGS solar cells with good performance [25]. As a result, the measured V_{oc} 's were lower than the calculated ones.

To investigate the lower values of the V_{oc} in these solar cells compared to the calculated ones using the band gap, open-circuit voltages were plotted as a function of band gap as shown in Fig. 5.9 (d). Dotted line was plotted via $V_{oc} = E_g/q - 0.5\text{V}$. The CIGS solar cells fabricated in this work showed smaller V_{oc} values (0.16 ~ 0.297 V) in comparison to the calculated ones. The difference between the measured V_{oc} and the calculated one using E_g was very large in the CIGS solar cell fabricated by using the $\text{Cu}_{0.9}(\text{In}_{0.7}\text{Ga}_{0.3})\text{Se}_2$ target, but decreased with increasing the selenium content in the CIGS target.

Furthermore, the XRD patterns after selenization of the CIGS precursor films fabricated by using the three targets were investigated. As shown in Fig. 5.10, all films had the CIGS phase with chalcopyrite structure but the ordered vacancy compound (OVC) phase ($\text{Cu}(\text{In,Ga})_3\text{Se}_5$) co-existed in the CIGS films fabricated by using Se-excess CIGS targets with a Cu-poor composition. The peak intensity of the OVC phase was increased with increasing Se content in the CIGS target. The content of the OVC phase can be inferred by checking the composition of CIGS films as shown in Table 5.3. The quantity of (In+Ga) was increased and the quantity of Cu was decreased with increasing Se content in the CIGS target. This result reveals that the content of the OVC phase, consisting of smaller amount of Cu and larger amount of (In+Ga) than those of $\text{Cu}(\text{In,Ga})\text{Se}_2$ phase, is increased. The OVC phase is

well-known to have a larger band gap than that of CIS compound [26]. Therefore, coexistence of the OVC phase can increase the band gap of the CIGS absorber layer although the ratio of Ga/(In+Ga), which is a critical parameter to determine band gap, is identical. Having this in consideration, the results on the band gap obtained in this work are acceptable.

The OVC phase also plays a key role in reducing interface recombination at the interface between the CdS layer and the CIGS layer by lowering the valence band maximum (VBM) [10]. In this case, the limiting factor for the open-circuit voltage is mainly the recombination in the bulk of the absorber material [27]. Therefore, as per experimental results, decrease of the difference between the measured V_{oc} and the calculated one as shown in Fig. 5.9 (d) may be due to the fact that the OVC phase increases the band gap by lowering the VBM resulting to suppressed interface recombination.

5.3.2 Effect of selenization condition on the CIGS layers

In this chapter, the characteristics before and after selenization of the CIGS precursor films deposited using the single CIGS targets with the nominal compositions of $Cu_{0.9}(In,Ga)Se_2$ and $Cu_{0.9}(In,Ga)Se_{2.5}$ were investigated. The CIGS precursor films were selenized using mixing powders with various weight ratios of alumina to selenium. Fig. 5.11 shows SEM images before and after selenization of the CIGS films fabricated using a single quaternary CIGS target with the nominal compositions of $Cu_{0.9}(In_{0.7}Ga_{0.3})Se_2$. As shown in Fig. 5.11 (b), grain growth did not occur when the CIGS precursor film was annealed in an Ar atmosphere without Se. However, when annealed with a

small quantity of selenium, grain growth occurred and grain size was increased with increasing the Se ratio of mixing powder. These results show that Se incorporation into the CIGS film plays an important role in grain growth of the CIGS precursor film. Also, after selenization process, the MoSe₂ layer was formed between the CIGS and the Mo layer and its thickness was increased with increasing the Se ratio of mixing powder. These tendencies are similar to those of increase of selenization temperature in the previous chapter. And also, the microstructure before and after selenization of the CIGS precursor films fabricated using a single quaternary CIGS target with the nominal compositions of Cu_{0.9}(In_{0.7}Ga_{0.3})Se_{2.5} was investigated. The results are in Fig. 5.12. As can be seen in Fig. 5.12 (b), grain growth also did not occur when the CIGS precursor film was annealed in an Ar atmosphere without Se. However, when annealed with a small quantity of selenium, grain growth occurred and grain size was increased with increasing the Se ratio of mixing powder. These results are similar to those of the CIGS films fabricated using the CIGS target with the nominal compositions of Cu_{0.9}(In_{0.7}Ga_{0.3})Se₂. However, in the case of the CIGS films fabricated using the Cu_{0.9}(In_{0.7}Ga_{0.3})Se_{2.5} target, the porous and rough surface morphology was observed and the pores were increased with increasing a selenium ratio in the mixing powder. And the thickness of the MoSe₂ layer of these films was thicker than that of the films fabricated using the Cu_{0.9}(In_{0.7}Ga_{0.3})Se₂ target.

Table 5.5 (a) and (b) show the composition of the CIGS films deposited using the single CIGS targets with the nominal compositions of Cu_{0.9}(In,Ga)Se₂ and Cu_{0.9}(In,Ga)Se_{2.5}, respectively. In the case of the CIGS films fabricated using the Cu_{0.9}(In_{0.7}Ga_{0.3})Se_{2.5} target, when the CIGS

precursor film was annealed in an Ar atmosphere without Se (0:0 in table 5.5 (b)), the Se amount of the CIGS film was significantly decreased. This result is thought to be related to the thickness reduction of the CIGS film shown in Fig. 5.12 (b). In other words, most of the selenium in the CIGS precursor film is not employed for grain growth of the CIGS film although the precursor film contains a large quantity of Se. Extra selenium atoms excepting Se used for forming the CIGS related phases are evaporated to the outside of the CIGS film. On the other hand, supplement of selenium atoms around the CIGS precursor film can induce grain growth of the CIGS film because of impeding the evaporation of selenium atoms in the CIGS precursor film. Additional selenium atoms around the CIGS precursor film are rather incorporated into the inside of the CIGS film. Hence, grain size of the CIGS film is increased with increasing the Se ratio of mixing powder. However, all CIGS films had the similar composition after selenization regardless the Se ratio of mixing powder. This means that the composition of CIGS film is influenced by the composition of the precursor film rather than selenization process. Also, the thickness of the MoSe₂ layer is increased with increasing the Se ratio of mixing powder. And the MoSe₂-layer thickness of the CIGS film fabricated using the Cu_{0.9}(In_{0.7}Ga_{0.3})Se_{2.5} target is thicker than that of the CIGS film fabricated using the Cu_{0.9}(In_{0.7}Ga_{0.3})Se₂ target because of a large amount of Se in the CIGS film fabricated using the Cu_{0.9}(In_{0.7}Ga_{0.3})Se_{2.5} target.

Fig. 5.13 (a) and (b) shows the XRD patterns of the CIGS films fabricated using the single quaternary CIGS targets with the nominal compositions of Cu_{0.9}(In_{0.7}Ga_{0.3})Se₂ and Cu_{0.9}(In_{0.7}Ga_{0.3})Se_{2.5}, respectively. In the case of the CIGS films fabricated using the Cu_{0.9}(In_{0.7}Ga_{0.3})Se₂ target, XRD patterns

revealed that all of the CIGS films after selenization consisted of the chalcopyrite structure without secondary phases and were crystallized to a random orientation. However, the full width at half maximum (FWHM) of the CIGS film annealed in an Ar atmosphere without Se was wider than that of selenized CIGS films. This result is attributed to the low crystallinity of the CIGS film annealed in an Ar atmosphere without Se. Meanwhile, all of the CIGS films fabricated using the $\text{Cu}_{0.9}(\text{In}_{0.7}\text{Ga}_{0.3})\text{Se}_{2.5}$ target exhibited the chalcopyrite structure including the ordered vacancy compound (OVC) phase regardless of the Se ratio of mixing powders used for selenization. This result reveals that the occurrence of the OVC phase is decided by the value of $\text{Cu}/(\text{In}+\text{Ga})$ rather than a quantity of selenium. The CIGS precursor film with the small value of $\text{Cu}/(\text{In}+\text{Ga})$ is easy to form the OVC phase during selenization.

To clarify the existence of the OVC phase, Raman spectra of the CIGS films were investigated. As shown in Fig. 5.14, the CIGS films fabricated using the single quaternary CIGS targets with the nominal compositions of $\text{Cu}_{0.9}(\text{In}_{0.7}\text{Ga}_{0.3})\text{Se}_2$ and $\text{Cu}_{0.9}(\text{In}_{0.7}\text{Ga}_{0.3})\text{Se}_{2.5}$ showed the single CIGS phase and the CIGS phase including an OVC phase, respectively. And it is found that these phases in each CIGS film are evenly distributed. Fig. 5.15 (a) and (b) show the auger electron spectroscopy (AES) depth profiles after selenization of the CIGS films fabricated using the single quaternary CIGS targets with the nominal compositions of $\text{Cu}_{0.9}(\text{In}_{0.7}\text{Ga}_{0.3})\text{Se}_2$ and $\text{Cu}_{0.9}(\text{In}_{0.7}\text{Ga}_{0.3})\text{Se}_{2.5}$, respectively. As can be seen in figures, each element of the CIGS film was evenly distributed in the CIGS films without grading of elements. It means that the single CIGS phase in the CIGS film fabricated

using the $\text{Cu}_{0.9}(\text{In}_{0.7}\text{Ga}_{0.3})\text{Se}_2$ target and the CIGS phase including the OVC phase in the CIGS film fabricated using $\text{Cu}_{0.9}(\text{In}_{0.7}\text{Ga}_{0.3})\text{Se}_{2.5}$ target are evenly distributed.

Meanwhile, the CIGS films fabricated using the two different CIGS targets showed the different photoluminescence(PL) spectrum as shown in Fig. 5.16. In the case of the CIGS films fabricated using the $\text{Cu}_{0.9}(\text{In}_{0.7}\text{Ga}_{0.3})\text{Se}_{2.5}$ target, PL spectrum of the CIGS film exhibited doublet peak and its position shifted to higher energy level. This is thought to be attributed to the existence of the OVC phase with the CIGS phase. The OVC phase is well-known to have the larger band gap than that of CIS compound [26]. Therefore, a coexistence of the OVC phases can increase the band gap of the CIGS absorber layer. In this point of view, doublet peak and its position at higher energy level of the CIGS film fabricated using the $\text{Cu}_{0.9}(\text{In}_{0.7}\text{Ga}_{0.3})\text{Se}_{2.5}$ target are acceptable.

Fig. 5.17. (a) and (b) shows the current-voltage characteristics of the CIGS solar cells fabricated using the single CIGS targets with the nominal compositions of $\text{Cu}_{0.9}(\text{In,Ga})\text{Se}_2$ and $\text{Cu}_{0.9}(\text{In,Ga})\text{Se}_{2.5}$, respectively. And the conversion efficiencies of these solar cells were summarized in the table 5.6. The open-circuit voltages of the CIGS solar cells fabricated using the $\text{Cu}_{0.9}(\text{In}_{0.7}\text{Ga}_{0.3})\text{Se}_{2.5}$ target were generally higher than those of solar cells fabricated using the $\text{Cu}_{0.9}(\text{In}_{0.7}\text{Ga}_{0.3})\text{Se}_2$ target. This result can be caused by effect of OVC phase in the CIGS film considering the results of the band gap in chapter 5.3.1 and PL spectrum in this study. However, the open-circuit voltage of the CIGS solar cells fabricated using the $\text{Cu}_{0.9}(\text{In}_{0.7}\text{Ga}_{0.3})\text{Se}_{2.5}$ target was decreased with decreasing Se ratio of mixing powder used for selenization. The defect density in the CIGS film can be increased with

decreasing the Se ratio in a furnace during selenization, which can lead to reduce the V_{oc} . Among them, the best efficiency was achieved from the CIGS solar cell fabricated using the $Cu_{0.9}(In_{0.7}Ga_{0.3})Se_{2.5}$ target and its value is 6.70 % with the open-circuit voltage of 0.530V, short-circuit current density of 23.97 mA/cm² and the fill factor of 52.67%. Considering the results of this study, Se-excess CIGS target with a Cu-poor composition is beneficial to the enhancement of efficiency of the solar cell fabricated using the single CIGS target.

5.3.3 CIGS layers prepared using nanocrystalline precursor film

X-ray diffraction pattern was used to select the nanocrystalline CIGS film among fabricated ones. Fig. 5.18 shows XRD patterns of the as-deposited CIGS films deposited at various temperatures using the single CIGS sputtering target with the nominal composition of $Cu_{0.9}(In_{0.7}Ga_{0.3})Se_{2.5}$. As seen in Fig. 5.18, the CIGS film deposited at room temperature is amorphous. And also, XRD patterns of CIGS films deposited at the temperatures ranging from 60 °C to 120 °C have no particular distinguishing features and are similar to that of CIGS film deposited at room temperature. However, when deposited at 130 °C, the CIGS film is crystallized to the (112) orientation, which is known as the main peak of CIGS compound, although full width at half maximum (FWHM) is wide. And the intensity of the (112) peak is increased when the film is deposited at 140 °C. However, intensity of the (112) peak is decreased in the as-deposited film deposited at the higher temperature of 150 °C. This is thought to be involved in growth of another

phase. In other words, the intensity of the (112) peak is decreased with growth of (220)/(204) and (312)/(116) peaks. In our previous study, not shown here, this tendency had also been observed in the film deposited by using the CIGS sputtering target with the nominal composition of $\text{Cu}(\text{In}_{0.7}\text{Ga}_{0.3})\text{Se}_2$.

Based on the results of XRD patterns, as-deposited CIGS films fabricated at the temperatures of 120 °C and 130 °C were considered as the nanocrystalline CIGS precursor films. To clarify the formation of the nanocrystalline CIGS precursor film, phases of the CIGS film deposited at 120 °C and 130 °C were investigated by TEM. Fig. 5.19 shows TEM images of the CIGS precursor films deposited at 120 °C and 130 °C. As shown in Fig. 5.19, nanocrystalline CIGS films were successfully fabricated at these temperatures. It was found that the CIGS film was composed of the mixed phases of amorphous phases and nanocrystalline phases.

These CIGS precursor films were selenized at the temperature of 475 °C for 30 min, which is optimum condition in our previous study. Fig. 5.20 shows XRD patterns of selenized CIGS films. The CIGS films after selenization of nanocrystalline CIGS precursor films deposited at 120 °C and 130 °C showed a (112) preferred orientation. However, intensity ratio of (112) to (220)/(204) was decreased with decreasing the deposition temperature and in the end the CIGS film deposited at room temperature showed a random orientation. Table 5.7 shows the intensity ratio of (112) to (220)/(204). In general, the intensity ratio of (112) to (220)/(204) of $\text{Cu}(\text{In}_{0.7}\text{Ga}_{0.3})\text{Se}_2$ powder (PDF #35-1102) is 2.5. This value is similar to that after selenization of the CIGS films deposited at room temperature. Therefore, it is found that CIGS films deposited at room temperature and higher temperatures (120 and 130 °C) are crystallized to a

random orientation and a (112) preferred orientation, respectively.

Table 5.8 shows the composition before and after selenization of the CIGS precursor films deposited at various temperatures. In the case of the as-deposited film, the CIGS film deposited at room temperature has the smaller amount of Cu and the larger amount of Se compared to the CIGS film deposited at 120 and 130 °C. However, after selenization of these as-deposited CIGS precursor films, the difference of the Cu and Se amount between them is decreased. In other words, after selenization of the CIGS film deposited at room temperature, Cu content is increased and Se content is decreased. And in the case of the CIGS film deposited at 120 and 130 °C, Cu content is slightly decreased and Se content is almost same. Finally, all of the selenized CIGS films have the similar composition, consisted of the smaller amount of Cu and the larger amount of (In+Ga) than those of stoichiometric Cu(In,Ga)Se_2 phase, regardless of deposition temperature although Cu contents in the films are slightly different. However, XRD patterns of the CIGS films showed some different characteristics even if the CIGS films had the similar compositions. After selenization, distinguishable peaks between ordered vacancy compound (OVC) phase and CIGS phase were observed in the CIGS film deposited at room temperature. However, these peaks were disappeared in the CIGS film deposited at 130 °C. This result is thought to be attributed to the preferred orientation of CIGS phase and OVC phase. The main peak position of CIGS ($\text{Cu(In}_{0.7}\text{Ga}_{0.3}\text{)Se}_2$, PDF#35-1102) phase is similar to that of OVC ($\text{Cu(In,Ga}_3\text{)Se}_5$, PDF #51-1222) phase. Therefore, if the OVC phase also has the (112) preferred orientation it is difficult to distinguish an existence of the OVC phase from the XRD pattern.

So, Raman spectra of the CIGS films were investigated to clarify the existence of an OVC phase. Figs. 5.21 (a) and (b) shows the raman spectra of the CIGS films selenized using mixing powders with the weight ratios of alumina to selenium of 8:1 and 4:1, respectively. As shown in figures, all of the films contained the OVC phase. Therefore, it is clear that the OVC phase also has the (112) preferred orientation. As a result, all of the CIGS films fabricated in this study have the OVC phase which can lead to decrease of open-circuit voltage loss as discussed in chapter 5.3.1.

Meanwhile, the microstructure of these CIGS films showed the different morphology. Figs. 5.22, 23 and 24 show SEM images of the CIGS films before and after selenization of the CIGS precursor films deposited at room temperature, 120 and 130 °C, respectively. As can be seen in figures, all of the as-deposited CIGS films show almost featureless microstructure. After selenization, grain growth occurred and grain size was increased with increasing a selenium ratio in a tube furnace. This tendency appeared in all of the selenized CIGS films regardless of deposition temperature of the CIGS precursor film. However, after selenization of the CIGS precursor film deposited at room temperature, the porous and rough surface morphology was observed and the pores were increased with increasing a selenium ratio in the mixed powder used for selenization. This surface morphology was improved to the dense surface morphology by selenization of the nano-crystalline CIGS precursor film. Finally, the CIGS film with the densely packed surface morphology as well as the large grain size was obtained by increase of Se ratio in a tube furnace and using the nano-crystalline CIGS precursor film. Root mean square (RMS) roughness of the CIGS films was investigated. As

shown in Fig. 5. 25. and Table 5.9, for the CIGS film deposited at room temperature, the RMS roughness of the selenized CIGS film was increased with increasing a selenium ratio in the mixed powder. However, the RMS roughness was decreased when the nano-crystalline CIGS precursor films were selenized. Dense and smooth surface morphology of the CIGS film is important to improve device performance because the surface of the CIGS film is the contact surface for the p-n junction. Hence, this result is meaningful for enhancement of device performance.

Meanwhile, in the cross-sectional SEM images, thickness of the CIGS film after selenization of the CIGS precursor film deposited at room temperature is greatly decreased. However, the ratio of thickness reduction from the as-deposited CIGS film is decreased with increasing deposition temperature. This is thought to be caused by difference of the film density between the as-deposited films. In other words, the thickness reduction of the amorphous CIGS film containing many pores is larger than that of the nano-crystalline CIGS film composed of relatively high density.

Also, the MoSe₂ layer was checked. A MoSe₂ layer is known to enhance the efficiency by forming the ohmic contact between the CIGS layer and the Mo electrode layer [28, 29]. However, very thick MoSe₂ layer is detrimental to the conversion efficiency [30]. In this experiment, the thickness of the MoSe₂ layer was decreased after selenization of the nano-crystalline CIGS precursor film compared to that of the amorphous CIGS precursor film. This is because the Se amount in the CIGS precursor film deposited at room temperature is larger than that in the CIGS precursor films deposited at 120 and 130 °C as shown in table 5.8. Hence, the formation of a MoSe₂ layer becomes easier in

the as-deposited CIGS film deposited at room temperature due to short diffusion length of selenium atoms to form a MoSe₂ layer. Also, compared with the film deposited at 120 °C, the thinner MoSe₂ layer was formed when deposited at 130 °C although the Se amount of these films is similar. This result shows that the density of the CIGS precursor film affects the formation of a MoSe₂ layer. This can be understood in the way that Se incorporation into the inside of the CIGS film during selenization is more difficult in the denser film. As a result, film density and Se amount of the CIGS precursor film have an important effect on the formation of the MoSe₂ layer. Therefore, the use of the nano-crystalline CIGS precursor film is beneficial to the improvement of the solar cell performance by reducing the thickness of a MoSe₂ layer.

By using these CIGS films, the CIGS thin film solar cells with the structure of Al/AZO/i-ZnO/CdS/CIGS/Mo/SLG were fabricated to measure the conversion efficiency. Fig. 5.26 (a), (b) and (c) show the current-voltage characteristics of the CIGS solar cells fabricated by using the CIGS precursor films deposited at room temperature, 120 and 130 °C, respectively. And the conversion efficiencies of these solar cells are summarized in the table 5.10. The open-circuit voltage was increased with increasing a selenium ratio of the mixed powder used for selenization although the short-circuit current density between them was similar. Lower V_{oc} of solar cell devices can be attributed to many defects and shunting paths in the CIGS film. Meanwhile, selenium has been known to decrease the defects in the CIGS film. Therefore, it is possible that defect density in the CIGS film can be increased with decreasing the Se ratio in a furnace during selenization, which can lead to reduction of the V_{oc} . Among them, the best efficiency was achieved from the CIGS solar cell

fabricated by using the CIGS precursor film deposited at 130 °C and its value is 8.09 % with the open-circuit voltage of 0.571V, short-circuit current density of 26.58 mA/cm² and the fill factor of 53.28%. This value is higher than that of the CIGS solar cell fabricated using amorphous CIGS precursor film. This result is thought to be achieved by the beneficial factors such as the existence of an OVC phase, the thickness reduction of a MoSe₂ layer, smooth surface morphology and the decrease of defect density achieved by dense CIGS film with large grain.

5.4. Summary

The characteristics of the CIGS thin film solar cells fabricated via single CIGS targets with various compositions were investigated. By employing the stoichiometric CIGS target, the Cu-rich CIGS film was obtained and very low conversion efficiency was achieved due to inappropriate composition and porous surface morphology. CIGS films with device-quality stoichiometry ratio were achieved from the Cu-poor CIGS target. This film showed a densely packed morphology and chalcopyrite structure without the second phases. A conversion efficiency of 3.54% was achieved from the CIGS film selenized at 475 °C. However, the open-circuit voltage (V_{oc}) of this solar cell was too low compared to V_{oc} derived from the band gap (E_g) of CIGS compound. The difference could be decreased with increasing Se contents in the CIGS target. Increase of the Se content in the CIGS target led to decrease of the Cu content and increase of the (In+Ga) content in the CIGS film, which created the ordered vacancy compound

(OVC) phase. As a result, the CIGS thin films fabricated by employing the Se-excess CIGS targets with a Cu-poor composition showed the chalcopyrite CIGS phase including an OVC phase. The OVC phase in the CIGS film was increased with increasing the Se content in the CIGS target. The difference between $E_g/q - 0.5V$ and V_{oc} was remarkably decreased with the formation of the OVC phases. The highest efficiency of 6.88% has been achieved from the CIGS solar cell fabricated using the $Cu_{0.9}(In_{0.7}Ga_{0.3})Se_{2.2}$ target. The performance of the CIGS solar cells fabricated in this study was summarized in the Table 5.4. This study reveals that the selenium content in the single CIGS target plays a key role in structural and electrical properties.

Characteristics of CIGS films selenized using mixing powders with various weight ratios of alumina to selenium was investigated. For this experiment, the CIGS precursor films were deposited using the single CIGS targets with the nominal compositions of $Cu_{0.9}(In,Ga)Se_2$ and $Cu_{0.9}(In,Ga)Se_{2.5}$. As the results, regardless of target composition, grain size was increased with increasing the Se ratio of mixing powder. The $MoSe_2$ layer was formed between the CIGS and the Mo layer and its thickness was also increased with increasing the Se ratio of mixing powder. The $MoSe_2$ -layer thickness of the CIGS film fabricated using the $Cu_{0.9}(In_{0.7}Ga_{0.3})Se_{2.5}$ target is thicker than that of the CIGS film fabricated using the $Cu_{0.9}(In_{0.7}Ga_{0.3})Se_2$ target because of larger amount of Se in the CIGS film fabricated using the $Cu_{0.9}(In_{0.7}Ga_{0.3})Se_{2.5}$ target. From the auger electron spectroscopy (AES) depth profiles after selenization of the CIGS films, it was found that each element of the CIGS film was evenly distributed in the CIGS films without grading of elements. This means that the CIGS phases including the OVC

phase in the CIGS film fabricated using $\text{Cu}_{0.9}(\text{In}_{0.7}\text{Ga}_{0.3})\text{Se}_{2.5}$ target are evenly distributed. The open-circuit voltages of the CIGS solar cells fabricated using the $\text{Cu}_{0.9}(\text{In}_{0.7}\text{Ga}_{0.3})\text{Se}_{2.5}$ target were generally higher than those of solar cells fabricated using the $\text{Cu}_{0.9}(\text{In}_{0.7}\text{Ga}_{0.3})\text{Se}_2$ target. However, the open-circuit voltage of the CIGS solar cells fabricated using the $\text{Cu}_{0.9}(\text{In}_{0.7}\text{Ga}_{0.3})\text{Se}_{2.5}$ target was decreased with decreasing Se ratio of mixing powder used for selenization.

Also, characteristics of the CIGS films selenized using nanocrystalline precursor film were investigated. The CIGS films were deposited at various temperatures using a single quaternary $\text{Cu}_{0.9}(\text{In}_{0.7}\text{Ga}_{0.3})\text{Se}_{2.5}$ target. Based on the results of XRD patterns, as-deposited CIGS films fabricated at the temperatures of 120 °C and 130 °C were considered as the nano-crystalline CIGS precursor films and selenized at 475 °C for 30min. The CIGS films showed a (112) preferred orientation. All of the selenized CIGS films have the similar composition regardless of deposition temperature although Cu content in the film is slightly different. From the Raman spectra of the CIGS films, the existence of OVC phase which can lead to decrease of open-circuit voltage loss was identified. The CIGS film with dense surface morphology as well as the large grain size was obtained by increase of Se ratio in a tube furnace and using the nano-crystalline CIGS precursor film. And the thickness of the MoSe_2 layer was decreased after selenization of the nano-crystalline CIGS precursor film compared to that of the amorphous CIGS precursor film. The highest efficiency was achieved from the CIGS solar cell fabricated using the nanocrystalline CIGS precursor film deposited at 130 °C and its value is 8.09 % with the open-circuit voltage of 0.571V, short-circuit

current density of 26.58 mA/cm^2 and the fill factor of 53.28%. This result is thought to be achieved by the beneficial factors such as the existence of an OVC phase, the thickness reduction of a MoSe_2 layer, smooth surface morphology and the decrease of defect density achieved by dense CIGS film with large grain.

References

- [1] P. Jackson, D. Hariskos, E. Lotter, S. Paetel, R. Wuerz, R. Menner, W. Wischmann, M. Powalla, *Prog. Photovolt. Res. Appl.* 19 (2011) 894.
- [2] S.D. Kim, H.J. Kim, K.H. Yoon, J. Song, *Sol. Energy Mater. Sol. Cells* 62 (2000) 357.
- [3] D.G. Moon, S. Ahn, J.H. Yun, A. Cho, J. Gwak, S. Ahn, K. Shin, K. Yoon, H.D. Lee, H. Pak, S. Kwon, *Sol. Energy Mater. Sol. Cells* 95 (2011) 2786.
- [4] M. Marudachalam, H. Hichri, R. Klenk, R.W. Birkmire, W.N. Shafarman, *Appl. Phys. Lett.* 67 (1995) 3978.
- [5] T. Nakada, A. Kunioka, *Jpn. J. Appl. Phys.* 37 (1998) L1065.
- [6] W. Li, Y. Sun, W. Liu, L. Zhou, *Solar Energy* 80 (2006) 191.
- [7] J.H. Shi, Z.Q. Li, D.W. Zhang, Q.Q. Liu, Z. Sun, S.M. Huang, *Prog. Photovolt. Res. Appl.* 19 (2011) 160.
- [8] J.A. Frantz, R.Y. Bekele, V.Q. Nguyen, J.S. Sanghera, A. Bruce, S.V. Frolov, M. Cyrus, I.D. Aggarwal, *Thin Solid Films* 519 (2011) 7763.
- [9] C.H. Chen, W.C. Shih, C.Y. Chien, C.H. Hsu, Y.H. Wu, C.H. Lai, *Sol. Energy Mater. Sol. Cells* 103 (2012) 25.
- [10] S.B. Zhang, S.H. Wei, A. Zunger, H. K. Yoshida, *Phys. Rev. B* 57 (1998) 9642.
- [11] L. Zhang, Q. He, W.L. Jiang, F.F. Liu, C.J. Li, Y. Sun, *Sol. Energy Mater. Sol. Cells* 93 (2009) 114.
- [12] T. Yamaguchi, T. Kobata, S. Niiyama, T. Nakamura, A. Yoshida, *Sol. Energy Mater. Sol. Cells* 75 (2003) 87.
- [13] P. Jackson, R. Wurz, U. Rau, J. Mattheis, M. Kurth, T. Schlotzer, G. Bilger, J.H. Werner, *Prog. Photovolt. Res. Appl.* 15 (2007) 507.
- [14] J.R. Tuttle, M. Contreras, M.H. Bode, D. Nilas, D.S. Albin, R. Matson, A.M. Gabor, A. Tennant, A. Duda, R. Noufi, *J. Appl. Phys.* 77 (1995) 153.
- [15] R. Klenk, T. Walter, H. W. Schock, D. Cahen, *Adv. Mater.* 5 (1993) 114.
- [16] J. Nelson, *The physics of solar cells*, 2004, p110.

- [17] W. Liu, J.G. Tian, Q. He, F.Y. Li, C.J. Li, Y. Sun, *Thin Solid Films* 519 (2010) 244.
- [18] R. Noufi, R. Axton, C. Herrington, and S. K. Deb, *Appl. Phys. Lett.* 45 (1984) 668.
- [19] S. Dongaonkar, J. D. Servaites, G. M. Ford, S. Loser, J. Moore, R. M. Gelfand, H. Mohseni, H. W. Hillhouse, R. Agrawal, M. A. Ratner, T. J. Marks, M. S. Lundstrom, and M. A. Alam, *J. Appl. Phys.* 108 (2010) 124509.
- [20] T. Walter, H. W. Schock, *Thin Solid Films* 224 (1993) 74.
- [21] X. Zhu, Z. Zhou, Y. Wang, L. Zhang, A. Li, F. Huang, *Sol. Energy Mater. Sol. Cells* 101 (2012) 57.
- [22] T. Sakurai, M.M. Islam, H. Uehigashi, S. Ishizuka, A. Yamada, K. Matsubara, S. Niki, K. Akimoto, *Sol. Energy Mater. Sol. Cells* 95 (2011) 227.
- [23] R. Caballero, C. Maffiotte, C. Guillen, *Thin Solid Films* 474 (2005) 70.
- [24] G. Zoppi, I. Forbes, R. W. Miles, P. J. Dale, J. J. Scragg, L. M. Peter, *Prog. Photovolt.: Res. Appl.* 17 (2009) 315.
- [25] S. R. Kodigala, *Thin films and nanostructures*, vol. 35 “Cu(In_{1-x}Ga_x)Se₂ based thin film solar cells”, 2010, p11.
- [26] T. Negami, N. Kohara, M. Nishitani, T. Wada, T. Hirao, *Appl. Phys. Lett.* 67 (1995) 825.
- [27] M. Turcu, O. Pakma, U. Rau, *Appl. Phys. Lett.* 80 (2002) 2598.
- [28] T. Wada, N. Kohara, S. Nishiwaki, T. Negami, *Thin Solid Films* 387 (2001) 118.
- [29] L. Assmann, J. C. Bernede, A. Drici, C. Amory, E. Halgand, M. Morsli, *Appl. Surf. Sci.* 171 (2001) 15.
- [30] X. Zhu, Z. Zhou, Y. Wang, L. Zhang, A. Li, F. Huang, *Sol. Energy Mater. Sol. Cells* 101 (2012) 57.

Table 5.1. Composition of the CIGS films fabricated using a stoichiometric CIGS target.

	Sel.temp. (°C)	Cu (%)	In (%)	Ga (%)	Se (%)	Cu/ (In+Ga)	Ga/ (In+Ga)
Batch		25	17.5	7.5	50	1	0.30
	As-dep.	24.3	16.5	7.2	52.0	1.03	0.30
	350	24.8	15.5	6.5	53.2	1.13	0.30
Film	375	24.4	16.3	7.3	52.0	1.03	0.31
	400	24.9	17.2	7.3	50.6	1.02	0.30
	425	25.6	17.3	7.0	50.1	1.05	0.29
	450	24.9	17.1	7.5	50.5	1.01	0.30

Table 5.2. Composition of the CIGS films fabricated using a Cu-poor CIGS target ($\text{Cu}_{0.9}(\text{In}_{0.7}\text{Ga}_{0.3})\text{Se}_2$).

	Sel.temp. (°C)	Cu (%)	In (%)	Ga (%)	Se (%)	Cu/ (In+Ga)	Ga/ (In+Ga)
Batch		23.08	17.95	7.69	51.28	0.90	0.30
	As-dep.	20.2	17.6	7.4	54.8	0.81	0.30
	400	17	15.9	6.2	60.9	0.77	0.28
Film	450	20.7	19.3	7.8	52.2	0.76	0.29
	475	20.5	18.6	8.0	52.9	0.77	0.30
	500	22.7	18.3	7.5	51.5	0.88	0.29

Table 5.3. Composition of the CIGS films fabricated using Se-excess CIGS targets with a Cu-poor composition.

Composition	Sample	Cu (%)	In (%)	Ga (%)	Se (%)	Cu/(In+Ga)	Ga/(In+Ga)
$\text{Cu}_{0.9}(\text{In,Ga})\text{Se}_{2.2}$	As-dep.	16.7	16.6	6.7	60.0	0.72	0.29
	After sel.	18.0	18.7	8.7	54.6	0.66	0.32
$\text{Cu}_{0.9}(\text{In,Ga})\text{Se}_{2.5}$	As-dep.	12.6	17.6	7.4	62.4	0.50	0.30
	After sel.	13.1	22.4	9.8	54.7	0.41	0.30

Table 5.4. Summary of efficiency of the CIGS solar cells fabricated in this study. (As a function of target composition and selenization temperature)

Sample	Nominal target composition	Selenization temperature (°C)	V_{oc} (V)	J_{sc} (mA/cm ²)	FF (%)	η (%)	E_g (eV)	$(\frac{E_g}{q} - 0.5V) - V_{oc}(sample)$ (V)
A	$Cu(In_{0.7}Ga_{0.3})Se_2$	400	0.090	1.70	35.1	0.05		
B	$Cu(In_{0.7}Ga_{0.3})Se_2$	450	0.163	1.89	31.2	0.10		
C	$Cu_{0.9}(In_{0.7}Ga_{0.3})Se_2$	400	0.267	2.35	43.5	0.27		
D	$Cu_{0.9}(In_{0.7}Ga_{0.3})Se_2$	450	0.284	12.50	44.0	1.57		
E	$Cu_{0.9}(In_{0.7}Ga_{0.3})Se_2$	475	0.343	22.33	46.1	3.54	1.14	0.297
F	$Cu_{0.9}(In_{0.7}Ga_{0.3})Se_2$	500	0.269	20.72	36.8	2.05		
G	$Cu_{0.9}(In_{0.7}Ga_{0.3})Se_{2.2}$	475	0.463	27.95	53.1	6.88	1.15	0.187
H	$Cu_{0.9}(In_{0.7}Ga_{0.3})Se_{2.5}$	475	0.530	23.97	52.7	6.70	1.19	0.160

Table 5.5. Composition before and after selenization of CIGS precursor films deposited using the single CIGS targets with the nominal compositions of (a) $\text{Cu}_{0.9}(\text{In,Ga})\text{Se}_2$ and (b) $\text{Cu}_{0.9}(\text{In,Ga})\text{Se}_{2.5}$. The CIGS films were selenized using mixing powders with various weight ratios of alumina to selenium.

(a)	$\text{Al}_2\text{O}_3\text{:Se}$ ratio	Cu (%)	In (%)	Ga (%)	Se (%)	Cu/ (In+Ga)	Ga/ (In+Ga)
	As-dep.	20.7	17.7	7.5	54.1	0.82	0.30
	4:1	23.3	17.9	7.6	51.2	0.91	0.30
	6:1	23.1	18.3	7.3	51.3	0.90	0.29
	8:1	22.8	18.4	7.4	51.4	0.88	0.29
	12:1	23.1	18.5	7.5	50.9	0.89	0.29
	0:0	23.3	19.1	7.7	49.9	0.87	0.29

(b)	$\text{Al}_2\text{O}_3\text{:Se}$ ratio	Cu (%)	In (%)	Ga (%)	Se (%)	Cu/ (In+Ga)	Ga/ (In+Ga)
	As-dep.	11	18	7.5	63.5	0.43	0.29
	4:1	13	22.5	9.3	55.2	0.41	0.29
	6:1	13	21.9	8.8	56.3	0.42	0.29
	8:1	13.1	22.7	9.3	54.9	0.41	0.29
	12:1	13.5	22.7	8.4	55.4	0.43	0.27
	0:0	13.8	23.1	9.4	53.6	0.42	0.29

Table 5.6. Summary of the conversion efficiencies shown in Fig. 5.17.

Sample	Nominal target composition	Al ₂ O ₃ : Se ratio	V _{oc} (V)	J _{sc} (mA/cm ²)	FF (%)	η (%)
A	Cu _{0.9} (In,Ga)Se ₂	4:1	0.277	28.87	42.7	3.42
B	Cu _{0.9} (In,Ga)Se ₂	6:1	0.347	24.94	43.9	3.80
C	Cu _{0.9} (In,Ga)Se ₂	8:1	0.340	18.48	38.3	2.40
D	Cu _{0.9} (In,Ga)Se ₂	12:1	0.283	25.13	35.9	2.56
E	Cu _{0.9} (In,Ga)Se _{2.5}	4:1	0.530	23.97	52.7	6.70
F	Cu _{0.9} (In,Ga)Se _{2.5}	6:1	0.514	21.90	39.3	4.43
G	Cu _{0.9} (In,Ga)Se _{2.5}	8:1	0.499	22.56	47.8	5.38
H	Cu _{0.9} (In,Ga)Se _{2.5}	12:1	0.364	20.02	34.6	2.52

Table 5.7. Intensity ratio of the CIGS films shown in Fig 5.20.

Sample	Dep. Temp. (°C)	Al ₂ O ₃ :Se ratio	I (112)/ I(220)(204)
A	R. T.	8:1	2.6
B	R. T.	6:1	2.3
C	R. T.	4:1	2.5
D	120	8:1	81
E	120	6:1	125
F	120	4:1	73
G	130	8:1	223
H	130	6:1	129
I	130	4:1	77

Table 5.8. Composition before and after selenization of the CIGS precursor films deposited at (a) room temperature, (b) 120 and (c) 130 °C

(a)	Al ₂ O ₃ :Se ratio	Cu (%)	In (%)	Ga (%)	Se (%)	Cu/ (In+Ga)	Ga/ (In+Ga)
	As-dep.	11	18	7.5	63.5	0.43	0.29
	8:1	13.1	22.7	9.3	54.9	0.41	0.29
	6:1	13	21.9	8.8	56.3	0.42	0.29
	4:1	13	22.5	9.3	55.2	0.41	0.29

(b)	Al ₂ O ₃ :Se ratio	Cu (%)	In (%)	Ga (%)	Se (%)	Cu/ (In+Ga)	Ga/ (In+Ga)
	As-dep.	16.4	20.4	8.5	54.7	0.57	0.29
	8:1	14.7	21.2	9.4	54.7	0.48	0.31
	6:1	14.5	23.6	8.4	53.5	0.45	0.26
	4:1	15.5	23.0	8.0	53.5	0.50	0.26

(c)	Al ₂ O ₃ :Se ratio	Cu (%)	In (%)	Ga (%)	Se (%)	Cu/ (In+Ga)	Ga/ (In+Ga)
	As-dep.	16.8	21.3	8.4	53.5	0.57	0.28
	8:1	14.9	21.9	9.1	54.1	0.48	0.29
	6:1	15.6	23.5	8.2	52.7	0.49	0.26
	4:1	15.2	23.4	7.8	53.6	0.49	0.25

Table 5.9. RMS roughness of the CIGS films shown in Fig. 5.25.

Dep. Temp. & Al₂O₃ : Se ratio	RMS roughness (nm)	Standard deviation (nm)
R.T. – 8:1	38.8	0.65
R.T. – 6:1	70.5	1.86
R.T. – 4:1	73.1	1.12
120 °C – 4:1	66.0	4.01
130 °C – 4:1	42.5	2.15

Table 5.10. Summary of the conversion efficiencies shown in Fig. 5.26.

Sample	Dep. Temp. (°C)	Al ₂ O ₃ : Se ratio	V _{oc} (V)	J _{sc} (mA/cm ²)	FF (%)	η (%)
A	R.T.	8:1	0.499	22.56	47.8	5.38
B	R.T.	6:1	0.514	21.90	39.3	4.43
C	R.T.	4:1	0.530	23.97	52.7	6.70
D	120	8:1	0.418	24.28	44.1	4.48
E	120	6:1	0.494	22.23	46.3	5.09
F	120	4:1	0.537	23.59	54.5	6.90
G	130	8:1	0.427	26.32	47.6	5.34
H	130	6:1	0.537	21.72	45.6	5.23
I	130	4:1	0.571	26.58	53.3	8.09

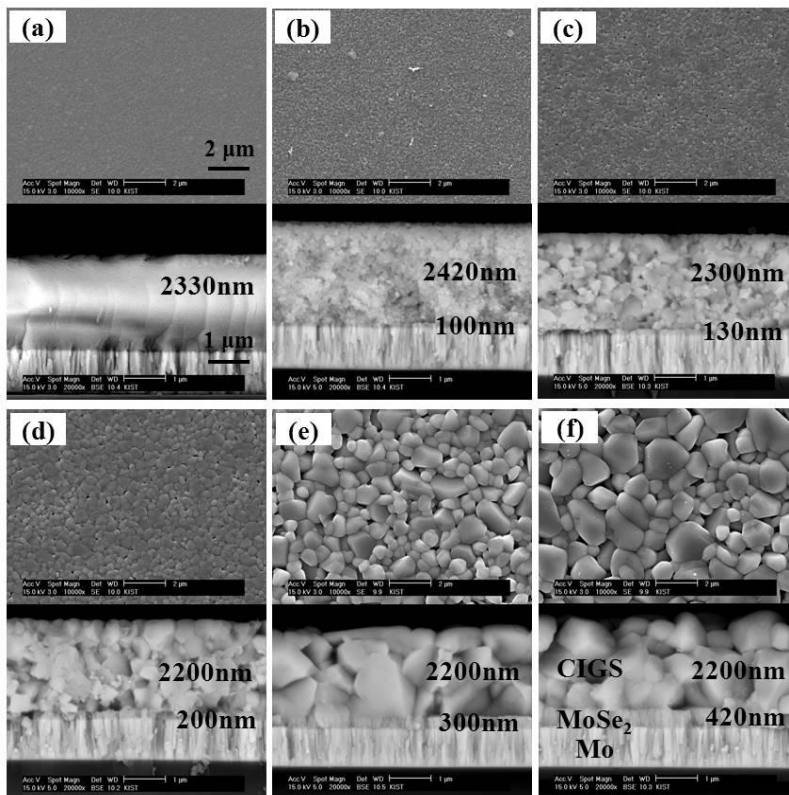


Fig. 5.1. FE-SEM images of the CIGS films (a) as-deposited and selenized at (b) 350 °C, (c) 375 °C, (d) 400 °C, (e) 425 °C and (f) 450 °C. CIGS precursor films were fabricated using a stoichiometric CIGS target and then selenized at various temperatures.

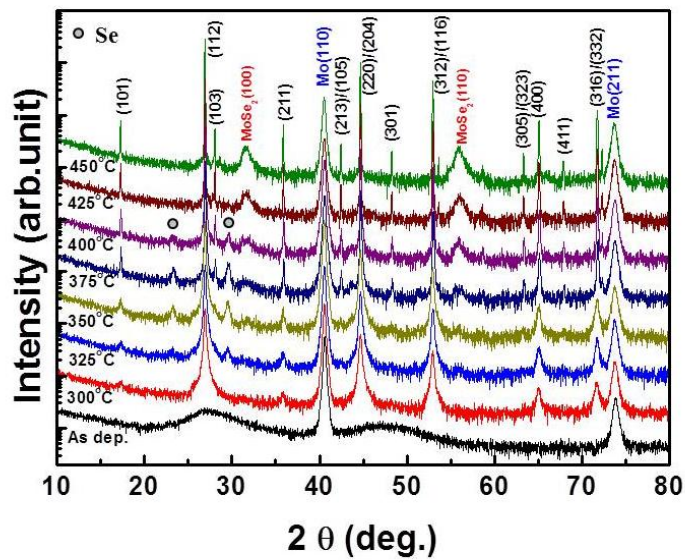


Fig. 5.2. XRD patterns of as-deposited and selenized CIGS films. CIGS precursor films were fabricated using a stoichiometric CIGS target and then selenized at the temperatures from 300 to 450 °C.

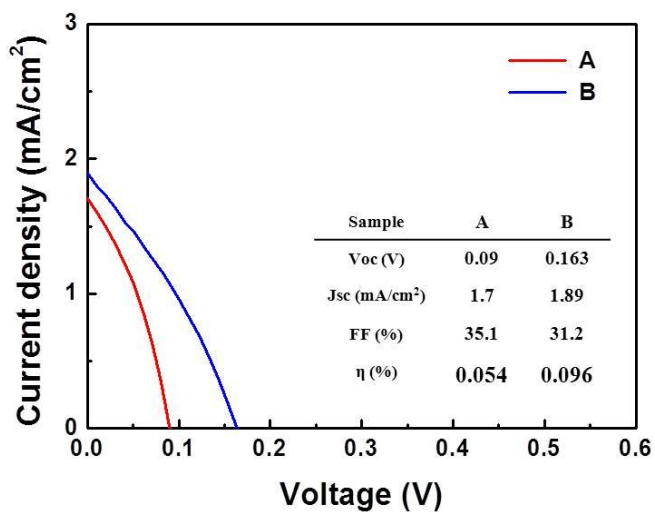


Fig. 5.3. Current-voltage characteristics of the CIGS solar cells fabricated using a stoichiometric CIGS target. The solar cell A and B are fabricated using the CIGS absorber layers selenized at the temperatures of 400 and 450 °C, respectively.

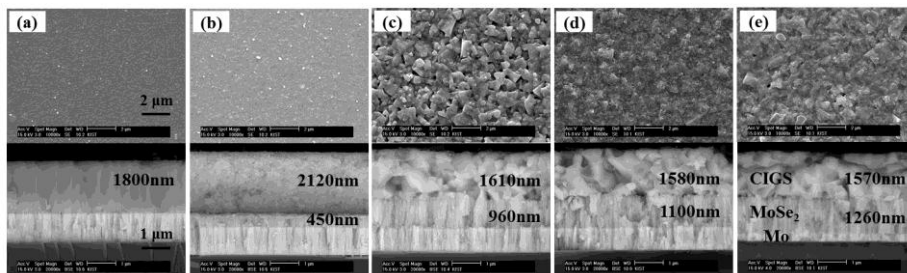


Fig. 5.4. FE-SEM images of the CIGS films (a) as-deposited and selenized at (b) 400 °C, (c) 450 °C, (d) 475 °C and (e) 500 °C. CIGS precursor films were fabricated using a Cu-poor CIGS target and then selenized at various temperatures.

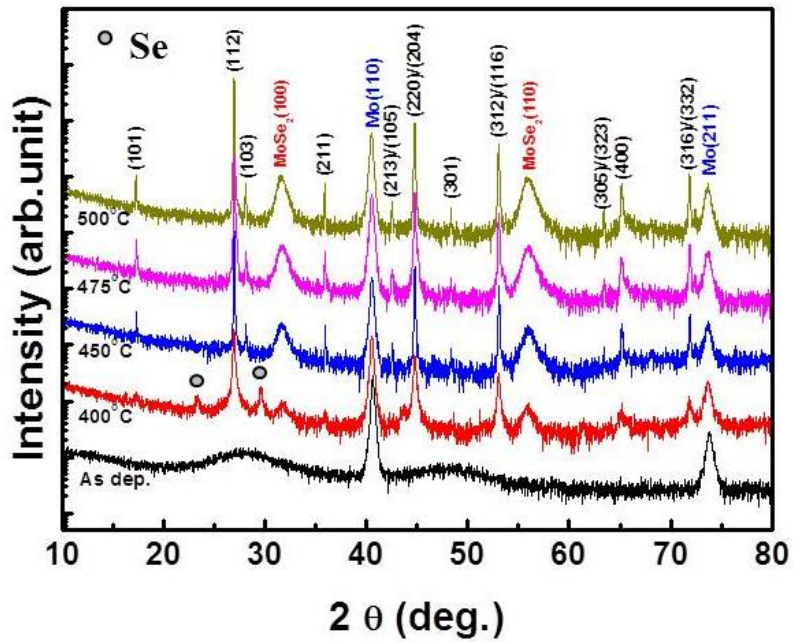


Fig. 5.5. XRD patterns of as-deposited and selenized CIGS films. CIGS precursor films were fabricated using a Cu-poor CIGS target and then selenized at the temperatures from 400 to 500 °C.

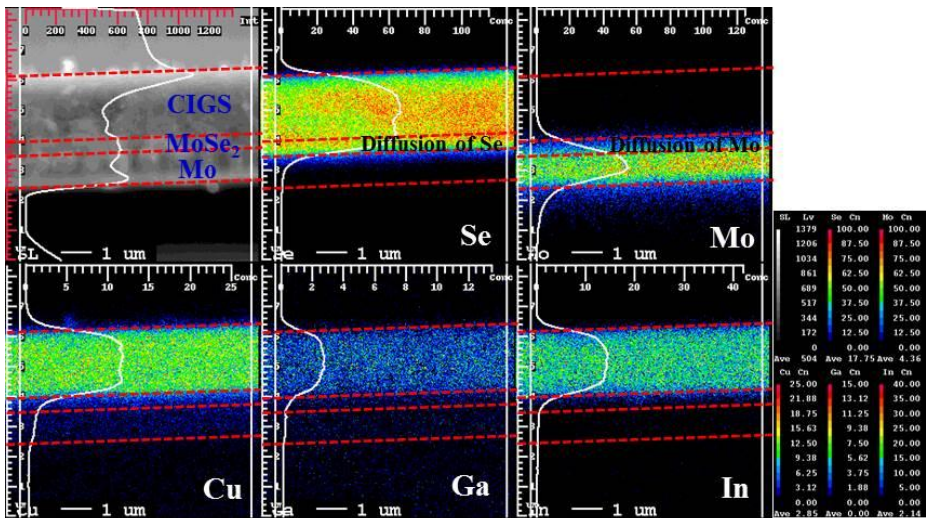


Fig. 5.6. Composition mapping images of the CIGS film selenized at the temperature of 400 °C.

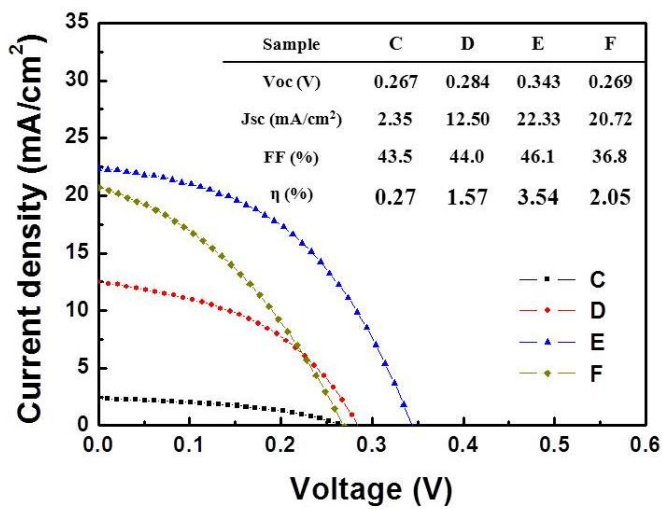


Fig. 5.7. Current-voltage characteristics of the CIGS solar cells fabricated using a Cu-poor CIGS target. The solar cell C, D, E and F are fabricated using the CIGS absorber layers selenized at the temperatures of 400, 450, 475 and 500 °C, respectively.

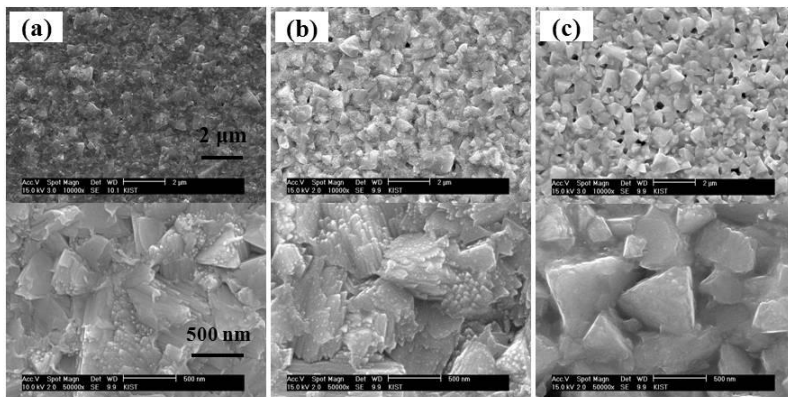


Fig. 5.8. FE-SEM images after selenization of the CIGS precursor films fabricated using (a) $\text{Cu}_{0.9}(\text{In}_{0.7}\text{Ga}_{0.3})\text{Se}_2$, (b) $\text{Cu}_{0.9}(\text{In}_{0.7}\text{Ga}_{0.3})\text{Se}_{2.2}$ and (c) $\text{Cu}_{0.9}(\text{In}_{0.7}\text{Ga}_{0.3})\text{Se}_{2.5}$ targets. All of the films are selenized at the temperature of 475°C for 30minutes.

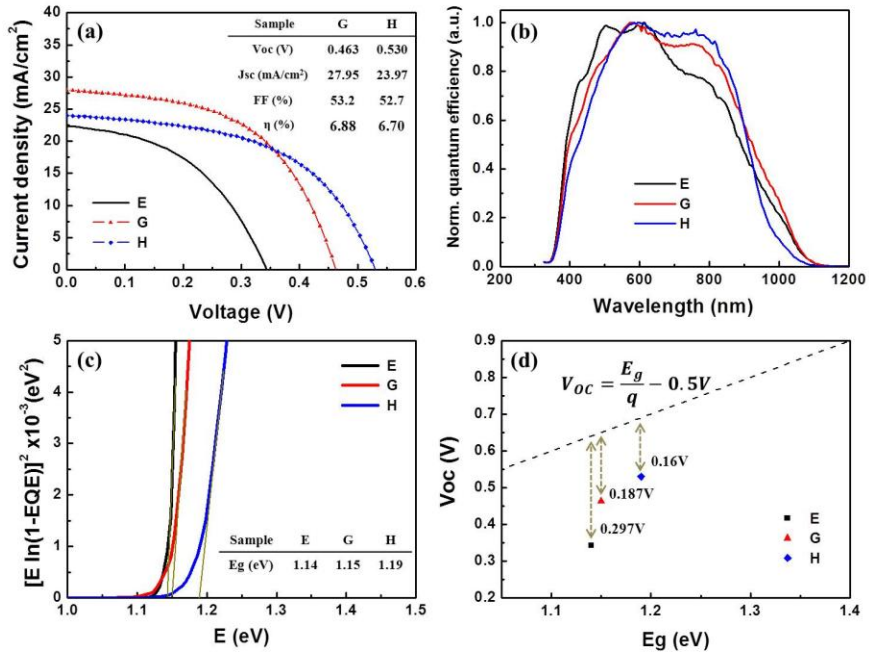


Fig. 5.9. (a) Current-voltage characteristics and (b) normalized quantum efficiency of the CIGS solar cells fabricated using various CIGS targets. (c) Band gap determination from EQE data. (d) A plot of V_{oc} versus band gap (E_g). The solar cell E, G and H are fabricated by using $\text{Cu}_{0.9}(\text{In,Ga})\text{Se}_2$, $\text{Cu}_{0.9}(\text{In,Ga})\text{Se}_{2.2}$ and $\text{Cu}_{0.9}(\text{In,Ga})\text{Se}_{2.5}$ target, respectively.

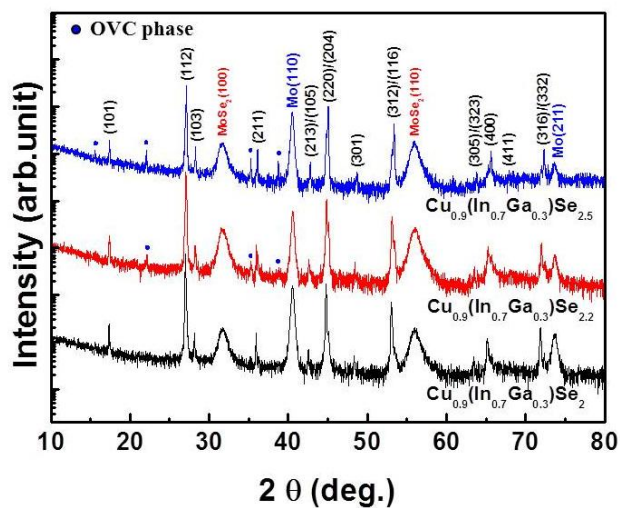


Fig. 5.10. XRD patterns after selenization of the CIGS precursor films fabricated using $\text{Cu}_{0.9}(\text{In}_{0.7}\text{Ga}_{0.3})\text{Se}_2$, $\text{Cu}_{0.9}(\text{In}_{0.7}\text{Ga}_{0.3})\text{Se}_{2.2}$ and $\text{Cu}_{0.9}(\text{In}_{0.7}\text{Ga}_{0.3})\text{Se}_{2.5}$ targets. All of the films are selenized at the temperature of 475°C for 30minutes.

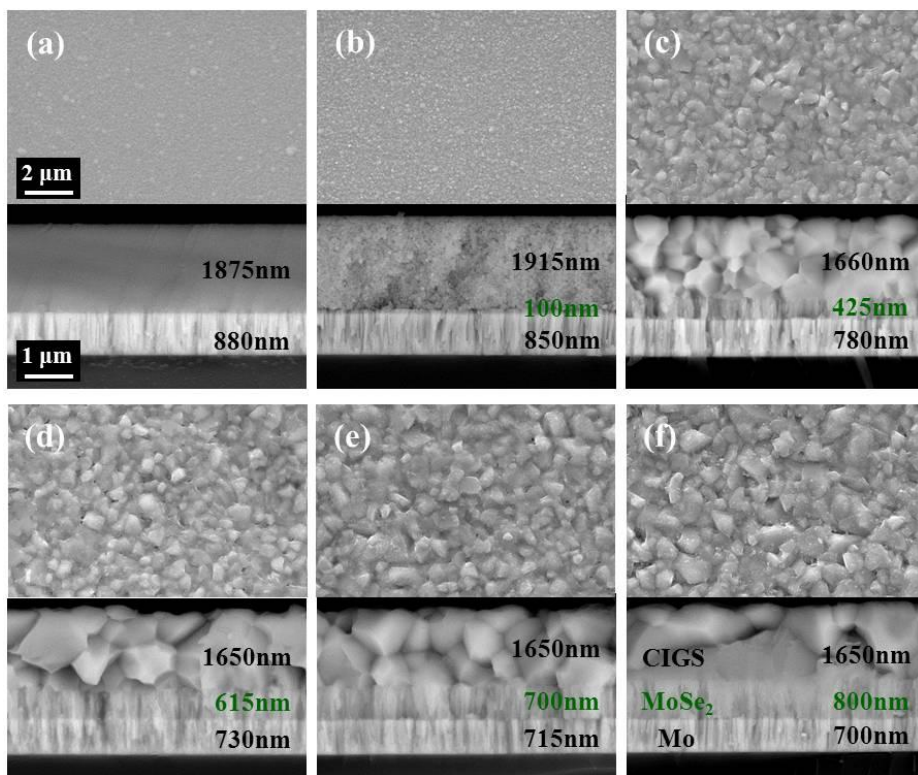


Fig. 5.11. FE-SEM images of the (a) as-deposited CIGS film and the CIGS films selenized using mixing powders with weight ratios of alumina to selenium of (b) 0:0, (c) 12:1, (d) 8:1, (e) 6:1 and (f) 4:1. The CIGS precursor film was fabricated using a single quaternary CIGS target with the nominal compositions of $\text{Cu}_{0.9}(\text{In}_{0.7}\text{Ga}_{0.3})\text{Se}_2$.

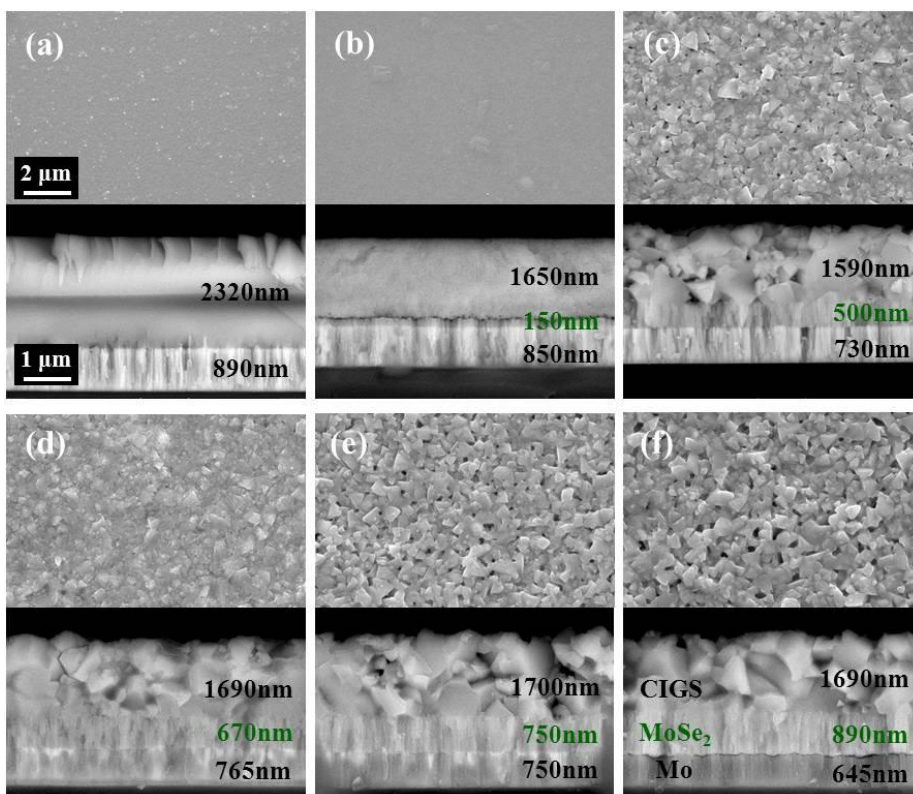


Fig. 5.12. FE-SEM images of the (a) as-deposited CIGS film and the CIGS films selenized using mixing powders with weight ratios of alumina to selenium of (b) 0:0, (c) 12:1, (d) 8:1, (e) 6:1 and (f) 4:1. The CIGS precursor film was fabricated using a single quaternary CIGS target with the nominal compositions of $\text{Cu}_{0.9}(\text{In}_{0.7}\text{Ga}_{0.3})\text{Se}_{2.5}$.

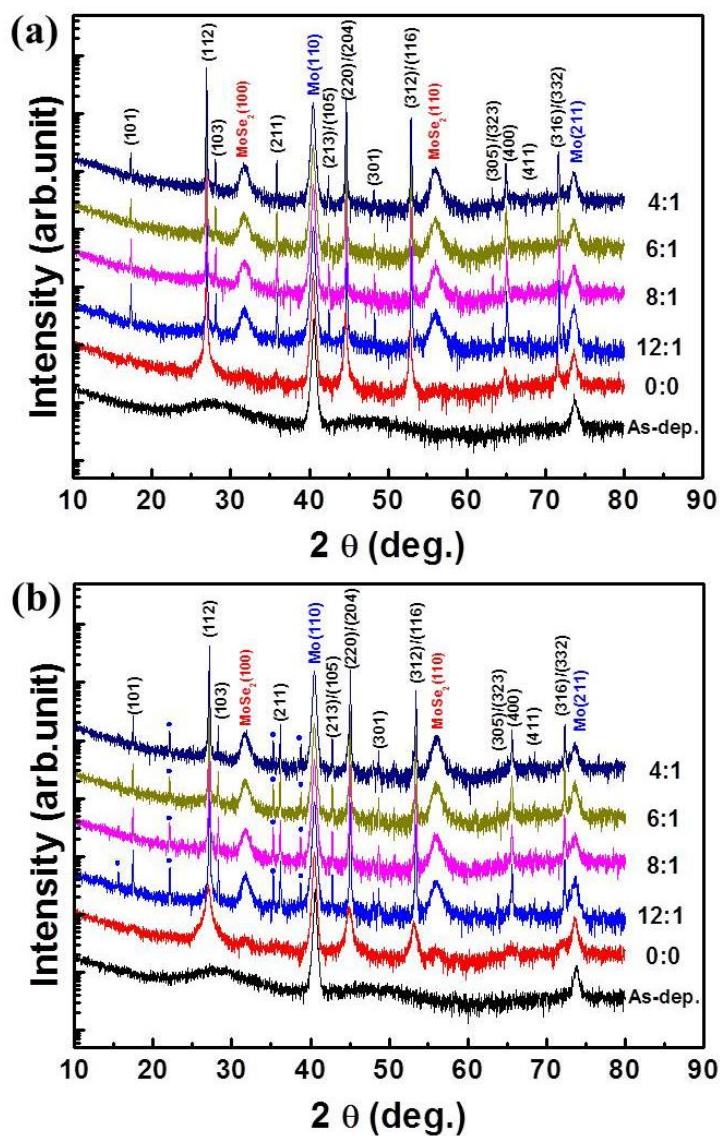


Fig. 5.13. XRD patterns before and after selenization of the CIGS precursor films fabricated using the single quaternary CIGS targets with the nominal compositions of (a) $\text{Cu}_{0.9}(\text{In}_{0.7}\text{Ga}_{0.3})\text{Se}_2$ and (b) $\text{Cu}_{0.9}(\text{In}_{0.7}\text{Ga}_{0.3})\text{Se}_{2.5}$. The CIGS films were selenized using mixing powders with the weight ratios of alumina to selenium of 0:0, 12:1, 8:1, 6:1 and 4:1, respectively.

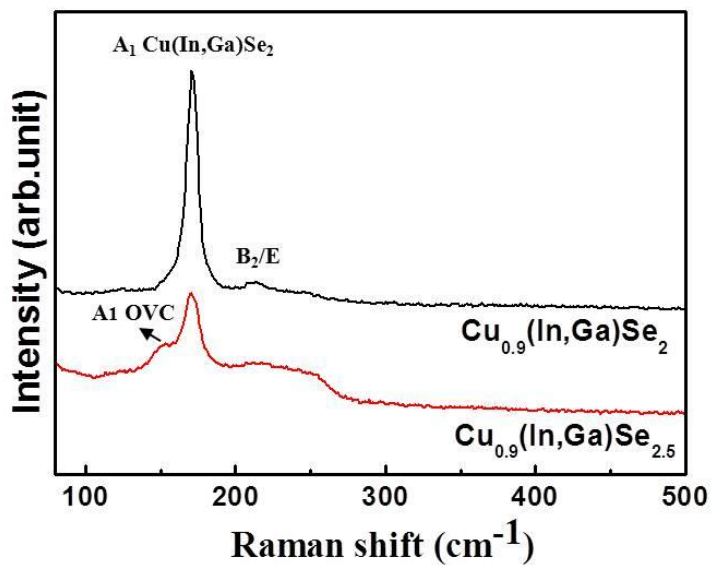


Fig. 5.14. Raman spectra after selenization of the CIGS films fabricated using the single quaternary CIGS targets with the nominal compositions of $\text{Cu}_{0.9}(\text{In}_{0.7}\text{Ga}_{0.3})\text{Se}_2$ and $\text{Cu}_{0.9}(\text{In}_{0.7}\text{Ga}_{0.3})\text{Se}_{2.5}$. The CIGS films were selenized using mixing powders with the weight ratio of alumina to selenium of 8:1.

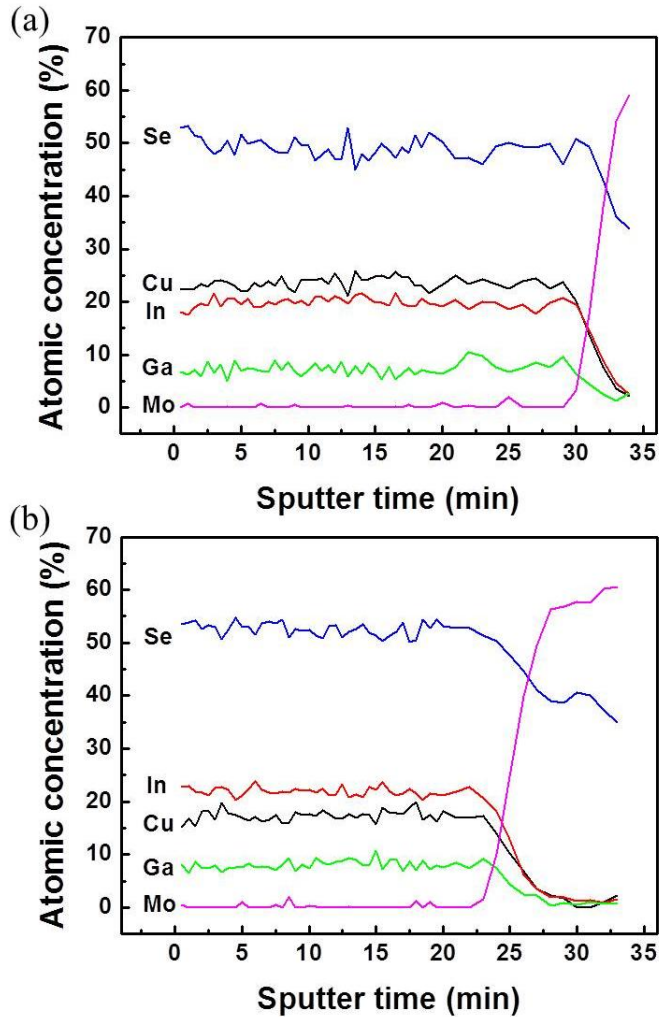


Fig. 5.15. Auger electron spectroscopy (AES) depth profiles after selenization of the CIGS films fabricated using the single quaternary CIGS targets with the nominal compositions of (a) $\text{Cu}_{0.9}(\text{In}_{0.7}\text{Ga}_{0.3})\text{Se}_2$ and (b) $\text{Cu}_{0.9}(\text{In}_{0.7}\text{Ga}_{0.3})\text{Se}_{2.5}$. The CIGS films were selenized using mixing powders with the weight ratio of alumina to selenium of 8:1.

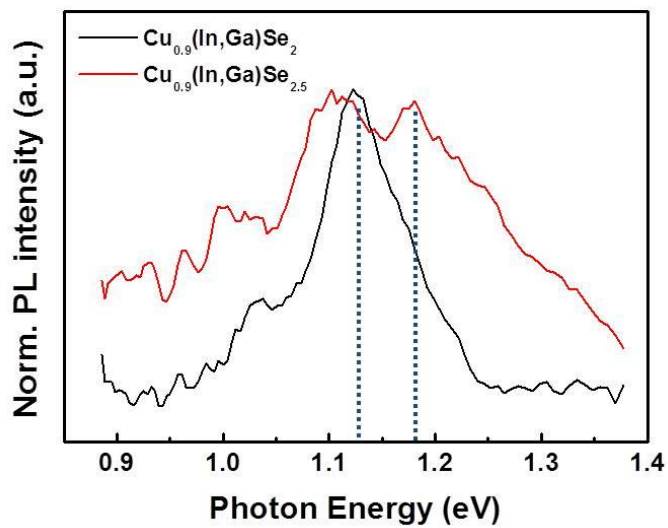


Fig. 5.16. Photoluminescence (PL) spectra after selenization of the CIGS films fabricated using the single quaternary CIGS targets with the nominal compositions of $\text{Cu}_{0.9}(\text{In}_{0.7}\text{Ga}_{0.3})\text{Se}_2$ and $\text{Cu}_{0.9}(\text{In}_{0.7}\text{Ga}_{0.3})\text{Se}_{2.5}$. The CIGS films were selenized using mixing powders with the weight ratio of alumina to selenium of 8:1.

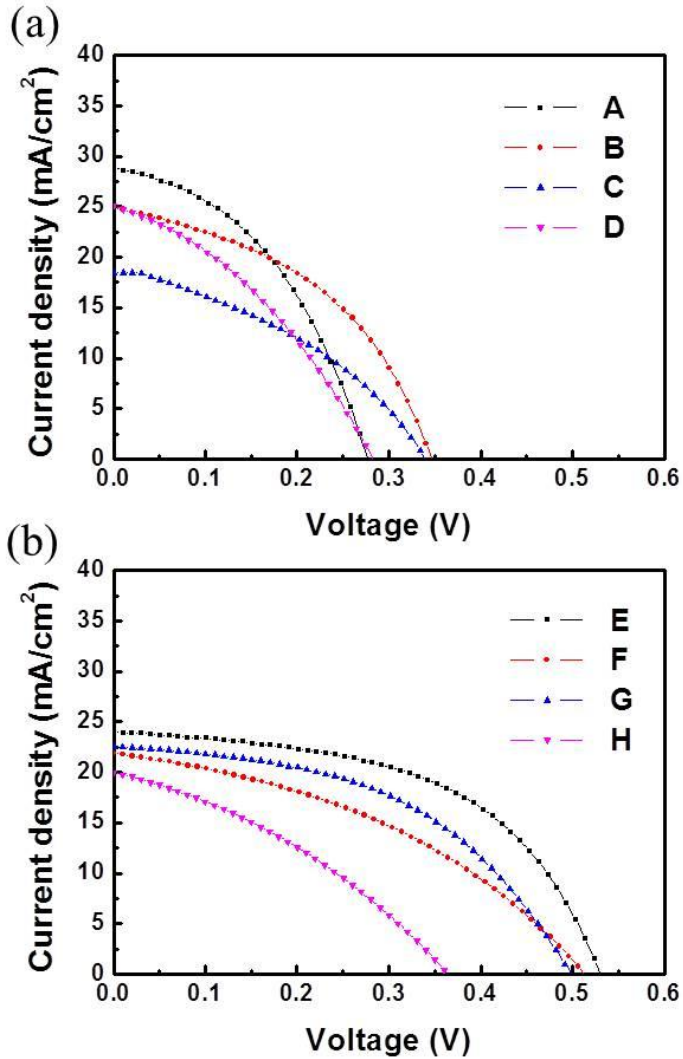


Fig. 5.17. Current-voltage characteristics of the CIGS solar cells fabricated using the single CIGS targets with the nominal compositions of (a) $\text{Cu}_{0.9}(\text{In,Ga})\text{Se}_2$ and (b) $\text{Cu}_{0.9}(\text{In,Ga})\text{Se}_{2.5}$. Detail conditions and values of the sample A to H are in table 5.6.

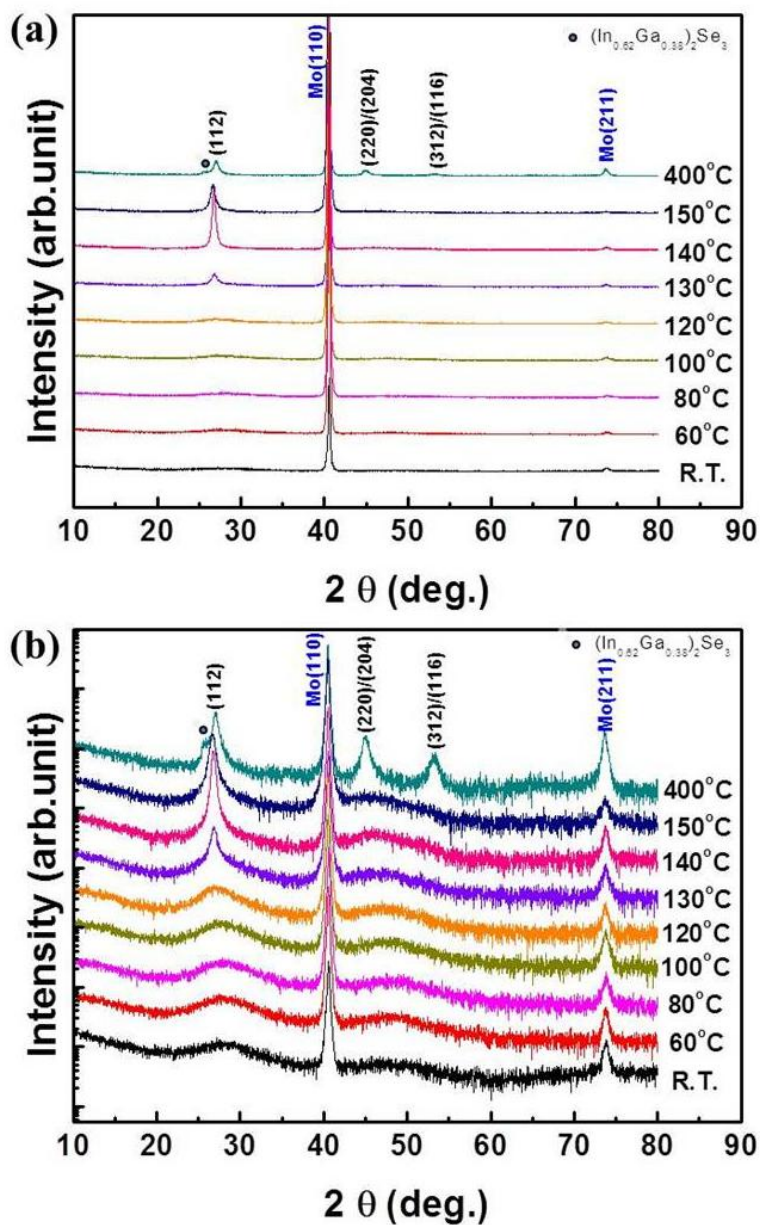


Fig. 5.18. (a) Linear scale and (b) logarithmic scale XRD patterns of the as-deposited CIGS films deposited at various temperatures using a single quaternary $\text{Cu}_{0.9}(\text{In}_{0.7}\text{Ga}_{0.3})\text{Se}_{2.5}$ target.

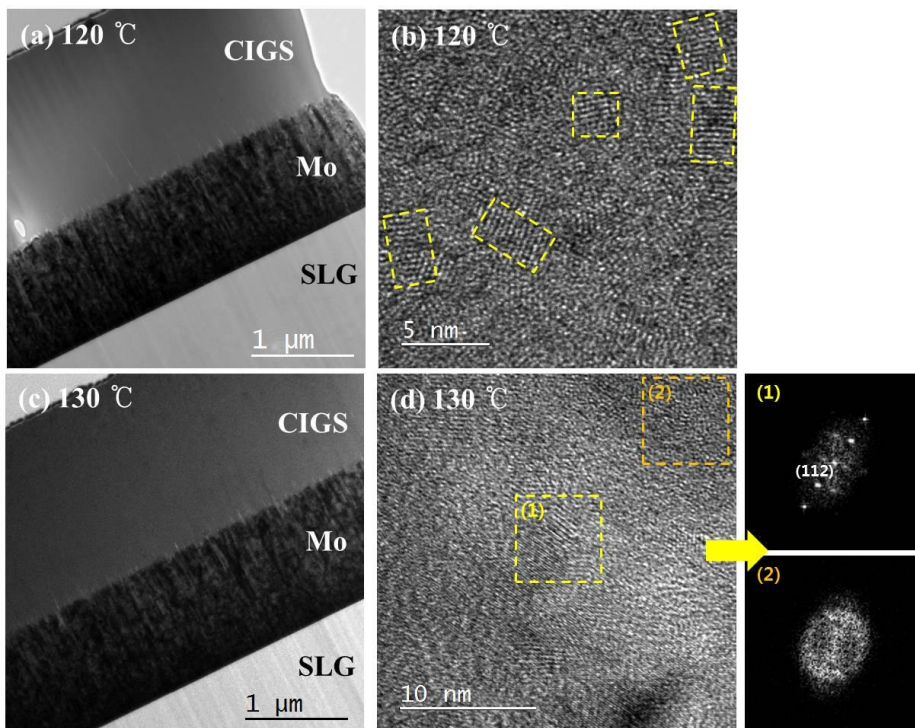


Fig. 5.19. (a), (c) TEM bright-field images and (b), (d) high resolution TEM images of the CIGS precursor films deposited at 120 and 130 °C. And Fast Fourier Transformation (FFT) patterns of region (1) and (2) in figure (d).

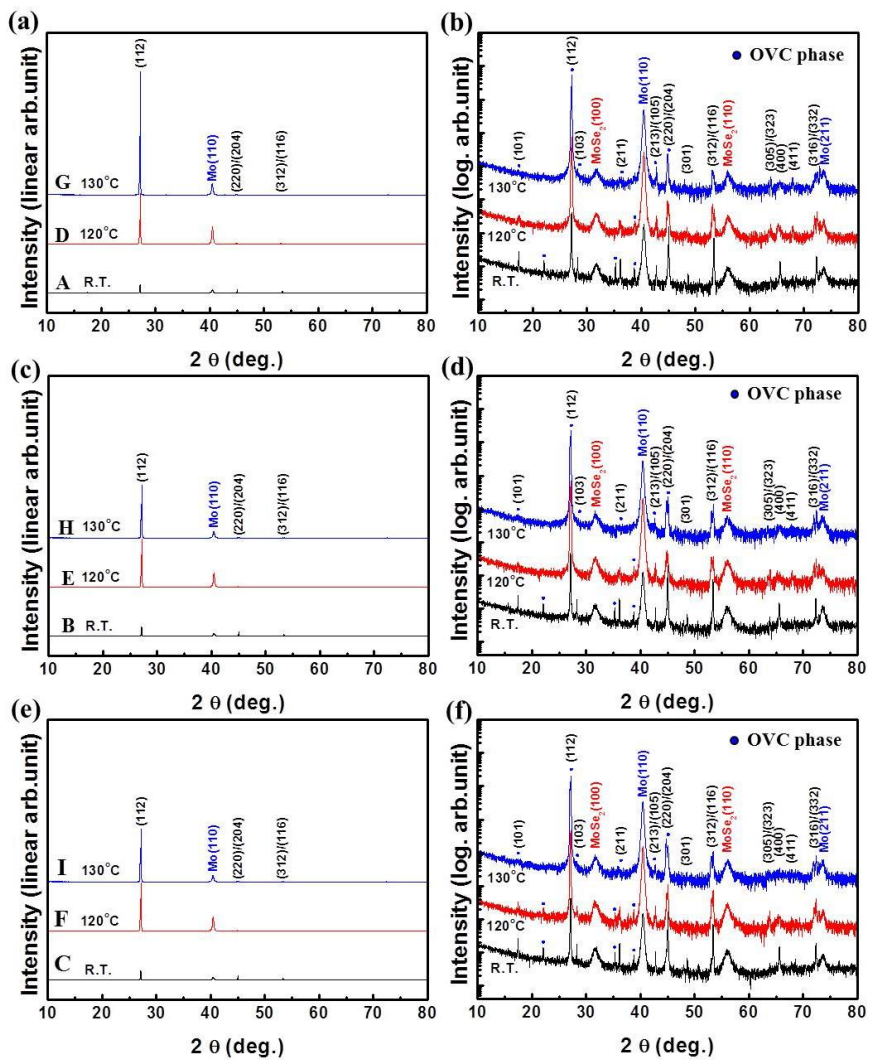


Fig. 5.20. XRD patterns of the CIGS films selenized using mixing powders with the weight ratios of alumina to selenium of (a)(b) 8:1, (c)(d) 6:1 and (e)(f) 4:1.

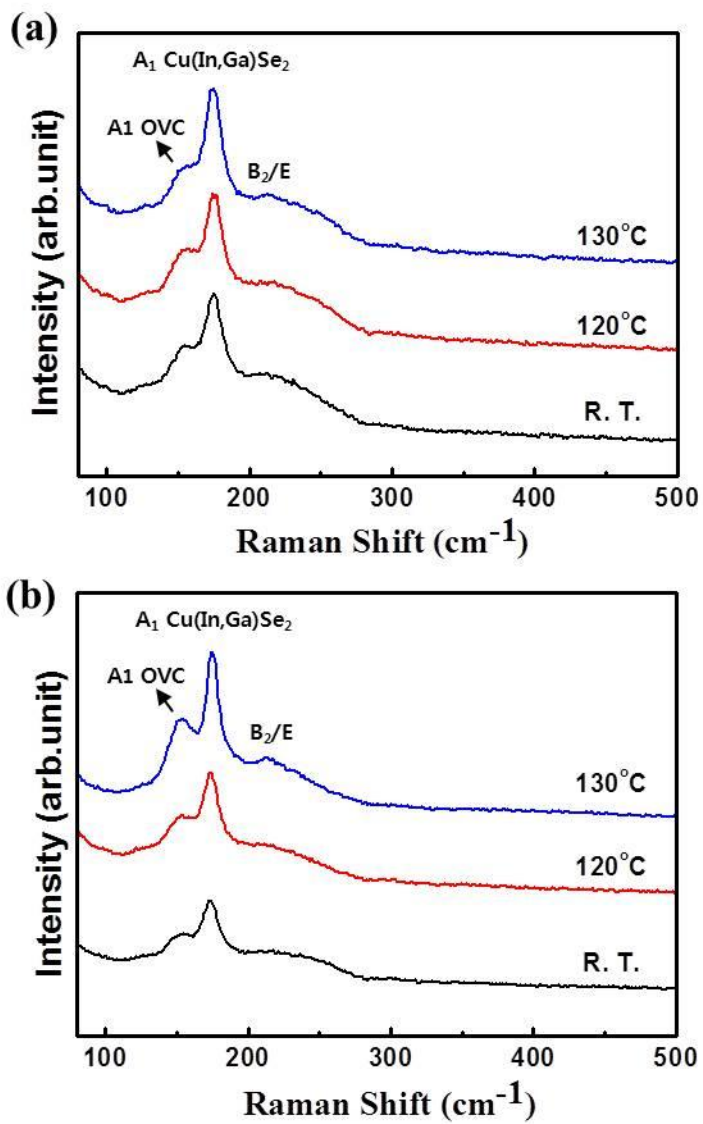


Fig. 5.21. Raman spectra of the CIGS films selenized using mixing powders with the weight ratios of alumina to selenium of (a) 8:1 and (b) 4:1

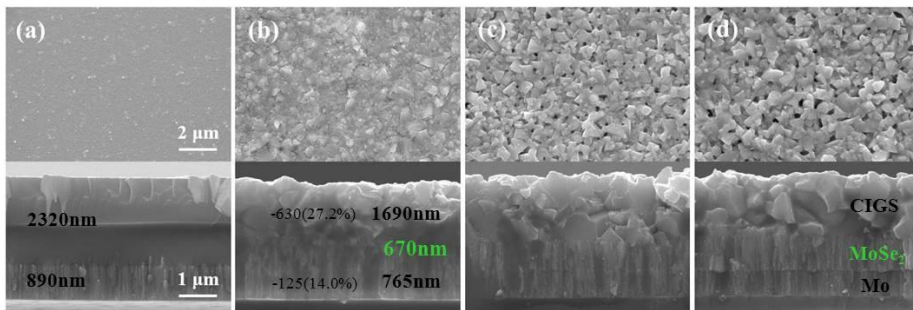


Fig. 5.22. FE-SEM images of the (a) as-deposited CIGS film deposited at room temperature and the CIGS films selenized using mixing powders with weight ratios of alumina to selenium of (b) 8:1, (c) 6:1 and (d) 4:1. CIGS precursor films were fabricated using a single quaternary CIGS target with the nominal composition of $\text{Cu}_{0.9}(\text{In}_{0.7}\text{Ga}_{0.3})\text{Se}_{2.5}$.

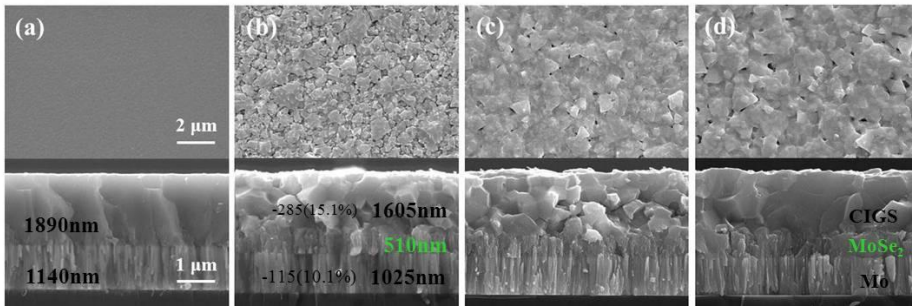


Fig. 5.23. FE-SEM images of the (a) as-deposited CIGS film deposited at 120 °C and the CIGS films selenized using mixing powders with weight ratios of alumina to selenium of (b) 8:1, (c) 6:1 and (d) 4:1. CIGS precursor films were fabricated using a single quaternary CIGS target with the nominal composition of $\text{Cu}_{0.9}(\text{In}_{0.7}\text{Ga}_{0.3})\text{Se}_{2.5}$.

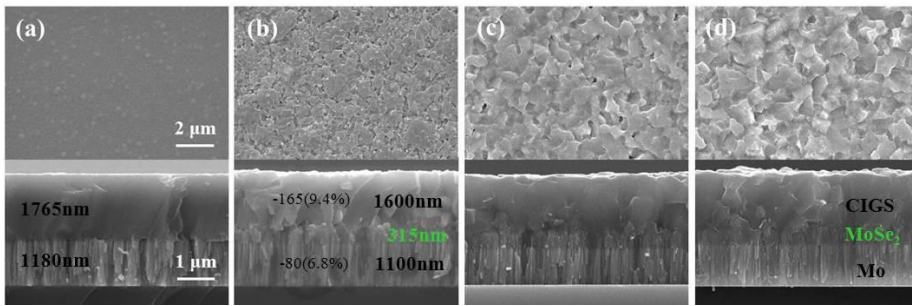


Fig. 5.24. FE-SEM images of the (a) as-deposited CIGS film deposited at 130 °C and the CIGS films selenized using mixing powders with weight ratios of alumina to selenium of (b) 8:1, (c) 6:1 and (d) 4:1. CIGS precursor films were fabricated using a single quaternary CIGS target with the nominal composition of $\text{Cu}_{0.9}(\text{In}_{0.7}\text{Ga}_{0.3})\text{Se}_{2.5}$.

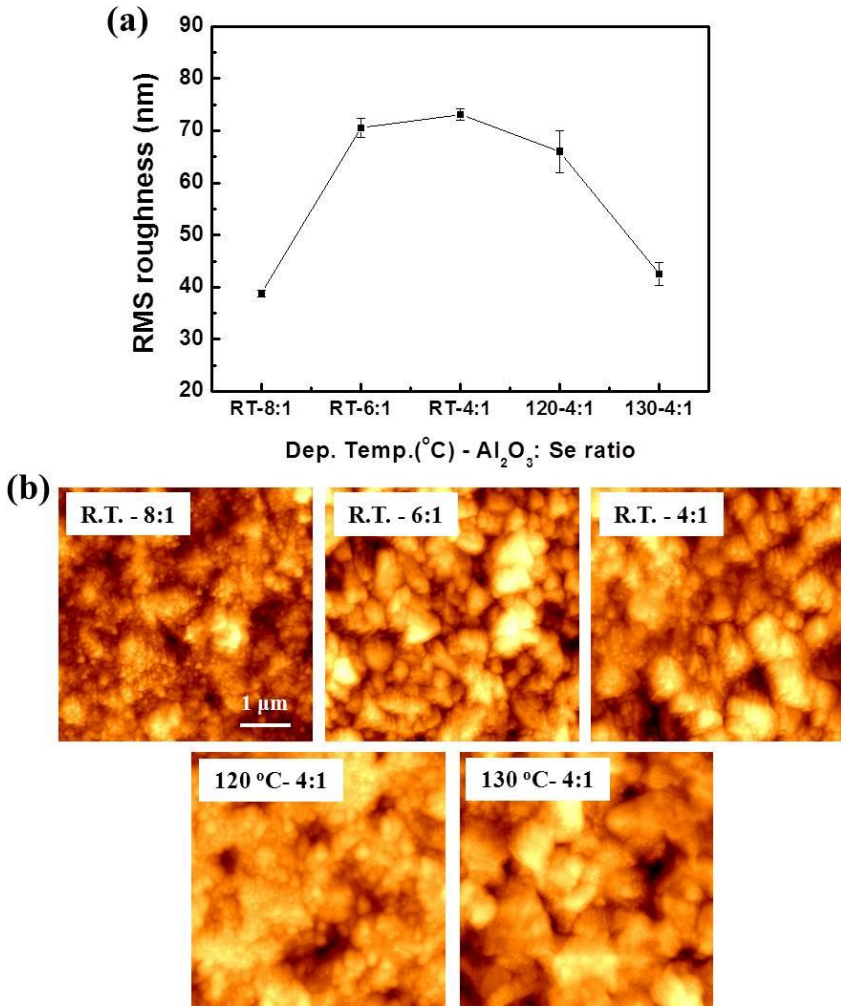


Fig. 5.25. (a) RMS roughness and (b) AFM image of the CIGS films as a function of deposition temperature and selenization condition with various weight ratios of alumina to selenium. Details for the deposition temperature and weight ratio of alumina to selenium are given in the figure.

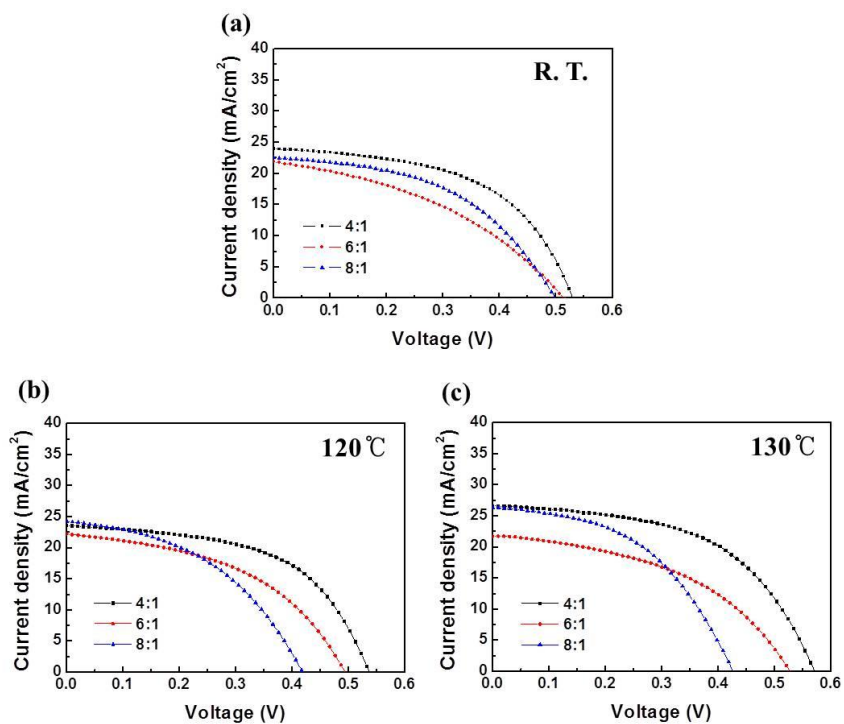


Fig. 5.26. Current-voltage characteristics of the CIGS solar cells fabricated using the CIGS precursor films deposited at (a) room temperature, (b) 120 °C and (c) 130 °C. The CIGS precursor films were selenized using mixing powders with weight ratios of alumina to selenium of 8:1, 6:1 and 4:1, respectively.

Chapter 6. Summary

In this thesis, the properties of CIGS films and CIGS solar cells prepared by RF sputtering of single CIGS targets were investigated. In addition, antireflection (AR) coating and transparent conducting Al-doped ZnO (AZO) films was studied, which are necessary to enhance conversion efficiency.

First, multi-layer antireflection (AR) coatings were investigated. For this study, ZnS and ZnS-MgF₂ composite films were prepared on soda-lime glass substrates and their optical constants were determined by envelope method. And MgF₂ film was deposited on GaAs substrate by rf magnetron sputtering and their optical constants were determined by spectroscopic ellipsometry. In particular, ZnS-MgF₂ composite films were fabricated by co-sputtering of ZnS and MgF₂ target to obtain intermediate refractive index material for a middle layer in the triple-layer AR coating and these films exhibited the desired intermediate refractive index. All films were highly transparent in the range from visible and near-infrared (IR). Based on the extracted optical constants, single-, double- and triple-layer AR coatings on GaAs substrates were designed by using a quarter-wave thickness at a normal incidence and fabricated by rf magnetron sputtering. The experimental results of AR coating were compared to simulated results. Experimental result was consistent with the simulated result. Low reflectance could be obtained from single-layer AR coating only at a specific wavelength and could be obtained from multi-layer AR coating at wide wavelength regime.

Second, the characteristics of the transparent conducting Al-doped ZnO

(AZO) films were investigated. AZO films were deposited on soda-lime glass substrates by using dc magnetron sputtering as a function of argon gas pressure, O₂/Ar gas ratio and substrate temperature, and their electrical and optical properties were investigated. As a result, the resistivity of the AZO films decreased with decreasing argon gas pressure or O₂/Ar gas ratio. As the substrate temperature was increased, resistivity decreased continuously and the lowest value of resistivity was obtained at the temperature of 250 °C in pure Ar and 250-300 °C in O₂/Ar ratio of 1.23%, respectively. The higher substrate temperature increased the resistivity a little. The transmittance was found to be very sensitive to O₂/Ar gas ratio and substrate temperature. Addition of a very small amount of oxygen to argon (1.23% of O₂/Ar ratio) or slight increase of the substrate temperature from room temperature to 150 °C enhanced the transmittance in visible region remarkably. Conclusively, the AZO films with low resistivity of order of 10⁻⁴ Ωcm and high transparency in visible region could be prepared at the substrate temperatures of above 150 °C (the lowest resistivity of 3.19 × 10⁻⁴ Ωcm at 250 °C) by dc magnetron sputtering.

Third, the properties of CIGS absorber layers prepared by RF sputtering without selenization were investigated. Employing various single CIGS sputtering targets with the nominal compositions of Cu_x(In_{0.7}Ga_{0.3})Se_y (where x=0.95 and 1, y=2 to 2.5), CIGS films were deposited on Mo coated soda lime glass (SLG) substrates by using RF magnetron sputtering. When the CIGS precursor film deposited at room temperature using a stoichiometric CIGS target was annealed in an Ar atmosphere, grain growth of the CIGS film did not occur regardless of the post-annealing temperature. Grain size of the CIGS

films was increased with increasing a deposition temperature. However, rough and porous surface morphology with the faceted grains was obtained and therefore very low efficiencies were achieved. For enhancing the efficiency and obtaining the smooth surface morphology, various CIGS targets with the nominal compositions of $\text{Cu}_{0.95}(\text{In}_{0.7}\text{Ga}_{0.3})\text{Se}_{2.5}$ and $\text{Cu}_{0.95}(\text{In}_{0.7}\text{Ga}_{0.3})\text{Se}_{2.1}$ were used to fabricate CIGS absorber layer. Grain size of these films was smaller than that of the CIGS film fabricated using a stoichiometric CIGS target. This result is thought to be caused by the Cu-poor composition of these CIGS targets. Although the CIGS films with a smoother surface morphology can be obtained by using Cu-poor CIGS targets, surface morphology becomes rough with increasing deposition temperature. And the films showed the Se-deficient composition. Conversion efficiency of about 2% was obtained from the CIGS solar cell fabricated using the $\text{Cu}_{0.95}(\text{In}_{0.7}\text{Ga}_{0.3})\text{Se}_{2.5}$ target. Meanwhile, for supplement of selenium, CIGS films fabricated by using the single target of $\text{Cu}(\text{In}_{0.7}\text{Ga}_{0.3})\text{Se}_{2.5}$ powder were annealed in Ar atmosphere with selenium. These films showed the densely packed surface morphology. Conversion efficiency was enhanced. Consequentially, selenization process is beneficial to improvement of structural and electrical properties. Hence, in the next study, the effect of selenization of CIGS precursor film was systematically investigated.

Finally, the characteristics of CIGS absorber layers after selenization of CIGS precursor film deposited at room temperature were systematically investigated. In this study, the CIGS targets with various compositions of $\text{Cu}_x(\text{In}_{0.7}\text{Ga}_{0.3})\text{Se}_y$ (where $x=0.9, 1$; $y=2, 2.2, 2.5$) were fabricated. Utilizing these targets, the CIGS precursor films were deposited by RF magnetron

sputtering and then selenized in a tube furnace under Se atmosphere using Se powder. From the stoichiometric CIGS target, Cu-rich CIGS films were obtained and very low conversion efficiencies were obtained due to inappropriate composition and porous and rough surface morphology with large grains. In contrast, the CIGS films fabricated by using the Cu-poor CIGS target showed the device-quality stoichiometry ratio and densely packed surface morphology with small grains, as well as the chalcopyrite structure without the second phases. Increase of the Se content in the single CIGS target led to decrease of the Cu content and increase of the (In+Ga) content in the CIGS film, which created the ordered vacancy compound (OVC) phases and increased the band gap (E_g) of the CIGS film resulting in increase of the open-circuit voltage (V_{oc}). The difference between $E_g/q - 0.5V$ and V_{oc} was remarkably decreased with the formation of the OVC phases. The highest efficiency of 6.88% could be achieved from the CIGS solar cell fabricated by using the Cu-poor and Se-excess target with the nominal composition of $Cu_{0.9}(In_{0.7}Ga_{0.3})Se_{2.2}$. Consequently, the composition of the single CIGS target was found to play a key role in the structural and electrical properties of the CIGS film and CIGS thin film solar cell efficiency.

Characteristics of CIGS films selenized using mixing powders with various weight ratios of alumina to selenium were investigated. For this experiment, the CIGS precursor films were deposited using the single CIGS targets with the nominal compositions of $Cu_{0.9}(In,Ga)Se_2$ and $Cu_{0.9}(In,Ga)Se_{2.5}$. As the results, regardless of target composition, grain size was increased with increasing the Se ratio of mixing powder. The $MoSe_2$ layer was formed between the CIGS and the Mo layer and its thickness was also increased with

increasing the Se ratio of mixing powder. The MoSe₂-layer thickness of the CIGS film fabricated using the Cu_{0.9}(In_{0.7}Ga_{0.3})Se_{2.5} target is thicker than that of the CIGS film fabricated using the Cu_{0.9}(In_{0.7}Ga_{0.3})Se₂ target because of larger amount of Se in the CIGS film fabricated using the Cu_{0.9}(In_{0.7}Ga_{0.3})Se_{2.5} target. From the auger electron spectroscopy (AES) depth profiles, it was found that each element of the CIGS film was evenly distributed in the CIGS films without grading of elements. This means that the CIGS phases including the OVC phase are evenly distributed. The open-circuit voltages of the CIGS solar cells fabricated using the Cu_{0.9}(In_{0.7}Ga_{0.3})Se_{2.5} target were commonly higher than those of the solar cells fabricated using the Cu_{0.9}(In_{0.7}Ga_{0.3})Se₂ target. The open-circuit voltage of the CIGS solar cells fabricated using the Cu_{0.9}(In_{0.7}Ga_{0.3})Se_{2.5} target was decreased with decreasing Se ratio of mixing powder used for selenization.

Also, characteristics of CIGS films selenized using nanocrystalline precursor film were investigated. CIGS precursor films were deposited at various temperatures using a single quaternary Cu_{0.9}(In_{0.7} Ga_{0.3})Se_{2.5} target. Base on the results of XRD patterns and TEM images, as-deposited CIGS films fabricated at the substrate temperatures of 120 °C and 130 °C were considered as the nano-crystalline CIGS precursor films. The CIGS films were selenized at 475 °C for 30min. The CIGS films showed a (112) preferred orientation. All of the selenized CIGS films had the similar composition regardless of deposition temperature although Cu content in the film was slightly different. From the Raman spectra of the CIGS films, the existence of OVC phase which can lead to decrease of open-circuit voltage loss was identified. The CIGS film with smooth and dense surface

morphology as well as the large grain size was obtained by increase of Se ratio in a tube furnace and using the nano-crystalline CIGS precursor film. And the thickness of the MoSe₂ layer was decreased after selenization of the nano-crystalline CIGS precursor film compared to that of the amorphous CIGS precursor film. The highest efficiency was achieved from the CIGS solar cell fabricated using the nanocrystalline CIGS precursor film deposited at 130 °C and its value is 8.09 % with the open-circuit voltage of 0.571V, short-circuit current density of 26.58 mA/cm² and the fill factor of 53.28%. This result is thought to be achieved by the beneficial factors such as the existence of an OVC phase, the thickness reduction of a MoSe₂ layer, smooth surface morphology and the decrease of defect density achieved by dense CIGS film with large grain.

Publications

Papers (SCI journals)

1. Sung-Mok Jung, Bong-Geun Song, Young-Hwan Kim, Jong-Ku Park, Seong-Il Kim, and Sang-Im Yoo, Cu(In,Ga)Se₂ thin film solar cells fabricated via RF sputter method using single CIGS targets, to be submitted.
2. Sung-Mok Jung, Young-Hwan Kim, Jong-Ku Park, Seong-Il Kim, and Sang-Im Yoo, Characteristics of CIGS absorber layers and devices fabricated using nanocrystalline CIGS precursor film, to be submitted.
3. Sung-Mok Jung, Young-Hwan Kim, Seong-Il Kim, and Sang-Im Yoo, Characteristics of transparent conducting Al-doped ZnO films prepared by dc magnetron sputtering, Current Applied Physics 11 (2011) S191.
4. Sung-Mok Jung, Young-Hwan Kim, Seong-Il Kim, and Sang-Im Yoo, Design and fabrication of multi-layer antireflection coating for III-V solar cell, Current Applied Physics 11 (2011) 538.
5. Sung-Mok Jung, Sang-Im Yoo, Young-Hwan Kim, Yong Tae Kim and Suk-Kyoung Hong, Characteristics of Sol-Gel Derived Bi_{3.15}Nd_{0.85}Ti₃O₁₂ Thin Films on Al₂O₃/Si for Metal-Ferroelectric-Insulator-Semiconductor Structure, Journal of the Korean Physical Society 49 (2006) S552.

Contributed papers (SCI journals)

6. Sung-Yun Lee, Young-Hwan Kim, Kyoung Jin Choi, Sung-Mok Jung and Sang-Im Yoo, Effect of copper-oxide segregation on the dielectric properties of $\text{CaCu}_3\text{Ti}_4\text{O}_{12}$ thin films fabricated by pulsed-laser deposition, Thin Solid Films 518 (2010) 5711.
7. D. S. Kim, C. E. Lee, Y. H. Kim, S. M. Jung, and Y. T. Kim, Growth and characterization of $\text{Pr}_{0.7}\text{Ca}_{0.3}\text{MnO}_3$ thin films for resistance random access memory, Journal of the Korean Physical Society 49 (2006) S557.

초 록

태양전지는 에너지 위기와 환경오염과 같은 문제들이 대두됨에 따라 많은 관심을 받아 왔다. 특히, 박막형 태양전지는 원료절감과 경량으로 만들 수 있다는 장점들 때문에 널리 연구되어 왔으며, 이중 CIGS (Cu(In,Ga)Se_2) 태양전지는 높은 광전변환효율과 안정성이 우수하다는 장점들 때문에 전 세계적인 관심을 받아 왔다. 하지만, 20% 이상의 고효율을 달성한 CIGS 태양전지 제조방법은 비교적 공정이 복잡한 삼단계 동시증발법(three-stage co-evaporation process)에 의해 달성 되어왔으며, 이 방법은 대면적에서 균일한 조성을 가진 박막을 제조하기가 어렵다는 단점을 갖는다. 따라서 본 학위 논문에서는 대면적에서 균일한 조성을 얻기 용이하며, 공정을 간략화 할 수 있는 방법을 채택 하였으며, 이를 위해 다양한 조성의 CIGS 단일 타겟들을 사용하여 RF(radio frequency) 스퍼터링 법으로 제조한 CIGS 박막과 CIGS 태양전지의 특성에 대해 살펴보았다. 추가적으로, 효율 향상을 위해 반드시 필요한 무반사 코팅 및 AZO(Al-doped ZnO) 투명전극층의 박막 특성에 대해 살펴보았다. 본 연구의 주요결과들은 다음과 같다.

첫째, ZnS 와 MgF_2 를 이용하여 제조한 이중 및 삼층 구조 등의 다층 무반사 코팅들의 특성에 대해 살펴보았다. 이 연구를 위해, ZnS와 ZnS- MgF_2 혼합 박막을 각각 소다라임유리(soda-lime glass) 기판 위에 증착하여 포락선 방법(envelope method)에 의해 광학상수들을 결정하였으며, 또한 GaAs 기판위에 MgF_2 박막을 증착하여 분광 타원계측법(spectroscopic ellipsometry)에 의해

광학상수들을 결정하였다. 특히, 삼층 구조 무반사 코팅의 중간층에 필요한 ZnS와 MgF₂ 사이의 중간 값의 굴절률을 가진 박막을 얻기 위해 ZnS와 MgF₂ 타겟을 동시 스퍼터링(co-sputtering)하였고, ZnS-MgF₂ 혼합 박막을 제조하여 중간 값의 굴절률을 가진 박막을 성공적으로 제조 할 수 있었다. 제조된 모든 박막들은 가시광 및 근적외선 범위에서 투명했다. ZnS-MgF₂ 혼합 박막의 경우, Mg와 F의 양이 증가함에 따라 광 흡수단은 단파장쪽으로 이동하였으며, 굴절률은 감소했다. 본 실험을 통해 구한 광학 상수들을 사용하여, GaAs에 대한 단층, 이중 및 삼층의 무반사 코팅은 설계 되었으며, 이것을 바탕으로하여 각 코팅층들을 RF 스퍼터링에 의해 제조하였고, 실험결과들을 설계된 결과들과 비교하였다. 단층 무반사 코팅을 통해 특정 파장에서 낮은 반사율을 얻을 수 있었으며, 다층 무반사 코팅을 통해 넓은 범위의 파장에서 낮은 반사율을 얻을 수 있었다. 추가적으로, 다층 무반사 코팅의 반사율에 대한 입사각 의존성을 살펴보았으며, 코팅 층의 수에 따라 다른 특성들을 나타냈다.

둘째, AZO 투명전극을 DC(direct current) 스퍼터링법으로 제조함 있어서, Ar 가스 압력, O₂/Ar 가스 비율 및 기판온도 등의 공정변수들이 AZO 투명전극의 전기적, 광학적 특성에 미치는 영향들을 살펴보았다. Ar 가스 압력 및 O₂/Ar 가스 비율이 작아 질수록 AZO 박막의 비저항은 감소했다. 또한, 기판 온도를 상온으로부터 증가시킬수록 비저항 값은 감소 하였으며, 250℃에서 가장 작은 비저항값을 얻을 수 있었으나, 기판 온도를 더욱 증가시켰을 때 비저항 값은 다소 증가하였다. 투과도는 O₂/Ar 가스 비율 및 기판 온도에 민감 했으며, Ar에 산소(1.23% 의 O₂/Ar

비율)를 다소 추가하거나, 상온으로부터 150℃까지 기판온도를 증가시켰을 때 가시광 영역에서의 투과도를 향상시킬 수 있었다. 결론적으로, 150℃ 이상의 기판 온도에서 AZO 박막을 증착했을 때, $\sim 10^{-4} \Omega\text{cm}$ 크기의 낮은 비저항과 가시광 영역에서 높은 투과도를 갖는 AZO 박막을 제조할 수 있었다.

셋째, 셀렌화 공정없이 CIGS 단일 타겟의 RF 스퍼터링에 의해 제조된 CIGS 흡수층의 특성에 대해 살펴보았다. 본 연구를 위해, $\text{Cu}_x(\text{In}_{0.7}\text{Ga}_{0.3})\text{Se}_y$ ($x=0.95\sim 1$, $y=2\sim 2.5$)의 공칭 조성들을 가진 다양한 CIGS 단일 타겟들을 제조하였으며, 이 CIGS 타겟들을 사용하여 Mo이 코팅된 소다라미유리 기판위에 RF 스퍼터링법을 통해 CIGS 박막을 제조하였다. 먼저, 정량 조성의 CIGS 타겟을 사용하여 상온에서 박막을 증착하였고, 이 CIGS 박막은 Ar 분위기에서 후 열처리 했을 때 열처리 온도와 상관없이 결정립 성장은 일어나지 않았으나, 증착 온도를 증가시켜 감에 따라 결정립의 크기는 증가하였다. 그러나 면들로 구성된 형상의 결정립들(the faceted grains)로 이루어진 거칠고 공극이 많은 표면 형상의 박막이 제조되었고, 따라서 효율은 매우 낮았다. 고른(평탄한) 표면 형상 및 효율 향상을 달성하기 위해 $\text{Cu}_{0.95}(\text{In}_{0.7}\text{Ga}_{0.3})\text{Se}_{2.5}$ 와 $\text{Cu}_{0.95}(\text{In}_{0.7}\text{Ga}_{0.3})\text{Se}_{2.1}$ 의 공칭조성을 가진 타겟들을 사용하여 CIGS 흡수층을 제조하였다. 이러한 타겟들을 사용하여 제조된 박막의 결정립 크기는 정량 조성타겟을 사용하여 제조한 박막의 결정립보다 작았으며, 이것은 위의 CIGS 타겟들의 Cu 부족한 조성에 의해 야기된 결과라 사료된다. 비록 Cu가 부족한 CIGS 타겟을 사용 하여 더 고른 표면 형상을 가진 CIGS 박막을 제조할 수 있었지만, 표면 형상은 증착온도를 증가 시켜 감에 따라 거칠어 졌다. 결과적으로,

$\text{Cu}_{0.95}(\text{In}_{0.7}\text{Ga}_{0.3})\text{Se}_{2.5}$ 타겟을 사용하여 제조된 태양전지로부터 약 2%의 광전 변환 효율을 달성 할 수 있었으나, 더욱 적은 양의 Se을 함유하고 있는 $\text{Cu}_{0.95}(\text{In}_{0.7}\text{Ga}_{0.3})\text{Se}_{2.1}$ 타겟을 사용해서 제조된 태양전지는 더욱 낮은 효율을 나타냈으며, 위의 세 가지 타겟으로 제조된 모든 CIGS 박막들은 공통적으로 Se이 부족한 조성을 가졌다. 그러므로 Se의 보충을 위해 타겟의 소결공정을 생략하고 $\text{Cu}(\text{In}_{0.7}\text{Ga}_{0.3})\text{Se}_{2.5}$ 의 공칭조성을 가진 파우더의 압착에 의해 제조한 타겟을 이용하여 CIGS 박막을 제조하였다. 결과적으로 CIGS 박막 내의 Se 함유량은 증가하였으나, 위의 경우와 마찬가지로 거칠고 공극이 많은 표면 형상을 나타냈으며, 효율은 매우 낮았다. 그러나 이 박막들은 Se 분위기에서 열처리 했을 때, 밀도가 높은 표면 형상을 가진 박막으로 바뀌었으며, 광전변환 효율은 3.3%까지 향상되었다. 이러한 결과들을 고려해 볼 때, 셀렌화 공정은 단일 CIGS 타겟을 사용하여 제조된 CIGS 박막의 구조적, 전기적 특성들을 개선시키며, 따라서 다음의 연구들을 통해 CIGS 박막의 셀렌화 후 특성들에 대해 체계적으로 살펴 보았다.

이 연구를 위해 우선, 상온에서 증착한 CIGS 전구체 박막의 셀렌화 후 특성에 대해 체계적으로 살펴보았다. $\text{Cu}_x(\text{In}_{0.7}\text{Ga}_{0.3})\text{Se}_y$ ($x=0.9, 1; y=2, 2.2, 2.5$)로 구성된 다양한 공칭 조성을 가진 단일 타겟들을 제조하였으며, 이러한 조성의 타겟들을 RF 마그네트론 스퍼터링에 의해 증착하여 CIGS 전구체 박막을 제조하였다. 제조된 CIGS 전구체 박막은 셀레늄 파우더를 사용하여 조성한 셀레늄 분위기의 튜브퍼니스 안에서 셀렌화 하였다. 정량조성의 CIGS 타겟을 사용하여 제조한 CIGS 전구체 박막은 셀렌화 후 Cu가 과량 함유된 CIGS 박막을 형성 했으며, 이것은 산발적으로 Cu_{2-x}Se 상을

형성시켰다. 또한 큰 결정립의 형성과 함께 거칠고 공극이 많은 표면 형상을 나타냈다. 결과적으로 이 박막을 사용하여 제조된 태양전지는 이러한 부적합한 표면 형상과 조성 때문에 매우 낮은 광전변환효율을 나타냈다. 이와 대조적으로, Cu-poor한 CIGS ($\text{Cu}_{0.9}(\text{In}_{0.7}\text{Ga}_{0.3})\text{Se}_2$) 타겟을 사용하여 제조된 CIGS 박막은 태양전지 소자에 적합한 화학량론비율(device-quality stoichiometry ratio)의 조성을 나타냈으며, 작은 결정립들로 구성된 밀도가 높은 표면 형상뿐 만 아니라 이차상이 없는 chalcopyrite CIGS 구조를 나타냈다. Cu-poor한 타겟에 Se의 함량을 증가시키기에 따라 CIGS 박막 내의 Cu 함량은 감소되었으며, (In+Ga) 함량은 증가 되었다. 이러한 박막 조성의 변화는 ordered vacancy compound (OVC) 상을 형성시켰고 CIGS 박막의 밴드갭을 증가시켜, 결국 개방전압(V_{oc} , open-circuit voltage)을 증가 시켰다. 특히, $E_g/q - 0.5V$ 와 V_{oc} 사이의 차이는 OVC 상의 형성과 함께 두드러지게 감소하였다. 결과적으로 $\text{Cu}_{0.9}(\text{In}_{0.7}\text{Ga}_{0.3})\text{Se}_{2.2}$ 의 공칭 조성 타겟을 사용하여 제조한 CIGS 태양전지로부터 6.88%의 광전 변환 효율을 달성 하였다. 위의 결과들을 미루어 볼 때, CIGS 단일 타겟의 조성은 CIGS 박막의 구조적, 전기적 특성 및 CIGS 태양전지 효율에 중요한 역할을 함을 알 수 있었다.

다음으로 셀렌화 분위기의 셀레늄 함량을 다양하게 변화시켜 셀렌화한 CIGS 박막들의 특성을 살펴보았다. 본 실험을 위해 $\text{Cu}_{0.9}(\text{In,Ga})\text{Se}_2$ 와 $\text{Cu}_{0.9}(\text{In,Ga})\text{Se}_{2.5}$ 의 공칭 조성을 가진 타겟들을 사용하였다. 타겟조성에 상관없이 셀렌화시 사용된 혼합 파우더의 Se 비율이 증가함에 따라(셀렌화 분위기의 셀레늄 함량증가) 결정립 크기는 증가 되었으며, CIGS 와 Mo층 사이에 형성된 MoSe_2

층의 두께 또한 증가하였다. 형성된 MoSe_2 층의 두께는 $\text{Cu}_{0.9}(\text{In}_{0.7}\text{Ga}_{0.3})\text{Se}_{2.5}$ 타겟을 사용했을 때 CIGS 전구체 박막이 더 많은 양의 Se을 함유 함으로 인해 $\text{Cu}_{0.9}(\text{In}_{0.7}\text{Ga}_{0.3})\text{Se}_2$ 타겟을 사용한 경우보다 더 두꺼웠다. 셀렌화 된 CIGS 박막의 깊이방향의 조성분석을 오제 전자 분광법(auger electron spectroscopy)으로 실시하였으며, CIGS 박막의 각 원소들은 조성의 변화 없이 고르게 분포하였다. 이것은 $\text{Cu}_{0.9}(\text{In}_{0.7}\text{Ga}_{0.3})\text{Se}_{2.5}$ 타겟을 사용하여 제조한 CIGS 전구체 박막을 셀렌화 했을 때 박막내에 CIGS 상과 OVC 상이 고르게 분포하고 있음을 나타낸다. 셀렌화 분위기의 셀레늄 함량과 상관없이, 일반적으로 $\text{Cu}_{0.9}(\text{In}_{0.7}\text{Ga}_{0.3})\text{Se}_{2.5}$ 타겟을 사용해서 제조한 CIGS 태양전지의 개방 전압은 $\text{Cu}_{0.9}(\text{In}_{0.7}\text{Ga}_{0.3})\text{Se}_2$ 타겟을 사용하여 제조한 CIGS 태양전지의 개방 전압보다 컸다. 하지만 셀렌화 분위기의 셀레늄 함량을 감소시킴에 따라 $\text{Cu}_{0.9}(\text{In}_{0.7}\text{Ga}_{0.3})\text{Se}_{2.5}$ 타겟을 사용해서 제조한 CIGS 태양전지의 개방전압은 감소 하는 경향을 나타냈다.

마지막으로 나노결정 CIGS 전구체 박막을 셀렌화 했을 때의 CIGS 박막 특성들을 살펴 보았다. 본 실험에서는 선행실험에서 큰 개방전압이 달성되어 고효율이 기대되는 $\text{Cu}_{0.9}(\text{In}_{0.7}\text{Ga}_{0.3})\text{Se}_{2.5}$ 의 공칭 조성 타겟을 사용 하였으며, 60°C 부터 150°C 까지의 다양한 온도에서 CIGS 전구체 박막을 증착하였다. 증착된 박막의 XRD 패턴과 TEM 사진 분석을 통해 나노결정 CIGS 박막이 120°C 와 130°C 에서 형성 되었음을 확인하였다. 이러한 나노결정 CIGS 전구체 박막들을 475°C 에서 30분 동안 셀렌화 하였고, 셀렌화 후 박막들은 (112) 우선 배향성을 나타냈다. 전구체 박막의 증착 온도에 상관없이, 셀렌화된 CIGS 박막들은 모두 비슷한 조성을

가졌으며, 정량 조성에 비해 Cu 함량이 적고, (In+Ga) 함량이 많았다. 다만 분광법에 의해 이 CIGS 박막들은 모두 개방전압의 손실을 줄일 것으로 기대되는 OVC 상을 포함 하고 있음을 확인 하였다. 특히, 나노결정 CIGS 전구체 박막을 셀레늄 함량을 증가시킨 분위기에서 셀렌화 하였을 때, 결정립이 크며 평탄하고 밀도가 높은 표면 형상을 나타냈다. 또한 상온에서 증착된 비정질 CIGS 전구체 박막의 경우 보다 나노 결정 CIGS 전구체 박막을 사용했을 때 더욱 얇은 MoSe₂층이 형성되었다. 본 연구에서 가장 높은 광전변환 효율은 130℃ 에서 증착된 나노결정 CIGS 전구체 박막을 사용해서 제조한 CIGS 태양전지로부터 달성되었으며, 0.571V 의 개방전압, 26.58 mA/cm² 의 단락전류밀도, 53.28%의 충전율과 함께 8.09%의 광전변환효율이 달성되었다. 이러한 결과는 OVC 상의 존재, MoSe₂ 층의 감소, 평탄한 표면 형상 및 큰 결정립들로 이루어진 밀도가 높은 박막 형성에 의한 결합 밀도의 감소 등이 태양전지 효율을 향상시키는 이로운 요인들로 작용했기 때문으로 사료된다.

주요어: CIGS 박막형 태양전지, 단일 사성분계 CIGS 타겟, 셀렌화, 나노결정 CIGS 전구체 박막, ordered vacancy compound (OVC) 상, ZnS, MgF₂, 무반사 코팅, 광학 상수, RF 마그네트론 스퍼터링, Al-doped ZnO, 기판온도, 산소분압, DC 마그네트론 스퍼터링.

학 번 : 2007-30808